NATIONAL TECHNICAL UNIVERSITY OF ATHENS

SCHOOL OF CHEMICAL ENGINEERING

Doctor of Philosophy Thesis

DIFFUSION OF AROMATICS IN SILICALITE-1: Predictions Using Hierarchical Molecular Simulations Based On Transition State Theory

PANAGIOTIS D. KOLOKATHIS

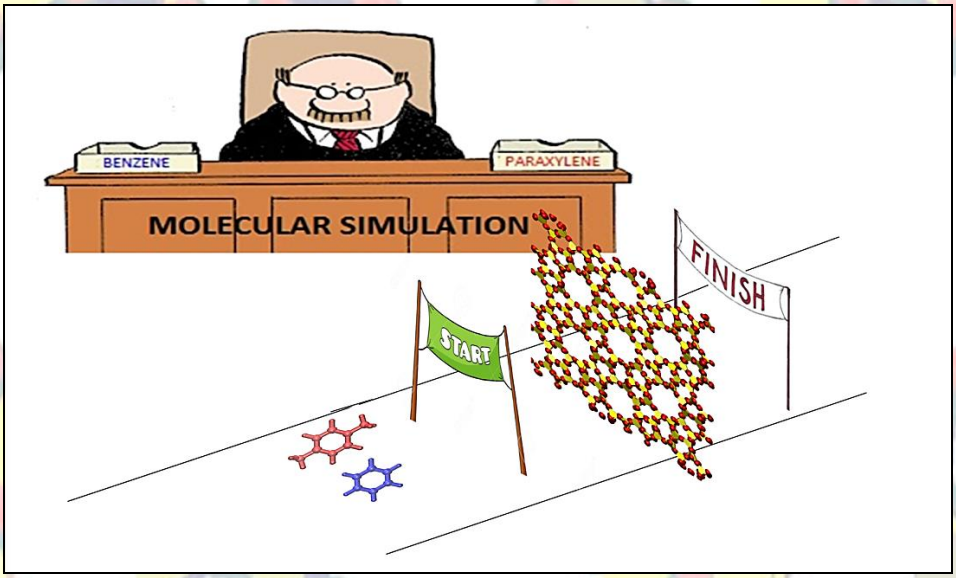

ATHENS, AUGUST 2016

ΕΘΝΙΚΟ ΜΕΤΣΟΒΙΟ ΠΟΛΥΤΕΧΝΕΙΟ

ΣΧΟΛΗ ΧΗΜΙΚΩΝ ΜΗΧΑΝΙΚΩΝ

ΔΙΔΑΚΤΟΡΙΚΗ ΔΙΑΤΡΙΒΗ

ΔΙΑΧΥΣΗ ΑΡΩΜΑΤΙΚΩΝ ΜΟΡΙΩΝ ΣΤΟ ΖΕΟΛΙΘΟ ΣΙΛΙΚΑΛΙΤΗ-1: Προβλέψεις από Ιεραρχικές Μοριακές Προσομοιώσεις Βασισμένες στη Θεωρία Μεταβατικών Καταστάσεων

ΠΑΝΑΓΙΩΤΗΣ Δ. ΚΟΛΟΚΑΘΗΣ

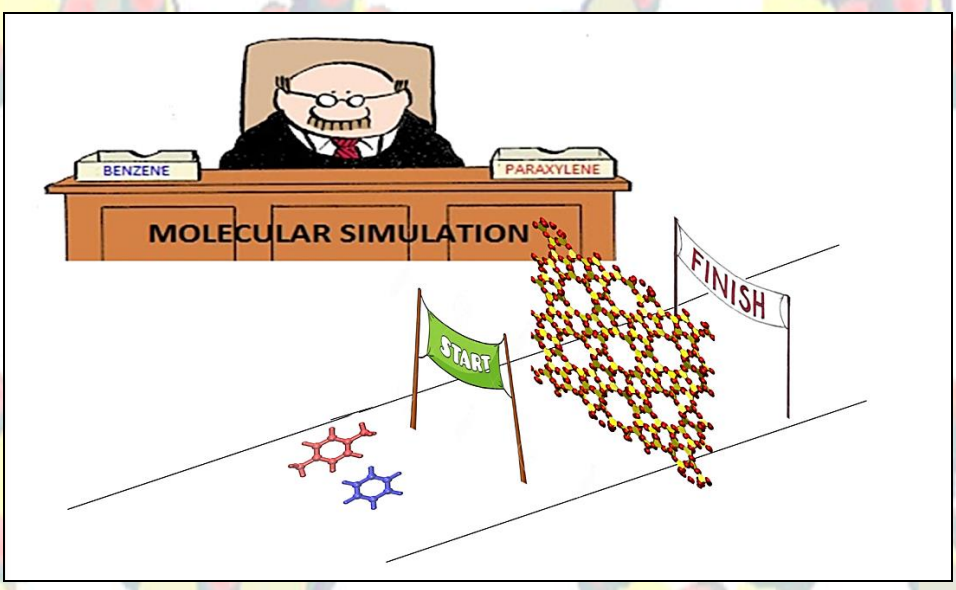

ΑΘΗΝΑ, ΑΥΓΟΥΣΤΟΣ 2016

Thesis examination committee

1. Professor **Doros N. Theodorou** (supervisor),
   School of *Chemical Engineering*
   National Technical University of Athens

2. Professor **Andreas Boudouvis** (member of the advisory commitee),
   School of *Chemical Engineering*,
   National Technical University of Athens

3. Professor **Nikolaos Papayannakos** (member of the advisory commitee),
   School of *Chemical Engineering*,
   National Technical University of Athens

4. Assistant Professor **George K. Papadopoulos**,
   School of *Chemical Engineering*,
   National Technical University of Athens

5. Professor **Vlasis Mavrantzas**,
   Department of *Chemical Engineering*,
   University of Patras

6. Professor **George E. Froudakis**,
   Department of *Chemistry*,
   University of Crete

7. Researcher Dr. **Hervé Jobic**,
   Institut de Recherches sur la Catalyse et l' Environnement de Lyon,
   CNRS, France

«Η συγκεκριμένη διδακτορική διατριβή εκπονήθηκε με χρηματοδότηση από τον Ειδικό Λογαριασμό Κονδυλίων και Έρευνας του Ε.Μ. Πολυτεχνείου μέσω υποτροφίας
καθώς επίσης και από τα ερευνητικά προγράμματα
FP7-NMP-2007-SMALL-1 NANOMODEL
(=αριθμός προγράμματος 211778) και
FP7-NMP-2008-EU-India-2 European Union–India AMCOS
(=αριθμός προγράμματος 233502)»

&

«Η έγκριση της διδακτορικής διατριβής από την Ανώτατη Σχολή Χημικών Μηχανικών του Ε. Μ. Πολυτεχνείου δεν υποδηλώνει αποδοχή των γνωμών του συγγραφέα. (Ν. 5343/1932, Άρθρο 202)»

This thesis is based on the following publications in international scientific articles and conferences:

I. Publications in scientific articles:
   1. Panagiotis D. Kolokathis, Doros N. Theodorou, On solving the master equation in spatially periodic systems, *J. Chem. Phys.* **2012**, 137, 034112, (DOI:10.1063/1.4733291)
   2. Panagiotis D. Kolokathis, Evangelia Pantatosaki, Christina Anna Gatsiou, Hervé Jobic, George K. Papadopoulos, Doros N. Theodorou, Dimensionality reduction of free energy profiles of benzene in silicalite-1: Calculation of diffusion coefficients using transition state theory, *Mol. Simul.* **2014**, *40*, 80-100, (DOI: 10.1080/08927022.2013.840895)
   3. Panagiotis D. Kolokathis, György Káli, Hervé Jobic, Doros N. Theodorou, Diffusion of aromatics in silicalite-1: Experimental and theoretical evidence of entropic barriers, *J. Phys. Chem. C*. **2016**, Article ASAP, (DOI: 10.1021/acs.jpcc.6b05462)

II. Publications in scientific conferences:
   1. Panagiotis D. Kolokathis, George K. Papadopoulos, Doros N. Theodorou, "Hierarchical Modeling of Transport Processes in Materials", *India-European Union Workshop on Environmental Materials and Modeling*, 23 November 2010, National Environmental Engineering Research Institute, CSIR, Nagpur, India, organized in the context of the AMCOS (Advanced Materials as CO_2 Removers) project.
   2. Panagiotis D. Kolokathis, Doros N. Theodorou, "Computing Diffusivities in Spatially Periodic Media from the Rate Constants of Elementary Jumps between Sorption Sites: Master Equation Solution by Recursive Reduction of Dimensionality", *Annual 2012 meeting of the American Institute of Chemical Engineers, Pittsburgh,* USA

"A part of this thesis won the 1st prize of the *9th Panhellenic Conference on Chemical Engineering*, held in Athens, Greece, 23-25 May 2013"

"This thesis is dedicated to the memory of ***Spiros Giannoukakis*** *for his humble way of life and for all the things he taught us all these years"*

Acknowledgements

First of all, I would like to thank my supervisor, Professor *Doros N. Theodorou* because he trusted me with this very interesting scientific problem and he gave me the opportunity to explore new things in Statistical Physics and Molecular Simulation field. It is important to add that I have learnt a lot of things from the way he deals with scientific problems and especially, the way he treats mathematics. It was always nice to work with him because his passion on science was always an extra motivation to complete this thesis. It is always nice to work with people that consider knowledge as a never ending process and people who are always thirsty to discover new things. Professor Theodorou is one of them and he was always there to answer my questions, even the trivial ones when I was still an undergraduate student. He had no problem to share the knowledge he had acquired with a lot of effort all these years. For all these things, I thank him from the bottom of my heart.

Secondly, I would like to thank Assistant Professor *George K. Papadopoulos*. Without George K. Papadopoulos, the laboratory would be very difficult to work properly. He was always there to help with every bureaucratic problem that arose, and he was present in the laboratory every day, giving to me an extra motivation to work. He was the first person I met there in the morning and the last person who left the laboratory in the evening. The discussions with him were always useful and, with his instructions, he was like a compass to me. I will never forget my first international conference in his presence, in India. There, George K. Papadopoulos helped me to meet scientists and exchange scientific opinions with other people. In this way, he made me realize that there were people who were interested in my scientific work. This was an extra motivation for me. I want to thank Assistant Professor George K. Papadopoulos because he trusted me to work on one of his projects in parallel with my PhD. This project provided very important financial support for me, as it helped me to work undistracted on important scientific problems. In addition, George K. Papadopoulos was also there to answer my questions, even the trivial ones, when still I was an undergraduate student.

Thirdly, I would like to thank Dr. *Evangelia (Evi) Pantatosaki*, as she was one of my closest collaborators. Evi is one of the most hard-working persons I have ever met, and this was an extra motivation for me. She is very passionate about science and she managed to transfer this passion to me. She was administrator of the Pericles computer cluster and she was always there to solve any technical problems with it, even when it was weekend or midnight. She is a very good team player and, next to her, I learnt how to work inside a team. She was very important to me especially in my first scientific steps, when she helped me by giving me useful guidelines.

Next, I would like to thank Dr. *Hervé Jobic* for the useful discussions we had all these years and because I was able to compare my simulations with the results Dr. Jobic produced using Quasi-Elastic Neutron Scattering. It was a great honor to collaborate with an excellent experimental scientist like Dr. Jobic and I was very lucky I met him in India. His interest in my thesis was a very important motivation.

In addition, I would like to thank Mrs *Christina-Anna (Christianna) Gatsiou* for the excellent cooperation we had during her diploma thesis and her major contribution she had in the Kinetic Monte Carlo code I used in this thesis. This thesis would be have been impossible to complete if Dr. *Nikolaos (Nikos) A. Romanos* and Dr. *Marco Sant* were not there to maintain the Pericles Cluster in the first years I was in the laboratory. Nikos Romanos also helped me with any technical problem I met in the beginning of my PhD.

Next, I want to thank Dr. *Stefanos D. Anogiannakis* because with the concentration and the patience he displayed when dealing with his scientific problems, inspired me to deal with my scientific problems too. *Stefanos* was also a paradigm of morality, as was *Panagiotis Nikolaos (Akis) Tzounis*, another member of the lab. Their morality was very important to me as they showed on an everyday basis that science is worth only if the people developing and using it are moral.

Furthermore, I want to thank the members of the examination committee of this thesis (Prof. *Andreas Boudouvis*, Prof. *Nikolaos Papayannakos*, Prof. *Vlasis Mavrantzas*, Prof. *George E. Froudakis*) for the useful discussions we had together.

Finally, I wish to thank the Research Committee of the National Technical University of Athens for the financial support they providing to me via a scholarship.

Summary

This doctoral thesis describes the development and application of a new computational methodology for calculating the rate constants governing the motion of sorbate molecules strongly confined within shape-selective nanoporous materials. An umbrella sampling strategy, employing repulsive walls to confine the sorbate within specific regions of the pore space or within specific orientations, is invoked to extract free energy profiles with respect to the sorbate degrees of freedom. Based on these profiles, it is shown how the multidimensional problem of translational diffusion of a sorbate (e.g., benzene) in a flexible nanoporous medium (e.g. in the zeolite silicalite-1) can be reduced first to a 6-dimensional problem, then to a 3-dimensional one, and finally to a 1-dimensional one. A 3-dimensional free energy distribution is accumulated as a function of the sorbate center of mass position and ultimately reduced to a set of 1-dimensional profiles for the sorbate center of mass along the pore axes. From these profiles, the rate constants for jumps executed by the sorbate molecule between sorption sites are calculated using Transition State Theory; from the latter rate constants, the low-occupancy self-diffusivity is obtained. The advantage of this modified methodology of Curvilinear Umbrella Sampling (CUS) in comparison with conventional umbrella sampling, on which it was based, is that it can be applied to curvilinear transition paths in addition to straight ones.

In this thesis, a new method was also invented to obtain the low-occupancy self-diffusivity from the rate constants of elementary jumps, in addition to the existing Kinetic Monte Carlo one. This new method solves the master equation for a system evolving on a spatially periodic network of states. The network contains 2^{ν} images of a "unit cell" of n states, arranged along one direction with periodic boundary conditions at the ends. We explore the structure of the symmetrized $(2^{\nu}n)\times(2^{\nu}n)$ rate constant matrix for this system and derive a recursive scheme for determining its eigenvalues and eigenvectors, and therefore analytically expressing the time-dependent probabilities of all states in the network, based on diagonalizations of $n\times n$ matrices formed by consideration of a single unit cell. We call the new method MESoRReD, for Master Equation Solution by Recurive Reduction of Dimensionality. MESoRReD is applied to the problem of low-temperature, low-occupancy diffusion of xenon in the zeolite silicalite-1 using

the states, interstate transitions, and transition state theory-based rate constants previously derived by R. L. June et al., J. Phys. Chem., **95**, 8866 (1991). MESoRReD yields a diffusion tensor for this system which differs by less than 3% from the values derived previously via Kinetic Monte Carlo (KMC) simulations and confirmed by new KMC simulations conducted in the present thesis. The computational requirements of MESoRReD are compared against those of KMC, numerical solution of the master equation by the Euler method, and direct molecular dynamics simulation. In the problem of diffusion of xenon in silicalite-1, the new method is shown to be faster than these alternative methods by factors of about 3.5×10^5, 1.3×10^6, and 1.7×10^7, respectively. The computational savings and ease of setting up calculations afforded by the MESoRReD in diagonalizing the rate constant matrix make it attractive as a means of predicting medium- and long-time dynamical phenomena in spatially periodic systems from atomic-level information.

Next, the specific computational methodologies we have described are applied for the calculation of the self-diffusion coefficients of para-xylene and benzene in silicalite-1 at infinite dilution. In addition, the orientational distributions of phenyl rings and methyl stems of para-xylene and benzene sorbed in the zeolite were studied and the existence of entropic barriers to translational motion was checked. A new reduction method for the states appearing in the free energy profiles is presented and used for the calculation of transition rate constants for elementary jumps. These results agree with Quasi-Elastic neutron scattering measurements. A major conclusion from simulations is that para-xylene diffuses roughly 100 times faster than benzene when sorbed at low occupancy in silicalite. Benzene encounters strong entropic barriers to translational motion at channel intersections, where it can adopt a variety of orientations. The corresponding barriers for para-xylene are much lower, reflecting the inability of its major axis to reorient within channel intersections. Finally, the paradox that the heavier and larger molecule diffuses faster than the lighter and smaller one inside silicalite-1 is explained for first time.

Περίληψη

Στην παρούσα διδακτορική διατριβή περιγράφεται η ανάπτυξη και η εφαρμογή μίας νέας μεθοδολογίας για τον υπολογισμό των σταθερών ρυθμού που διέπουν τις κινήσεις των ροφημένων μορίων μέσα σε νανοπορώδη υλικά που λειτουργούν ως μοριακά κόσκινα. Η μεθοδολογία αυτή, βασισμένη στη μεθοδολογία της 'δειγματοληψίας ομπρέλλας', εφαρμόζει απωστικούς τοίχους οι οποίοι περιορίζουν το ροφημένο μόριο σε συγκεκριμένες περιοχές των πόρων ενός νανοπορώδους υλικού και βοηθούν στην εξαγωγή των προφίλ της τοπικής ελεύθερης ενέργειας. Με βάση αυτά τα προφίλ, δείχνεται πως το πολυδιάστατο πρόβλημα πρόβλεψης της μεταφορικής διάχυσης του ροφούμενου μορίου μπορεί να αναχθεί πρώτα σ'ένα 6-διάστατο, έπειτα σε ένα 3-διάστατο και τελικά σε 1-διάστατο πρόβλημα. Από τα μονοδιάστατα προφίλ προκύπτουν, με χρήση της θεωρίας μεταβατικών καταστάσεων, οι σταθερές ρυθμού για τις μεταβασεις των ροφούμενων μορίων μεταξύ των θέσεων ρόφησης. Ένα πλεονέκτημα της τροποποιημένης αυτής μεθοδολογίας, που ονομάστηκε Καμπυλόγραμμη Δειγματοληψία Ομπρέλας ή CUS (Curvilinear Umbrella Sampling) σε σχέση με την απλή δειγματοληψία ομπρέλας, είναι ότι μπορεί να εφαρμοστεί και σε μή ευθύγραμμα μονοπάτια μετάβασης.

Από τις σταθερές ρυθμού που υπολογιζονται με χρήση της CUS, υπολογίζεται ο συντελεστής αυτοδιάχυσης με χρήση μίας επίσης νέας μεθοδολογίας που εισάγεται σε αυτήν τη διατριβή. Πιο συγκεκριμένα, εφευρέθηκε μια νέα μεθοδολογία για τον υπολογισμό του συντελεστή αυτοδιάχυσης από τις σταθερές ρυθμού των στοιχειωδών αλμάτων και γενικά την ακριβή περιγραφή της μεσοσκοπικής συμπεριφοράς των ροφούμενων μορίων μέσα σε νανοπορώδη υλικά τόσο για μικρούς όσο και για μεγάλους χρόνους. Η μεθοδολογία αυτή είναι εναλλακτική προς την κινητική προσομοίωση Monte Carlo (kinetic Monte Carlo, KMC) και εμφανίζει σαφή πλεονεκτήματα έναντι της τελευταίας. Η νέα μέθοδος επιλύει την εξίσωση εξέλιξης (εξίσωση Master) για ένα σύστημα που προσλαμβάνει διακριτές καταστάσεις που εμφανίζουν περιοδικότητα στο χώρο. Το θεωρούμενο δίκτυο καταστάσεων περιέχει 2^{ν} εικόνες μιας μοναδιαίας κυψελίδας n καταστάσεων, διατεταγμένες κατά μήκος μιας διεύθυνσης του χώρου. Στα άκρα του δικτύου επικρατούν περιοδικές οριακές συνθήκες. Αναλύθηκε η δομή του $(2^{\nu}n)\times(2^{\nu}n)$ συμμετρικού πίνακα των σταθερών ρυθμού και βρέθηκε ένα αναδρομικό σχήμα για τον υπολογισμό των ιδιοτιμών και των ιδιοδιανυσμάτων. Ως αποτέλεσμα εκφράστηκαν

αναλυτικά οι πιθανότητες κατάληψης, συναρτήσει του χρόνου, όλων των καταστάσεων που μπορεί να προσλάβει το σύστημα ξεκινώντας από συγκεκριμένες αρχικές συνθήκες. Οι αναλυτικές αυτές εκφρασεις βασίζονται στη διαγωνοποίηση $n \times n$ πινάκων οι οποίοι σχηματίζονται από τις καταστάσεις μίας και μόνο μίας κυψελίδας. Αυτή η νέα μέθοδος, εν ονόματι MESoRReD (Master Equation Solution by Rercursive Reduction of Dimensionality) εφαρμόστηκε στο πρόβλημα της διάχυσης το Ξένου στο ζεόλιθο σιλικαλίτη-1 όταν αυτό βρίσκεται σε χαμηλές συγκεντρώσεις και σε χαμηλές θερμοκρασίες, χρησιμοποιώντας τις σταθερες ρυθμού από την δουλειά των June et al., J. Phys. Chem., **95**, 8866 (1991). Η μέθοδος MESoRReD μας δίνει ένα τανυστή διαχυτότητας για το συγκεκριμένο σύστημα ο οποίος διαφέρει κατά λιγότερο από 3% από τις τιμές που είχαν παραχθεί στο παρελθόν από προσομοιώσεις Κινητικής Monte Carlo (KMC) αλλά και από προσομοιώσεις KMC που διεξάχθηκαν στα πλαίσια της παρούσας διδακτορική διατριβή. Οι υπολογιστικές απαιτήσεις της συγκεκριμενης μεθόδου συγκρίνονται με εκείνες της KMC, και της αριθμητικής επίλυσης της εξίσωσης Master με την μεθοδο Euler, καθώς και με άμεσες προσομοιώσεις Μοριακής Δυναμικής. Στο πρόβλημα της διάχυσης του Ξένου στο σιλικαλίτη-1, η νέα μέθοδος είναι γρηγορότερη από αυτές τις εναλλακτικές μεθόδους κατά παράγοντες 3.5×10^5, 1.3×10^6, and 1.7×10^7 αντίστοιχα. Ο υπολογιστικός χρόνος που εξοικονομείται από την νέα μέθοδο MESoRReD στη διαγωνοποίηση του πίνακα σταθερών ρυθμού την καθιστά ιδιαίτερα ελκυστική ως μέσο πρόβλεψης δυναμικών φαινομένων μεσαίας αλλά και μεγάλης διάρκειας χρησιμοποιώντας πληροφορίες βασισμένες στο ατομικό επίπεδο.

Στην συνέχεια, οι υπολογιστικές μεθοδολογίες που περιγράψαμε εφαρμόστηκαν για την πρόβλεψη του συντελεστή αυτοδιάχυσης του παρα-ξυλολίου και του βενζολίου στο ζεόλιθο σιλικαλίτη-1 όταν τα μόρια αυτά βρίσκονται σε άπειρη αραίωση. Επιπλέον μελετήθηκαν οι κατανομές προσανατολισμού των φαινυλικών δακτυλίων και των μεθυλίων του παραξυλολίου και του βενζολίου ροφημένων στο ζεόλιθο και ελέγχθηκε η ύπαρξη εντροπικών φραγμάτων στη μεταφορική κίνηση. Αναπτύχθηκε μια νέα μέθοδος αναγωγής των καταστάσεων που εμφανίζονται στα προφίλ της τοπικής ελεύθερης ενέργειας και χρησιμοποιήθηκε για τον υπολογισμό των σταθερών ρυθμού στοιχειωδών αλμάτων μέσα στο ζεόλιθο. Τα αποτελέσματα που προέκυψαν για τη διάχυση συμφωνούν με μετρήσεις οιονεί ελαστικής σκέδασης νετρονίων. Το κύριο συμπέρασμα από τις προσομοιώσεις είναι ότι το παραξυλόλιο διαχεέται περίπου 100 φορές γρηγορότερα από το βενζόλιο όταν και τα δύο είναι ροφημένα σε άπειρη αραίωση. Το

βενζόλιο υπόκειται σε ισχυρά εντροπικά φράγματα όταν βρίσκεται στην περιοχή διασταύρωσης των καναλιών του σιλικαλίτη, όπου μπορεί να προσλαμβάνει πολλούς προσανατολισμούς. Τα αντίστοιχα φράγματα για το παρα-ξυλόλιο είναι πολύ χαμηλότερα, αντικατοπτρίζοντας τη δυσκολία του κύριου αξονά του να αναπροσανατολιστεί μέσα στις διασταυρώσεις των καναλιών. Εν τέλει εξηγείται για πρώτη φορά το παράδοξο ότι το βαρύτερο και μεγαλύτερο σε μέγεθος μόριο (παρα-ξυλόλιο) διαχέεται γρηγορότερα από ένα ελαφρύτερο και μικρότερο (βενζόλιο) μέσα στο σιλικαλίτη.

List of Symbols

Latin alphabet

A	Local Free Energy profile
a	Unit cell length along x direction
a_j	Coefficients used in MESoRReD (only in Chapter 3)
b	Unit cell length along y direction
c	Unit cell length along z direction
D	Self-diffusion coefficient
D_0	Diffusion prefactor
dt	Timestep
$dP_{i\to j}$	Probability for a sorbate to be in the dividing surface with direction to state j
E_a	Activation Energy
$\mathbf{F}$	Vector of force
f	Transmission coefficient
I_{xx}	Moment of inertia in x direction
$\mathbf{i}$	Tangent vector to the path
i	Imaginary unit (only Chapter 3)
$\mathbf{i}_1$	Tangent vector to the path for the 1st wall
$\mathbf{i}_2$	Tangent vector to the path for the 2nd wall
$\mathbf{K}$	Rate constant matrix
$\tilde{\mathbf{K}}$	Reduced rate constant matrix
k	Spring constant
$k_{i\to j}$	Transition-rate constant for the transition from i state to j state
k_B	Boltzmann constant
l	Distance between two states
L_d	Unit cell length in x, y, or z direction
L_p	Box length in x, y, or z direction
m	Mass
N	Number of atoms in the system
N_d	Number of points for which overlap occurs during stitching process
$N_i(t)$	Number of walkers in state i an time t
n	Number of states per unit cell (only in Chapter 3)
n($\mathbf{r}_{CM}$)	Probability density of sorbate center of mass
$\mathbf{P}$	Probability matrix
P	Probability
$\tilde{\mathbf{P}}(t)$	Reduced Probability matrix at time t

Q_{st} Isosteric heat
$\mathbf{q}$ Vector of mass-reduced coordinates
q Mass-reduced coordinates
$q_{i\to j}$(t) Conditional probabilities for a transition from i to j and time t during Kinetic Monte Carlo simulation
R Gas constant
R_1 Distance from the plane of wall up to which wall potential is a Lennard-Jones potential
R_2 Distance from the plane of the wall up to which wall potential is a polynomial
$R_{i\to j}(t)$ Flux from i state to j state and time t during Kinetic Monte Carlo simulation
$\mathbf{r}$ Vector of coordinates
$\mathbf{r}_{o.p.}$ Point of the path on which the wall is vertical
$\mathbf{r}_{n.p.}$ Point of the plane of the wall derived using $\mathbf{r}_{o.p}$ and tangent vector i
S Entropy
s Pseudorandom number
T Temperature
t Time
$\mathcal{V}$ Potential energy
U Internal energy
$\tilde{\mathbf{u}}_m$ Eigenvector of reduced rate constant matrix $\tilde{\mathbf{K}}$
$\mathbf{v}$ Velocity vector
$\mathbf{v}_i$ Velocity vector of atom i
$\mathbf{x}$ Eigenvector
x Cartesian coordinate
y Cartesian coordinate
z Cartesian coordinate

Greek alphabet

α split parameter (only in subchapter 4.3)
δ_{ml} Kronecker delta
ε Machine precision (only in Chapter 3)
ε^{W} Depth of Lennard-Jones potential well from walls
ζ multiplying factor of eigenvector
λ Eigenvalue
ξ Reaction coordinate
ξ Multiplying factor of eigenvector (only in Chapter 3)
π Mathematical constant of the ratio of a circle's circumference to its diameter
ρ_{ξ} Probability density of the projection of the center of the sorbate on ξ point of the path
ρ_{cell} Probability density to be in a specific unit cell
σ Standard deviation

σ^{W} Sigma of Lennard-Jones potential well from walls

τ_{ij} Reverse rate constant

ψ Principal root

Subscripts and superscripts

TST denotes transition state theory

CM denotes center of mass of the sorbate

W denotes walls

u^{LJ} denotes Lennard-Jones

T denotes matrix transpose

† denotes maximum of the 1-dimensional local free energy profile

U Up

D Down

R Right

L Left

$I \underset{a}{\rightarrow} Z$ Transition from state I to state Z via *a* route

Special conventions

<.....> Average of a variable

$<.....>_{NVT}$ Average in canonical ensemble

$\frac{\partial}{\partial t}$ Partial derivative

$\frac{\partial^2}{\partial t^2}$ Second Partial derivative

$\| \|_2$ Euclidian norm of a matrix

erf Error function

Abbreviations

1-D One dimensional

3-D Three dimensional

COMPASS Consensed-phase Optimized Potentials for Atomistic Simulation Studies

CUS Curvilinear Umbrella Sampling

DD Direct Diagonalisation

DHFF-O Demontis Harmonic Force Field-Original

I Intersection state

I_S Intersection state,when the sorbate has the orientation prefers in straight channel

I_Z Intersection state, when the sorbate has the orientation prefers in zig-zag channel

KMC Kinetic Monte Carlo

MESoRReD Master Equation Solution by Recursive Reduction of Dimensionality
MD Molecular dynamics
NSE Neutron spin-echo
p-xylene Paraxylene
PFG NMR Pulsed field gradient nuclear magnetic resonance
P^3M Particle Particle Mesh Ewald
QENS Quasi-Elastic Neutron Scattering

RESPA Reference System Propagation Algorithm
SGVFF-O Simplified Generalized Force Field-Original
SSD Sum of Square Deviations
S Straight channel state
TST Transition State Theory
WHAM Weighted Histogram Analysis Method
Z Zig-zag channel state

Contents

Chapter 1

Introduction

1.1 Silicalite-1: Why is it important and what are its properties

Zeolites are microporous aluminosilicates widely used in the petroleum and petrochemical industries as catalysts or storage materials for sorbates such as CO_2, CH_4, and aromatic molecules.[1] A widely used zeolite is ZSM-5 (acronym for Zeolite Socony Mobil 5) which belongs to the pentasil family of zeolites. ZSM-5 in its purely siliceous form is known as silicalite-1.[2,3] Silicalite-1 is an MFI[1,4] (Mobil FIve) -type zeolite which consists of SiO_2 tetrahedra and can be found in 3 phases: Mono[5], Ortho[6], and Para[7,8]. Ortho and Para are orthorhombic, while Mono is monoclinic. At low temperatures, silicalite-1 takes its Mono form, while at high temperatures it prefers the Ortho. Para has been observed when there is large loading of sorbates in silicalite-1.[9] Distortion of silicalite-1 by sorbates at large loadings is described extensively in the work of Sartbaeva et al.[10] At atmospheric pressure, the first-order transition from the Mono to the Ortho phase takes place at 300-350K[11,12] according to most experimental studies. Some experimental measurements show a kind of smooth transition,[13,14] where the α monoclinic angle of the unit cell becomes approximately 90 degrees at 400K. An explanation of these transitions has been proposed in terms of the displacement of SiO_2 tetrahedra, which are considered to be very rigid according to the rigid unit mode (RUM)[15] theory. This displacement of SiO_2 tetrahedra explains transitions in a wide range of silicate materials. Tetrahedra have common edges which constrain their degrees of freedom. We can see these tetrahedra and the silicalite-1 structure in the Ortho phase in Figure 1.1.

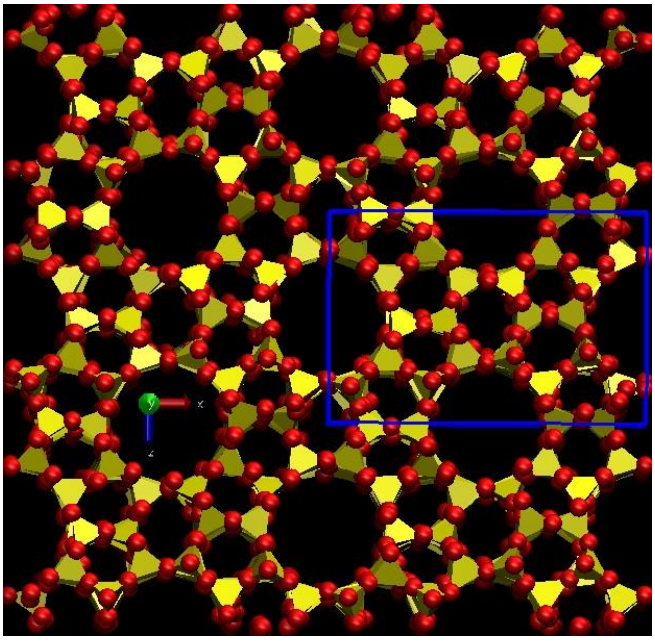

Figure 1.1 Silicalite-1 projection on the *x*-*z* plane of 2×2×3 unit cells in Ortho phase. Oxygens are illustrated with red spheres and the tetrahedra which have silicon as their central atom are illustrated with yellow color. The blue lines are the limits of one unit cell.

Silicalite-1 has two kinds of channels, both of diameter approximately 5.5 Å, which are called sinusoidal or zigzag (Z) and straight (S) channels, respectively. The channel diameter is similar with the kinetic diameter of benzene (~6 Å).[16,17] These channels communicate in areas called intersections (I). The network of channels is depicted schematically in Figure 1.2. The topology and geometry of this network and the relatively hydrophobic nature of the channel walls impart to silicalite-1 its unique molecular sieving properties. Silicalite-1 can be used in the separation of small aromatic molecules with different kinetic diameters such as benzene, toluene and the three xylene isomers, known in the petroleum industry as BTX. There are a lot of chemicals which are produced from BTX compounds,[18] such as Nylon-6 from benzene, terephtalic acid and polyester fibers from p-xylene, and phtalic anhydride from o-xylene.

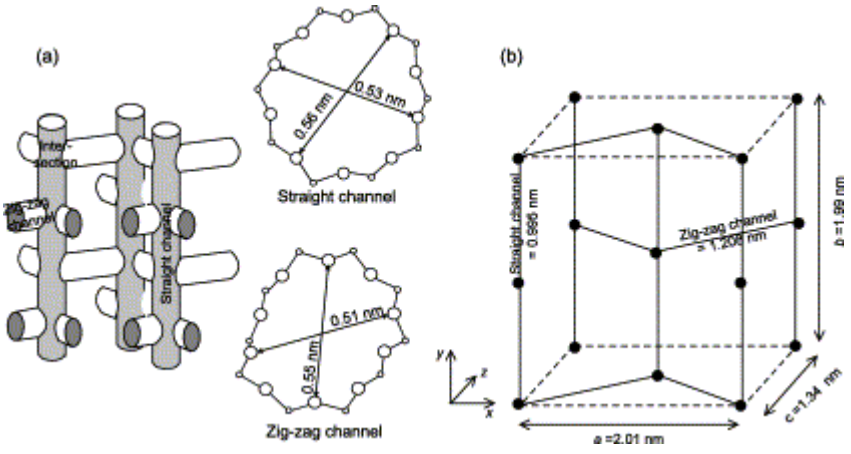

Figure 1.2 (a) Schematic of structure of silicalite-1 (MFI). (b) Diffusion unit cell for silicalite-1 connecting intersection sites (large black dots) via straight and zig–zag channels.

1.2 Controversy among the experimental measurements of diffusion of aromatics in silicalite-1 in the literature and the role of past molecular simulations

1.2.1 Controversy among the experimental measurements

A wide range of experimental measurements have been carried out for the transport of BTX molecules in silicalite. Some controversy still exists concerning the diffusivity of p-xylene. Some studies[19-22] show that the diffusion of p-xylene is of the same order as that of benzene[23-28] (actually slightly faster), while others[29-32] support that p-xylene's diffusivity is 2 orders of magnitude higher than that of benzene. These experiments have been performed for sorbates at infinite dilution in the Ortho[6] phase of silicalite. Molecular simulations can be used to shed light on this controversy.

1.2.2 Past molecular simulations of the system benzene-silicalite-1

A wide range of computational studies of benzene in silicalite-1 have been undertaken in the past. The first were those of Nowak et al.[33] and Pickett et al.,[34] in which some 1-D potential energy profiles along the straight channel are presented. These works managed to convey a first idea of the barriers encountered by benzene in its translational motion through silicalite-1. However, their accuracy is very limited, as only few points were used and the symmetry rules

that should hold along the straight channel for the free energy profile are not satisfied. Better accuracy, but still not sufficient for use in the context of Transition State Theory (TST) to calculate diffusion, was provided by the work of Talu.[35] He approximated benzene free energy profiles as minimized potential energies by allowing only specific moves in his Monte Carlo simulation, while the force field parameters he invoked do not yield Henry's constant values that are consistent with experiment, as he mentions. One should bear in mind that the computational tools at the time of these early studies were very modest in comparison to those available nowadays.

A pioneering TST-based study of benzene diffusion in silicalite-1 was conducted by Snurr et al.[36] Here, rigid models were considered for both silicalite-1 and benzene. Local minima of the energy were calculated exhaustively in six degrees of freedom (coordinates of the center of mass and Euler angles of the benzene molecule). Saddle points between these minima were obtained with Baker's[37] algorithm and transition paths connecting adjacent minima via the saddle points were constructed in six-dimensional space. The possibility was shown of lumping states constructed around individual minima into macrostates for the purpose of calculating transition rate constants. The use of six degrees of freedom made an exhaustive calculation of all paths and the use of Baker's algorithm feasible. The force field parameters invoked were able to predict the sorption of benzene in silicalite-1.[38] The long-time evolution of the system as a succession of infrequent transitions was tracked via Kinetic Monte Carlo simulation. The self-diffusion coefficient was underestimated by two order of magnitude (predicted D=1.1 10^{-16}m^{2}s^{-1} at 300K), a fact attributed to the use of a rigid model for silicalite-1. Consequently, an investigation of benzene in a flexible silicalite-1 was recommended.

Forester and Smith[39] dealt with the problem of computing the diffusivity of benzene in silicalite-1 via infrequent event analysis in a flexible silicalite model. For this purpose they used the bluemoon ensemble.[40] For the first time they showed the large difference in barriers between rigid and flexible crystals and the major importance of flexibility of the crystal for tightly fitting sorbates. They calculated 1-Dimensional (1-D) free energy profiles for flexible and rigid crystal models, but gave rate constants only for the flexible one. To perform these calculations, they made some assumptions: a) their paths were not accurate enough, as there are discontinuities in their computed points, while it is not examined if these paths describe the dividing surface well;

b) the possible existence of states differentiated by benzene's orientation were not studied; c) they used an average rate for the intersection to sinusoidal channel transition, instead of two different rates that are generally needed; d) they did not invoke the usual Kinetic Monte Carlo[41] algorithm to compute self-diffusivities from their rate constants. More specifically, they considered a specific mean timestep for each Monte Carlo move, instead of choosing the timestep from an exponential distribution. Consequently, their results for the diffusivity are one order of magnitude off from what would be predicted from their rate constants (D=6.17 10^{-13} m^2s^{-1}) through a more rigorous Kinetic Monte Carlo approach. The same offset is observed from estimates of the diffusivities obtained via the semiempirical relationships of Eq. (1.1) proposed by Kärger[42,43] where a, b, c are the lengths of the silicalite-1 unit cell for x, y, z direction respectively and k is the symbol of the rate constant from a transition from one intersection I to other intersection I.

$$D_{xx} = \frac{1}{4} k_{x,\mathrm{I}\to\mathrm{I}} a^2,\ D_{yy} = \frac{1}{4} k_{y,\mathrm{I}\to\mathrm{I}} b^2,\ \mathrm{D}_{zz} = \frac{1}{4} \frac{k_{y,\mathrm{I}\to\mathrm{I}} k_{x,\mathrm{I}\to\mathrm{I}}}{k_{y,\mathrm{I}\to\mathrm{I}} + k_{x,\mathrm{I}\to\mathrm{I}}} c^2 \qquad \text{Eq. (1.1)}$$

Here we remind the reader that, for one-dimensional diffusion from a state I to another state I, the diffusion coefficient is described by Eq. (1.2).

$$D_{xx} = k_{x,\mathrm{I}\to\mathrm{I}} l_{\mathrm{I}\to\mathrm{I}}{}^2 \qquad \text{Eq. (1.2)}$$

where $l_{\mathrm{I}\to\mathrm{I}}$ is the distance between the two states.

e) a transmission coefficient was computed along the y direction in the straight channel and not in the direction of their path at the saddle point; f) they actually constrained the benzene center of mass at specific points of a path, while its projection on the path should be constrained instead. As a result, the phase space was sampled insufficiently and this was the reason for the short duration of their molecular dynamics simulations; the total time was 30 ps with 1.2 fs timestep, and 50ps with 12 fs timestep for their flexible and rigid silicalite models, respectively. These times were sufficient to sample the phase space of a specific center of mass position, however, as already mentioned, the phase space of the center of mass projection should be sampled instead and much more time should be needed for this. g) In addition to these

assumptions, their flexible and rigid free energy profiles for the sinusoidal channel show different minimum positions (differing by 2 Å along the reaction coordinate path); this may be attributable to a drift of the crystal because of collisions of the benzene with it. h) In their simulations, Forester and Smith[39] used a flexible model for silicalite-1 described by the force field and parameters of Schröder et al.,[44] and a rigid benzene. They chose to work with half the charges of benzene, because Schröder et al.'s[44] zeolite has twice the charges of Snurr et al.'s[36] rigid ion and rigid lattice model. This trick is admissible for benzene at infinite dilution in silicalite-1. However, the force field they used does not keep silicalite atoms around their crystallographic positions. This is very important for the prediction of sorption properties if we consider the work of Clark and Snurr[45].

Another more recent relevant work is that of Rungsirisakun et al.[46] In this work molecular dynamics (MD) simulations of benzene in silicalite-1 were performed. They used for the first time a flexible benzene molecule proposed by Sastre et al.[47] Using these parameters they calculated a self diffusivity $D_{T=300K} = 2.50\times10^{-10}\,\frac{\mathrm{m}^2}{\mathrm{s}}$ for a loading of 2 benzenes per unit cell, which is 4 orders of magnitude higher than experimental values at infinite dilution.[23-28] This shows that diffusivity is extremely sensitive to the flexibility of benzene. Judging from experimental values, diffusion of benzene in silicalite is too slow to be predicted reliably by molecular dynamics.[17]

Another work that deserves to be mentioned in relation to the calculation of free energy profiles is that of Amirjalayer and Schmid,[48] which studies the mechanism of benzene diffusion in MOF-5 via molecular dynamics. This work calculates 3-D and 1-D free energy profiles of benzene in MOF for different loadings. However, because benzene diffuses fast in such materials ($D_{T=300K} = 2.00\times10^{-9}\,\frac{\mathrm{m}^2}{\mathrm{s}}$), no special infrequent event technique is needed to study diffusion. In those studies, diffusion was calculated from the mean square displacement via the Einstein Diffusion Equation.[17] It is important to note that Transition State Theory is appropriate only if the free energy profiles show that diffusion occurs as a succession of infrequent jumps of the sorbate in the zeolite.

In this thesis we revisit the problem of computing the diffusivity of benzene in a flexible silicalite model through infrequent event analysis. Our work aims at complementing the pioneering studies of Snurr et al.[36] and Forester and Smith.[39] It differs from Forester and Smith's work[39] in the following respects: (1) It invokes a new methodology, based on umbrella sampling, to calculate free energy profiles in the zeolite crystal; (2) it explicitly considers orientational degrees of freedom and checks whether transitions between different orientational states are fast enough or slow enough to allow consideration of a three-dimensional free energy depending only on the center of mass coordinates for the purpose of analyzing elementary jumps leading to translational diffusion in the zeolite; (3) Calculations are performed with a different flexible model than invoked by Forester and Smith[39] at three different temperatures and estimates for the activation energy and the diffusion prefactor are extracted.

1.2.3 Past molecular simulations of the system para-xylene - silicalite-1

The first computational work on para-xylene in silicalite-1 was that of Pickett et al.[49] They used a rigid silicalite-1 model and they described the pairwise interactions using a Lennard-Jones potential without electrostatic interactions. Using this force field they followed an energy mimimization procedure to find the potential energy minima of para-xylene (p-xylene) in silicalite-1. These minima do not always show us the favorite macrostates p-xylene prefers, as entropy effects are also important and must also be considered. Better accuracy, but still not sufficient for use in the context of Transition State Theory (TST) to calculate diffusion, was provided by the work of Talu.[35] He approximated p-xylene free energy profiles as minimized potential energies by allowing only specific moves in his Monte Carlo simulation, while the force field parameters he invoked do not yield Henry's constant values that are consistent with experiment, as he mentions. As we have pointed out previously, one should bear in mind that the computational tools at the time of these early studies were very modest in comparison to those available nowadays. Force field parameters that describe well the isosteric heat, Henry's constant and the isotherm of p-xylene in silicalite-1 were used in the work of Snurr et al.[38,50] To our knowledge, the current thesis is the first time that diffusion of p-xylene in silicalite-1 is studied computationally. This can probably be attributed to the small self-diffusion coefficients of p-

xylene in silicalte-1[19-22, 29-32] which makes extremely difficult the use of conventional molecular dynamics simulations for their calculations. Transition state theory techniques should be applied in conjuction to molecular dynamics simulations.

Chapter 2

A new modified umbrella sampling methodology

2.1 Why is a new modified umbrella sampling necessary?

As mentioned before, inordinately long computation times would be required in order to compute the diffusion coefficient of benzene in silicalite-1 via "brute force" MD simulations. Thus, it is necessary to resort to a methodology capable of estimating the rates of infrequent transitions in configuration space, through which diffusion occurs. Forester and Smith[39] chose to work with the bluemoon ensemble.[40,51,52] Later, it will be shown that it is impossible to use the bluemoon ensemble in such a way that all phase space can be sampled and simultaneously projected to onto one reaction coordinate if the projection refers to the center of mass of the sorbate along curved lines. In this work we invoke another method of constraint dynamics, inspired by umbrella sampling.[52,53] Here, it is important to mention that umbrella sampling is a biased dynamics method while bluemoon is a constraint dynamics one.

There are three reasons why we chose to adopt a new umbrella sampling method. First, we choose to bias the system in such a way that the Jacobian matrix of transformation from the original Cartesian coordinates of the sorbate center of mass to those invoked in the projection is not needed for the calculation of the constraint force.[52] Even so, 3-dimensional umbrella sampling could be used, as it does not require a Jacobian matrix calculation[54] by default. For example, the Weighted Histogram Analysis method (WHAM)[55,56] could be used for 3-dimensional calculations, but it would be difficult to implement for our 1-dimensional calculations. 3-dimensional calculations of the free energy profile with extensive enough sampling to provide estimates of the rate constants of elementary diffusive jumps with acceptably low statistical error would be computationally very demanding, however.

Secondly, conventional umbrella sampling cannot be applied along curved paths. As will be discussed extensively later, in case the sorbate's center of mass can be projected on more than one points along a path, a distance criterion must be used to decide on which point it will ultimately be projected. In Figure 2.1, we see the center of mass of a sorbate that it is initially

projected on ξ_1 and the bias potential energy it experiences is $\mathcal{V}(\xi_1)$. After elapse of time d*t*, the sorbate's center of mass is projected on ξ_2 and its bias potential energy is $\mathcal{V}(\xi_2)$. This leads to a discontinuity in the bias potential energy and, consequently, the umbrella force is impossible to calculate for this case. This problem does not exist along straight paths, where conventional umbrella sampling can be applied correctly.

Thirdly, from our experience we have seen that, if we choose to use WHAM, we need to change the spring constant of the harmonic umbrella sampling force very often if we want to sample specific areas with high accuracy. This is a consequence of the "ruggedness" of the atomistic benzene - silicalite-1 potential.

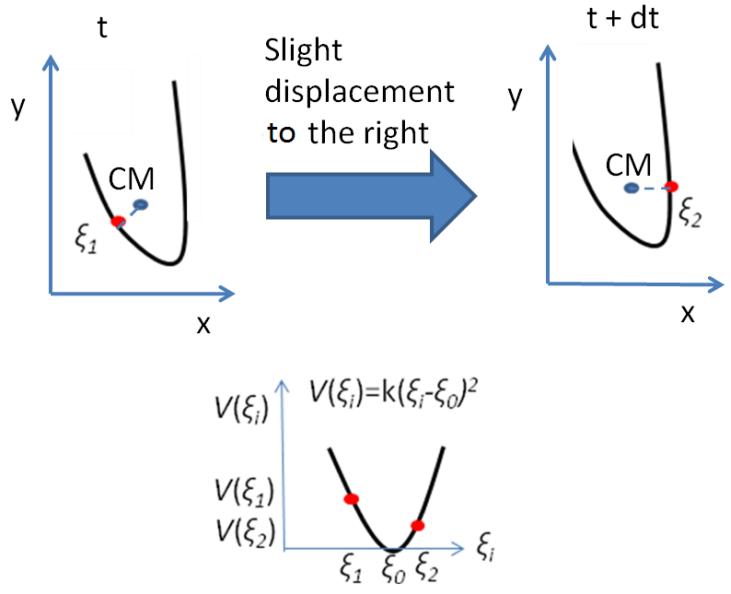

Figure 2.1 Projection of benzene's center of mass (CM) on a curvilinear path at two different instants and the bias potential energy it experiences in each case.

As we mentioned before, the projection definition does not allow using classical umbrella sampling along curvilinear paths. This problem does not arise for straight paths. Straight paths and classical umbrella sampling have been recently used by Verploegh et al.[57] and Camp et al. [58] to study the diffusion of hydrocarbon molecules in zeolitic imidazolate frameworks and light gas diffusion in a porous organic cage crystal 3 (CC3), respectively. Curvilinear paths are impossible to avoid in some crystals, however, as in the case of silicalite-1, because of its sinusoidal channels. In addition, curved paths help us describe well the dimensionality reduction of a multi-

dimensional dividing surface to a single point along a one-dimensional curved path coordinate without losing any information. Such loss of information is common when we use straight paths. The calculation of transmission coefficients[59] (ratios of the number of transitions that actually take place divided by the number of transitions that are predicted to take place based on the TST approximation) is one way to compensate for this loss, without being able to eliminate it, as can be understood from the 2-dimensional free energy profiles of Figure 2.2. Using curvilinear paths derived from the 3-dimensional free energy landscape, one can ensure that transmission coefficient values depend only on the strength of coupling to the thermostat process of the crystal and, as a result, are expected to be near unity for sharply peaked free energy profiles. For this reason we have decided to apply the new modified umbrella sampling method we introduce here and not the classical umbrella sampling in the present work. Both classical umbrella sampling and our new modified umbrella sampling are biased dynamics methods, while the bluemoon ensemble[40,51] (another method used with transition state theory) is a constraint dynamics one[52]. As already mentioned, bluemoon ensemble cannot be used for curved paths with the definition of projection we suggest, because it is not possible to calculate the Jacobian determinant it needs.[52] As a result, a new modified umbrella sampling method seems to be a one-way road for our problem.

In Figure 2.2 we can see that an area of the channel intersection state can be wrongly attributed to the sinusoidal channel state. This cannot be corrected by transmission coefficients if the one-dimensional projection includes areas away from the 3-D saddle point, such as the one shown in Figure 2.2. As a result, transmission coefficients from right to left will be different from transmission coefficients from left to right. Equality of the latter transmission coefficients can also be used as a check for the correctness of the path.

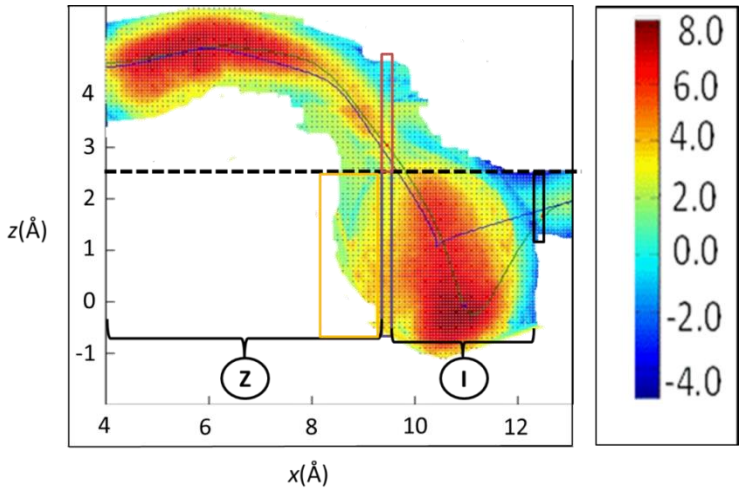

Figure 2.2 2-Dimensional cross-section (at plane *y*=14.94Å) of the 3-D Free Energy Profile of benzene in sinusoidal channel of silicalite-1 (we will explain later extensively the way it is derived). The colorbar is in -RT units and the temperature is 300K. The dashed black line traces a possible straight path. Blue and red boxes outline areas of the dividing surface as determined based on the dashed black line path. The orange box includes a part of the area of the intersection (I) which is projected to the Z state (see sections 3.4 and 4.6 later) based on the dashed black line path. The black box outlined the dividing surface around the second saddle point for the straight black line path. Blue and green lines will be examined as alternative reaction paths.

2.2 Description of a new modified umbrella sampling methodology

To adjust constraint dynamics to our problem, we have added some initial steps before invoking the 1-Dimensional (1-D) umbrella sampling technique, as explained in detail in Figure 2.3.

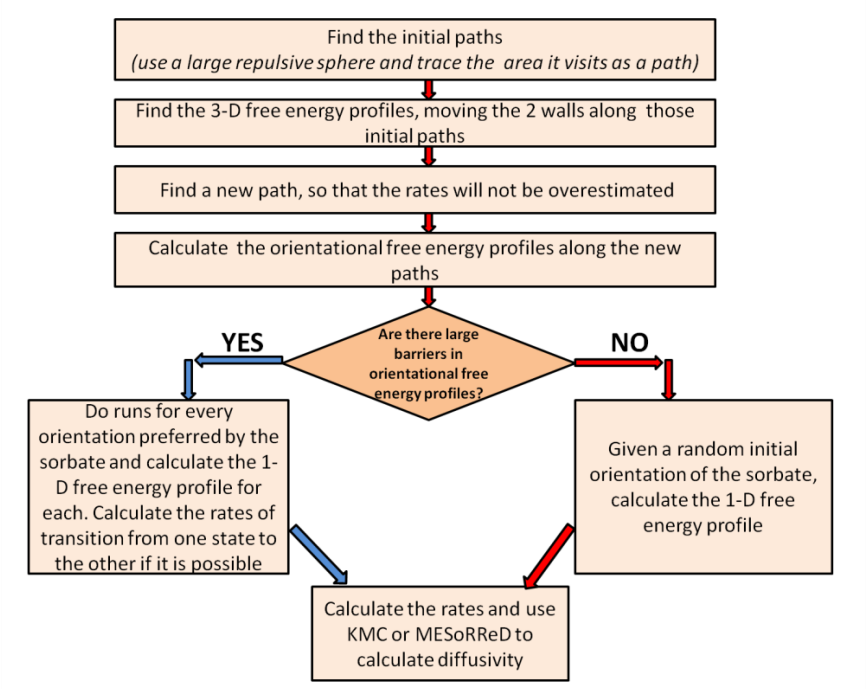

Figure 2.3 Algorithm designed to find the diffusion of benzene in silicalite-1. With red color is the route we follow in this work.

The first steps of this algorithm are extremely important before applying 1-D umbrella sampling. The estimated diffusion coefficient is sensitive to the choices made in these steps (see below). If these steps are not performed correctly, the diffusivity will be overestimated. The algorithm of Figure 2.3 is generally applicable to any sorbate, rigid or flexible, and to any nanoporous material, whether it is considered rigid or not. When a rigid sorbent model is considered, a separate thermostat for the sorbate is essential. In the following we examine each step of the algorithm of Figure 2.3 separately.

The algorithm primarily aims at calculating the diffusivity, which first demands the calculation of rate constants for all jumps that control diffusive progress of the sorbate. The rate constant for moving from state i to a neighboring state j is defined in Eq. (2.1) and calculated by Eq. (2.2).[36] It is actually the conditional probability per unit time that a move from state i to state j will occur, provided the system starts off in state i. In the first order phenomenological law expressed by Eq. (2.1), $P_{i\to j}$ is the probability of observing a transition from state i to state j within time t and P_i is the probability of occupancy of state i. If the conditions of time scale

separation are valid which make the transition from *i* to *j* an infrequent event, $k_{i\to j}$ is practically a constant, independent of time. An analogous expression is valid for the inverse transition, from state *j* to state *i*. In our case, **r** is the vector of coordinates specifying the configuration of the zeolite plus sorbate system, *N* is the dimensionality of that vector, and **q** is the vector of mass-reduced coordinates ($\mathbf{q}_i = m_i^{1/2}\ \mathbf{r}_i$ for every atom *i*). Eq. (2.2) requires the calculation of configurational integrals, or free energies, over a (*N*-1)-dimensional bottleneck (hyper)surface separating states *i* and *j* in configuration space, and also over the origin state *i*. It is obvious that the free energy profile must be calculated along the considered path leading from state *i* to state *j*. If we are able to define an appropriate 1-dimensional transition path spanned by a reaction coordinate leading from state *i* to state *j* and compute a free energy profile with respect to that reaction coordinate, the rate constant will be proportional to the ratio of the Boltzmann factor of the free energy at the barrier between *i* and *j* divided by the integral of the Boltzmann factor of the free energy over the origin state *i*.

$$k_{i\to j} \equiv \frac{1}{P_i}\frac{dP_{i\to j}}{dt} \qquad \text{Eq. (2.1)}$$

$$k_{i\to j}^{\mathrm{TST}} = \left(\frac{k_B T}{2\pi}\right)^{1/2} \frac{\int_{\text{bottleneck surface}} \exp\left(-\frac{\mathcal{V}(\mathbf{q})}{k_{\mathrm{B}}T}\right) d^{(N-1)}q}{\int_{\textit{state}\ \text{i volume}} \exp\left(-\frac{\mathcal{V}(\mathbf{q})}{k_{\mathrm{B}}T}\right) d^{N}q} \qquad \text{Eq. (2.2)}$$

In this thesis, Eq. (2.2) is implemented by taking the following steps:

2.2.1 Step (1)- Finding initial estimates of the transition paths

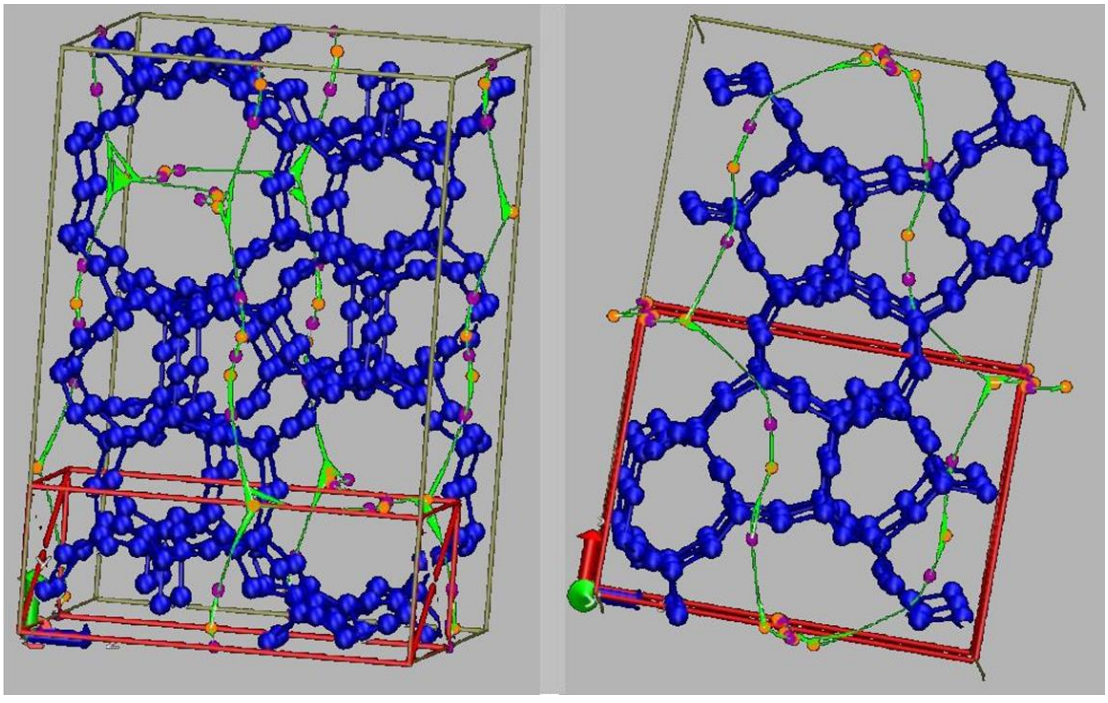

Figure 2.4 Unit cell of silicalite-1 viewed along the *x* (left) and along the *y* (right) crystallographic axes. Silicalite-1 atoms are represented in blue color. Red outline shows the asymmetric cell, from which the unit cell is constructed using symmetry rules. Paths obtained by for the repulsive sphere method are illustrated with green color. Minima of the energy felt by the soft spherical probe are shown in orange and saddle points in purple.

Nanoporous materials have channels. We will use paths constructed in the three-dimensional void space of these pores and channels as initial estimates of the transition paths required for application of Eq. (2.2). As initial path we define a line in 3-D space which satisfies the following properties: i) it lies entirely inside the pores (i.e., in the free volume of the material); ii) it is continuous and its tangent unit vector is continuous; iii) it does not intersect itself; iv) it satisfies the periodic boundary conditions of the crystal. One way to form an initial path[60] is to place a soft repulsive sphere of size commensurate with the pore diameter in the pore space, determine all local energy minima for that sphere in a rigid model of the medium, locate first order saddle points between the minima, e.g. by application of Baker's[37] algorithm in the

three translational degrees of freedom of the sphere, and trace reaction paths connecting the minima via the saddle points based on Fukui's intrinsic reaction coordinate approach.[61] This method is designed to be used in the general case of nanoporous sorbent-sorbate systems where paths are not geometrically obvious. A good example of such a system is the xenon-silicalite-1 system[62], where direct channel-to-channel transitions that circumvent the channel intersection are encountered. For the system of benzene/p-xylene in silicalite-1 that we examine here, the channels are obvious and a more straightforward, empirical method could be used for the identification of paths, such as tracing a smooth line through a set of points chosen by visual inspection of the intracrystalline pore system. In this thesis we have used the soft repulsive sphere approach of Maginn et al[60] described by the repulsive term of the Lennard-Jones potential with A=1398858.3kJ mol^{-1} Å^{12}, to locate initial transition paths in 3-D space, as we can see in Figure 2.4. Note that, if all subsequent calculations are conducted correctly, the exact choice of the initial transition path does not influence the final value of the diffusivity that we calculate later; it may affect the efficiency of computing 3-D free energy profiles, as we will see later in **Step (2)**. For the straight channel we also worked with a different path than was obtained by Maginn et al.'s repulsive sphere approach. This alternative path was a straight line consisting of points with coordinates (x=10.00 Å, y=y, z=0.0), where y is the only variable that can change values.

2.2.2 Step (2)- Introduction of soft repulsive walls and calculation of 3-D free energy profiles along the initial paths

Initial transition paths are defined so that we can move the sorbate (in our case a single sorbate in the periodic simulation box consisting of 3×3×3 unit cells) in areas that it rarely visits.

Our strategy is to drag the sorbate to any region we choose to examine within the void space of the nanoporous medium using pairs of soft repulsive walls. A repulsive wall will be represented by a pair of planes, Plane 1 and Plane 2, a distance R_2 apart, Plane 1 being normal to the transition path and proximal to the sorbate molecule (see Figure 2.5). In Figure 2.6 we see that only with a wall that is perpendicular to the path can one be sure about the intervals along the path in which the sorbate is not influenced by the walls. Of course this remains a problem in

very curved paths. We can deal with these problems by adjusting the distance between the two walls. We will elaborate on this later.

The wall generates a potential $\mathcal{V}^{w}(r)$ that depends on the distance r between the sorbate center of mass and Plane 2. $\mathcal{V}^{w}(r)$ is harshly repulsive in the vicinity of Plane 2 and drops to zero on Plane 1, where its first and second derivatives are also zero. It has the form of a Lennard-Jones potential for $0 < r < R_1$ and a quintic spline for $R_1 < r < R_2$. $\mathcal{V}^{w}(r)$, its first and second derivatives are continuous. The wall potential is given by the following expression, first proposed in Ref. 63.

$$\mathcal{V}^{\mathrm{w}}(r) = \begin{cases} u^{\mathrm{LJ}}(r) = 4\varepsilon_{\mathrm{w}}\left\{\left(\dfrac{\sigma_w}{r}\right)^{12} - \left(\dfrac{\sigma_w}{r}\right)^{6}\right\} & , \; r_1 \le R_1 \\ \varepsilon_{\mathrm{w}}(1-\zeta)^3\left\{\dfrac{u_1^{\mathrm{LJ}}}{\varepsilon_{\mathrm{w}}} + \left(3\dfrac{u_1^{\mathrm{LJ}}}{\varepsilon_{\mathrm{w}}} + \Delta\dfrac{u_1'^{\mathrm{LJ}}}{\varepsilon_{\mathrm{w}}/\sigma_{\mathrm{w}}}\right)\zeta + \right. & \\ \left.\left(6\dfrac{u_1^{\mathrm{LJ}}}{\varepsilon_{\mathrm{w}}} + 3\Delta\dfrac{u_1'^{\mathrm{LJ}}}{\varepsilon_{\mathrm{w}}/\sigma_{\mathrm{w}}} + \dfrac{\Delta^2}{2}\dfrac{u_1''^{\mathrm{LJ}}}{\varepsilon_{\mathrm{w}}/\sigma_{\mathrm{w}}^2}\right)\zeta^2\right\} & , \quad R_1 < r \le R_2 \\ 0 & , \quad r > R_2 \end{cases} \qquad \text{Eq. (2.3)}$$

where we have used the abbreviations

$$u_1^{\mathrm{LJ}} = u^{\mathrm{LJ}}(R_1), \quad u_1'^{\mathrm{LJ}} = \left.\frac{du^{\mathrm{LJ}}}{dr}\right|_{R_1}, \quad u_1''^{\mathrm{LJ}} = \left.\frac{d^2u^{\mathrm{LJ}}}{dr^2}\right|_{R_1}, \quad \zeta = \frac{r-R_1}{R_2-R_1}, \quad \Delta = \frac{R_2-R_1}{\sigma_{\mathrm{w}}} \qquad \text{Eq. (2.4)}$$

The parameter values σ_{w} =2.5 Å, ε_{w} =0.5975 kcal/mol = 2.5×10^2 amu Å^2/ps^2, R_1/σ_{w} = 0.60, R_2/σ_{w} =0.80 were used in all calculations reported here.

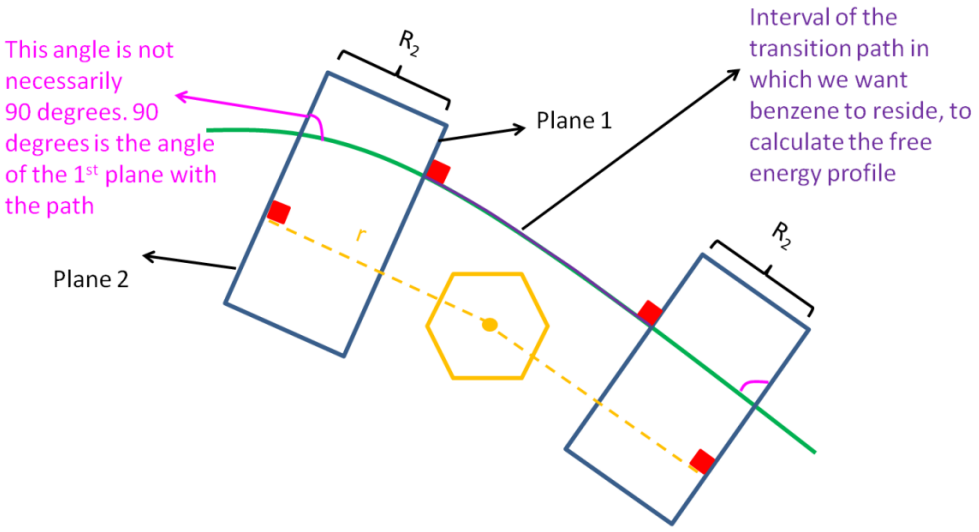

Figure 2.5 Walls along a path. Green line shows the path, blue boxes are the walls

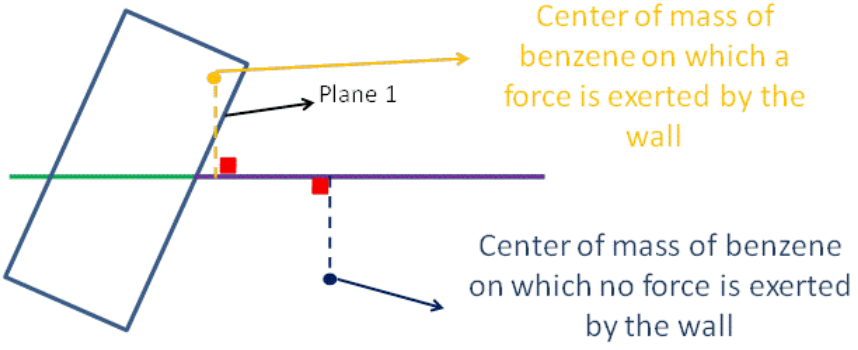

Figure 2.6 Projection of benzene's center of mass (CM) on a path which is not normal to the wall.

The two wall potentials $\mathcal{V}^{w}(r)$ are introduced on either side of the penetrant in integrating the equations of motion of the penetrant plus flexible nanoporous medium. In this way, the penetrant's center of mass is confined to reside in a region of the intracrystalline void space corresponding to a specific region around a chosen transition path and bounded by the two walls and the internal surface of the nanoporous medium. This confinement is graphically depicted in Figure 2.7. The walls exert a force on the sorbate's center of mass only, which is added to the force exerted by the crystal on the sorbate. However, the torques and the orientations of the sorbate are not influenced by the walls. Here we remind the reader that the Verlet leapfrog algorithm we invoke uses only torques and forces exerted on the sorbate center of mass. The

force of the walls is exerted on the sorbate's center of mass. As a result, it treats the sorbate as a pointwise 1-dimensional object. From Newton's law, the velocity change due to the wall force will be

$$\delta \mathbf{v}_{\mathrm{CM}} = \frac{\mathbf{F}^{\mathrm{w}}}{m} dt \qquad \text{Eq. (2.5)}$$

This change of the velocity of the center of mass is added to the velocity vector of each atom of the sorbate. In other words,

$$\mathbf{v}_i = \mathbf{v}_{i,\mathrm{unconstrained}} + \delta \mathbf{v}_{\mathrm{CM}} \qquad \text{Eq. (2.6)}$$

From Figure 2.7 the reader can appreciate that the wall potential is very steep and that most of the path interval considered is free of interactions with the walls. The way walls work in MD simulation can be seen in Video 1 provided with this thesis.

We stress the need for the proximal wall to be normal to the transition path considered (Figure 2.6). If this condition is not fulfilled, the void space cannot be projected uniquely onto the path. Transition paths are stored as sequences of points (x_i, y_i, z_i) in 3-D space. The tangent vector to the path at point (x_i, y_i, z_i) is approximated as $\mathbf{i}/i = \mathbf{i}/|\mathbf{i}|$ with $\mathbf{i}=(x_{i+1}-x_i,\ y_{i+1}-y_i,\ z_{i+1}-z_i)$. This is a good approximation, given that the distance between adjacent stored points along the path is only i=0.05 Å. To confine the penetrant in the interval between two points, $\mathbf{r}_{\mathrm{o.p.1}}$ and $\mathbf{r}_{\mathrm{o.p.2}}$, on the transition path, we erect the proximal wall planes (Planes 1) at $\mathbf{r}_{\mathrm{o.p.1}}$ and $\mathbf{r}_{\mathrm{o.p.2}}$ with normal vectors $\mathbf{i}_1$ and $\mathbf{i}_2$, respectively. We then construct the distal planes (Planes 2) with the same normal vectors, at positions

$$\mathbf{r}_{\mathrm{n.p.1}} = \mathbf{r}_{\mathrm{o.p.1}} - R_2 \cdot \frac{\mathbf{i}_1}{i_1} \quad \text{(wall 1)}$$
$$\mathbf{r}_{\mathrm{n.p.2}} = \mathbf{r}_{\mathrm{o.p.2}} + R_2 \cdot \frac{\mathbf{i}_2}{i_2} \quad \text{(wall 2)} \qquad \text{Eq. (2.7)}$$

The procedure is explained pictorially in Figure 2.8. This methodology is not constrained by the rigidity or the flexibility of the sorbate.

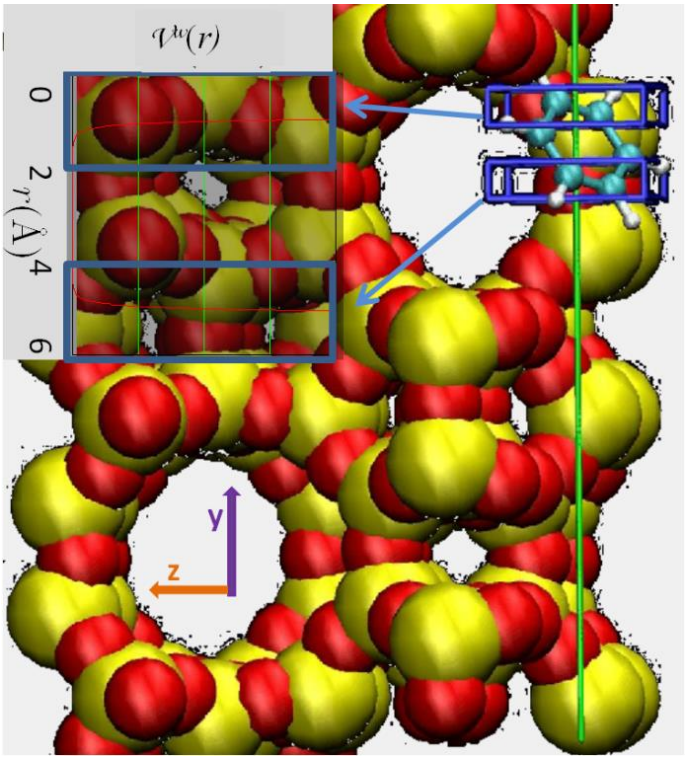

Figure 2.7 Silicalite-1 unit cell with soft repulsive walls added to confine the benzene penetrant. The walls are shown as blue boxes. Oxygen and silicon atoms are illustrated in red and yellow, respectively. The transition path along which the benzene is moved, in this case a straight line directed along a straight channel axis of silicalite-1, is shown in green. The potential energy $\mathcal{V}^w$ exerted on benzene center of mass by each of the two walls is shown in the inset.

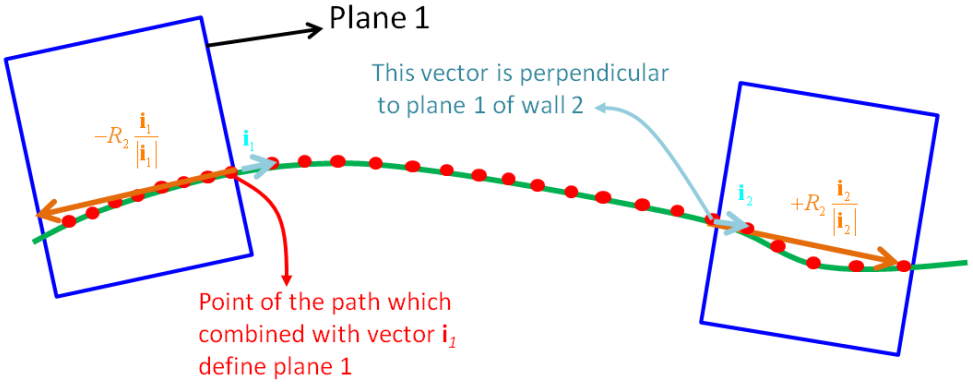

Figure 2.8 Construction of the walls.

If we assume that the diffusive progress of the sorbate is not associated with structural transitions of the sorbent framework and that the characteristic times of vibrational motion of the framework are short in comparison to the waiting times spent by the sorbate in a sorption state, as has been shown by neutron experiments for benzene,[64] the reaction coordinate for infrequent jumps between sorption states will be dominated by the 6 degrees of freedom (three translational and three orientational) of the sorbate. If, in addition, we assume that the orientational relaxation time of the sorbate while it is confined in a state is much shorter than the waiting time in the state, the dimensionality of the problem can be reduced further; the reaction coordinate can be considered to be dominated by the three translational degrees of freedom of the sorbate center of mass. We will return to the problem of assessing the role of orientational degrees of freedom in **Step 4**. For the time being we will assume that the translational degrees of freedom of the sorbate center of mass dominate the reaction coordinate. Under these conditions, the rate constants of transitions between sorption states described by the multidimensional expression, Eq. (2.2), will be expressible in terms of a local free energy field depending on the center of mass coordinates, $\mathbf{r}_{CM}$:

$$A(\mathbf{r}_{CM}) = -k_B T \ln\left(\frac{\int \delta\left(\mathbf{r}_{CM} - f_{CM}(\mathbf{r})\right) \exp\left(-\frac{\mathcal{V}(\mathbf{r})}{k_B T}\right) d^N r}{\int \exp\left(-\frac{\mathcal{V}(\mathbf{r})}{k_B T}\right) d^N r} \right) + \text{const.}$$

or

$$A(\mathbf{r}_{CM}) = -k_B T \ln\left(n(\mathbf{r}_{CM})\right) + \text{const.} \qquad \text{Eq. (2.8)}$$

where $f_{CM}(\mathbf{r})$ is a known function which yields the center of mass position vector given the vector $\mathbf{r}$ of all configurational degrees of freedom of the system and $\mathcal{V}(\mathbf{r})$ is the system's total potential energy, also appearing in Eq. (2.2). In the second line of Eq. (2.8),[65] the local free energy $A(\mathbf{r}_{CM})$ is expressed in terms of the equilibrium probability density $n(\mathbf{r}_{CM})$ of the sorbate center of mass. The presence of free energy barriers in $A(\mathbf{r}_{CM})$ that are high relative to $k_B T$ precludes a direct calculation of $n(\mathbf{r}_{CM})$ by "brute-force" MD simulation. This is why the idea of umbrella sampling using artificial wall potentials $\mathcal{V}^w$ (compare Eqs. (2.3), (2.4)) was introduced.

We will use the constraining walls in order to accumulate density profiles $n(\mathbf{r}_{CM})$ within small regions of the 3-D space spanned by $\mathbf{r}_{CM}$. Within such a small region, $\mathcal{V}(\mathbf{r})$ will not vary dramatically; thus, a reasonable estimate of the equilibrium distribution $n(\mathbf{r}_{CM})$ will be obtained. Hence, the local free energy $A(\mathbf{r}_{CM})$ in the region can be extracted via Eq. (2.8), up to an additive constant. Near the edges of the region this estimate will be affected by the artificial wall potentials imposed in order to confine the system in the region. In a broad central part of the region, however, these potentials are zero and the accumulated $A(\mathbf{r}_{CM})$ will be representative of the original, wall-free system. If the calculation of $A(\mathbf{r}_{CM})$ is undertaken in overlapping small regions and artifactual results for the edges of the regions are discarded, the remaining profiles for $A(\mathbf{r}_{CM})$ at the central intervals of the regions can be stitched together by translation into a global three-dimensional free energy field. Once $A(\mathbf{r}_{CM})$ is available in 3-D, rate constants for infrequent transitions between sorption sites, surrounding local minima of $A(\mathbf{r}_{CM})$, can be computed via a three-dimensional analog of Eq. (2.9):

$$k_{i\to j}^{TST} = \left(\frac{k_B T}{2\pi m}\right)^{1/2} \frac{\int_{\substack{\text{dividing surface}\\ \text{between } i \text{ and } j}} \exp\left(-\frac{A(\mathbf{r}_{CM})}{RT}\right) d^2 r_{CM}}{\int_{\text{state } i} \exp\left(-\frac{A(\mathbf{r}_{CM})}{k_B T}\right) d^3 r_{CM}} \qquad \text{Eq. (2.9)}$$

with *m* being the mass of the sorbate molecule.

The density distribution $n(\mathbf{r}_{CM})$ was accumulated on a cubic grid with edge length 0.1 Å. The procedure we have devised for stitching together local free energy profiles derived from MD simulations within regions delimited by the wall potentials is outlined in Figure 2.9. In this Figure, for the overlapping points i of green and red fragments it is valid that $-\ln(n(\xi_{i,1st})) = -\ln(n(\xi_{i,2nd})) + c$ where n is the value of the histogram accumulating the density along the reaction coordinate, 1^{st} denotes the green and 2^{nd} the red fragment. These fragments are stitched using a constant c, which is estimated as the average value of the difference between the overlapping parts of the red and green fragments. More specifically, with N_d being the number of points for which overlap occurs,

$$c = \frac{\sum_{i=1}^{N_d} \left(-\ln(n(\xi_{i,1st})) + \ln(n(\xi_{i,2nd})) \right)}{N_d} \qquad \text{Eq. (2.10)}$$

This is a consequence of applying a least squares method with known slope to match the two fragments. After the calculation of *c*, we move the red fragment by *c*. It is possible that the points of fragments accumulated with small accuracy (=not statistically equilibrated) may not be stitched perfectly. If they diverge a lot, these points are omitted. This can happen if the distance between the two walls is large for points where the slope of the free energy profile is large. After stitching, a new red fragment is created which contains the old red fragment plus the points of the green fragment that are not overlapping. The same procedure is repeated by stitching a new green fragment, with the red fragment growing in extent until all green fragments are exhausted. The fact that the periodicity and the symmetries imposed by the crystal structure on the free energy profile are satisfied to an excellent approximation and that deviations between corresponding points of the stitched fragments are very small constitutes a proof of good stitching.

In our problem, 3-D free energy profiles are very helpful in understanding where minima of the free energy $A(\mathbf{r}_{CM})$ (sorption sites) are and where saddle points and dividing surfaces between these minima are located. The location of saddle points and dividing surfaces is most critical for the calculation of diffusivity. As stated by Smit and Maesen,[66] although a transmission coefficient can be used to correct an unfortunate choice of reaction coordinate, if the transmission coefficient is very small, it is expensive to compute it accurately.

This is why we proceed to refine our one-dimensional transition paths based on the information we have accumulated concerning $A(\mathbf{r}_{CM})$.

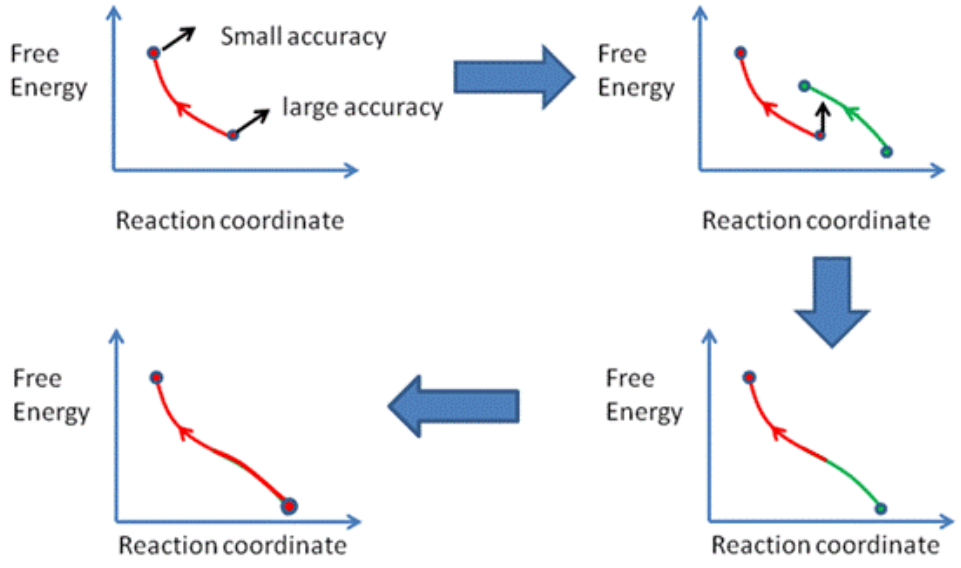

Figure 2.9 Procedure used to stitch together local free energy profiles over successive overlapping regions along a transition path. The optimal vertical displacement of the green profile in order to link it with the red profile is determined via a least squares method. Next, from the common part of red and green fragment, we keep only the red one. The joint fragment is now made all red and the same process is repeated.

2.2.3 Step (3)- Refining transition paths

Knowing the 3-D free energy profile helps us choose a better transition path for tracking the translational progress of the sorbate center of mass between two states. The first criterion that this new path must satisfy is that all points of the dividing surface and only these points must be projected on the point of maximal free energy along the path. The second criterion is that the path should work as a "rail" for the walls and statistically enrich the area the sorbate rarely visits, better than other candidate paths. This area is known because of the 3-D free energy profile. This improved transition path is used to compute a 1-D free energy profile along the path, as outlined in Eq. (2.8). In this equation ξ is the length measured along the, in general curvilinear, transition path. A point on the path is arbitrarily assigned the value ξ=0. $n(\xi)$ is a one-dimensional probability distribution of the center of mass of the sorbate along the path. The

rate constant for transition from state *i* to state *j* is computed from the one-dimensional free energy profile $A(\xi)$ via Eq. (2.12). Here $\xi_1^{(i)}$ and $\xi_2^{(i)}$ stand for the curvilinear coordinates, along the path, of the local maxima in $A(\xi)$ which delimit state *i*. The value $\xi^{\dagger}$, on the other hand, is the curvilinear coordinate, along the transition path, of the highest maximum in $A(\xi)$ (free energy barrier) which controls the rate of transitions from state *i* to state *j*.

$$A(\xi) = -k_{\mathrm{B}}T \ln(n(\xi)) + \text{const.} \qquad \text{Eq. (2.11)}$$

$$k_{i\to j}^{\mathrm{TST}} = \left(\frac{k_{\mathrm{B}}T}{2\pi m}\right)^{1/2} \frac{\exp\left(-\frac{A(\xi^{\dagger})}{k_{\mathrm{B}}T}\right)}{\int_{\xi_1^{(i)}}^{\xi_2^{(i)}} \exp\left(-\frac{A(\xi)}{k_{\mathrm{B}}T}\right) d\xi} \qquad \text{Eq. (2.12)}$$

From Eq. (2.12), we can see that the path does not actually influence the denominator (its value is shaped by a very small area around the free energy minimum of state *i*, where the Boltzmann factor of the local free energy is appreciable). The numerator, on the other hand, is strongly influenced by the exact value of the free energy maximum. An error of $k_{\mathrm{B}}T$ in the free energy barrier brings about an error of a factor of e in the rate constant. This sensitivity of the rate constant to the saddle point free energy can be seen in Eq. (2.13).

$$\begin{aligned} k_{i\to j,err} &= \left(\frac{k_{\mathrm{B}}T}{2\pi m}\right)^{1/2} \frac{\exp\left(-\frac{A(r_{\mathrm{CM},pr}) - A^{\mathrm{error}}}{k_{\mathrm{B}}T}\right)}{\int_{state} \exp\left(-\frac{A(r_{\mathrm{CM},pr})}{k_{\mathrm{B}}T}\right) dr} = \\ &= \underbrace{\left(\frac{k_{\mathrm{B}}T}{2\pi m}\right)^{1/2} \frac{\exp\left(-\frac{A(r_{\mathrm{CM},pr})}{k_{\mathrm{B}}T}\right)}{\int_{state} \exp\left(-\frac{A(r_{\mathrm{CM},pr})}{k_{\mathrm{B}}T}\right) dr}}_{k_{i\to j}} \exp\left(+\frac{A^{\mathrm{error}}}{k_{\mathrm{B}}T}\right) \\ &= k_{i\to j} \exp\left(+\frac{A^{\mathrm{error}}}{k_{\mathrm{B}}T}\right)^{A^{\mathrm{error}}=1k_{\mathrm{B}}T} = 2.7182 k_{i\to j} \end{aligned} \qquad \text{Eq. (2.13)}$$

This shows the enormous importance of the transition path on which center of mass projections are made. To understand this better, we first have to define what we mean by projection. Because we are dealing with curves in three-dimensional space, it is possible that a given position of the center of mass of the sorbate may be projected onto more than one points along the same transition path. This should be avoided, to avoid ambiguities in the definition of the local free energy. To deal with this, we have added the criterion of minimum distance in case more than one projections to the path exist. In Figure 2.10, we can see how the projection is calculated exactly.

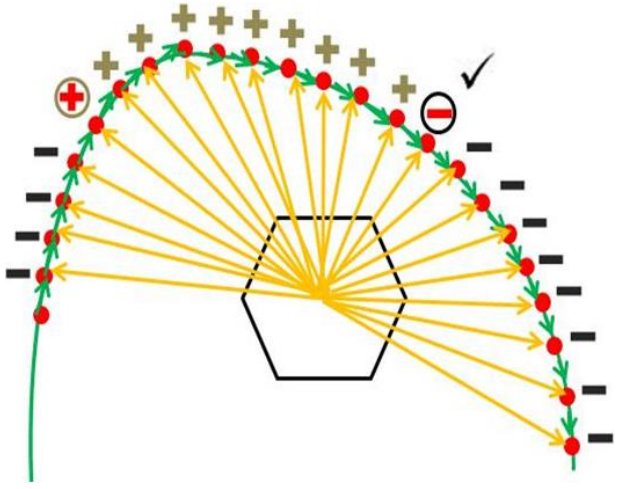

Figure 2.10 Projection of center of mass of benzene. Points considered along the transition path are shown in red, while the path itself is depicted as a green line. At the encircled points the inner product of the vector from the benzene center of mass to the path and the tangent vector to the path changes sign. These are candidate projection points. Of the two candidate points in this example, the one lying closer to the benzene center of mass is chosen.

2.2.4 Step (4)-Calculation of rotational free energy profiles

Before continuing to the reduction to the 1-D free energy profile using Eq. 2.11, we must confirm that the rotational degrees of freedom do not play a significant role in the elementary transitions through which translational diffusion occurs and that the 1-D free energy profile is independent of orientation. To do this, we move the sorbate with the walls to areas which it rarely visits, sample its orientations there as vigorously as possible and accumulate distributions of the orientations it adopts.

2.2.5 Step (5)-Calculation of the 1-D free energy profiles

We examine overlapping intervals of contour length 0.75Å or 15 points along the transition paths of the straight channel and 1Å or 20 points along the sinusoidal channel. We chose to work with more points along the sinusoidal channel than the straight, because the sinusoidal channel is curved and we wanted to avoid the case of two walls intersecting each other.

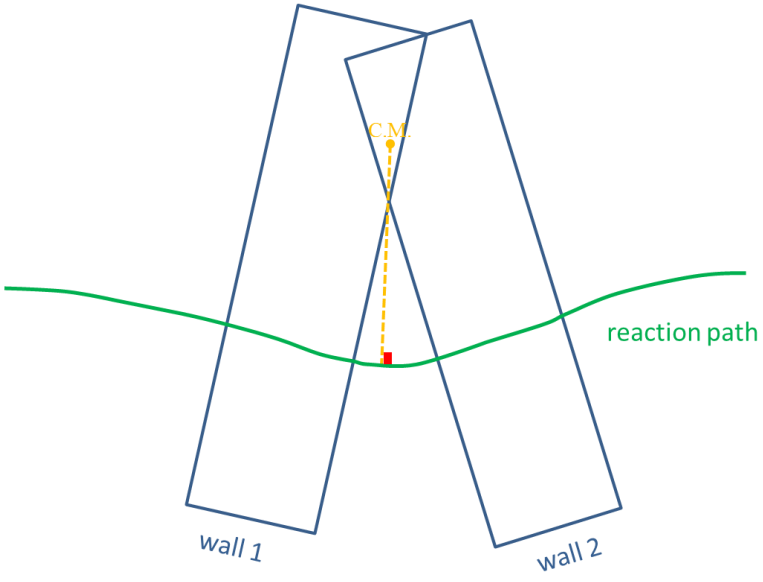

Figure 2.11 Two walls which intersect each other and, if applied simultaneously, do not allow the sorbate center of mass to visit areas that we must sample. This leads to a wrong calculation of the free energy profile value at the point of projection. This can also be the reason for the case that two consecutive free energy fragments do not stitch perfectly. 3-Dimensional free energy profiles help us define the distance between the walls.

To sample each interval, we move the walls by two points every time (=0.1Å) along the paths, place the sorbate molecule with its center in the wall-free region of the interval at a random initial orientation, and integrate the equations of motion of the flexible sorbent plus sorbate system with MD for 7.5 ns with a time step of 0.5fs. A previously sampled configuration from an already examined overlapping interval may serve as initial configuration for the MD run. Every 0.5fs we project the center of mass of the sorbate on the sinusoidal and straight channel paths, assign it to the considered interval if the minimum distance criterion discussed in Figure 2.10 is fulfilled and determine its ξ value along the considered interval based on the projection.

At the end of the MD simulation we recover the density distribution of centers of mass $n(\xi)$ over the considered interval and take its logarithm to determine the one-dimensional local free energy profile $A(\xi)$ in the interval via Eq. (2.11). As already mentioned, values of $A(\xi)$ near the edges of the interval may be affected by the wall potential and therefore not be representative of the wall-free system. Such artifacts become obvious during the stitching of local free energy profiles from overlapping intervals.

To make sure that the final free energy profiles obtained from stitching are completely independent of the wall potentials, we repeated the whole calculation at 465 K for benzene using a different value for ε_w = 0.05975 kcal/mol (see section 4 for a more extensive description). The free energy profiles obtained were identical. Smaller ε_w means weaker (less steep) walls, which in turn means that more time may be required for equilibrating the center of mass distributions within each interval, as the sorbate will spend more time near the wall on the side of the interval where $\mathcal{V}$ due to the zeolite is lower. On the other hand, walls that are too hard (very high ε_w) may impart very high momenta to the sorbate upon collision, preventing thermal equilibration with the crystal over reasonable time scales. The wall potential parameters used in our production runs and stated above were optimized based on results of preliminary simulations.

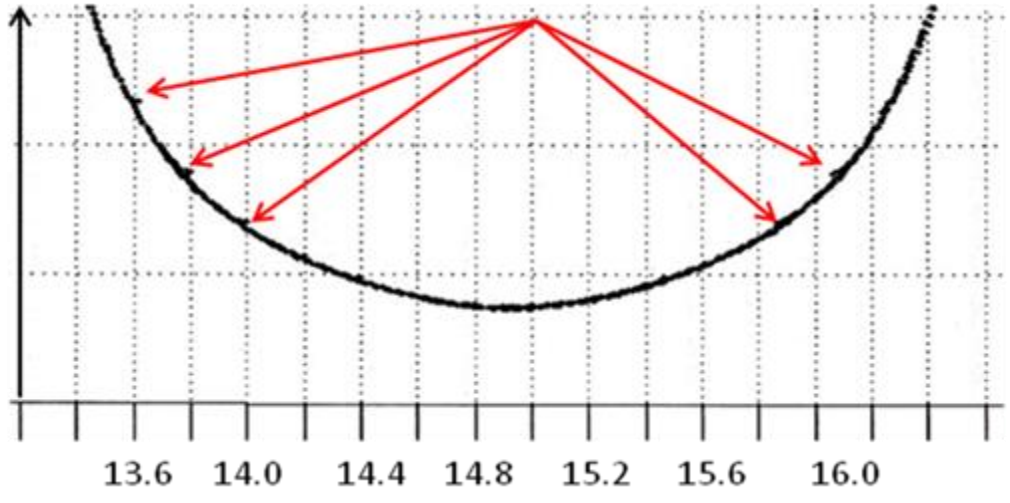

Figure 2.12 Unsucessful stitching because of very steep walls. Red arrows show points where perfect overlap is not achieved because the accumulated free energy profile is affected by the confining walls. Such terminal sections of local free energy profiles are discarded during the stitching process.

2.2.6 Step (6)-Calculation of rate constants and diffusivities via Kinetic Monte Carlo (KMC) and Isosteric heat calculations

From the 1-D free energy profiles, we can calculate the transition rate constants using Eq. (2.14) as soon as we define the states (areas between two maxima of the free energy). In Eq. (2.14), ($\xi_1^{(i)}, \xi_2^{(i)}$) is the interval, along the reaction coordinate, corresponding to state *i* and $\xi^{\dagger}$ is the reaction coordinate value at the free energy maximum separating states *i* and *j*; *m* is the mass of the diffusing molecule. In the cases we studied, a large number of states have been found. To be able to compare exactly the transition rate constants calculated here from different force-fields we should have the same states in all these force fields. We will see later that we propose a reduction of the total number of macro-states to 4 for p-xylene. These states are the Intersection state in which the sorbate has the orientation of the straight channel (I_S), the Intersection state in which the sorbate has the orientation of the zig-zag channel (I_Z), the Straight Channel state (S), and the Zig-zag or sinusoidal channel state (Z). In the case of benzene, the total number of macro-states is 3, as we have only one state in the intersection (I). If the suggested reduction in the number of states is correct, it should not influence the predicted values of the diffusion coefficients. Also, this reduction has the advantage of simplifying the description of the systems we study without losing any important information.

$$k_{i\to j}^{\mathrm{TST}} = \left(\frac{k_{\mathrm{B}}T}{2\pi m}\right)^{1/2} \frac{\exp\left(-\dfrac{A(\xi^{\dagger})}{k_{\mathrm{B}}T}\right)}{\displaystyle\int_{\xi_1^{(i)}}^{\xi_2^{(i)}} \exp\left(-\frac{A(\xi)}{k_{\mathrm{B}}T}\right) d\xi} = \left(\frac{k_{\mathrm{B}}T}{2\pi m}\right)^{1/2} \frac{\rho_{\xi^{\dagger}}}{\displaystyle\int_{\xi_1^{(i)}}^{\xi_2^{(i)}} \rho_{\xi} d\xi} \qquad \text{Eq. (2.14)}$$

In the sketch of Figure 2.13 two cases are illustrated, which we encountered in our 1-D free energy profiles. In the first case, two states with low energy barriers between them (< 1*RT*) and four transition rate constants are reduced to one state and two transition rate constants (see Figure 2.13a). In the second case, two states with high energy barriers (states 1 and 3) separated by a state with low energy barrier (state 2) are reduced to two states with high energy barriers (see Figure 2.13b). In addition, the new rates produced after the reduction must also satisfy the

microscopic reversibility condition. A proof that this is always the case for the states defined here is given in Eq. (2.15).

$$\rho_{\xi_2}\left(\frac{\rho_{\xi_3}}{\rho_{\xi_2}+\rho_{\xi_3}}\right)=\rho_{\xi_3}\left(\frac{\rho_{\xi_2}}{\rho_{\xi_2}+\rho_{\xi_3}}\right)\xrightarrow{\times\left(\frac{k_BT}{2\pi m}\right)^{1/2}}\left(\frac{k_BT}{2\pi m}\right)^{1/2}\rho_{\xi_2}\left(\frac{\rho_{\xi_3}}{\rho_{\xi_2}+\rho_{\xi_3}}\right)=\left(\frac{k_BT}{2\pi m}\right)^{1/2}\rho_{\xi_3}\left(\frac{\rho_{\xi_2}}{\rho_{\xi_2}+\rho_{\xi_3}}\right)\rightarrow$$

$$\rightarrow\underbrace{\left(\frac{k_BT}{2\pi m}\right)^{1/2}\frac{\rho_{\xi_2}}{\int_{\xi_1}^{\xi_2}\rho_\xi d\xi}\left(\frac{\rho_{\xi_3}}{\rho_{\xi_2}+\rho_{\xi_3}}\right)}_{k_{1\to3}^{TST}}\underbrace{\left(\int_{\xi_1}^{\xi_2}\rho_\xi d\xi\right)}_{P_1}=\underbrace{\left(\frac{k_BT}{2\pi m}\right)^{1/2}\frac{\rho_{\xi_3}}{\int_{\xi_3}^{\xi_4}\rho_\xi d\xi}\left(\frac{\rho_{\xi_2}}{\rho_{\xi_2}+\rho_{\xi_3}}\right)}_{k_{3\to1}^{TST}}\underbrace{\left(\int_{\xi_3}^{\xi_4}\rho_\xi d\xi\right)}_{P_3}\rightarrow$$

$$\rightarrow k_{1\to3}^{TST}P_1=k_{3\to1}^{TST}P_3$$

Eq. (2.15)

To our knowledge, this is the first time this method is used for rate constant calculation after a reduction in the number of states. In the first case, the transition rates are calculated for the values ξ_1 to ξ_3 of the reaction coordinate for the state 1 of Figure 2.13a. In the second case, a special manipulation is needed. Because of the high free energy of state 2 of Figure 2.13b, the sorbate resides there with low probability. In case the sorbate enters state 2, it will move on quickly to another state, because the free energy barrier that must be overcome in order to escape from state 2 is low. The probability for a transition from state 2 via the ξ_2 saddle point to state 1 to take place will be different from the probability for a transition from state 2 via the ξ_3 saddle point to state 3 to take place. The two probabilities are described by Eq. (2.16). $P_{\xi i}$ is the conditional probability that a transition out of state 2 will take place via the route of ξ_i and ρ is proportional to the probability density of the sorbate center of mass. In other words, a fraction of the trajectories which lead to transition from state 1 to state 2, will manage to pass successfully to state 3. This, of course, has similarities with the transmission coefficient definition[67,68].

$$P_{\xi_2}=\frac{\rho_{\xi_2}}{\rho_{\xi_2}+\rho_{\xi_3}},\quad P_{\xi_3}=\frac{\rho_{\xi_3}}{\rho_{\xi_2}+\rho_{\xi_3}},\text{ where }\rho_{\xi_i}=e^{-\frac{A_{1-D}(\xi_i)}{RT}}$$

Eq. (2.16)

As a result, the rate constant for the transition from state 1 of Figure 2.13b to state 3 of the same Figure will be described by Eq. (2.17).

$$k_{1\to 3}^{\mathrm{TST}} = k_{1\to 2}^{\mathrm{TST}} P_{\xi_3} = \left(\left(\frac{k_{\mathrm{B}} T}{2\pi m} \right)^{1/2} \frac{\rho_{\xi_2}}{\int_{\xi_1}^{\xi_2} \rho_{\xi} d\xi} \right) \left(\frac{\rho_{\xi_3}}{\rho_{\xi_2} + \rho_{\xi_3}} \right) \qquad \text{Eq. (2.17)}$$

Combining the 1-D free energy profiles and the method of Figure 2.13, we get the final macro-states. For these macro-states, using Eq. (2.17), we calculate the transition rate constants. Solving a linear system of equations obeying microscopic reversibility $\left(k_{i\to j}^{\mathrm{TST}} P_i = k_{j\to i}^{\mathrm{TST}} P_j \right)$, we calculate the equilibrium probability P_i for each macro-state i.

To compute the isosteric heat of sorption, we place repulsive walls at the entrances to each state (maxima in the 1-D free energy profiles) to trap the sorbate in this state. Then, we write out the sorbate-silicalite-1 potential energy ($\mathcal{V}_{\text{S-Z}}$) in every timestep of an MD trajectory confined to the state. From the recorded values we compute a mean energy of interactions for each state. The isosteric heat is then obtained from Eq. (2.18).[50]

$$Q_{st} = -\left\langle \mathcal{V}_{S-Z} \right\rangle_{NVT} + RT, \quad \text{or} \quad Q_{st} = -\sum_{i=1}^{\text{states}} P_i \left\langle \mathcal{V}_{S-Z}^{\text{state}_i} \right\rangle_{NVT} + RT \qquad \text{Eq. (2.18)}$$

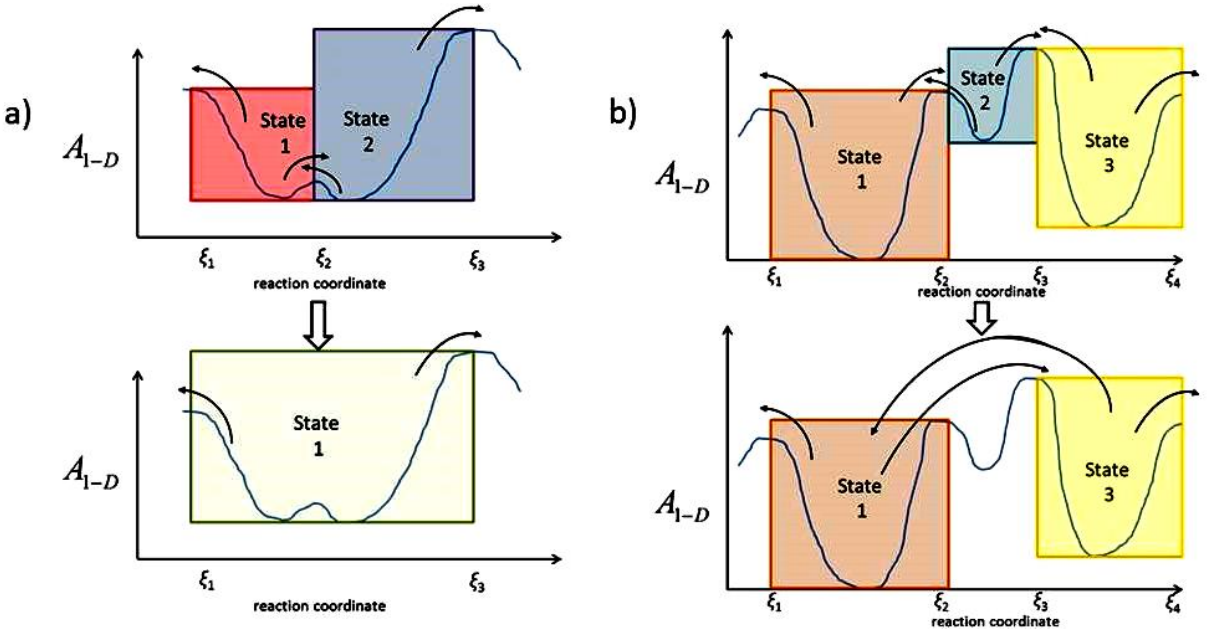

Figure 2.13 Two different methods of reduction in the number of states are illustrated. (a) two states with low energy barriers between them (< 1*RT*) and four transition rate constants are reduced to one state and two transition rate constants, (b) two states with high energy barriers (states 1 and 3) divided by a state with low energy barrier (state 2) are reduced to two states with high energy barriers

Knowing the rates for all interstate transitions, one only has to solve the Master equation, Eq. (2.19), in the probabilities of occupancy of the states $P_i(t)$ subject to given initial conditions in order to determine the self-diffusion tensor.

$$\frac{\mathrm{d}P_i}{\mathrm{d}t} = -\sum_j k_{i\to j}P_i + \sum_j k_{j\to i}P_j \qquad \text{Eq. (2.19)}$$

The master equation, Eq. (2.19), can be written in compact form for all states as

$$\frac{\partial \mathbf{P}(t)}{\partial t} = \mathbf{K}\ \mathbf{P}(t) \qquad \text{Eq. (2.20)}$$

We have used two methods to solve Eq. (2.20): Kinetic Monte Carlo simulation (KMC)[17,41,69] and the analytical approach known as Master Equation Solution by Recursive Reduction of Dimensionality (MESoRReD). Now, we will elaborate on KMC and we will refer to

MESoRReD in the next chapter extensively, as MESoRReD is a new method invented in this thesis.

KMC is the most common method for solving the Master Equation. However, there is a risk that it may be very slow if interstate rate constants are very broadly distributed. The Kinetic Monte Carlo method was applied to a single unit cell satisfying periodic boundary conditions.

In this work for the diffusion coefficient of benzene, 4000 noninteracting walkers were deployed among the states of a unit cell according to the equilibrium probabilities of occupancy of the states Let $N_i(t)$ be the number of walkers in state (site) i at time t . After initialization, the KMC simulation proceeded as follows:

(i) For each state i that is occupied at the current time t, we calculate the expected fluxes $R_{i\to j}(t) = N_i(t)\ k_{i\to j}$ to all states j to which state i is connected. We also compute the overall flux $R(t) = \sum_i \sum_j R_{i\to j}(t)$ and the conditional probabilities $q_{i\to j}(t) = R_{i\to j}(t)/R(t)$.

(ii) We generate a uniformly distributed pseudorandom number $s \in [0,1)$. We then choose the time for occurrence of the next transition (jump event) in the network as $\Delta t = -\ln(1-s)/R(t)$. We also choose the type of the next transition by picking one of the possible transitions $i\to j$ according to the conditional probabilities $q_{i\to j}(t)$.

(iii) Of the $N_i(t)$ walkers present in state i we pick one with probability $1/N_i(t)$ and move it to state j.

(iv) We advance the simulation time by Δt. We update the array that keeps track of the current positions of all walkers to reflect the implemented transition. We update the occupancy numbers $N_i(t+\Delta t) = N_i(t) - 1$ and $N_j(t+\Delta t) = N_j(t) + 1$.

(v) We return to step (i) to implement the next transition.

In KMC, the elements of the self-diffusivity tensor are calculated by tracking the mean square displacement of the walkers as a function of time, via the Einstein relation[17].

$$D_{aa} = \lim_{t\to+\infty} \frac{\left\langle (r_a(t) - r_a(0))^2 \right\rangle}{2t} \qquad \text{Eq. (2.21)}$$

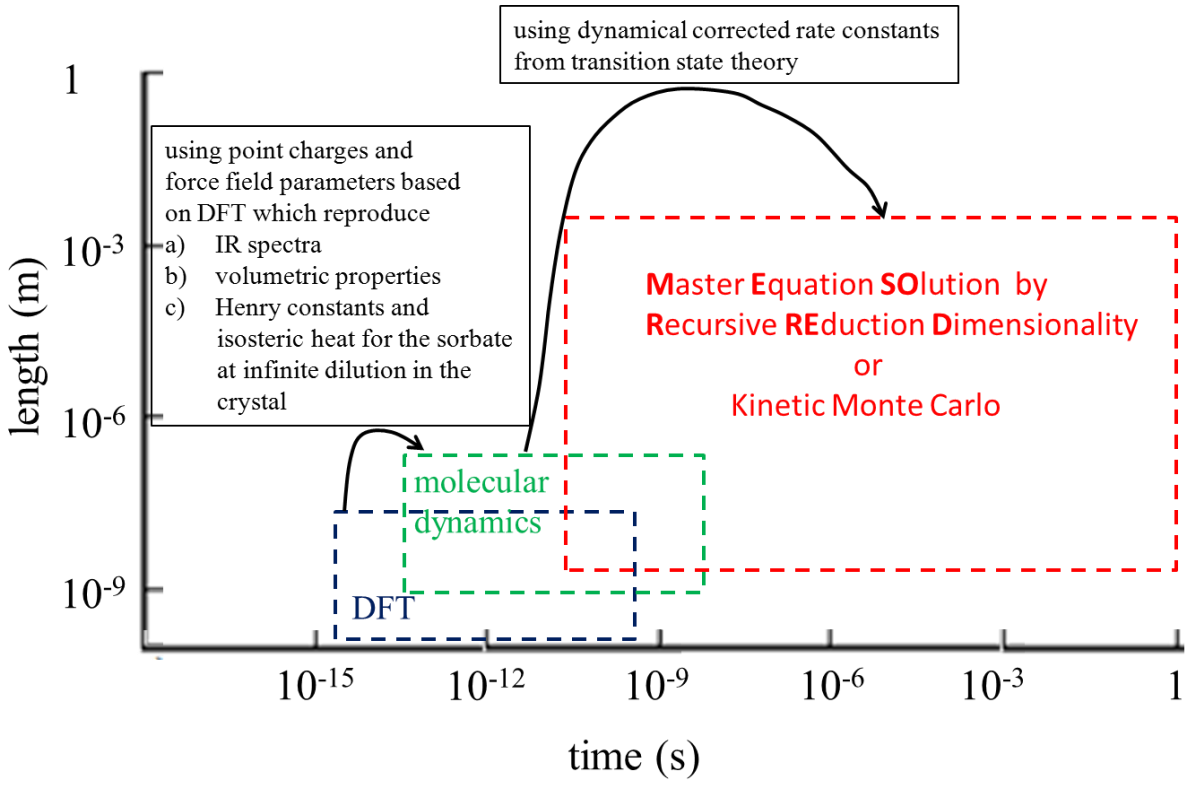

Figure 2.14 Computational methods which must be used to arrive at accurate predictions of macroscopic properties for systems of tight-fitting sorbates inside nanoporous materials.

The results from the Kinetic Monte Carlo for benzene will be presented later extensively in Chapter 4.

Here, it is important to add that the algorithm we described in this Chapter 2 helps to predict macroscopic properties from the miscroscopic ones (in this case using molecular dynamics). In Figure 2.14, we can see all stages of modeling and simulation that must be undertaken in order to arrive at accurate macroscopic predictions for the diffusion of tight-fitting sorbates in nanoporous materials.

Chapter 3

On solving the master equation on orthorhombic spatially periodic systems

3.1 Introduction to the problem

3.1.1 States, transition rate constants, and Master Equation

Consider a system capable of adopting discrete states *i*. The evolution of the system is described as a succession of elementary transitions between its states. These elementary transitions are assumed to be infrequent events, in the sense that the waiting time of the system within each state *i*, before it jumps to another state, is long in comparison with the time required to visit all configurations internal to state *i* and establish a restricted equilibrium within that state. Under this condition of time scale separation, the probability per unit time of observing a transition from state *i* into a new state *j* at time *t* is expressed by the first-order kinetic law $k_{i\to j}P_i(t)$, where $k_{i\to j}$ is the rate constant for transitions from state *i* to state *j* and $P_i(t)$ is the probability that the system finds itself in state *i* at time *t*.[67-70] The rate of change of $P_i(t)$ with time emerges as an algebraic sum of efflux of probability from *i* to other states *j* and influx of probability from other states *j* to *i*, according to the Master Equation:

$$\frac{\mathrm{d}P_i}{\mathrm{d}t} = -\sum_j k_{i\to j}P_i + \sum_i k_{j\to i}P_j \qquad \text{Eq. (3.1)}$$

Forward and reverse transition rate constants satisfy the condition of microscopic reversibility:

$$P_i^{\mathrm{eq}}k_{i\to j} = P_j^{\mathrm{eq}}k_{j\to i} \qquad \text{Eq. (3.2)}$$

where P_i^{eq} stands for the probability of occupancy of state *i* when an equilibrium distribution among all states has been established. From Eqs. (3.1) and (3.2) it is obvious that the equilibrium distribution is a steady-state solution of the master equation.

Let the total number of states be n. We collect the state probabilities $P_i(t)$ to form an n-dimensional vector $\mathbf{P}(t)$. $\mathbf{P}(t)$ will be normalized over all states at all times:

$$\sum_{i=1}^{n} P_i(t) = 1 \quad \forall t \qquad \text{Eq. (3.3)}$$

The master equation, Eq. (3.1), can be written in compact form for all states as

$$\frac{\partial \mathbf{P}(t)}{\partial t} = \mathbf{K}\ \mathbf{P}(t) \qquad \text{Eq. (3.4)}$$

with initial condition $\mathbf{P}(0)$. The $n \times n$ rate constant matrix $\mathbf{K}$ is defined by $K_{ij} = k_{j \to i}$ for $j \neq i$ and $K_{ii} = -\sum_{j \neq i} k_{i \to j}$.

3.1.2 Solution of the Master Equation

A number of methods are available for solving the Master Equation for the time-dependent probabilities of occupancy of the states, subject to the initial condition of a prescribed distribution $\mathbf{P}(0)$ at t=0.

One popular numerical solution strategy is to employ Kinetic Monte Carlo (KMC) simulations. A starting ensemble of systems is sampled according to the initial distribution $\mathbf{P}(0)$. A number of stochastic trajectories is then generated for each system in the starting ensemble. Each stochastic trajectory consists of a long succession of elementary jumps between states. The time at which each jump will occur and the destination state of the jump are chosen by pseudo-random number generation, utilizing the known connectivity of the network of states, the known rate constants $k_{i \to j}$, and the properties of Poisson processes.[71-73] By analyzing the states at which all sampled trajectories find themselves at time t, the distribution $\mathbf{P}(t)$ can be obtained. Furthermore, time-dependent averages and correlation functions characterizing the dynamics of the system can be accumulated.

In many physical problems, such as ageing of glasses, protein folding, and diffusion in complex media, the eigenvalues of the rate constant matrix $\mathbf{K}$ cover several decades. This is usually a consequence of a very rugged energy landscape, exhibiting a wide distribution of barrier heights between local minima of the potential energy in the space of microscopic configurational degrees of freedom. For such problems KMC simulation becomes inefficient,

since the time step it takes at every point along a trajectory is commensurate with the inverse rate constant of the fastest elementary jump that can occur out of the current state. KMC may thus end up sampling, over and over again, fast transitions within small subsets of states that are connected with each other by passages of high $k_{i\to j}$ but to the rest of the state space only through passages of much lower $k_{i\to j}$. In other words, KMC trajectories may be trapped for long periods of time within small subsets of states. In such cases it is more advantageous to proceed with a direct analytical solution for the time-dependent state probabilities **P**(*t*).

Schemes for solving the master equation analytically express the solution as a sum of exponentially decaying functions of time, after diagonalizing the rate constant matrix.[74-76] To solve Eq. (3.4) for given **P**(0) it is advantageous[74-76] to transform the state probability vector **P**(*t*) into a reduced vector $\tilde{\mathbf{P}}(t)$ with elements

$$\tilde{P}_i(t) = P_i(t) / \sqrt{P_i^{\mathrm{eq}}} \qquad \text{Eq. (3.5)}$$

This satisfies the reduced master equation

$$\frac{\partial \tilde{\mathbf{P}}(t)}{\partial t} = \tilde{\mathbf{K}}\ \tilde{\mathbf{P}}(t) \qquad \text{Eq. (3.6)}$$

with $\tilde{K}_{ij} = K_{ij}\sqrt{P_j^{\mathrm{eq}}} / \sqrt{P_i^{\mathrm{eq}}}$. The matrix $\tilde{\mathbf{K}}$ is symmetric by virtue of detailed balance, Eq. (3.2). One can readily show that $\tilde{\mathbf{K}}$ has the same eigenvalues[77] as **K**. These eigenvalues are real, because $\tilde{\mathbf{K}}$ is symmetric. Of these eigenvalues, one (corresponding to the establishment of the equilibrium distribution among states) is zero, and the remaining eigenvalues are negative because $\tilde{\mathbf{K}}$ is a negative semidefinite matrix.

The reader is reminded that a real symmetric matrix **A** is negative semidefinite if $\mathbf{y}^{\mathrm{T}} \cdot \mathbf{A} \cdot \mathbf{y} \le 0$ for all non-zero vectors **y** with real entries $(\mathbf{y} \in \mathbb{R}^n)$. Superscript T on vectors and matrices is used here to indicate a matrix transpose. For the particular case of matrix $\tilde{\mathbf{K}}$ we obtain:

$$\mathbf{y}^{\mathrm{T}} \cdot \tilde{\mathbf{K}} \cdot \mathbf{y} = \sum_{i=1}^{n}\sum_{j=1}^{n} \tilde{K}_{ij} y_i y_j = \sum_{i=1}^{n} \tilde{K}_{ii} y_i^2 + \sum_{i=1}^{n}\sum_{\substack{j=1 \\ j\neq i}}^{n} \tilde{K}_{ij} y_i y_j = \sum_{i=1}^{n}\left(-\sum_{\substack{j=1 \\ j\neq i}}^{n} k_{i\to j} \right) y_i^2 + \sum_{i=1}^{n}\sum_{\substack{j=1 \\ j\neq i}}^{n} k_{j\to i} \left(\frac{P_j^{\mathrm{eq}}}{P_i^{\mathrm{eq}}} \right)^{1/2} y_i y_j$$

$$= -\sum_{i=1}^{n}\sum_{\substack{j=1 \\ j\neq i}}^{n} k_{i\to j} y_i^2 + \sum_{i=1}^{n}\sum_{\substack{j=1 \\ j\neq i}}^{n} k_{i\to j} \left(\frac{P_i^{\mathrm{eq}}}{P_j^{\mathrm{eq}}} \right)^{1/2} y_i y_j = -\frac{1}{2}\sum_{i=1}^{n}\sum_{\substack{j=1 \\ j\neq i}}^{n} k_{i\to j} P_i^{\mathrm{eq}} \left[\frac{y_j}{\left(P_j^{\mathrm{eq}}\right)^{1/2}} - \frac{y_i}{\left(P_i^{\mathrm{eq}}\right)^{1/2}} \right]^2$$

where the microscopic reversibility condition, Eq. (3.2), has been used in the algebraic manipulations. This proves that the symmetric real matrix $\tilde{\mathbf{K}}$ is negative semidefinite. This proof seems to have been given for the first time by Shuler.[78] Now, if λ is one of the real eigenvalues of $\tilde{\mathbf{K}}$ with corresponding real eigenvector $\mathbf{x}$, $\tilde{\mathbf{K}} \cdot \mathbf{x} = \lambda \mathbf{x}$ and therefore $\mathbf{x}^{\mathrm{T}} \cdot \tilde{\mathbf{K}} \cdot \mathbf{x} = \mathbf{x}^{\mathrm{T}} \lambda \mathbf{x}$, which means that $\mathbf{x}^{\mathrm{T}} \cdot \tilde{\mathbf{K}} \cdot \mathbf{x} = \lambda \|\mathbf{x}\|_2^2$ with $\|\mathbf{x}\|_2$ being the Euclidean norm of $\mathbf{x}$ and $\|\mathbf{x}\|_2^2 \geq 0$. Because $\tilde{\mathbf{K}}$ is negative semidefinite, the left-hand side $\mathbf{x}^{\mathrm{T}} \cdot \tilde{\mathbf{K}} \cdot \mathbf{x}$ is always negative or zero, hence $\lambda \leq 0$.

As a real, symmetric negative semidefinite matrix, therefore, $\tilde{\mathbf{K}}$ has zero or negative eigenvalues. We denote these eigenvalues by $\lambda_0 = 0 \geq \lambda_1 \geq \ldots \geq \lambda_{n-1}$. We symbolize by $\tilde{\mathbf{u}}_m = (\tilde{u}_{1,m}, \tilde{u}_{2,m}, \ldots, \tilde{u}_{i,m}, \ldots, \tilde{u}_{n,m})$ the eigenvector of $\tilde{\mathbf{K}}$ corresponding to eigenvalue λ_m, $0 \leq m \leq n-1$. Note that $\tilde{u}_{i,0} = \tilde{P}_i^{\mathrm{eq}} = \sqrt{P_i^{\mathrm{eq}}}$, corresponding to the equilibrium distribution among states. The Euclidean norm of $\tilde{\mathbf{u}}_0$ is unity by the normalization of P_i^{eq}. The solution of the master equation can be written (see also Appendix A) as:

$$\tilde{\mathbf{P}}(t) = \sum_{m=0}^{n-1} \left[\tilde{\mathbf{u}}_m \cdot \tilde{\mathbf{P}}(0) \right] \mathrm{e}^{\lambda_m t} \tilde{\mathbf{u}}_m = \tilde{\mathbf{P}}^{\mathrm{eq}} + \sum_{m=1}^{n-1} \left[\tilde{\mathbf{u}}_m \cdot \tilde{\mathbf{P}}(0) \right] \mathrm{e}^{\lambda_m t} \tilde{\mathbf{u}}_m \qquad \text{Eq. (3.7)}$$

where the normalization condition $\sum_{i=1}^{n} P_i(0) = 1$ has been used in separating out the equilibrium contribution ($\lambda_0 = 0$). The eigenvectors $\tilde{\mathbf{u}}_m$ form an orthonormal basis set:

$\tilde{\mathbf{u}}_m \cdot \tilde{\mathbf{u}}_l = \delta_{ml}$, $0 \leq m, l \leq n\text{-}1$.[79] Eq. (3.8)

with δ_{ml} being the Kronecker delta. They also satisfy[79] $\sum_{m=0}^{n-1} \tilde{u}_{i,m} \tilde{u}_{j,m} = \delta_{ij}$.

3.1.3. Spatially periodic sets of states

In many physical problems the set of states is characterized by spatial periodicity, i.e. can be obtained by periodic replication of a "unit cell" of states in one or more directions. These directions may correspond to spatial coordinate axes, or to generalized coordinates. Obvious examples are the set of sorption sites where a penetrant molecule can reside within a crystalline

porous or nonporous material in the context of diffusion in three directions, the set of surface sites where an adsorbate can reside on a crystal surface in the context of surface diffusion, or the set of rotational states adopted by the torsion angles of a flexible organic molecule.

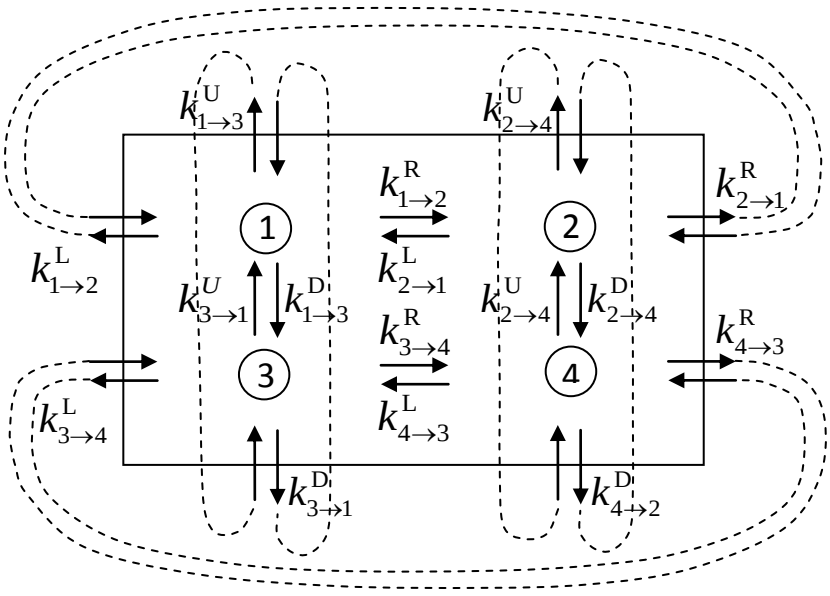

$$\tilde{\mathbf{K}}_1 = \begin{bmatrix} -(k^{R}_{1\to2}+k^{L}_{1\to2}+k^{U}_{1\to3}+k^{D}_{1\to3}) & \left(k^{R}_{2\to1}+k^{L}_{2\to1}\right)\left(P^{eq}_2/P^{eq}_1\right)^{1/2} & \left(k^{U}_{3\to1}+k^{D}_{3\to1}\right)\left(P^{eq}_3/P^{eq}_1\right)^{1/2} & 0 \\ \left(k^{R}_{1\to2}+k^{L}_{1\to2}\right)\left(P^{eq}_1/P^{eq}_2\right)^{1/2} & -(k^{R}_{2\to1}+k^{L}_{2\to1}+k^{U}_{2\to4}+k^{D}_{2\to4}) & 0 & \left(k^{U}_{4\to2}+k^{D}_{4\to2}\right)\left(P^{eq}_4/P^{eq}_2\right)^{1/2} \\ \left(k^{U}_{1\to3}+k^{D}_{1\to3}\right)\left(P^{eq}_1/P^{eq}_3\right)^{1/2} & 0 & -(k^{U}_{3\to1}+k^{D}_{3\to1}+k^{R}_{3\to4}+k^{L}_{3\to4}) & \left(k^{R}_{4\to3}+k^{L}_{4\to3}\right)\left(P^{eq}_4/P^{eq}_3\right)^{1/2} \\ 0 & \left(k^{U}_{2\to4}+k^{D}_{2\to4}\right)\left(P^{eq}_2/P^{eq}_4\right)^{1/2} & \left(k^{R}_{3\to4}+k^{L}_{3\to4}\right)\left(P^{eq}_3/P^{eq}_4\right)^{1/2} & -(k^{U}_{4\to2}+k^{D}_{4\to2}+k^{R}_{4\to3}+k^{L}_{4\to3}) \end{bmatrix}$$

Figure 3.1 Example of a system characterized by periodic boundary conditions with n=4 states in the unit cell. Broken curves indicate equalities between rate constants for entering and exiting the unit cell, arising from the periodic boundary conditions. 16 distinct rate constants are defined. The symmetrized rate constant matrix for the system, $\tilde{\mathbf{K}}_1$, is also given.

An example of periodicity in two directions is shown schematically in Figure 3.1. Here, four states are considered within the unit cell. The right and left sides of the unit cell are connected via periodic boundary conditions, and so are the top and bottom sides, as indicated by the broken lines. States are assumed to be connected with a coordination number of four.

Sixteen distinct rate constants are indicated, pairs of forward and reverse rate constants satisfying the microscopic reversibility condition, Eq. (3.2). The superscripts "R" and "L" are used to indicate transitions to the right and to the left, respectively, along the horizontal axis. The superscripts "U" and "D" are used to indicate transitions upwards and downwards, respectively, along the vertical axis. In the following, we will use the symbol n to indicate the total number of states in the unit cell (in our example, n=4). The unit cell is characterized by a $n \times n$ rate constant matrix, which we shall call $\mathbf{K}_1$, and a corresponding symmetrized matrix $\tilde{\mathbf{K}}_1$, obtained from $\mathbf{K}_1$ as outlined above.

Let us now consider the periodic set of states as resulting from periodic replication of two adjacent unit cells, as shown in Figure 3.2. Now there are $2n$ states (8 in our example, the primed states being images of the unprimed states) in the doubled unit cell, but the number of distinct rate constants remains equal to that in the original unit cell (16 in our example). Clearly, the description of Figure 3.2 allows accessing fluctuations in the time-dependent occupancy probabilities of states with greater characteristic length than the description of Figure 3.1. One can write a $2n \times 2n$ rate constant matrix $\mathbf{K}_2$ and a corresponding symmetrized matrix $\tilde{\mathbf{K}}_2$ for the description of Figure 3.2 in terms of the doubled unit cell. $\tilde{\mathbf{K}}_2$ is also given in the figure for our example. One readily sees that $\tilde{\mathbf{K}}_2$ is related to $\tilde{\mathbf{K}}_1$ of the original unit cell (compare Figure 3.1) as

$$\tilde{\mathbf{K}}_2 = \begin{bmatrix} \tilde{\mathbf{K}}_1 - \tilde{\mathbf{K}}_{\mathrm{RL1}} & \tilde{\mathbf{K}}_{\mathrm{RL1}} \\ \tilde{\mathbf{K}}_{\mathrm{RL1}} & \tilde{\mathbf{K}}_1 - \tilde{\mathbf{K}}_{\mathrm{RL1}} \end{bmatrix} \qquad \text{Eq. (3.9)}$$

The $n \times n$ matrix $\tilde{\mathbf{K}}_{\mathrm{RL1}}$ is defined as

$$\tilde{\mathbf{K}}_{\mathrm{RL1}} = \tilde{\mathbf{K}}_{\mathrm{R1}} + \tilde{\mathbf{K}}_{\mathrm{L1}} \qquad \text{Eq. (3.10)}$$

The $n \times n$ matrix $\tilde{\mathbf{K}}_{\mathrm{R1}}$ (respectively, $\tilde{\mathbf{K}}_{\mathrm{L1}}$) collects those entries in $\tilde{\mathbf{K}}_1$ which correspond to transitions taking place across the right (respectively, left) boundary of the original unit cell (Figure 3.1), all other entries being zero. By virtue of the microscopic reversibility condition, Eq. (3.2), applied to every connection traversing the right and left periodic boundaries, one obtains

$$\tilde{\mathbf{K}}_{\mathrm{L1}} = \tilde{\mathbf{K}}_{\mathrm{R1}}^{\mathrm{T}} \qquad \text{Eq. (3.11)}$$

As a consequence, matrix $\tilde{\mathbf{K}}_{\mathrm{RL1}}$ is symmetric. Given that $\tilde{\mathbf{K}}_1$ and $\tilde{\mathbf{K}}_{\mathrm{RL1}}$ are symmetric, the $2n \times 2n$ matrix $\tilde{\mathbf{K}}_2$, as defined in Eq. (3.9), is also symmetric. Figures 3.1 and 3.2 refer to a specific example. It is easy to convince oneself that, given $\tilde{\mathbf{K}}_1$ and the connectivity of states in the original unit cell, $\tilde{\mathbf{K}}_{\mathrm{R1}}$, $\tilde{\mathbf{K}}_{\mathrm{L1}}$ and, consequently, $\tilde{\mathbf{K}}_{\mathrm{RL1}}$ can be written down by inspection.

We can extend this idea, stringing together 4, 8, …, 2^{ν} adjacent copies of the original unit cell along the horizontal direction, in order to form larger and larger unit cells.

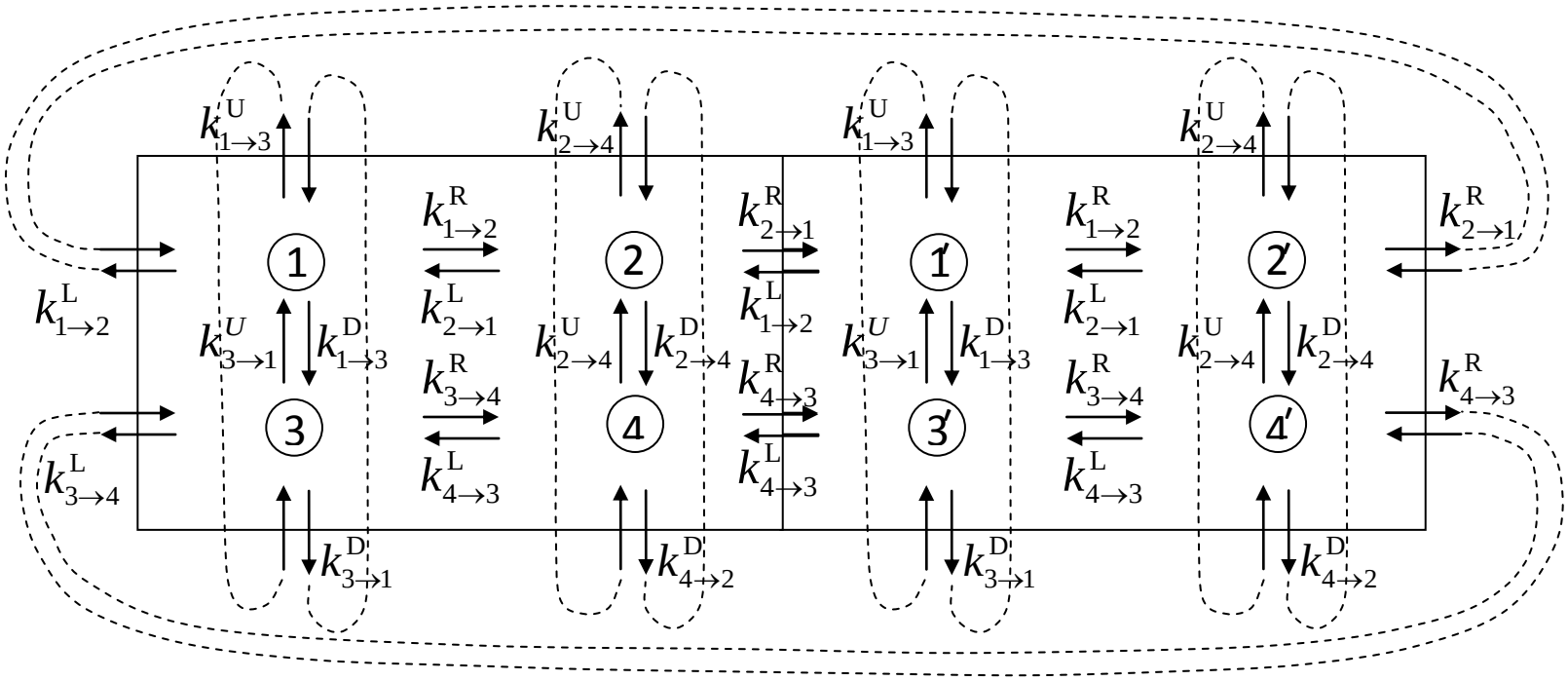

$$\tilde{\mathbf{K}}_2 = \begin{bmatrix}
-\left(k^{\mathrm{R}}_{1\to2}+k^{\mathrm{L}}_{1\to2}+k^{\mathrm{U}}_{1\to3}+k^{\mathrm{D}}_{1\to3}\right) & k^{\mathrm{L}}_{2\to1}\left(P_2^{\mathrm{eq}}/P_1^{\mathrm{eq}}\right)^{1/2} & \left(k^{\mathrm{U}}_{3\to1}+k^{\mathrm{D}}_{3\to1}\right)\left(P_3^{\mathrm{eq}}/P_1^{\mathrm{eq}}\right)^{1/2} & 0 & 0 & k^{\mathrm{R}}_{2\to1}\left(P_2^{\mathrm{eq}}/P_1^{\mathrm{eq}}\right)^{1/2} & 0 & 0 \\
k^{\mathrm{R}}_{1\to2}\left(P_1^{\mathrm{eq}}/P_2^{\mathrm{eq}}\right)^{1/2} & -\left(k^{\mathrm{R}}_{2\to1}+k^{\mathrm{L}}_{2\to1}+k^{\mathrm{U}}_{2\to4}+k^{\mathrm{D}}_{2\to4}\right) & 0 & \left(k^{\mathrm{U}}_{4\to2}+k^{\mathrm{D}}_{4\to2}\right)\left(P_4^{\mathrm{eq}}/P_2^{\mathrm{eq}}\right)^{1/2} & k^{\mathrm{L}}_{2\to1}\left(P_1^{\mathrm{eq}}/P_2^{\mathrm{eq}}\right)^{1/2} & 0 & 0 & 0 \\
\left(k^{\mathrm{U}}_{1\to3}+k^{\mathrm{D}}_{1\to3}\right)\left(P_1^{\mathrm{eq}}/P_3^{\mathrm{eq}}\right)^{1/2} & 0 & -\left(k^{\mathrm{U}}_{3\to1}+k^{\mathrm{D}}_{3\to4}+k^{\mathrm{R}}_{3\to4}+k^{\mathrm{L}}_{3\to4}\right) & k^{\mathrm{L}}_{4\to3}\left(P_4^{\mathrm{eq}}/P_3^{\mathrm{eq}}\right)^{1/2} & 0 & 0 & 0 & k^{\mathrm{R}}_{4\to3}\left(P_4^{\mathrm{eq}}/P_3^{\mathrm{eq}}\right)^{1/2} \\
0 & \left(k^{\mathrm{U}}_{2\to4}+k^{\mathrm{D}}_{2\to4}\right)\left(P_2^{\mathrm{eq}}/P_4^{\mathrm{eq}}\right)^{1/2} & k^{\mathrm{R}}_{3\to4}\left(P_3^{\mathrm{eq}}/P_4^{\mathrm{eq}}\right)^{1/2} & -\left(k^{\mathrm{U}}_{4\to2}+k^{\mathrm{D}}_{4\to2}+k^{\mathrm{R}}_{4\to3}+k^{\mathrm{L}}_{4\to3}\right) & 0 & 0 & k^{\mathrm{L}}_{3\to4}\left(P_3^{\mathrm{eq}}/P_4^{\mathrm{eq}}\right)^{1/2} & 0 \\
0 & k^{\mathrm{R}}_{2\to1}\left(P_2^{\mathrm{eq}}/P_1^{\mathrm{eq}}\right)^{1/2} & 0 & 0 & -\left(k^{\mathrm{R}}_{1\to2}+k^{\mathrm{L}}_{1\to2}+k^{\mathrm{U}}_{1\to3}+k^{\mathrm{D}}_{1\to3}\right) & k^{\mathrm{L}}_{2\to1}\left(P_2^{\mathrm{eq}}/P_1^{\mathrm{eq}}\right)^{1/2} & \left(k^{\mathrm{U}}_{3\to1}+k^{\mathrm{D}}_{3\to1}\right)\left(P_3^{\mathrm{eq}}/P_1^{\mathrm{eq}}\right)^{1/2} & 0 \\
k^{\mathrm{L}}_{1\to2}\left(P_1^{\mathrm{eq}}/P_2^{\mathrm{eq}}\right)^{1/2} & 0 & 0 & 0 & k^{\mathrm{R}}_{1\to2}\left(P_1^{\mathrm{eq}}/P_2^{\mathrm{eq}}\right)^{1/2} & -\left(k^{\mathrm{R}}_{2\to1}+k^{\mathrm{L}}_{2\to1}+k^{\mathrm{U}}_{2\to4}+k^{\mathrm{D}}_{2\to4}\right) & 0 & \left(k^{\mathrm{U}}_{4\to2}+k^{\mathrm{D}}_{4\to2}\right)\left(P_4^{\mathrm{eq}}/P_2^{\mathrm{eq}}\right)^{1/2} \\
0 & 0 & 0 & k^{\mathrm{R}}_{4\to3}\left(P_4^{\mathrm{eq}}/P_3^{\mathrm{eq}}\right)^{1/2} & \left(k^{\mathrm{U}}_{1\to3}+k^{\mathrm{D}}_{1\to3}\right)\left(P_1^{\mathrm{eq}}/P_3^{\mathrm{eq}}\right)^{1/2} & 0 & -\left(k^{\mathrm{U}}_{3\to1}+k^{\mathrm{D}}_{3\to1}+k^{\mathrm{R}}_{3\to4}+k^{\mathrm{L}}_{3\to4}\right) & k^{\mathrm{L}}_{4\to3}\left(P_4^{\mathrm{eq}}/P_3^{\mathrm{eq}}\right)^{1/2} \\
0 & 0 & k^{\mathrm{L}}_{3\to4}\left(P_3^{\mathrm{eq}}/P_4^{\mathrm{eq}}\right)^{1/2} & 0 & 0 & \left(k^{\mathrm{U}}_{2\to4}+k^{\mathrm{D}}_{2\to4}\right)\left(P_2^{\mathrm{eq}}/P_4^{\mathrm{eq}}\right)^{1/2} & k^{\mathrm{R}}_{3\to4}\left(P_3^{\mathrm{eq}}/P_4^{\mathrm{eq}}\right)^{1/2} & -\left(k^{\mathrm{U}}_{4\to2}+k^{\mathrm{D}}_{4\to2}+k^{\mathrm{R}}_{4\to3}+k^{\mathrm{L}}_{4\to3}\right)
\end{bmatrix}$$

$$\tilde{\mathbf{K}}_2 = \begin{bmatrix} \tilde{\mathbf{K}}_1 - \tilde{\mathbf{K}}_{\mathrm{RL1}} & \tilde{\mathbf{K}}_{\mathrm{RL1}} \\ \tilde{\mathbf{K}}_{\mathrm{RL1}} & \tilde{\mathbf{K}}_1 - \tilde{\mathbf{K}}_{\mathrm{RL1}} \end{bmatrix}$$

$$\tilde{\mathbf{K}}_{\mathrm{RL1}} = \tilde{\mathbf{K}}_{\mathrm{R1}} + \tilde{\mathbf{K}}_{\mathrm{L1}}$$

$$\tilde{\mathbf{K}}_{\mathrm{R1}} = \begin{bmatrix} 0 & k^{\mathrm{R}}_{2\to1}\left(P_2^{\mathrm{eq}}/P_1^{\mathrm{eq}}\right)^{1/2} & 0 & 0 \\ 0 & 0 & 0 & 0 \\ 0 & 0 & 0 & k^{\mathrm{R}}_{4\to3}\left(P_4^{\mathrm{eq}}/P_3^{\mathrm{eq}}\right)^{1/2} \\ 0 & 0 & 0 & 0 \end{bmatrix}$$

$$\tilde{\mathbf{K}}_{\mathrm{L1}} = \begin{bmatrix} 0 & 0 & 0 & 0 \\ k^{\mathrm{L}}_{1\to2}\left(P_1^{\mathrm{eq}}/P_2^{\mathrm{eq}}\right)^{1/2} & 0 & 0 & 0 \\ 0 & 0 & 0 & 0 \\ 0 & 0 & k^{\mathrm{L}}_{3\to4}\left(P_3^{\mathrm{eq}}/P_4^{\mathrm{eq}}\right)^{1/2} & 0 \end{bmatrix}$$

Figure 3.2 Same system as in Figure 1, considered as resulting from periodic replication of two adjacent unit cells. The symmetrized rate constant matrix $\tilde{\mathbf{K}}_2$ and its relation to rate constant matrices $\tilde{\mathbf{K}}_1$, $\tilde{\mathbf{K}}_{\mathrm{R1}}$, $\tilde{\mathbf{K}}_{\mathrm{L1}}$ are explained.

Periodic boundary conditions hold between the two sides of the string, as shown schematically in Figure 3.3. Formulating the master equation in terms of these larger unit cells is useful, as it allows studying the dynamics over larger and larger length scales. The symmetrized $(2^{\nu}n)\times(2^{\nu}n)$ rate constant matrix corresponding to a supercell consisting of 2^{ν} original cells and containing $2^{\nu}n$ states is

$$\tilde{\mathbf{K}}_{2^{\nu}} = \begin{bmatrix} \tilde{\mathbf{K}}_1 - \tilde{\mathbf{K}}_{RL1} & \tilde{\mathbf{K}}_{L1} & \mathbf{0} & . & . & \mathbf{0} & \mathbf{0} & \tilde{\mathbf{K}}_{R1} \\ \tilde{\mathbf{K}}_{R1} & \tilde{\mathbf{K}}_1 - \tilde{\mathbf{K}}_{RL1} & \tilde{\mathbf{K}}_{L1} & . & . & . & \mathbf{0} & \mathbf{0} \\ \mathbf{0} & \tilde{\mathbf{K}}_{R1} & \tilde{\mathbf{K}}_1 - \tilde{\mathbf{K}}_{RL1} & \tilde{\mathbf{K}}_{L1} & . & . & . & \mathbf{0} \\ \mathbf{0} & . & \tilde{\mathbf{K}}_{R1} & \tilde{\mathbf{K}}_1 - \tilde{\mathbf{K}}_{RL1} & \tilde{\mathbf{K}}_{L1} & . & . & . \\ . & . & . & . & . & . & . & . \\ . & . & . & \tilde{\mathbf{K}}_{R1} & \tilde{\mathbf{K}}_1 - \tilde{\mathbf{K}}_{RL1} & \tilde{\mathbf{K}}_{L1} & . & . \\ \mathbf{0} & . & . & . & \tilde{\mathbf{K}}_{R1} & \tilde{\mathbf{K}}_1 - \tilde{\mathbf{K}}_{RL1} & \tilde{\mathbf{K}}_{L1} & \mathbf{0} \\ \mathbf{0} & \mathbf{0} & . & . & . & \tilde{\mathbf{K}}_{R1} & \tilde{\mathbf{K}}_1 - \tilde{\mathbf{K}}_{RL1} & \tilde{\mathbf{K}}_{L1} \\ \tilde{\mathbf{K}}_{L1} & \mathbf{0} & \mathbf{0} & . & . & \mathbf{0} & \tilde{\mathbf{K}}_{R1} & \tilde{\mathbf{K}}_1 - \tilde{\mathbf{K}}_{RL1} \end{bmatrix} \quad \text{Eq. (3.12)}$$

expressed in terms of the $n \times n$ matrices $\tilde{\mathbf{K}}_1$, $\tilde{\mathbf{K}}_{R1}$, $\tilde{\mathbf{K}}_{L1}$, $\tilde{\mathbf{K}}_{RL1}$ introduced above and the $n \times n$ matrix $\mathbf{0}$ with all elements equal to zero. By virtue of the symmetry of $\tilde{\mathbf{K}}_1$ and Eq. (3.11) one can readily prove that $\tilde{\mathbf{K}}_{2^{\nu}}$ is symmetric, and therefore has real eigenvalues.

Given an initial probability distribution $\mathbf{P}(0)$ among the states contained in the supercell of $2^{\nu}n$ states, one can determine the time-dependent probabilities of the states $\mathbf{P}(t)$ as the system evolves, subject to periodic boundary conditions at its boundaries, via Eq. (3.7) with n replaced by $2^{\nu}n$ and λ_m, $\tilde{\mathbf{u}}_m$ standing for the eigenvalues and corresponding eigenvectors of the $(2^{\nu}n)\times(2^{\nu}n)$ symmetrized rate constant matrix $\tilde{\mathbf{K}}_{2^{\nu}}$. Diagonalizing a matrix of such high dimensionality in order to determine λ_m, $\tilde{\mathbf{u}}_m$, however, requires considerable computational effort. It is highly desirable to express the eigenvalues and eigenvectors of $\tilde{\mathbf{K}}_{2^{\nu}}$ in terms of eigenvalues and eigenvectors of matrices of smaller dimensionality, which can be obtained with much less effort. If possible, we would like to reduce the calculation of all eigenvalues and eigenvectors of $\tilde{\mathbf{K}}_{2^{\nu}}$ to a diagonalization of mere $n\times n$ matrices, such as $\tilde{\mathbf{K}}_1$, as the latter presents no computational difficulty.

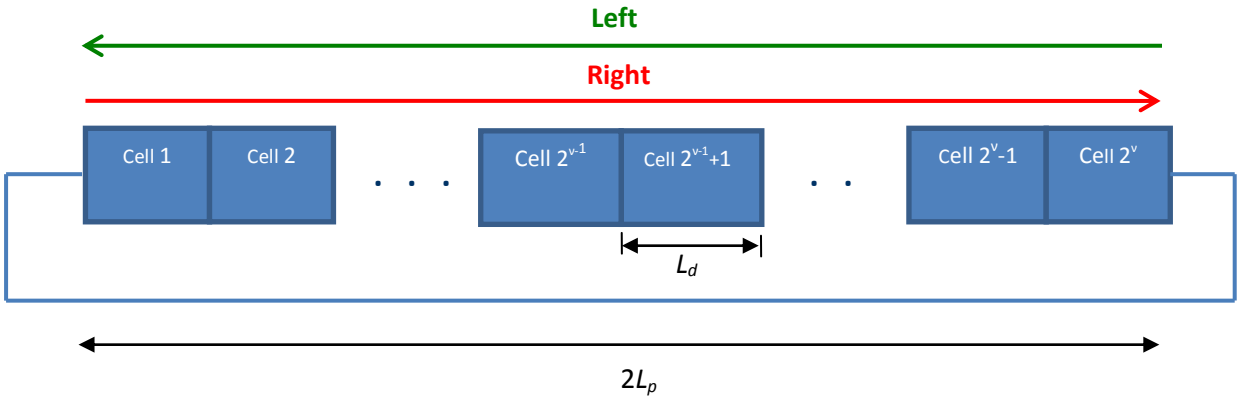

Figure 3.3 Periodic system of 2^{ν} unit cells arranged in the l direction (l = x, y, or z), considered in the theoretical derivations and applications. Periodic boundary conditions apply in directions normal to the l direction. Boxes represent unit cells and arrows indicate the "right" and "left" senses invoked in the theoretical development. The blue line shows that the right edge of the last unit cell communicates with the left edge of the first unit cell, by virtue of periodic boundary conditions. The lengths of a unit cell, L_d, and of the entire system, $2L_p$, in the l direction, are also shown.

Reducing the diagonalization of $\tilde{\mathbf{K}}_{2^\nu}$ to a diagonalization of matrices of smaller dimension is the major focus of this paper. We will show that it is possible to achieve this reduction in a recursive manner, by utilizing the structure of $\tilde{\mathbf{K}}_{2^\nu}$ [Eq. (3.12)], which reflects the spatial periodicity of the set of states in the l-direction. We develop a methodology for obtaining λ_m, $\tilde{\mathbf{u}}_m$ though diagonalization of matrices of smaller dimension than $\tilde{\mathbf{K}}_{2^\nu}$. Furthermore, we apply this methodology to obtain $\mathbf{P}(t)$ in a specific problem, that of low-temperature diffusion of xenon in the zeolite silicalite, using rate constants computed from atomistic analysis of the potential energy hypersurface within a unit cell of the zeolite. Starting from an initial distribution $\mathbf{P}(0)$ localized in the middle of the periodic array of states, we show that $\mathbf{P}(t)$, summed over unit cells, exhibits a diffusive behavior in space and time. We use this diffusive response to extract the self-diffusivity and compare with corresponding estimates obtained through (a) diagonalization of the entire $\tilde{\mathbf{K}}_{2^\nu}$ and subsequent application of Eq. (3.7); (b) numerical solution of the master equation, Eq. (3.4), with $\mathbf{K}_{2^\nu}$ in place of $\mathbf{K}$, for the entire supercell; (c) Kinetic Monte Carlo simulation in an infinite array of states. Furthermore, we

compare the computational requirements of these approaches and demonstrate the superiority of the new recursive reduction approach.

3.2 Mathematical and Algorithmic development

3.2.1. Recursive relations satisfied by $\tilde{\mathbf{K}}_{2^\nu}$, its eigenvalues and eigenvectors

From Eq. (3.12) one sees that $\tilde{\mathbf{K}}_{2^\nu}$ can be written as

$$\tilde{\mathbf{K}}_{2^\nu} = \begin{bmatrix} \tilde{\mathbf{K}}_{2^{\nu-1}} - \tilde{\mathbf{K}}_{\mathrm{RL}2^{\nu-1}} & \tilde{\mathbf{K}}_{\mathrm{RL}2^{\nu-1}} \\ \tilde{\mathbf{K}}_{\mathrm{RL}2^{\nu-1}} & \tilde{\mathbf{K}}_{2^{\nu-1}} - \tilde{\mathbf{K}}_{\mathrm{RL}2^{\nu-1}} \end{bmatrix} \qquad \text{Eq. (3.13)}$$

where $\tilde{\mathbf{K}}_{2^{\nu-1}}$ is the $(2^{\nu-1}n)\times(2^{\nu-1}n)$ symmetrized rate constant matrix characterizing a string of $2^{\nu-1}$ unit cells with periodic boundary conditions between its right and left extremities, of the same structure as $\tilde{\mathbf{K}}_{2^\nu}$, and $\tilde{\mathbf{K}}_{\mathrm{RL}2^{\nu-1}}$ is the sum of two $(2^{\nu-1}n)\times(2^{\nu-1}n)$ matrices $\tilde{\mathbf{K}}_{\mathrm{R}2^{\nu-1}}, \tilde{\mathbf{K}}_{\mathrm{L}2^{\nu-1}}$, defined by:

$$\tilde{\mathbf{K}}_{\mathrm{RL}2^{\nu-1}} = \tilde{\mathbf{K}}_{\mathrm{R}2^{\nu-1}} + \tilde{\mathbf{K}}_{\mathrm{L}2^{\nu-1}} \qquad \text{Eq. (3.14)}$$

$$\tilde{\mathbf{K}}_{\mathrm{R}2^{\nu-1}} = \begin{bmatrix} \mathbf{0} & . & \mathbf{0} & \tilde{\mathbf{K}}_{\mathrm{R1}} \\ . & . & . & \mathbf{0} \\ \mathbf{0} & . & . & . \\ \mathbf{0} & . & \mathbf{0} & \mathbf{0} \end{bmatrix}, \quad \tilde{\mathbf{K}}_{\mathrm{L}2^{\nu-1}} = \begin{bmatrix} \mathbf{0} & . & \mathbf{0} & \mathbf{0} \\ . & . & . & \mathbf{0} \\ \mathbf{0} & . & . & . \\ \tilde{\mathbf{K}}_{\mathrm{L1}} & \mathbf{0} & . & \mathbf{0} \end{bmatrix} \qquad \text{Eq. (3.15)}$$

Note that all elements of $\tilde{\mathbf{K}}_{\mathrm{R}2^{\nu-1}}$ are zero, except the $n \times n$ elements at its top right, which comprise the matrix $\tilde{\mathbf{K}}_{\mathrm{R1}}$, introduced above. Likewise, all elements of $\tilde{\mathbf{K}}_{\mathrm{L}2^{\nu-1}}$ are zero, except the $n \times n$ elements at its bottom left, which comprise the matrix $\tilde{\mathbf{K}}_{\mathrm{L1}}$, introduced above. Because $\tilde{\mathbf{K}}_{\mathrm{R1}}$ and $\tilde{\mathbf{K}}_{\mathrm{L1}}$ are transpose of each other, by Eq. (3.11), matrices $\tilde{\mathbf{K}}_{\mathrm{R}2^{\nu-1}}$ and $\tilde{\mathbf{K}}_{\mathrm{L}2^{\nu-1}}$ are also transpose, hence $\tilde{\mathbf{K}}_{\mathrm{RL}2^{\nu-1}}$ is symmetric, as is required for $\tilde{\mathbf{K}}_{2^\nu}$ to be symmetric.

Let $\lambda_{\tilde{\mathbf{K}}_{2^\nu}}$ be an eigenvalue of $\tilde{\mathbf{K}}_{2^\nu}$, with corresponding eigenvector $\mathbf{x}_{\tilde{\mathbf{K}}_{2^\nu}} = \begin{bmatrix} \mathbf{x}_{2^{\nu-1},\mathrm{A}} \\ \mathbf{x}_{2^{\nu-1},\mathrm{B}} \end{bmatrix}$, with $\mathbf{x}_{2^{\nu-1},\mathrm{A}}$, $\mathbf{x}_{2^{\nu-1},\mathrm{B}}$ being $2^{\nu-1}n$-long vectors. Since $\tilde{\mathbf{K}}_{2^\nu}$ is symmetric, its eigenvalue $\lambda_{\tilde{\mathbf{K}}_{2^\nu}}$ will be real, as pointed out for the matrix $\tilde{\mathbf{K}}$ in the general form of the master equation, Eq. (3.16). The norm of eigenvector $\mathbf{x}_{\tilde{\mathbf{K}}_{2^\nu}}$ is related to the norm of sub-vectors $\mathbf{x}_{2^{\nu-1},\mathrm{A}}$ and $\mathbf{x}_{2^{\nu-1},\mathrm{B}}$ via the equation

$$\left\|\mathbf{x}_{2^\nu}\right\|_2^2 = \left\|\mathbf{x}_{2^{\nu-1},\mathrm{A}}\right\|_2^2 + \left\|\mathbf{x}_{2^{\nu-1},\mathrm{B}}\right\|_2^2 \qquad \text{Eq. (3.16)}$$

If we require that $\mathbf{x}_{\tilde{\mathbf{K}}_{2^\nu}}$ be normalized, then both sides of Eq. (3.16) should equal 1. Here we will not require that eigenvectors be necessarily normalized, i.e. we will assume that eigenvectors are defined up to a multiplicative constant; as discussed in Appendix A normalization corresponds to a particular choice of that constant. $\tilde{\mathbf{K}}_{2^\nu}$, $\lambda_{\tilde{\mathbf{K}}_{2^\nu}}$, $\mathbf{x}_{2^{\nu-1},\mathrm{A}}$ and $\mathbf{x}_{2^{\nu-1},\mathrm{B}}$ satisfy the eigenvalue equation:

$$\tilde{\mathbf{K}}_{2^\nu}\begin{bmatrix} \mathbf{x}_{2^{\nu-1},\mathrm{A}} \\ \mathbf{x}_{2^{\nu-1},\mathrm{B}} \end{bmatrix} = \lambda_{\tilde{\mathbf{K}}_{2^\nu}}\begin{bmatrix} \mathbf{x}_{2^{\nu-1},\mathrm{A}} \\ \mathbf{x}_{2^{\nu-1},\mathrm{B}} \end{bmatrix} \qquad \text{Eq. (3.17)}$$

Substituting $\tilde{\mathbf{K}}_{2^\nu}$ from Eq. (3.13), we find that Eq. (3.17) is equivalent to the following set of equations:

$$\begin{aligned} \left(\tilde{\mathbf{K}}_{2^{\nu-1}} - \tilde{\mathbf{K}}_{\mathrm{RL}2^{\nu-1}}\right)\mathbf{x}_{2^{\nu-1},\mathrm{A}} + \tilde{\mathbf{K}}_{\mathrm{RL}2^{\nu-1}}\mathbf{x}_{2^{\nu-1},\mathrm{B}} &= \lambda_{\tilde{\mathbf{K}}_{2^\nu}}\mathbf{x}_{2^{\nu-1},\mathrm{A}} \\ \tilde{\mathbf{K}}_{\mathrm{RL}2^{\nu-1}}\mathbf{x}_{2^{\nu-1},\mathrm{A}} + \left(\tilde{\mathbf{K}}_{2^{\nu-1}} - \tilde{\mathbf{K}}_{\mathrm{RL}2^{\nu-1}}\right)\mathbf{x}_{2^{\nu-1},\mathrm{B}} &= \lambda_{\tilde{\mathbf{K}}_{2^\nu}}\mathbf{x}_{2^{\nu-1},\mathrm{B}} \end{aligned} \qquad \text{Eq. (3.18)}$$

Adding and subtracting Eqs. (3.18) from each other, one obtains the equivalent set of equations:

$$\begin{aligned} \tilde{\mathbf{K}}_{2^{\nu-1}}\left(\mathbf{x}_{2^{\nu-1},\mathrm{A}} + \mathbf{x}_{2^{\nu-1},\mathrm{B}}\right) &= \lambda_{\tilde{\mathbf{K}}_{2^\nu}}\left(\mathbf{x}_{2^{\nu-1},\mathrm{A}} + \mathbf{x}_{2^{\nu-1},\mathrm{B}}\right) \\ \left(\tilde{\mathbf{K}}_{2^{\nu-1}} - 2\tilde{\mathbf{K}}_{\mathrm{RL}2^{\nu-1}}\right)\left(\mathbf{x}_{2^{\nu-1},\mathrm{A}} - \mathbf{x}_{2^{\nu-1},\mathrm{B}}\right) &= \lambda_{\tilde{\mathbf{K}}_{2^\nu}}\left(\mathbf{x}_{2^{\nu-1},\mathrm{A}} - \mathbf{x}_{2^{\nu-1},\mathrm{B}}\right) \end{aligned} \qquad \text{Eq. (3.19)}$$

Eq. (3.19) is equivalent to the following requirement:

$$\begin{cases} \lambda_{\tilde{\mathbf{K}}_{2^\nu}} \text{ is an eigenvalue of } \tilde{\mathbf{K}}_{2^{\nu-1}} \text{ with eigenvector } \mathbf{x}_{2^{\nu-1},\mathrm{A}} + \mathbf{x}_{2^{\nu-1},\mathrm{B}} \text{ and } \mathbf{x}_{2^{\nu-1},\mathrm{A}} - \mathbf{x}_{2^{\nu-1},\mathrm{B}} = 0 & \text{, or} \\ \lambda_{\tilde{\mathbf{K}}_{2^\nu}} \text{ is an eigenvalue of } \tilde{\mathbf{K}}_{2^{\nu-1}} - 2\tilde{\mathbf{K}}_{\mathrm{RL}2^{\nu-1}} \text{ with eigenvector } \mathbf{x}_{2^{\nu-1},\mathrm{A}} - \mathbf{x}_{2^{\nu-1},\mathrm{B}} \text{ and } \mathbf{x}_{2^{\nu-1},\mathrm{A}} + \mathbf{x}_{2^{\nu-1},\mathrm{B}} = 0 & \text{, or} \\ \lambda_{\tilde{\mathbf{K}}_{2^\nu}} \text{ is an eigenvalue of both } \tilde{\mathbf{K}}_{2^{\nu-1}} \text{ (eigvec. } \mathbf{x}_{2^{\nu-1},\mathrm{A}} + \mathbf{x}_{2^{\nu-1},\mathrm{B}}) \text{ and of } \tilde{\mathbf{K}}_{2^{\nu-1}} - 2\tilde{\mathbf{K}}_{\mathrm{RL}2^{\nu-1}} \text{ (eigvec. } \mathbf{x}_{2^{\nu-1},\mathrm{A}} - \mathbf{x}_{2^{\nu-1},\mathrm{B}}) & \end{cases}$$

Eq. (3.20)

We examine each of the cases in Eq. (3.20) separately.

Case A:

$\lambda_{\tilde{\mathbf{K}}_{2^\nu}}$ is an eigenvalue of $\tilde{\mathbf{K}}_{2^{\nu-1}}$ with eigenvector $\mathbf{x}_{2^{\nu-1},\mathrm{A}} + \mathbf{x}_{2^{\nu-1},\mathrm{B}}$ and $\mathbf{x}_{2^{\nu-1},\mathrm{A}} - \mathbf{x}_{2^{\nu-1},\mathrm{B}} = 0$.

In this case we obtain $\mathbf{x}_{2^{\nu-1},\mathrm{B}} = \mathbf{x}_{2^{\nu-1},\mathrm{A}}$ and, from Eq. (3.19), the eigenvector $\mathbf{x}_{\tilde{\mathbf{K}}_{2^{\nu-1}}}$ of $\tilde{\mathbf{K}}_{2^{\nu-1}}$ corresponding to eigenvalue $\lambda_{\tilde{\mathbf{K}}_{2^\nu}}$ is $2\,\mathbf{x}_{2^{\nu-1},\mathrm{A}}$ or, more generally, $1/\zeta\,\mathbf{x}_{2^{\nu-1},\mathrm{A}}$ where $1/\zeta$ is a multiplying factor. The number $\lambda_{\tilde{\mathbf{K}}_{2^\nu}}$, originally defined as an eigenvalue of $\tilde{\mathbf{K}}_{2^\nu}$, is also an eigenvalue of $\tilde{\mathbf{K}}_{2^{\nu-1}}$, and the eigenvectors of the two matrices are related via

$$\mathbf{x}_{\tilde{\mathbf{K}}_{2^\nu}} = \zeta \begin{bmatrix} \mathbf{x}_{\tilde{\mathbf{K}}_{2^{\nu-1}}} \\ \mathbf{x}_{\tilde{\mathbf{K}}_{2^{\nu-1}}} \end{bmatrix} \qquad \text{Eq. (3.21)}$$

If $\lambda_{\tilde{\mathbf{K}}_{2^\nu}}$ happens to be a multiple eigenvalue of $\tilde{\mathbf{K}}_{2^{\nu-1}}$, then $\mathbf{x}_{\tilde{\mathbf{K}}_{2^\nu}}$ is more generally of the form

$$\mathbf{x}_{\tilde{\mathbf{K}}_{2^\nu}} = \sum_i \zeta_i \begin{bmatrix} \mathbf{x}^{(i)}_{\tilde{\mathbf{K}}_{2^{\nu-1}}} \\ \mathbf{x}^{(i)}_{\tilde{\mathbf{K}}_{2^{\nu-1}}} \end{bmatrix}$$

where $\mathbf{x}^{(i)}_{\tilde{\mathbf{K}}_{2^{\nu-1}}}$ are the eigenvectors corresponding to the multiple eigenvalue $\lambda_{\tilde{\mathbf{K}}_{2^\nu}}$ of $\tilde{\mathbf{K}}_{2^{\nu-1}}$. Therefore, $\lambda_{\tilde{\mathbf{K}}_{2^\nu}}$ is a multiple eigenvalue of $\tilde{\mathbf{K}}_{2^\nu}$ as well, with the same multiplicity.

Case B:

$\lambda_{\tilde{\mathbf{K}}_{2^\nu}}$ is an eigenvalue of $\tilde{\mathbf{K}}_{2^{\nu-1}} - 2\tilde{\mathbf{K}}_{\mathrm{RL}2^{\nu-1}}$ with eigenvector $\mathbf{x}_{2^{\nu-1},\mathrm{A}} - \mathbf{x}_{2^{\nu-1},\mathrm{B}}$ and $\mathbf{x}_{2^{\nu-1},\mathrm{A}} + \mathbf{x}_{2^{\nu-1},\mathrm{B}} = 0$.

In this case we obtain $\mathbf{x}_{2^{\nu-1},\mathrm{B}} = -\mathbf{x}_{2^{\nu-1},\mathrm{B}}$. From Eq. (3.19), the eigenvector $\mathbf{x}_{\tilde{\mathbf{K}}_{2^{\nu-1}} - 2\tilde{\mathbf{K}}_{\mathrm{RL}2^{\nu-1}}}$ of $\tilde{\mathbf{K}}_{2^{\nu-1}} - 2\tilde{\mathbf{K}}_{\mathrm{RL}2^{\nu-1}}$ corresponding to eigenvalue $\lambda_{\tilde{\mathbf{K}}_{2^\nu}}$ is $2\,\mathbf{x}_{2^{\nu-1},\mathrm{A}}$ or, more generally, $1/\zeta\,\mathbf{x}_{2^{\nu-1},\mathrm{A}}$

where $1/\xi$ is a multiplying factor. The number $\lambda_{\tilde{\mathbf{K}}_{2^\nu}}$, originally defined as an eigenvalue of $\tilde{\mathbf{K}}_{2^\nu}$, is also an eigenvalue of $\tilde{\mathbf{K}}_{2^{\nu-1}} - 2\tilde{\mathbf{K}}_{\mathrm{RL}\,2^{\nu-1}}$, and the eigenvectors of the two matrices are related via

$$\mathbf{x}_{\tilde{\mathbf{K}}_{2^\nu}} = \xi \begin{bmatrix} \mathbf{x}_{\tilde{\mathbf{K}}_{2^{\nu-1}} - 2\tilde{\mathbf{K}}_{\mathrm{RL}\,2^{\nu-1}}} \\ -\mathbf{x}_{\tilde{\mathbf{K}}_{2^{\nu-1}} - 2\tilde{\mathbf{K}}_{\mathrm{RL}\,2^{\nu-1}}} \end{bmatrix} \qquad \text{Eq. (3.22)}$$

If $\lambda_{\tilde{\mathbf{K}}_{2^\nu}}$ happens to be a multiple eigenvalue of $\tilde{\mathbf{K}}_{2^{\nu-1}} - 2\tilde{\mathbf{K}}_{\mathrm{RL}\,2^{\nu-1}}$, then $\mathbf{x}_{\tilde{\mathbf{K}}_{2^\nu}}$ is more generally of the form

$$\mathbf{x}_{\tilde{\mathbf{K}}_{2^\nu}} = \sum_i \xi_i \begin{bmatrix} \mathbf{x}^{(i)}_{\tilde{\mathbf{K}}_{2^{\nu-1}} - 2\tilde{\mathbf{K}}_{\mathrm{RL}\,2^{\nu-1}}} \\ -\mathbf{x}^{(i)}_{\tilde{\mathbf{K}}_{2^{\nu-1}} - 2\tilde{\mathbf{K}}_{\mathrm{RL}\,2^{\nu-1}}} \end{bmatrix}$$ where $\mathbf{x}^{(i)}_{\tilde{\mathbf{K}}_{2^{\nu-1}} - 2\tilde{\mathbf{K}}_{\mathrm{RL}\,2^{\nu-1}}}$ are the eigenvectors corresponding to the multiple eigenvalue λ_{2^ν} of $\tilde{\mathbf{K}}_{2^{\nu-1}} - 2\tilde{\mathbf{K}}_{\mathrm{RL}\,2^{\nu-1}}$. Therefore, $\lambda_{\tilde{\mathbf{K}}_{2^\nu}}$ is a multiple eigenvalue of $\tilde{\mathbf{K}}_{2^\nu}$ as well, with the same multiplicity.

Case C:

$\lambda_{\tilde{\mathbf{K}}_{2^\nu}}$ is an eigenvalue of both $\tilde{\mathbf{K}}_{2^{\nu-1}}$, with eigenvector $\mathbf{x}_{2^{\nu-1},\mathrm{A}} + \mathbf{x}_{2^{\nu-1},\mathrm{B}}$ and of $\tilde{\mathbf{K}}_{2^{\nu-1}} - 2\tilde{\mathbf{K}}_{\mathrm{RL}\,2^{\nu-1}}$, with eigenvector $\mathbf{x}_{2^{\nu-1},\mathrm{A}} - \mathbf{x}_{2^{\nu-1},\mathrm{B}}$

We have:

$$\begin{aligned} \mathbf{x}_{\tilde{\mathbf{K}}_{2^{\nu-1}}} &= \mathbf{x}_{2^{\nu-1},\mathrm{A}} + \mathbf{x}_{2^{\nu-1},\mathrm{B}} \\ \mathbf{x}_{\tilde{\mathbf{K}}_{2^{\nu-1}} - 2\tilde{\mathbf{K}}_{\mathrm{RL}\,2^{\nu-1}}} &= \mathbf{x}_{2^{\nu-1},\mathrm{A}} - \mathbf{x}_{2^{\nu-1},\mathrm{B}} \end{aligned} \qquad \text{Eq. (3.23)}$$

with $\mathbf{x}_{\tilde{\mathbf{K}}_{2^{\nu-1}}}$, $\mathbf{x}_{\tilde{\mathbf{K}}_{2^{\nu-1}} - 2\tilde{\mathbf{K}}_{\mathrm{RL}\,2^{\nu-1}}}$ being eigenvectors of matrices $\tilde{\mathbf{K}}_{2^{\nu-1}}$, $\tilde{\mathbf{K}}_{2^{\nu-1}} - 2\tilde{\mathbf{K}}_{\mathrm{RL}\,2^{\nu-1}}$, respectively, both corresponding to eigenvalue $\lambda_{\tilde{\mathbf{K}}_{2^\nu}}$. From Eqs. (3.23) we obtain:

$$\begin{aligned} \mathbf{x}_{2^{\nu-1},\mathrm{A}} &= \frac{\mathbf{x}_{\tilde{\mathbf{K}}_{2^{\nu-1}}} + \mathbf{x}_{\tilde{\mathbf{K}}_{2^{\nu-1}} - 2\tilde{\mathbf{K}}_{\mathrm{RL}\,2^{\nu-1}}}}{2} \\ \mathbf{x}_{2^{\nu-1},\mathrm{B}} &= \frac{\mathbf{x}_{\tilde{\mathbf{K}}_{2^{\nu-1}}} - \mathbf{x}_{\tilde{\mathbf{K}}_{2^{\nu-1}} - 2\tilde{\mathbf{K}}_{\mathrm{RL}\,2^{\nu-1}}}}{2} \end{aligned} \qquad \text{Eq. (3.24)}$$

or, more generally,

$$\mathbf{x}_{\tilde{\mathbf{K}}_{2^\nu}} = \zeta \begin{bmatrix} \mathbf{x}_{\tilde{\mathbf{K}}_{2^{\nu-1}}} \\ \mathbf{x}_{\tilde{\mathbf{K}}_{2^{\nu-1}}} \end{bmatrix} + \xi \begin{bmatrix} \mathbf{x}_{\tilde{\mathbf{K}}_{2^{\nu-1}} - 2\tilde{\mathbf{K}}_{\mathrm{RL}\,2^{\nu-1}}} \\ -\mathbf{x}_{\tilde{\mathbf{K}}_{2^{\nu-1}} - 2\tilde{\mathbf{K}}_{\mathrm{RL}\,2^{\nu-1}}} \end{bmatrix} \qquad \text{Eq. (3.25)}$$

We note that the expression of Eq. (3.25), which has been derived for case C, contains Eqs.(3.21) and (3.22), derived for cases A and C, as special cases.

From the above discussion of cases (A,B,C) one sees that finding the eigenvalues and eigenvectors of the $2^\nu n$-dimensional matrix $\tilde{\mathbf{K}}_{2^\nu}$ has been reduced to finding the eigenvalues and eigenvectors of the $2^{\nu-1}n$-dimensional matrices $\tilde{\mathbf{K}}_{2^{\nu-1}}$ and $\tilde{\mathbf{K}}_{2^{\nu-1}} - 2\tilde{\mathbf{K}}_{\mathrm{RL}\,2^{\nu-1}}$. Recursive application of this strategy can be symbolized by the tree diagram:

$$\left\{ \tilde{\mathbf{K}}_{2^\nu} \left\{ \tilde{\mathbf{K}}_{2^{\nu-1}} \left\{ \tilde{\mathbf{K}}_{2^{\nu-2}} \left\{ \tilde{\mathbf{K}}_{2^{\nu-3}} \left\{ \tilde{\mathbf{K}}_{2^{\nu-4}} \left\{ \begin{matrix} \cdots \\ \cdots \end{matrix} \right. \right. \right. \right. \right. \right.$$
$$\left. \left. \left. \left. \tilde{\mathbf{K}}_{2^{\nu-4}} - 2\tilde{\mathbf{K}}_{\mathrm{RL}\,2^{\nu-4}} \right. \right. \right. \right.$$
$$\left. \left. \left. \tilde{\mathbf{K}}_{2^{\nu-3}} - 2\tilde{\mathbf{K}}_{\mathrm{RL}\,2^{\nu-3}} \right. \right. \right.$$
$$\left. \left. \tilde{\mathbf{K}}_{2^{\nu-2}} - 2\tilde{\mathbf{K}}_{\mathrm{RL}\,2^{\nu-2}} \right. \right.$$
$$\left. \tilde{\mathbf{K}}_{2^{\nu-1}} - 2\tilde{\mathbf{K}}_{\mathrm{RL}\,2^{\nu-1}} \right. \qquad \text{Eq. (3.26)}$$

3.2.2. Reduction of the diagonalization of matrix $\tilde{\mathbf{K}}_{2^{\nu-1}} - 2\tilde{\mathbf{K}}_{\mathrm{RL}\,2^{\nu-1}}$ to that of $(2^{\nu-2}n)\times(2^{\nu-2}n)$-dimensional matrices

We now seek to express the eigenvalues of matrix $\tilde{\mathbf{K}}_{2^{\nu-1}} - 2\tilde{\mathbf{K}}_{\mathrm{RL}\,2^{\nu-1}}$ in terms of the eigenvalues of lower-dimensional matrices. For this purpose, it is useful to prove the following

Theorem 1: The eigenvalues of the $(2^{\nu-1}n)\times(2^{\nu-1}n)$-dimensional matrix $\tilde{\mathbf{K}}_{2^{\nu-1}} - 2\tilde{\mathbf{K}}_{\mathrm{RL}\,2^{\nu-1}}$ are the same as the eigenvalues of the $(2^{\nu-2}n)\times(2^{\nu-2}n)$-dimensional matrices $\left(\tilde{\mathbf{K}}_{2^{\mu-2}} - \tilde{\mathbf{K}}_{\mathrm{RL}\,2^{\mu-2}}\right) \pm i\left(\tilde{\mathbf{K}}_{\mathrm{R}\,2^{\mu-2}} - \tilde{\mathbf{K}}_{\mathrm{L}2^{\mu-2}}\right)$.

A proof of Theorem 1 is provided in Appendix B. In the same Appendix expressions are derived for the eigenvectors of matrix $\tilde{\mathbf{K}}_{2^{\nu-1}} - 2\tilde{\mathbf{K}}_{\mathrm{RL}\,2^{\nu-1}}$ in terms of the eigenvectors of matrices $\left(\tilde{\mathbf{K}}_{2^{\mu-2}} - \tilde{\mathbf{K}}_{\mathrm{RL}\,2^{\mu-2}}\right) \pm i\left(\tilde{\mathbf{K}}_{\mathrm{R}\,2^{\mu-2}} - \tilde{\mathbf{K}}_{\mathrm{L}2^{\mu-2}}\right)$ that correspond to the same eigenvalue.

In discussing the eigenvalue equations for matrices $\left(\tilde{\mathbf{K}}_{2^{\nu-2}}-\tilde{\mathbf{K}}_{\mathrm{RL}2^{\nu-2}}\right)\pm i\left(\tilde{\mathbf{K}}_{\mathrm{R}2^{\nu-2}}-\tilde{\mathbf{K}}_{\mathrm{L}2^{\nu-2}}\right)$ we make use of the following

Theorem 2: Matrix $\left(\tilde{\mathbf{K}}_{2^{\nu-2}}-\tilde{\mathbf{K}}_{\mathrm{RL}2^{\nu-2}}\right)-i\left(\tilde{\mathbf{K}}_{\mathrm{R}2^{\nu-2}}-\tilde{\mathbf{K}}_{\mathrm{L}2^{\nu-2}}\right)$ is the transpose of matrix $\left(\tilde{\mathbf{K}}_{2^{\nu-2}}-\tilde{\mathbf{K}}_{\mathrm{RL}2^{\nu-2}}\right)+i\left(\tilde{\mathbf{K}}_{\mathrm{R}2^{\nu-2}}-\tilde{\mathbf{K}}_{\mathrm{L}2^{\nu-2}}\right)$.
Theorem 2 is proved in Appendix C.

Corollary: Each of the matrices $\left(\tilde{\mathbf{K}}_{2^{\nu-2}}-\tilde{\mathbf{K}}_{\mathrm{RL}2^{\nu-2}}\right)-i\left(\tilde{\mathbf{K}}_{\mathrm{R}2^{\nu-2}}-\tilde{\mathbf{K}}_{\mathrm{L}2^{\nu-2}}\right)$ and $\left(\tilde{\mathbf{K}}_{2^{\nu-2}}-\tilde{\mathbf{K}}_{\mathrm{RL}2^{\nu-2}}\right)+i\left(\tilde{\mathbf{K}}_{\mathrm{R}2^{\nu-2}}-\tilde{\mathbf{K}}_{\mathrm{L}2^{\nu-2}}\right)$ equals the transpose of its complex conjugate, and is therefore Hermitian. This ensures that $\left(\tilde{\mathbf{K}}_{2^{\nu-2}}-\tilde{\mathbf{K}}_{\mathrm{RL}2^{\nu-2}}\right)-i\left(\tilde{\mathbf{K}}_{\mathrm{R}2^{\nu-2}}-\tilde{\mathbf{K}}_{\mathrm{L}2^{\nu-2}}\right)$ and $\left(\tilde{\mathbf{K}}_{2^{\nu-2}}-\tilde{\mathbf{K}}_{\mathrm{RL}2^{\nu-2}}\right)+i\left(\tilde{\mathbf{K}}_{\mathrm{R}2^{\nu-2}}-\tilde{\mathbf{K}}_{\mathrm{L}2^{\nu-2}}\right)$ have real eigenvalues.

Now, the eigenvalues of a square matrix are equal to the eigenvalues of its transpose. Hence, $\left(\tilde{\mathbf{K}}_{2^{\nu-2}}-\tilde{\mathbf{K}}_{\mathrm{RL}2^{\nu-2}}\right)-i\left(\tilde{\mathbf{K}}_{\mathrm{R}2^{\nu-2}}-\tilde{\mathbf{K}}_{\mathrm{L}2^{\nu-2}}\right)$ and $\left(\tilde{\mathbf{K}}_{2^{\nu-2}}-\tilde{\mathbf{K}}_{\mathrm{RL}2^{\nu-2}}\right)+i\left(\tilde{\mathbf{K}}_{\mathrm{R}2^{\nu-2}}-\tilde{\mathbf{K}}_{\mathrm{L}2^{\nu-2}}\right)$ actually have the *same* eigenvalues (but different eigenvectors). This means that the eigenvalues $\lambda_{\tilde{\mathbf{K}}_{2^{\nu-1}}-2\tilde{\mathbf{K}}_{\mathrm{RL}2^{\nu-1}}}$ of matrix $\tilde{\mathbf{K}}_{2^{\nu-1}}-2\tilde{\mathbf{K}}_{\mathrm{RL}2^{\nu-1}}$ are actually double, and can be obtained by diagonalizing either $\left(\tilde{\mathbf{K}}_{2^{\nu-2}}-\tilde{\mathbf{K}}_{\mathrm{RL}2^{\nu-2}}\right)+i\left(\tilde{\mathbf{K}}_{\mathrm{R}2^{\nu-2}}-\tilde{\mathbf{K}}_{\mathrm{L}2^{\nu-2}}\right)$ or $\left(\tilde{\mathbf{K}}_{2^{\nu-2}}-\tilde{\mathbf{K}}_{\mathrm{RL}2^{\nu-2}}\right)-i\left(\tilde{\mathbf{K}}_{\mathrm{R}2^{\nu-2}}-\tilde{\mathbf{K}}_{\mathrm{L}2^{\nu-2}}\right)$.

From the tree diagram of Eq. (3.26) we see that diagonalizing the $(2^{\nu}n)\times(2^{\nu}n)$ matrix $\tilde{\mathbf{K}}_{2^{\nu}}$ is ultimately reduced to diagonalizing the $n\times n$ matrix $\tilde{\mathbf{K}}_1$, as well as the $(2^{\mu-1}n)\times(2^{\mu-1}n)$ matrices $\tilde{\mathbf{K}}_{2^{\mu-1}}-2\tilde{\mathbf{K}}_{\mathrm{RL}2^{\mu-1}}$, with $1\le\mu\le\nu$. On the other hand, application of the derivations outlined in the present section for $\mu=\nu$ shows that diagonalization of $\tilde{\mathbf{K}}_{2^{\mu-1}}-2\tilde{\mathbf{K}}_{\mathrm{RL}2^{\mu-1}}$, $2\le\mu\le\nu$ is reduced to diagonalization of the $(2^{\mu-2}n)\times(2^{\mu-2}n)$ matrices $\left(\tilde{\mathbf{K}}_{2^{\mu-2}}-\tilde{\mathbf{K}}_{\mathrm{RL}2^{\mu-2}}\right)\pm i\left(\tilde{\mathbf{K}}_{\mathrm{R}2^{\mu-2}}-\tilde{\mathbf{K}}_{\mathrm{L}2^{\mu-2}}\right)$, which are transpose of each other and therefore have the same eigenvalues. In the following section we show that this stepdown in the size of matrices to be diagonalized in order to find the eigenvalues and eigenvectors of each $(2^{\mu-}$

$^1n)\times(2^{\mu-1}n)$ matrix $\tilde{\mathbf{K}}_{2^{\mu-1}}-2\tilde{\mathbf{K}}_{\mathrm{RL}2^{\mu-1}}$, $2\le\mu\le\nu$ can be extended, ultimately reducing the problem of diagonalizing $\tilde{\mathbf{K}}_{2^{\mu-1}}-2\tilde{\mathbf{K}}_{\mathrm{RL}2^{\mu-1}}$ to one of diagonalizing $2^{\mu-1}$ matrices of size $n\times n$.

3.2.3. Reduction of diagonalization of $\tilde{\mathbf{K}}_{2^{\mu-1}}-2\tilde{\mathbf{K}}_{\mathrm{RL}2^{\mu-1}}$ to the diagonalization of $n\times n$ matrices

Theorem 3: Consider the matrices $\left(\tilde{\mathbf{K}}_{2^{\mu-b}}-\tilde{\mathbf{K}}_{\mathrm{RL}2^{\mu-b}}\right)+\left[a_b\tilde{\mathbf{K}}_{\mathrm{R}2^{\mu-b}}+\left(a_1...a_b\right)\tilde{\mathbf{K}}_{\mathrm{L}2^{\mu-b}}\right]$ with index b being an integer, $2\le b\le\mu-1$, and the (generally complex) coefficients a_j given by $a_1=-1$, $a_j=\pm\sqrt{a_{j-1}}$, $2\le j\le b+1$. (Note that a_j assumes multiple values for $j\ge 2$.) Let $\lambda_{2^{\mu-b}}$ be an eigenvalue of one of these matrices, formed using a specific choice of pluses and minuses in the definition of the a_j's, and let $\mathbf{x}_{2^{\mu-b}}=\begin{bmatrix}\mathbf{x}_{2^{\mu-b-1},\mathrm{E}}\\ \mathbf{x}_{2^{\mu-b-1},\mathrm{F}}\end{bmatrix}$ be the eigenvector of this matrix corresponding to eigenvalue $\lambda_{2^{\mu-b}}$, with $\mathbf{x}_{2^{\mu-b-1},\mathrm{E}}$, $\mathbf{x}_{2^{\mu-b-1},\mathrm{F}}$ being $2^{\mu-b-1}n$-dimensional vectors. Then, at least one of the following statements is true: (a) $\lambda_{2^{\mu-b}}$ is an eigenvalue of matrix $\left(\tilde{\mathbf{K}}_{2^{\mu-b-1}}-\tilde{\mathbf{K}}_{\mathrm{RL}2^{\mu-b-1}}\right)+\left[a_{b+1}\tilde{\mathbf{K}}_{\mathrm{R}2^{\mu-b-1}}+\left(a_1...a_{b+1}\right)\tilde{\mathbf{K}}_{\mathrm{L}2^{\mu-b-1}}\right]$, with corresponding eigenvector $\mathbf{x}_{2^{\mu-b-1},\mathrm{E}}+a_{b+1}\mathbf{x}_{2^{\mu-b-1},\mathrm{F}}$; (b) $\mathbf{x}_{2^{\mu-b-1},\mathrm{E}}+a_{b+1}\mathbf{x}_{2^{\mu-b-1},\mathrm{F}}=0$.

A proof of Theorem 3 is provided in Appendix D.

From the proof of Theorem 3, it is clear that, given a set of $a_1,a_2,...,a_b$, if a_{b+1} is used to denote one of the values $a_{b+1}=\pm\sqrt{a_b}$, the following equations will be satisfied simultaneously:

$$\left\{\left(\tilde{\mathbf{K}}_{2^{\mu-b-1}}-\tilde{\mathbf{K}}_{\mathrm{RL}2^{\mu-b-1}}\right)+\left[a_{b+1}\tilde{\mathbf{K}}_{\mathrm{R}2^{\mu-b-1}}+\left(a_1...a_ba_{b+1}\right)\tilde{\mathbf{K}}_{\mathrm{L}2^{\mu-b-1}}\right]\right\}\left(\mathbf{x}_{2^{\mu-b-1},\mathrm{E}}+a_{b+1}\mathbf{x}_{2^{\mu-b-1},\mathrm{F}}\right)=\lambda_{2^{\mu-b}}\left(\mathbf{x}_{2^{\mu-b-1},\mathrm{E}}+a_{b+1}\mathbf{x}_{2^{\mu-b-1},\mathrm{F}}\right)$$
$$\left\{\left(\tilde{\mathbf{K}}_{2^{\mu-b-1}}-\tilde{\mathbf{K}}_{\mathrm{RL}2^{\mu-b-1}}\right)-\left[a_{b+1}\tilde{\mathbf{K}}_{\mathrm{R}2^{\mu-b-1}}+\left(a_1...a_ba_{b+1}\right)\tilde{\mathbf{K}}_{\mathrm{L}2^{\mu-b-1}}\right]\right\}\left(\mathbf{x}_{2^{\mu-b-1},\mathrm{E}}-a_{b+1}\mathbf{x}_{2^{\mu-b-1},\mathrm{F}}\right)=\lambda_{2^{\mu-b}}\left(\mathbf{x}_{2^{\mu-b-1},\mathrm{E}}-a_{b+1}\mathbf{x}_{2^{\mu-b-1},\mathrm{F}}\right)$$
Eq. (3.27)

Eq. (3.27) tells us that the following three cases are possible:

A. $\lambda_{2^{\mu-b}}$ is an eigenvalue of the $2^{\mu-b-1}n\times 2^{\mu-b-1}n$ matrix $\left(\tilde{\mathbf{K}}_{2^{\mu-b-1}}-\tilde{\mathbf{K}}_{\mathrm{RL}2^{\mu-b-1}}\right)+\left[a_{b+1}\tilde{\mathbf{K}}_{\mathrm{R}2^{\mu-b-1}}+\left(a_1...a_b a_{b+1}\right)\tilde{\mathbf{K}}_{\mathrm{L}2^{\mu-b-1}}\right]$ with corresponding eigenvector $\mathbf{x}_{2^{\mu-b-1}+}=\mathbf{x}_{2^{\mu-b-1},\mathrm{E}}+a_{b+1}\mathbf{x}_{2^{\mu-b-1},\mathrm{F}}$ and $\mathbf{x}_{2^{\mu-b-1},\mathrm{E}}-a_{b+1}\mathbf{x}_{2^{\mu-b-1},\mathrm{F}}=0$

B. $\lambda_{2^{\mu-b}}$ is an eigenvalue of the $2^{\mu-b-1}n\times 2^{\mu-b-1}n$ matrix $\left(\tilde{\mathbf{K}}_{2^{\mu-b-1}}-\tilde{\mathbf{K}}_{\mathrm{RL}2^{\mu-b-1}}\right)-\left[a_{b+1}\tilde{\mathbf{K}}_{\mathrm{R}2^{\mu-b-1}}+\left(a_1...a_b a_{b+1}\right)\tilde{\mathbf{K}}_{\mathrm{L}2^{\mu-b-1}}\right]$ with corresponding eigenvector $\mathbf{x}_{2^{\mu-b-1}-}=\mathbf{x}_{2^{\mu-b-1},\mathrm{E}}-a_{b+1}\mathbf{x}_{2^{\mu-b-1},\mathrm{F}}$ and $\mathbf{x}_{2^{\mu-b-1},\mathrm{E}}+a_{b+1}\mathbf{x}_{2^{\mu-b-1},\mathrm{F}}=0$

C. $\lambda_{2^{\mu-b}}$ is an eigenvalue of the $2^{\mu-b-1}n\times 2^{\mu-b-1}n$ matrix $\left(\tilde{\mathbf{K}}_{2^{\mu-b-1}}-\tilde{\mathbf{K}}_{\mathrm{RL}2^{\mu-b-1}}\right)+\left[a_{b+1}\tilde{\mathbf{K}}_{\mathrm{R}2^{\mu-b-1}}+\left(a_1...a_b a_{b+1}\right)\tilde{\mathbf{K}}_{\mathrm{L}2^{\mu-b-1}}\right]$ with corresponding eigenvector $\mathbf{x}_{2^{\mu-b-1}+}=\mathbf{x}_{2^{\mu-b-1},\mathrm{E}}+a_{b+1}\mathbf{x}_{2^{\mu-b-1},\mathrm{F}}$ and at the same time an eigenvalue of the $2^{\mu-b-1}n\times 2^{\mu-b-1}n$ matrix $\left(\tilde{\mathbf{K}}_{2^{\mu-b-1}}-\tilde{\mathbf{K}}_{\mathrm{RL}2^{\mu-b-1}}\right)-\left[a_{b+1}\tilde{\mathbf{K}}_{\mathrm{R}2^{\mu-b-1}}+\left(a_1...a_b a_{b+1}\right)\tilde{\mathbf{K}}_{\mathrm{L}2^{\mu-b-1}}\right]$ with corresponding eigenvector $\mathbf{x}_{2^{\mu-b-1}-}=\mathbf{x}_{2^{\mu-b-1},\mathrm{E}}-a_{b+1}\mathbf{x}_{2^{\mu-b-1},\mathrm{F}}$.

We proceed to determine $\mathbf{x}_{2^{\mu-b-1},\mathrm{E}}$ and $\mathbf{x}_{2^{\mu-b-1},\mathrm{F}}$, hence the eigenvector $\mathbf{x}_{2^{\mu-b}}$ of the $2^{\mu-b}n\times 2^{\mu-b}n$ matrix $\left(\tilde{\mathbf{K}}_{2^{\mu-b}}-\tilde{\mathbf{K}}_{\mathrm{RL}2^{\mu-b}}\right)+\left[a_b\tilde{\mathbf{K}}_{\mathrm{R}2^{\mu-b}}+\left(a_1...a_b\right)\tilde{\mathbf{K}}_{\mathrm{L}2^{\mu-b}}\right]$, for each one of these cases by analogy to the development following Eq. (3.20).

Case A

We have

$$\begin{aligned}&\mathbf{x}_{2^{\mu-b-1},\mathrm{E}}+a_{b+1}\mathbf{x}_{2^{\mu-b-1},\mathrm{F}}=\mathbf{x}_{2^{\mu-b-1}+}\\&\mathbf{x}_{2^{\mu-b-1},\mathrm{E}}-a_{b+1}\mathbf{x}_{2^{\mu-b-1},\mathrm{F}}=0\end{aligned},$$

hence

$$\mathbf{x}_{2^{\mu-b-1},\mathrm{E}}=\mathbf{x}_{2^{\mu-b-1}+}/2$$

$$\mathbf{x}_{2^{\mu-b-1},\mathrm{E}}=\mathbf{x}_{2^{\mu-b-1}+}/\left(2a_{b+1}\right)$$

or, allowing for a multiplicative constant,

$$\mathbf{x}_{2^{\mu-b}}=\zeta\begin{bmatrix}\mathbf{x}_{2^{\mu-b-1}+}\\ \mathbf{x}_{2^{\mu-b-1}+}/a_{b+1}\end{bmatrix} \qquad \text{Eq. (3.28)}$$

Case B

We have

$$\begin{matrix}\mathbf{x}_{2^{\mu-b-1},\mathrm{E}}-a_{b+1}\mathbf{x}_{2^{\mu-b-1},\mathrm{F}}=\mathbf{x}_{2^{\mu-b-1}\_}\\ \mathbf{x}_{2^{\mu-b-1},\mathrm{E}}+a_{b+1}\mathbf{x}_{2^{\mu-b-1},\mathrm{F}}=0\end{matrix},$$

hence

$$\mathbf{x}_{2^{\mu-b-1},\mathrm{E}}=\mathbf{x}_{2^{\mu-b-1}\_}/2$$

$$\mathbf{x}_{2^{\mu-b-1},\mathrm{F}}=-\mathbf{x}_{2^{\mu-b-1}\_}/\left(2a_{b+1}\right)$$

or, allowing for a multiplicative constant,

$$\mathbf{x}_{2^{\mu-b}}=\xi\begin{bmatrix}\mathbf{x}_{2^{\mu-b-1}\_}\\ -\mathbf{x}_{2^{\mu-b-1}\_}/a_{b+1}\end{bmatrix} \qquad \text{Eq. (3.29)}$$

Case C

We have

$$\mathbf{x}_{2^{\mu-b-1},\mathrm{E}}+a_{b+1}\mathbf{x}_{2^{\mu-b-1},\mathrm{F}}=\mathbf{x}_{2^{\mu-b-1}+}$$

$$\mathbf{x}_{2^{\mu-b-1},\mathrm{E}}-a_{b+1}\mathbf{x}_{2^{\mu-b-1},\mathrm{F}}=\mathbf{x}_{2^{\mu-b-1}\_}$$

hence

$$\mathbf{x}_{2^{\mu-b-1},\mathrm{E}}=\left(\mathbf{x}_{2^{\mu-b-1}+}+\mathbf{x}_{2^{\mu-b-1}\_}\right)/2$$

$$\mathbf{x}_{2^{\mu-b-1},\mathrm{F}}=\left(\mathbf{x}_{2^{\mu-b-1}+}-\mathbf{x}_{2^{\mu-b-1}\_}\right)/\left(2a_{b+1}\right)$$

or, allowing for multiplicative constants in the eigenvalues,

$$\mathbf{x}_{2^{\mu-b}}=\zeta\begin{bmatrix}\mathbf{x}_{2^{\mu-b-1}+}\\ \mathbf{x}_{2^{\mu-b-1}+}/a_{b+1}\end{bmatrix}+\xi\begin{bmatrix}\mathbf{x}_{2^{\mu-b-1}\_}\\ -\mathbf{x}_{2^{\mu-b-1}\_}/a_{b+1}\end{bmatrix} \qquad \text{Eq. (3.30)}$$

We note that the general expression of Eq. (3.30) contains Eqs. (3.28) and (3.29) as special cases, and can therefore be used to cover all cases. We also note that Eq. (30) remains invariant upon assigning the value $-a_{b+1}$ to a_{b+1}, as expected from the definition $a_{b+1}=\pm\sqrt{a_b}$

We have shown that the diagonalization of a $(2^{\mu-b}n)\times(2^{\mu-b}n)$ –dimensional matrix $\left(\tilde{\mathbf{K}}_{2^{\mu-b}}-\tilde{\mathbf{K}}_{\mathrm{RL}2^{\mu-b}}\right)+\left[a_b\tilde{\mathbf{K}}_{\mathrm{R}2^{\mu-b}}+\left(a_1...a_b\right)\tilde{\mathbf{K}}_{\mathrm{L}2^{\mu-b}}\right]$ is reduced to the diagonalization of the two $(2^{\mu-b-1}n)\times(2^{\mu-b-1}n)$-dimensional matrices $\left(\tilde{\mathbf{K}}_{2^{\mu-1-b}}-\tilde{\mathbf{K}}_{\mathrm{RL}2^{\mu-1-b}}\right)+\left[a_{b+1}\tilde{\mathbf{K}}_{\mathrm{R}2^{\mu-1-b}}+\left(a_1...a_{b+1}\right)\tilde{\mathbf{K}}_{\mathrm{L}2^{\mu-1-b}}\right]$ with $a_{b+1}=\pm\sqrt{a_b}$ and obtained straightforward recursive relations for the eigenvectors of the former matrix in terms of the eigenvectors of the latter.

According to the tree diagram of Eq. (3.26) and by virtue of Theorems 1 and 3 and the recursive expressions for the determination of eigenvalues and eigenvectors developed in conjunction with these theorems, the diagonalization of $\tilde{\mathbf{K}}_{2^\nu}$ is ultimately reduced to 2^ν diagonalizations of matrices of dimension $n \times n$. These are the matrix $\tilde{\mathbf{K}}_1$, the matrix $\tilde{\mathbf{K}}_1 - 2\tilde{\mathbf{K}}_{\mathrm{RL1}}$, and the matrices $\left(\tilde{\mathbf{K}}_1 - \tilde{\mathbf{K}}_{\mathrm{RL1}}\right) + \left[a_\mu \tilde{\mathbf{K}}_{\mathrm{R1}} + \left(a_1 a_2 ... a_\mu\right) \tilde{\mathbf{K}}_{\mathrm{L1}} \right]$, with $a_1 = -1$, $a_j = \pm\sqrt{a_{j-1}}$, $2 \le j \le \mu$, for $\mu = 2,...,\nu$.

As a result, we reduce the determination of eigenvalues and eigenvectors of $\tilde{\mathbf{K}}_{2^\nu}$ to the determination of these quantities for 2^ν matrices coming from the procedure we mentioned above. Actually, we need only the diagonalization of $\sum_{i=3}^{\nu} 2^{i-2} + 2 = 2^{\nu-1}$ matrices for the determination of the eigenvalues of $\tilde{\mathbf{K}}_{2^\nu}$. As shown in Appendix E, there is a way to assign each double eigenvalue to the lower-dimensional matrices where it comes from, within the recursive scheme. The minimum number of double eigenvalues is $\sum_{i=3}^{\nu} 2^{i-2}$, considering that, if an eigenvalue is 4-fold, it counts as 2 double eigenvalues. Similarly, if an eigenvalue is 8-fold, it counts as 4 double eigenvalues, etc.

Here it is important to remind the definition of the "principal" square root, the "principal" cubic root, the "principal" forth root,…,etc. When a positive real number ψ is presented under the radical symbol $\sqrt[\gamma]{\ }$, it must return only one result like a function, so a non-negative real root, called the principal γth root, is preferred to others and it is symbolized it as $\psi^{1/\gamma}$ or $\sqrt[\gamma]{\psi}$. For example, $\psi^2 = 4 \rightarrow \psi = \pm 2$ and the principal square root is 2 not −2. So, $\sqrt[2]{4} = 2$. Similarly, $\psi^3 = 1 \rightarrow \psi = \begin{cases} 1 \\ -\frac{1}{2} + i\frac{1}{2}\sqrt{3} \\ -\frac{1}{2} - i\frac{1}{2}\sqrt{3} \end{cases}$ and the principal cubic root of 1 is 1. So, $\sqrt[3]{1} = 1$. In complex numbers, if $-\pi < \theta < \pi$, the principal γth root of the complex number $\psi = re^{i\theta}$ is defined to be $\psi^{1/\gamma} = r^{1/\gamma} e^{i\theta/\gamma}$, while all the γ roots are $\psi_{set}{}^{1/\gamma} = r^{1/\gamma} e^{i\theta/\gamma} e^{2w\pi i/\gamma}$, $w = 0, \gamma - 1$ and r, θ are the polar coordinates of a complex number. We emphasize that when we mention a root in our text, we mean the prinicipal one.[79]

3.2.4. Recursive algorithm for the diagonalization of $\tilde{\mathbf{K}}_{2^\nu}$ based on diagonalization of $n \times n$ matrices.

Based on the theoretical developments outlined above, we have designed an algorithm for computing all the eigenvalues and eigenvectors of the symmetrized rate constant matrix $\tilde{\mathbf{K}}_{2^\nu}$ of the periodic system consisting of 2^ν unit cells and containing $2^\nu n$ states based on diagonalizations of strictly $n \times n$ matrices. The general flow of the calculations is indicated in Figure 3.4. The light green, light blue, and grey-brown boxes in the flow diagram of Figure 3.4 are analyzed further in Figures 3.5 and 3.6. Both the colors and the lines bordering these boxes have been designed so as to make obvious what fits where. The part of the algorithm that accomplishes the diagonalization of matrices $\left(\tilde{\mathbf{K}}_1 - \tilde{\mathbf{K}}_{\mathrm{RL1}}\right) + \left[a_\mu \tilde{\mathbf{K}}_{\mathrm{R1}} + \left(a_1 a_2 \ldots a_\mu\right) \tilde{\mathbf{K}}_{\mathrm{L1}} \right]$ discussed in Theorem 3 and the associated discussion, shown in Figure 3.6, involves $v-1$ levels of recursion. The flow diagram in Figure 3.7 has been drawn for the particular case $v=5$. It is obvious, however, how this diagram can be extended, by further branching, to deal with larger v. The contents of the orange and purple boxes appearing at all levels in the recursive flow sheet of Figure 3.6 are explained in detail in Figure 3.7. In the same figure is provided an explanation of the grey box performing the level initialization and of the red and blue decision diamonds controlling the flow of calculations at each level. We can see that the algorithm of Figure 3.6 actually involves 4 internal loops and can be very easily constructed, despite the apparent complexity of the Figure.

Eigenvalues and eigenvectors determined through the recursive scheme outlined above are used to calculate the probabilities of occupancy of states at any time, starting from a given initial probability distribution, via Eq. (3.7) as shown in Figure 3.8. We shall call the algorithm of Figures 3.4-3.8, applied to the solution of the master equation of a spatially periodic system with given initial conditions, "Master Equation Solution by Recursive Reduction of Dimensionality" of the symmetric rate constant matrix, or MESoRReD.

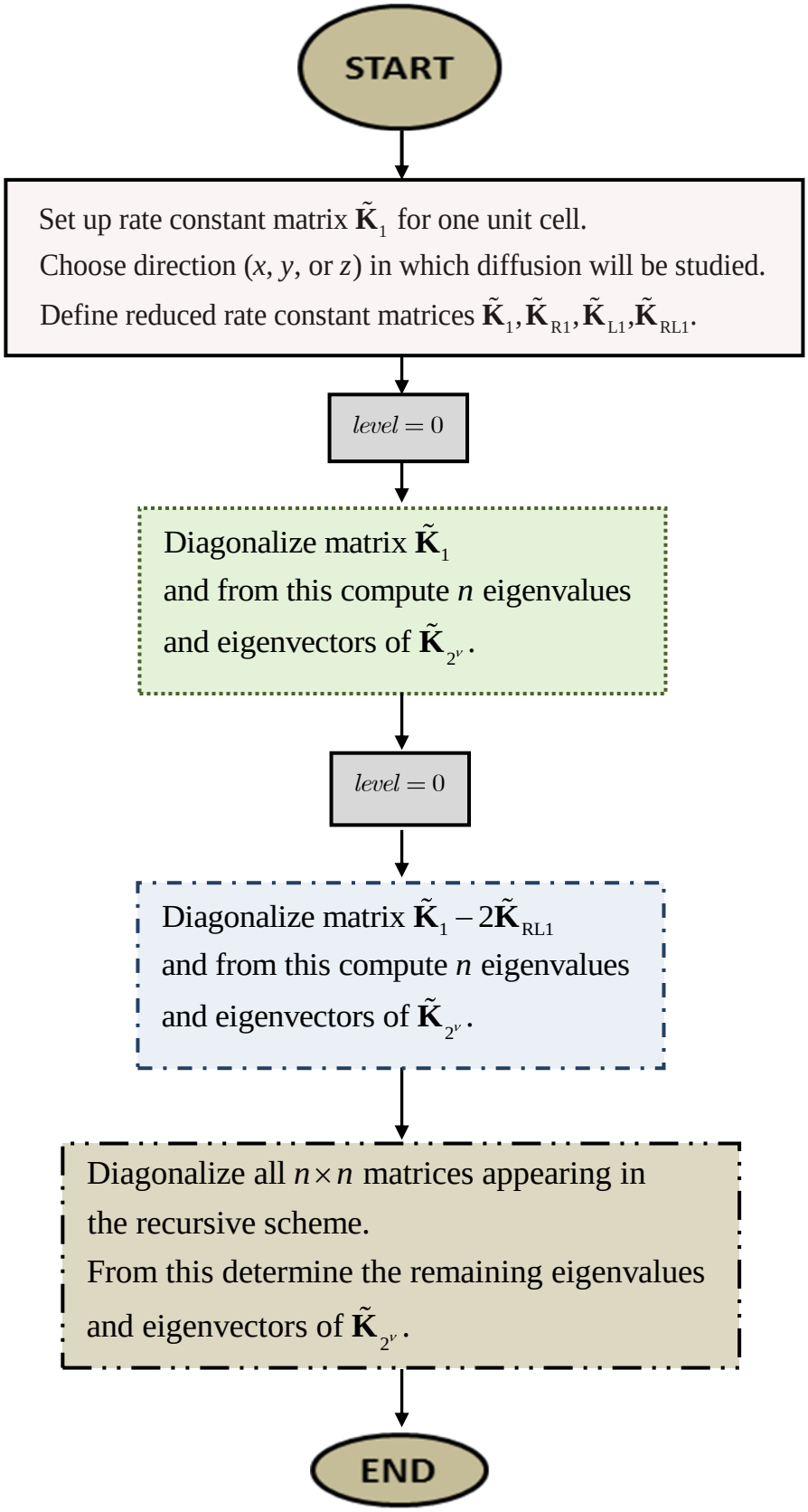

Figure 3.4 Overall algorithm for finding all the eigenvalues and eigenvectors of matrix $\tilde{\mathbf{K}}_{2^\nu}$. The contents of boxes shown with different colors and outlines in the flow diagram are explained in detail in Figures 3.5 and 3.6.

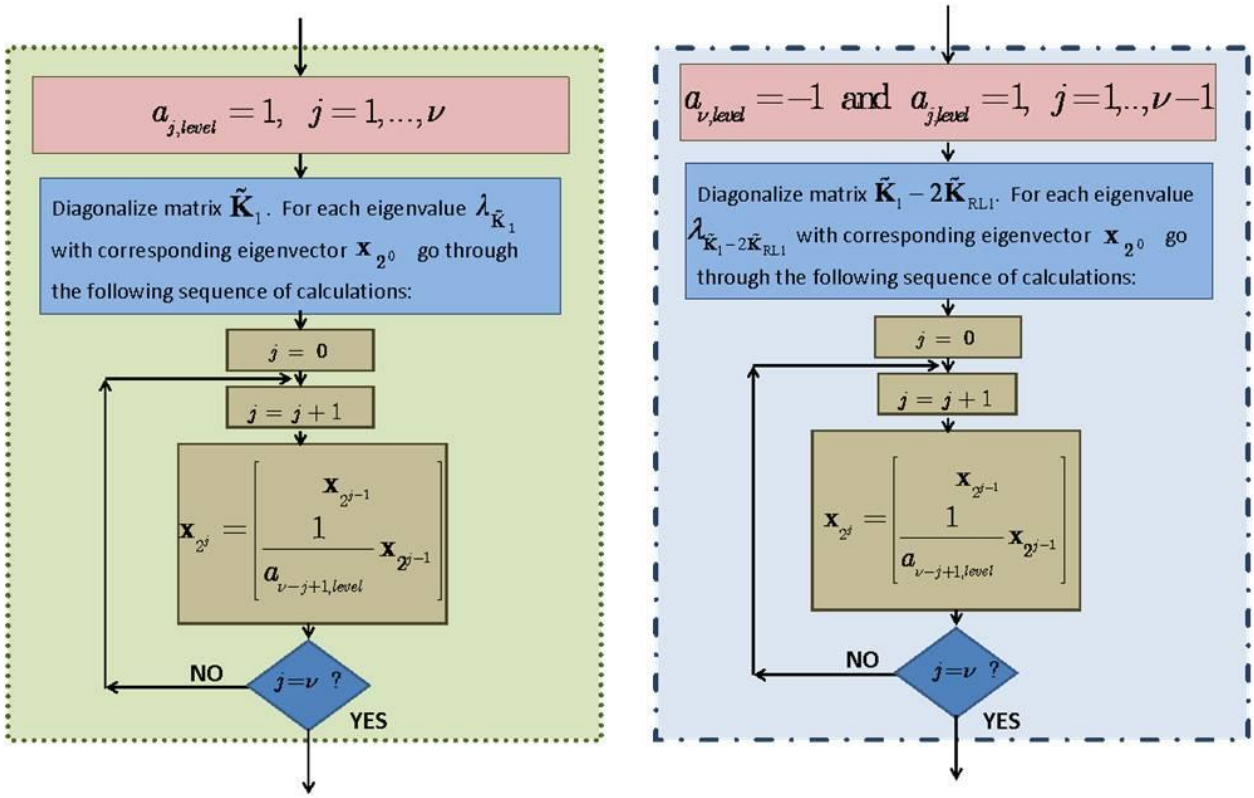

Figure 3.5 Algorithm for diagonalization of $\tilde{\mathbf{K}}_1$ and of $\tilde{\mathbf{K}}_1 - 2\tilde{\mathbf{K}}_{RL1}$ and determination of the contributions of these matrices to the eigenvalues (here denoted as $\lambda_{\tilde{\mathbf{K}}_1}$ and $\lambda_{\tilde{\mathbf{K}}_1 - 2\tilde{\mathbf{K}}_{RL1}}$) and eigenvectors (here denoted as $\mathbf{x}_{2^\nu}$) of $\tilde{\mathbf{K}}_{2^\nu}$.

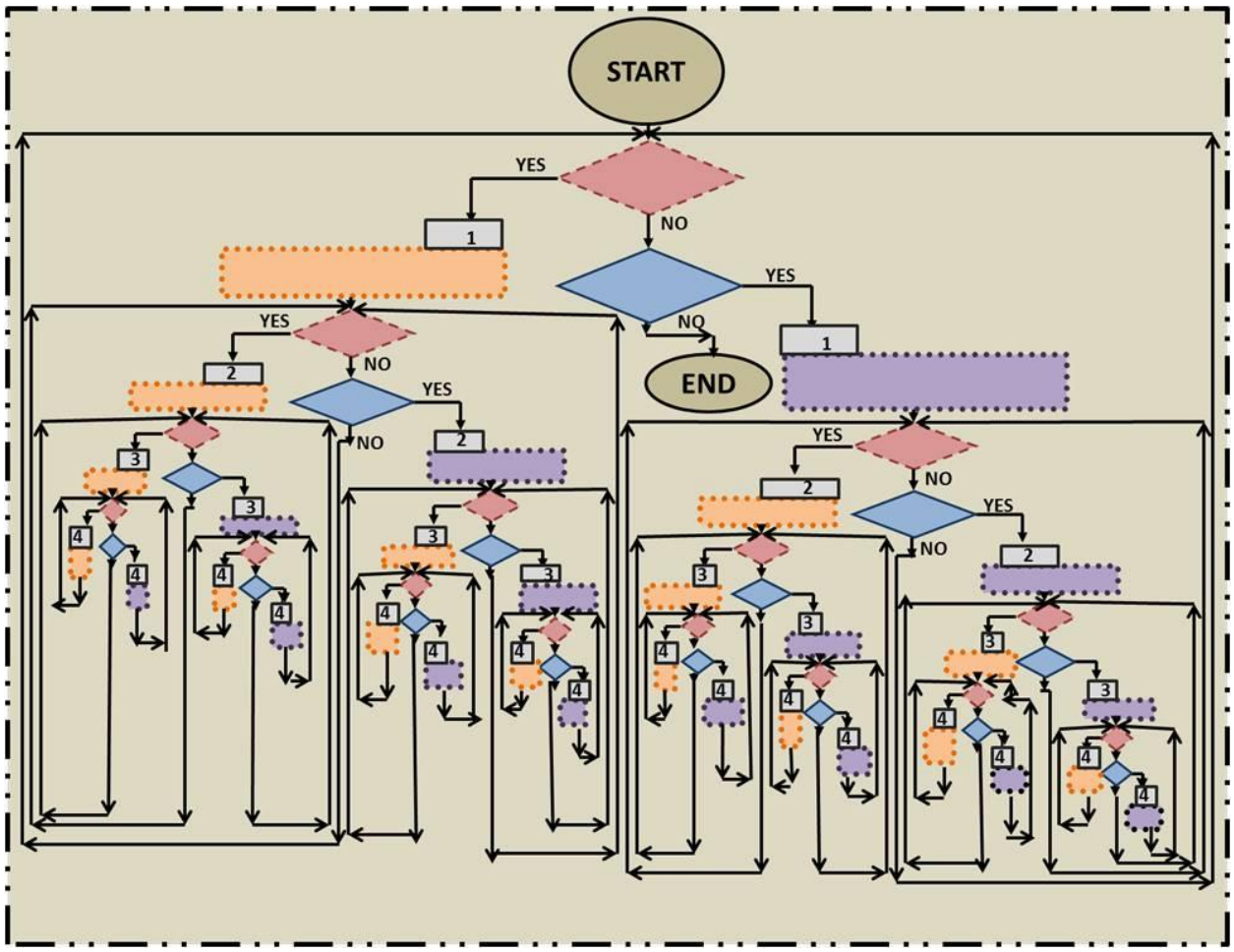

Figure 3.6 Algorithm for diagonalization of $n \times n$-dimensional matrices $\left(\tilde{\mathbf{K}}_1 - \tilde{\mathbf{K}}_{\mathrm{RL1}}\right) + \left[a_\mu \tilde{\mathbf{K}}_{\mathrm{R1}} + \left(a_1 a_2 \ldots a_\mu\right) \tilde{\mathbf{K}}_{\mathrm{L1}} \right]$ appearing in the recursive scheme and for finding the contribution of these matrices to the eigenvalues and eigenvectors of $\tilde{\mathbf{K}}_{2^\nu}$. Recursive scheme is shown here for ν=5. The contents of the colored boxes and diamonds are further explained in Figure 3.7.

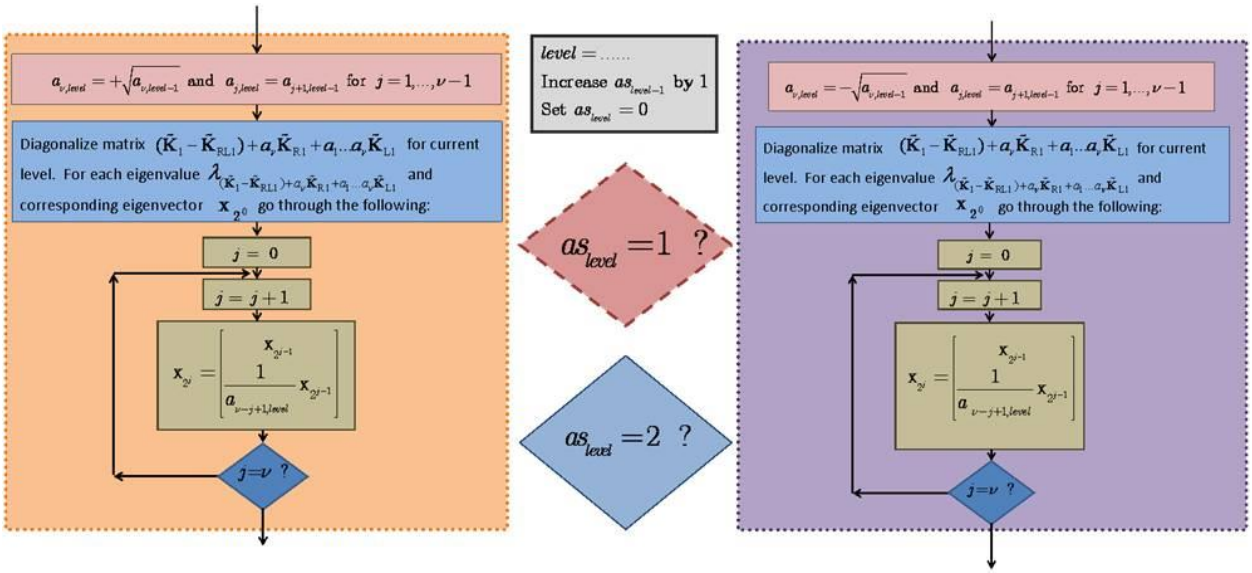

Figure 3.7 Details of the algorithm for finding all the eigenvectors and eigenvalues contributed to $\tilde{\mathbf{K}}_{2^\nu}$ from $n \times n$ matrices $\left(\tilde{\mathbf{K}}_1 - \tilde{\mathbf{K}}_{\mathrm{RL1}}\right) + \left[a_\mu \tilde{\mathbf{K}}_{\mathrm{R1}} + \left(a_1 a_2 \ldots a_\mu\right)\tilde{\mathbf{K}}_{\mathrm{L1}}\right]$

according to the recursive scheme described in the theory section. The boxes and diamonds should be inserted in all similarly colored and bordered boxes and diamonds appearing in the flow diagram of Figure 3.6, at all levels of recursion indicated in that figure. The index as_{level} is a decision variable indicating whether a plus or minus sign will be used in forming the coefficient a_ν for the current level of recursion from the corresponding coefficient of the previous level, or whether the calculation has been completed for the current level.

3.3. Calculation of diffusivity in a spatially periodic medium

3.3.1. Setup of the diffusion problem

We now apply Direct Diagonalization of the rate constant matrix $\tilde{\mathbf{K}}_{2^\nu}$ and MESoRReD to the problem of unidimensional diffusion in a periodic medium. Our objective is to calculate the diffusivity along a particular direction from microscopic information concerning the geometrical arrangement of sorption sites in a unit cell and the rate constants for jumps between the sites.

The particular system on which we focus our attention consists of an array of 2^ν unit cells ($\nu >> 1$) arranged along the l-direction, along which diffusion will be studied. (In the application considered below, l will be x, y, or z.) Periodic boundary conditions hold

between the left and right extremities of the array, as well as in the two transverse directions. Let L_d be the length of a unit cell along the l-direction and $2L_p = 2^{\nu} L_d$ be the length of the entire array of unit cells (see Figure 3.3). We determine the diffusivity along l by studying the response of the system to a transient experiment. Initially, all mass is placed in the two central unit cells, i.e. cells $2^{\nu-1}$ and $2^{\nu-1}+1$ in Figure 3.3. The initial probability of occupancy of each state in each of these cells will be proportional to the state's equilibrium probability. In other words, the initial probability distribution among states is:

$$P_i(0) = \begin{cases} \dfrac{1}{2}\dfrac{P_i^{\text{eq}}}{\sum_{j=1}^{n} P_j^{\text{eq}}}, & \text{if } i \in \text{cell } 2^{\nu-1} \text{ or cell } 2^{\nu-1}+1 \\ 0, & \text{otherwise} \end{cases} \qquad \text{Eq. (3.31)}$$

The time-dependent probabilities of all states, $P_i(t)$, are then calculated based on the MESoRReD scheme developed in Section 3.2 for solving the master equation, Eq. (3.6), up to a maximum time $t_{\max}$. A flow sheet for this calculation is given in Figure 3.8.

As a test for the analytically based MESoRReD, we also solve the master equation numerically, as a set of first-order differential equations constituting an initial value problem, using the Euler method (see below).

3.3.2. Continuum formulation of the diffusion problem

The diffusivity along direction l (l=x, y, or z) will be computed by matching the evolving probability profiles for the transient diffusion problem described above with the corresponding solution of the continuum diffusion equation.[80] For convenience, we place l=0 at the interface between unit cells $2^{\nu-1}$ and $2^{\nu-1}+1$ of Figure 3.3. In the continuum formulation we speak of a probability density $\rho_{\text{cell}}(l,t)$, resolved at the level of entire unit cells. This probability density is related to the discrete probabilities of the previous section by:

$$\rho_{\text{cell}}(l,t) = \frac{P_{\text{cell},l}(t)}{L_d} = \frac{1}{L_d} \sum_{\substack{i \in \text{unit cell} \\ \text{centered at } l}} P_i(t) \qquad \text{Eq. (3.32)}$$

The probability density $\rho_{\text{cell}}(l,t)$ evolves according to the diffusion equation:

$$\frac{\partial \rho_{\text{cell}}}{\partial t} = D \frac{\partial^2 \rho_{\text{cell}}}{\partial l^2} \qquad \text{Eq.(3.33)}$$

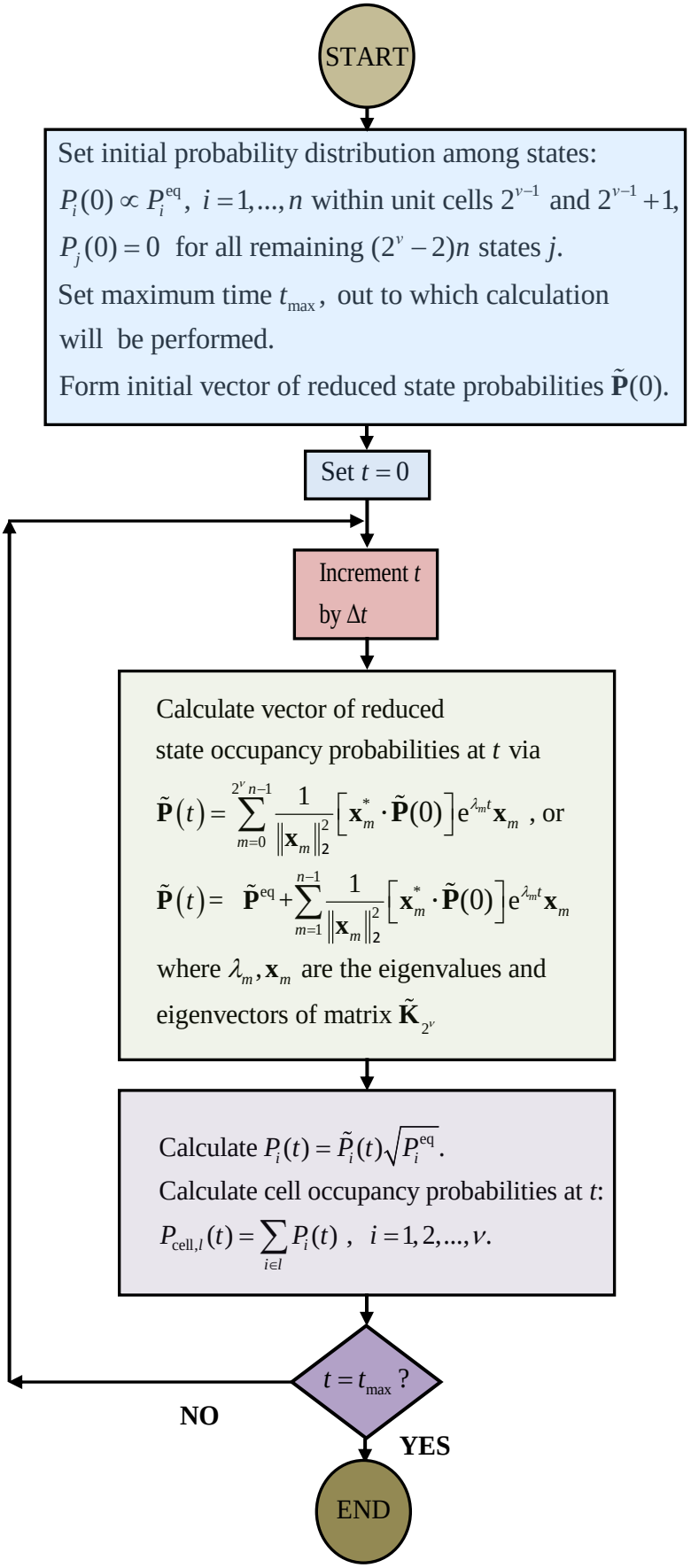

Figure 3.8 Algorithm for calculating the probability density profile for one-dimensional diffusion based on the MESoRReD scheme.

where D is the diffusivity along the l direction. The function $\rho_{\text{cell}}(l,t)$ obeys the boundary conditions:

$$\rho_{\text{cell}}(L_p,t)=\rho_{\text{cell}}(-L_p,t),\ \text{and}\ \left.\frac{\partial\rho_{\text{cell}}}{\partial l}\right|_{L_p,t}=\left.\frac{\partial\rho_{\text{cell}}}{\partial l}\right|_{-L_p,t} \qquad \text{Eq. (3.34)}$$

and the initial condition:

$$\rho_{\text{cell}}(l,0)=\begin{cases}\dfrac{1}{2L_d}, & -L_d\le l\le L_d\\ 0, & \text{otherwise}\end{cases} \qquad \text{Eq. (3.35)}$$

With this initial condition, the profile $\rho_{\text{cell}}(l,t)$ evolves so as to remain symmetric around l=0 and $\partial\rho_{\text{cell}}/\partial l$ equals zero at $l=-L_p,0,$ and L_p at all times.

As shown in Appendix F, the solution to the continuum diffusion problem of Eqs. (3.33) to (3.35) is:

$$\rho_{\text{cell}}(l,t)=\frac{1}{2L_p}+\left(\sum_{f=1}^{+\infty}\frac{\sin\left(\dfrac{f\pi L_d}{L_p}\right)}{f\pi L_d}\cos\left(\frac{f\pi l}{L_p}\right)e^{-D\left(\frac{f\pi}{L_p}\right)^2 t}\right) \qquad \text{Eq. (3.36)}$$

For short times ($t << L_p^2/D$) , a large number of terms (f>>1) is required in Eq. (3.36) to obtain accurate results. For such times an excellent approximation of the solution is provided by the solution to the problem of unidimensional diffusion into an infinite medium starting from the initial probability density of Eq. (3.35). In that problem, the boundary conditions of Eq. (3.34) are replaced by the conditions:

$$\lim_{l\to+\infty}\rho_{\text{cell}}(l,t)=\lim_{l\to-\infty}\rho_{\text{cell}}(l,t)=0 \qquad \text{Eq. (3.37)}$$

The solution to the problem of Eqs. (3.33), (3.35), and (3.37) is:[79]

$$\rho_{\text{cell}}(l,t)=\frac{1}{4L_d}\left(\text{erf}\left(\frac{L_d+l}{2\sqrt{Dt}}\right)+\text{erf}\left(\frac{L_d-l}{2\sqrt{Dt}}\right)\right) \qquad \text{Eq. (3.38)}$$

with erf(x) being the error function of x.

On the other hand, for $t << L_p^2/D$ and $|l|>>L_d$, a reasonable approximation to Eq. (3.38), and therefore, to Eq. (3.36), is provided by the solution to the problem of unidimensional diffusion in an infinite medium starting from an initial probability density profile[81,82] that has the form of a delta function in l. That problem is comprised of the partial differential Eq. (3.33), the boundary conditions of Eq. (3.37) and the initial condition

$$\rho_{\text{cell}}(l,0)=\delta(l) \qquad \text{Eq. (3.39)}$$

The solution to this problem is

$$\rho_{\text{cell}}(l,t) = \frac{1}{4\pi Dt}^{1/2} \exp\left(\frac{l^2}{4Dt}\right) \qquad \text{Eq. (3.40)}$$

In the iterative schemes used below to fit solutions of the discrete master equation to the corresponding solution of the continuum diffusion problem, Eq. (3.40) will be employed as a basis for obtaining an initial estimate of the diffusivity from the probability density at the origin, as

$$D \approx \frac{1}{4\pi t\left[\frac{\rho_{\text{cell}}(-L_d/2,t)+\rho_{\text{cell}}(L_d/2,t)}{2}\right]^2} \qquad \text{Eq. (3.41)}$$

where the approximation

$$\rho_{\text{cell}}(0,t) = \frac{\rho_{\text{cell}}(-L_d/2,t)+\rho_{\text{cell}}(L_d/2,t)}{2} \qquad \text{Eq. (3.42)}$$

has been invoked. The probability density values $\rho_{\text{cell}}(-L_d/2,t)$ and $\rho_{\text{cell}}(L_d/2,t)$ are obtained from the total probabilities of occupancy of unit cells 2^{v-1} and $2^{v-1}+1$, respectively, via Eq. (3.32).

3.3.3. Fitting of continuum solution to the solution of the master equation

Values of the diffusivity D in the l-direction are obtained by fitting the solution for $\rho_{\text{cell}}(l,t)$ from the continuum formulation, Eq. (3.36), and its short-time approximation, Eq. (3.38), to the profile of values $\rho_{\text{cell}}(l,t)$ in all unit cells of the system obtained from the solution of the master equation for the evolution of state probabilities via Eq. (3.32). The algorithm used to perform this fitting (nonlinear regression) is outlined in Figure 3.9. As seen from the algorithm, a separate estimate for the diffusivity, $D(t)$, is obtained at each time t through the nonlinear regression. The Gaussian solution, Eq. (3.40), is employed to obtain an initial guess $D_{\text{guess}}(t)$ for the diffusivity at each time. The discreteness of the network of states is expected to have a strong effect on the solution to the master equation at short times, when only a few states are populated. At longer times, however, $D(t)$ is expected to fluctuate around a constant asymptotic value. The mean of $D(t)$ extracted from the fit is taken as our best estimate of D in the studied direction, while the standard deviation of these values is taken as an estimate of the error in estimating D from the master equation results.

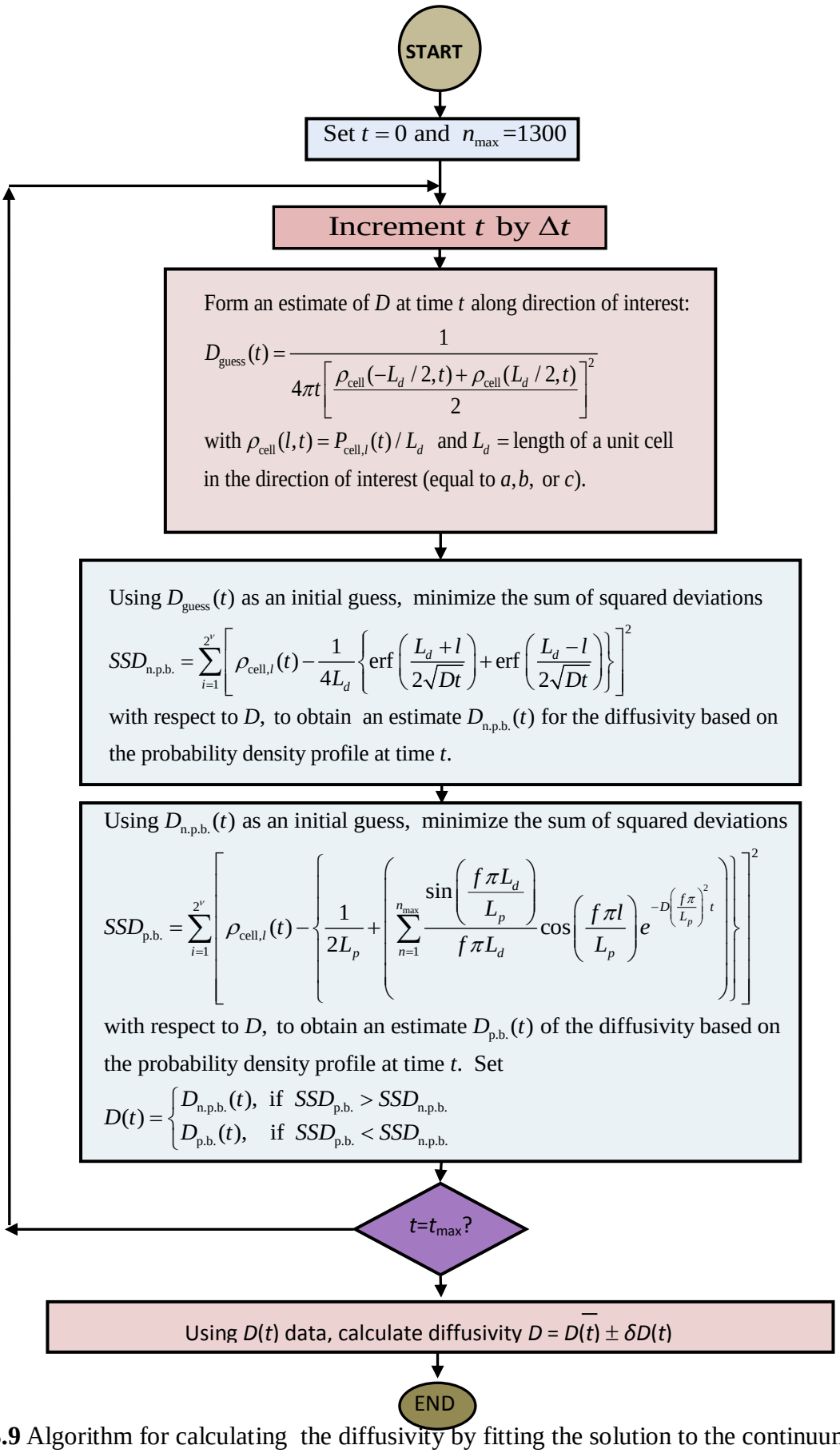

Figure 3.9 Algorithm for calculating the diffusivity by fitting the solution to the continuum diffusion equation to the probability density profile from MESoRReD.

Fitting the continuum solution to the master equation is not necessary for obtaining the diffusivity, however. As shown below, D can be obtained directly from the spectrum of eigenvalues of matrix $\tilde{\mathbf{K}}_{2^v}$ computed via MESoRRED through a term-by-term comparison of the arguments of the exponentials appearing in the solution to the master equation, Eq. (3.7), and the continuum solution, Eq. (3.36).

3.4. Application to the diffusion of Xenon in Silicalite-1

3.4.1. Brief description of the system and setup of transition rate constant matrices

The zeolite silicalite-1 is a microporous crystalline material whose unit cell has the chemical constitution $Si_{96}O_{192}$. Calculations here will be conducted with its orthorhombic form, which has lattice parameters (edge lengths of the unit cell) a= 20.07Å, b=19.92Å, and c=13.42Å along the x, y, and z directions respectively. This zeolite is of great importance in separation applications.[83] It possesses two intersecting systems of channels, both of diameter around 5.5Å: Straight channels, which run along the b crystallographic axis (y-direction), and sinusoidal or zig-zag channels, which run along the a crystallographic axis (x-directions). The channel systems come together at intersections, which are more spacious (diameter around 9Å). Xenon (Xe) is one of the simplest molecules whose diffusion has been studied in silicalite-1, both experimentally and theoretically. Molecular dynamics simulations of Xe in silicalite-1 at a variety of temperatures and occupancies, as well as a Transition State Theory-based analysis of its diffusion at low temperature and low occupancy, have been conducted by June et al.[84,62] Here we apply our MESoRReD method to Xe in a periodic array of unit cells of silicalite using the TST-based model developed by June et al.[62] This offers us the advantage of immediate comparability of our results against theirs, in terms of diffusivity values obtained, memory (RAM) and central processor unit (CPU) time required.

In the work of June et al.,[84,62] silicalite was considered as rigid and its interaction with Xe was described as a sum of Lennard-Jones potentials between each oxygen in its framework and the Xe molecule. These authors conducted a thorough analysis of the potential energy hypersurface experienced by Xe within the zeolite as a function of its three translational degrees of freedom, identified states and transitions between them, and computed rate constants $k_{i\to j}$ for all transitions using Transition State Theory with and without dynamical corrections.[62] Our study will be conducted at 150K and will employ the

dynamically uncorrected transition state theory-based rate constants of June et al. Although these values are expected to provide a less realistic (too high) estimate for the diffusivity than the dynamically corrected ones,[84,62] they are adopted here because they (or, more precisely, their inverses $\tau_{ij}^{TST} = 1/k_{i\to j}$) are reported in full detail in Table 3.4 of June et al.'s paper,[62] allowing reproduction of the diffusivity calculations presented in that paper.

June et al.'s[62] analysis led to the identification of n=12 sorption states per unit cell for Xe in silicalite-1 at very low loading. These fall in three categories: states in the interior of straight channel segments (S), states in the interior of sinusoidal, or zig-zag, channel segments (Z), and states inside intersections (I). There are four states of each category in a unit cell, as a result of the P*nma* symmetry of the considered silicalite crystal. The spatial arrangement of these states in a unit cell is shown in Figure 3.10, based on Ref. 62.

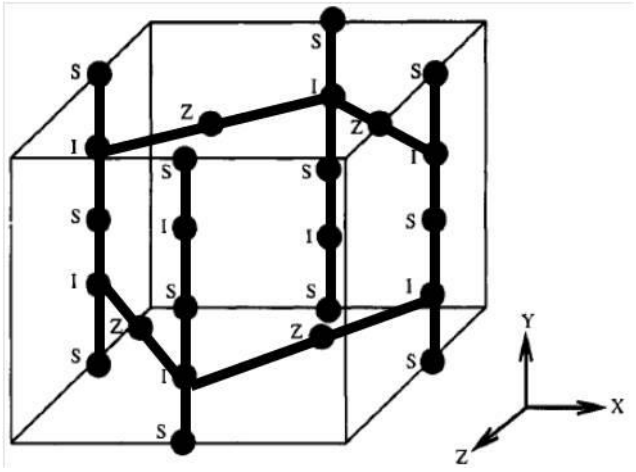

Figure 3.10 Schematic outline of the pore structure of a unit cell of silicalite. Spheres represent the three types of sorption states (Z = sinusoidal-channel state, S = straight-channel state, and I = intersection state) on the zeolite-sorbate potential hypersurface. The thick lines provide a rough depiction of the axes of straight and sinusoidal (zig-zag) channels.

For Xe, which is a small molecule, Z and I states are more favorable, since they allow the sorbed molecule to maximize its attractive dispersive interactions with the surrounding zeolite framework. I states, corresponding to the more spacious intersections, are less favorable. The equilibrium probabilities of occupancy of the three types of states are shown in Table 3.1.

Table 3.1: Corrected Equilibrium Probabilities[62] for Sorption States of Xenon in Silicalite-1 at 150K

$P_{\mathrm{I}}^{\mathrm{eq}}$	$P_{\mathrm{S}}^{\mathrm{eq}}$	$P_{\mathrm{Z}}^{\mathrm{eq}}$
0.014	0.412	0.574

There is a rich connectivity among the states. Apart from I to S and I to Z transitions and their inverses, there are direct transitions between S and Z states which circumvent the intersection regions, as defined in Ref. 62. There are eleven distinct types of transitions. These types, and their associated rate constants, taken from Table 3.4 of Ref. 62, are shown in Table 3.2.

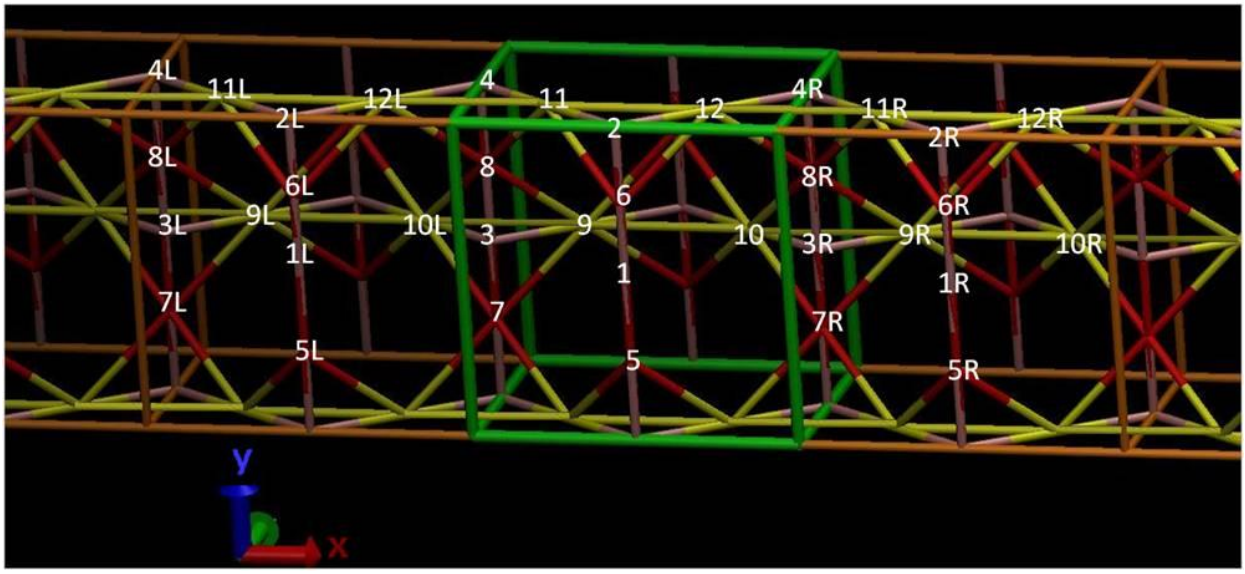

Figure 3.11 Transitions of xenon in silicalite-1, depicted as straight lines in three-dimensional space. Red color shows S (straight channel) states, yellow color shows Z (zig zag channel) states, pink color shows I (intersection) states. Green box defines the borders of one unit cell. Orange color shows the borders of cells along the *x* axis.

Figure 3.11 provides a pictorial depiction of the spatial arrangement of sorption states 1-12 in a central unit cell (outlined with green borders) and of the periodic images of these states within adjacent unit cells located to the right (R) and to the left (L) of the central unit cell. The numbering of states adopted here is different from that of June et al.[62] Here states 1-4 are

I states; states 5-8 are S states; and states 9-12 are Z states. Figure 3.11 also shows the network of transitions as a set of straight line segments connecting the states.

Each I, S, and Z state is connected to another 4, 6, and 8 states, respectively. Thus, there are 72 transitions per unit cell where forward and reverse transitions are counted separately. The third column of Table 3.2 summarizes all transitions originating or terminating in states of the central unit cell; to each of these transitions a type and a rate constant are assigned in the first and second columns of Table 3.2. The rate constants of Table 3.2, along with the equilibrium occupancy probabilities of Table 3.1, are used in forming the 12×12 matrix $\tilde{\mathbf{K}}_1$ as well as the 12×12 matrices $\tilde{\mathbf{K}}_{\mathrm{L1}}$ and $\tilde{\mathbf{K}}_{\mathrm{R1}} = \tilde{\mathbf{K}}_{\mathrm{L1}}{}^{\mathrm{T}}$ for transport in the *x* (considered in Figure 3.11), *y*, and *z* directions. However, we first must check if the rates of Table 3.2 satisfy the equations of microscopic reversibility (Eq. (3.2)). If this does not happen, then $\tilde{\mathbf{K}}_{2^\nu}$ will not be symmetric, resulting in accumulation of error in the eigenvalue and eigenvector calculation. To overcome this obstacle, we first find how many types of states we have in the system we examine. In our case, we have 3. This means that we have to calculate the 3 equilibrium probabilities ($P_{\mathrm{S}}^{\mathrm{eq}}, P_{\mathrm{Z}}^{\mathrm{eq}}, P_{\mathrm{I}}^{\mathrm{eq}}$), while we already know that $P_{\mathrm{S}}^{\mathrm{eq}} + P_{\mathrm{Z}}^{\mathrm{eq}} + P_{\mathrm{I}}^{\mathrm{eq}} = 1$ within a unit cell. So, we need just 2 microscopic reversibility equations to calculate the 3 probabilities at equilibrium. We arbitrarily chose the rates of $\mathrm{I} \to \mathrm{S}$, $\mathrm{S} \to \mathrm{I}$, $\mathrm{I} \underset{a}{\to} \mathrm{Z}$, $\mathrm{Z} \underset{a}{\to} \mathrm{I}$ transitions reported by June et al.[62] as a basis for our calculations and used them in 2 equations of microscopic reversibility. From this process we found the probabilities listed in Table I, which are slightly different from the probabilities reported by June et al.[62] Next, we arbitrarily chose the $\mathrm{I} \underset{b}{\to} \mathrm{Z}$, $\mathrm{Z} \underset{b}{\to} \mathrm{S}$, $\mathrm{S} \underset{a}{\to} \mathrm{Z}$ rate constants reported by June et al.[62] as a basis for calculating all remaining rate constants. The refined rate constants obtained in this way are listed in Table 3.2.

Table 3.2: Rate Constants[62] for Interstate Transitions of Xenon in Silicalite at 150K

Type of Transitions	**Rate constant (s^{-1})** $k_{i\to j} = \frac{1}{\text{time constant } \tau_{ij}^{TST}}$	**Transitions**
$I \to S$	1.309×10^{11}	$1\to5,\ 1\to6,\ 2\to5,\ 2\to6,$ $3\to7,\ 3\to8,\ 4\to7,\ 4\to8$
$S \to I$	4.444×10^{9}	$5\to1,\ 5\to2,\ 6\to1,\ 6\to2,$ $7\to3,\ 7\to4,\ 8\to3,\ 8\to4$
$I \underset{a}{\to} Z$	2.958×10^{10}	$1\to9,\ 2\to12,\ 3\underset{L}{\to}10,\ 4\to11$
$Z \underset{a}{\to} I$	7.241×10^{8}	$9\to1,\ 10\underset{R}{\to}3,\ 11\to4,\ 12\to2$
$I \underset{b}{\to} Z$	1.501×10^{10}	$1\to10,\ 2\to11,\ 3\to9,\ 4\underset{L}{\to}12$
$Z \underset{b}{\to} I$	3.673×10^{8}	$9\to3,\ 10\to1,\ 11\to2,\ 12\underset{R}{\to}4$
$S \underset{a}{\to} Z$	3.974×10^{8}	$5\to9,\ 6\to9,\ 7\underset{L}{\to}10,\ 8\underset{L}{\to}10,$ $7\to11,\ 8\to11,\ 5\to12,\ 6\to12$
$Z \underset{a}{\to} S$	2.853×10^{8}	$9\to5,\ 9\to6,\ 10\underset{R}{\to}7,\ 10\underset{R}{\to}8,$ $11\to7,\ 11\to8,\ 12\to5,\ 12\to6$
$S \underset{b}{\to} Z$	8.570×10^{8}	$5\to10,\ 5\to11,\ 6\to10,\ 6\to11,$ $7\to9,\ 7\underset{L}{\to}12,\ 8\to9,\ 8\underset{L}{\to}12$
$Z \underset{b}{\to} S$	6.150×10^{8}	$10\to5,\ 11\to5,\ 10\to6,\ 11\to6,$ $9\to7,\ 12\underset{R}{\to}7,\ 9\to8,\ 12\underset{R}{\to}8$
$Z \to Z$	9.737×10^{8}	$9\to10,\ 9\underset{L}{\to}10,\ 10\to9,\ 10\underset{R}{\to}9,$ $11\to12,\ 11\underset{L}{\to}12,\ 12\to11,\ 12\underset{R}{\to}11$

I *represents a channel intersection,* S *represents a straight channel,* Z *represents a sinusoidal channel state. The indices under the arrows label the route of the transition from a state i to a state j .*

3.4.2. Application of the recursive reduction method

We chose to work with 2^7(=128) cells in a row along the *a*, *b*, or *c* crystallographic directions (v=7) and applied MESoRReD (Figures 3.4-3.8) and direct diagonalization (DD) of $\tilde{\mathbf{K}}_{2^v}$, along with fitting to the solution of the corresponding continuum diffusion problem (Figure 3.9). The diffusivity in each of the three directions was extracted from the temporal evolution of the occupancy probabilities of states, starting from the initial probability distribution of Eq. (3.31). A periodic system consisting of 128 cells in a row was considered long enough to be described satisfactorily by the continuum diffusion problem, Eqs. (3.33) – (3.35), at long times. Evidence that this is true is provided below.

All diagonalizations required in our recursive reduction algorithm were performed with the appropriate IMSL[85,86] and LAPACK[87] subroutines. From IMSL we used:
a) the DRLIN[85] subroutine to find the diffusivity which minimized the sum of square deviations as shown in Figure 3.9; b) the DEVCCG[86] subroutine for calculation of eigenvalues and eigenvectors of a complex or real general matrix ; c) the DEPICG[86] subroutine for calculating a performance index, as defined in Eq. (3.43). From LAPACK we used the ZGEEV[87] routine for eigenvalue and eigenvector calculation of a complex or real general matrix . For DD we used the IMSL routine DEVCSF which calculates the eigenvalues and the eigenvectors of a symmetric matrix. We note here that we use DEVCCG instead of DEVCSF because the matrices appearing in MESoRReD are not necessarily symmetric. We also used the PGPLOT library to plot the occupancy probability profile for different times and assess the fitting process visually (see Figure 3.12). DEVCCG, ZGEEV and DEVCSF have in common that they use the QR method.[88] Unfortunately, these routines invoke a default tolerance for convergence of the calculations. As shown in the work of Ma et al,[89] the tolerance sets the CPU time. Given that the tolerance is common, we expect that MESoRReD and DD will compute eigenvalues with the same or very similar accuracy. We can use the routine estimate for the zero eigenvalue of $\tilde{\mathbf{K}}_1, \tilde{\mathbf{K}}_{2^7}$ as a criterion for the accuracy of our diagonalizations. IMSL and LAPACK routines give -105.37 s^{-1} instead of zero for this eigenvalue (worse accuracy than MATLAB R2009b-see below); this is actually satisfactorily close to zero, if one considers that the eigenvalue of largest absolute value is –3.140 $\times 10^{11}$ s^{-1}.

The eigenvalues determined for the $n\times n$=12×12 matrices $\tilde{\mathbf{K}}_1$, $\tilde{\mathbf{K}}_1 - 2\tilde{\mathbf{K}}_{\mathrm{RL1}}$, and $(\tilde{\mathbf{K}}_1 - \tilde{\mathbf{K}}_{\mathrm{RL1}}) + a_\nu \tilde{\mathbf{K}}_{\mathrm{R1}} + a_1 ... a_\nu \tilde{\mathbf{K}}_{\mathrm{L1}}$ via the IMSL routine exhibited an absolute deviation of less than $10^{-3}\mathrm{s}^{-1}$ from those determined via the LAPACK routines, while the eigenvalue of smallest absolute value was $-5.8105\times10^{5}\mathrm{s}^{-1}$. This similarity of results between IMSL and LAPACK is reflected in the eigenvalue spectra obtained for $\tilde{\mathbf{K}}_{2^\nu}$ via MESoRReD and shown in Figure 3.12a,b. The eigenvalues determined by DD of the $2^\nu n\times 2^\nu n$=1536×1536 matrix $\tilde{\mathbf{K}}_{2^\nu}$ via the IMSL routines (Figure 3.13c) exhibited a maximum absolute deviation of 1.03×10^{-3} s^{-1} from the eigenvalues determined using MESoRReD. We note here that, if the rate constants of Table 3.2 did not satisfy microscopic reversibility exactly, then DD would incur a very large error; in other words, DD exhibits extreme sensitivity to microscopic reversibility. On the other hand, MESoRReD, which merely diagonalizes 12×12 matrices, is much less sensitive to how well the condition of microscopic reversibility is satisfied. This robustness to small deviations from microscopic reversibility is a significant advantage of MESoRReD relative to DD as a method for solving the master equation of the spatially periodic system.

As an additional check of the accuracy of numerical diagonalizations provided by the IMSL and LAPACK routines, we have calculated the Perfomance Index as

$$PI = \max_{1\le j\le M} \frac{\left\| \mathbf{A}\cdot\mathbf{x}_j - \lambda_j \mathbf{x}_j \right\|_2}{M\ \varepsilon \left\|\mathbf{A}\right\|_2 \left\|\mathbf{x}_j\right\|_2} \qquad \text{Eq. (3.43)}$$

where M is dimensionality of the matrix $\mathbf{A}$ whose eigenvalues λ and eigenvectors $\mathbf{x}$ we calculate and $\|\ \|_2$ symbolizes the Euclidean norm of a matrix. The machine precision ε is an upper bound on the relative error due to rounding in floating point arithmetic. In our case, ε is 1.192×10^{-7}. We have found that PI<1 for the $n\times n$=12×12 matrices $\tilde{\mathbf{K}}_1$, $\tilde{\mathbf{K}}_1 - 2\tilde{\mathbf{K}}_{\mathrm{RL1}}$, and $(\tilde{\mathbf{K}}_1 - \tilde{\mathbf{K}}_{\mathrm{RL1}}) + a_\nu \tilde{\mathbf{K}}_{\mathrm{R1}} + a_1 ... a_\nu \tilde{\mathbf{K}}_{\mathrm{L1}}$ involved in MESoRReD, which indicates excellent numerical performance.[86] The Performance Index applied to $\tilde{\mathbf{K}}_{2^7}$ with the eigenvalues and eigenvectors obtained from MESoRReD is 32.2, indicating merely good performance. We attribute this to loss of accuracy in the recursive calculations invoked for finding the eigenvectors. The Performance Index for DD of $\tilde{\mathbf{K}}_{2^7}$, on the other hand, is 1.568×10^{-2}, indicating that DD of a strictly symmetric $\tilde{\mathbf{K}}_{2^7}$ can yield better performance than MESoRReD in the calculation of eigenvectors. An additional criterion of performance in the

diagonalization of $\tilde{\mathbf{K}}_{2^7}$ is the sum of square deviations (SSD) obtained at the end of the regression process described in Figure 3.9. Worst case values for this SSD for times between $t_{\text{initial}}=10^{-8}$s and $t_{\max}=2\times10^{-5}$s using either MESoRReD or DD to diagonalize $\tilde{\mathbf{K}}_{2^7}$ were on the order of 10^{-10} Å^{-2}.

All eigenvalues were computed in units of s^{-1}, while all eigenvectors were dimensionless. The routines we used for the diagonalization of small matrices yielded complex eigenvalues, where the absolute value of the imaginary part was lower than the absolute value of the real part by a factor of at least 10^6, confirming that the eigenvalues are real, as theoretically expected from the symmetry of $\tilde{\mathbf{K}}_{2^\nu}$. Most of the eigenvectors computed for matrices of the type $(\tilde{\mathbf{K}}_1-\tilde{\mathbf{K}}_{\text{RL1}})+a_\nu\tilde{\mathbf{K}}_{\text{R1}}+a_1...a_\nu\tilde{\mathbf{K}}_{\text{L1}}$ (Figure 3.7) contained complex elements. Upon using all computed eigenvectors and eigenvalues within Eq. (3.7), however, the absolute value of the complex part of the state occupancy probabilities was lower than the absolute value of the real part of the same probabilities by a factor of more than 10^{11}. This indicates that the computed state and, therefore, unit cell [compare Eq. (3.32)] probabilities are practically real numbers, providing additional evidence for the validity and accuracy of the MESoRReD approach.

MESoRReD significantly reduces the CPU time required for calculation of the eigenvectors of $\tilde{\mathbf{K}}_{2^7}$. The calculation of the eigenvalues and the eigenvectors of $\tilde{\mathbf{K}}_{2^7}$ by DD demands 35.12 s of CPU time on the machine we have used (see below), in addition to being very sensitive to the exact symmetry of $\tilde{\mathbf{K}}_{2^7}$, as discussed above. Of this CPU time, 4.51 s goes to the calculation of eigenvalues. On the other hand, MESoRReD requires 0.14 CPU s to compute the eigenvalues and eigenvectors of $\tilde{\mathbf{K}}_{2^7}$, of which less than 0.0059 CPU s goes to the calculation of eigenvalues. The number of arithmetic operations needed for calculating the eigenvalues of an $M\times M$ symmetric matrix scales as $\mathcal{O}(M^2)$ with the matrix dimension M when M is large, while we need $\mathcal{O}(M^3)$ operations to calculate the eigenvalues of a large $M\times M$ general matrix.[88] We remind the reader that the recursive scheme of MESoRReD involves the diagonalization of $2^{\nu-1}$ in general non-symmetric matrices of dimension $n\times n$, instead of a single symmetric $(2^\nu n)\times(2^\nu n)$ matrix. The time required by MESoRReD to calculate the eigenvalues is by a factor of 765 lower than the time required for DD. This ratio is significantly larger than the factor $(2^\nu n)^2/2^{\nu-1}\,n^3 = 2^{\nu+1}/n = 21$ expected from scaling assuming the same prefactors.

The state occupancy probability profile was calculated from the eigenvalues and eigenvectors of $\tilde{\mathbf{K}}_{2^7}$ as outlined in Figure 3.8 from $t_{initial}=10^{-8}$s to $t_{max}=2\times10^{-5}$s with step $\Delta t=10^{-8}$s . For $t>t_{max}$, $\rho_{cell}(l=0) - \rho_{cell}(l=L_p) < 10^{-5}$Å^{-1}. Beyond t_{max} the system is practically at equilibrium and it is impossible to obtain an accurate estimate of the diffusion coefficient by fitting the profile to the solution of the continuum diffusion equation. Fitting of the probability density profile to extract a diffusivity at every time examined followed the algorithm outlined in Figure 3.9. The SSD at the minimum oscillates in the area of 10^{-10}Å^{-2}. Performing the fitting for a specific time requires 2.69 CPU s on the machine we have used (see also Table 3.3).

Probability density profiles calculated from our recursive reduction method at times of 10^{-8}s, 2×10^{-8}s and 4×10^{-8}s are shown in Figure 3.14 with the colored points. The symmetry of the profiles in Figure 3.12 around $l=0$ is a criterion for success of the calculations. Lines drawn through each set of points with the same color display the fittings with the solution to the continuum diffusion equation. All three profiles along each direction yielded the same value for the diffusion coefficient along that direction. These values are listed in the sixth row of Table 3.4 (row labeled "MESoRReD-TST").

Setting up the matrices $\tilde{\mathbf{K}}_1$,$\tilde{\mathbf{K}}_{L1}$ is a prerequisite for applying MESoRReD. The effort required of an experienced user of the code to do this is very small. In fact, only half of the elements of these matrices need be declared, the other half being calculable via the microscopic reversibility condition, Eq. (3.2).

The FORTRAN program we have developed to implement MESoRReD required 42MB of RAM. All calculations reported in this paper were undertaken on a personal computer with the following characteristics:

a) Intel Celeron CPU E200 at 2.40 GHz

b) 1.99GB RAM

c) Microsoft Windows XP Professional, Version 2002, Service Pack 3

d) Compaq Visual Fortran Version 6.6

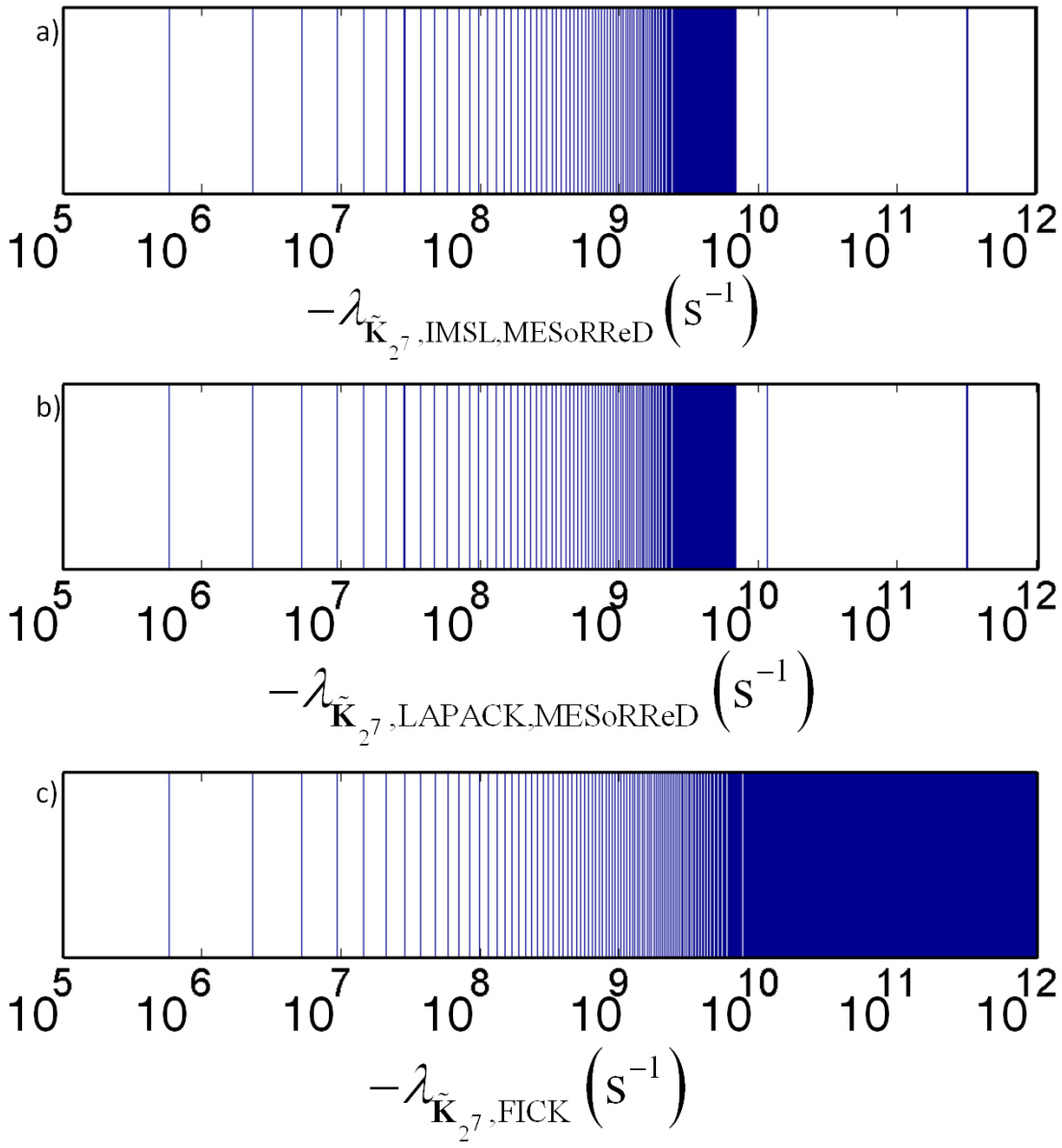

Figure 3.12 Spectrum of eigenvalues λ in the 128 unit cell system [see Eq. (3.7)] for diffusion in the x direction using a) MESoRReD and the IMSL routine; b) MESoRReD and the LAPACK routine. c) Factors $-\lambda_{\mathrm{FICK}} = D_{xx}(f\pi/L_p)^2$, f=1, 2, … multiplying time within the exponentials in the macroscopic solution to the diffusion equation, Eq. (3.36), for D_{xx}= $9.7132\times10^{-10}\,\frac{\mathrm{m}^2}{\mathrm{s}}$. The value λ=0 is not included.

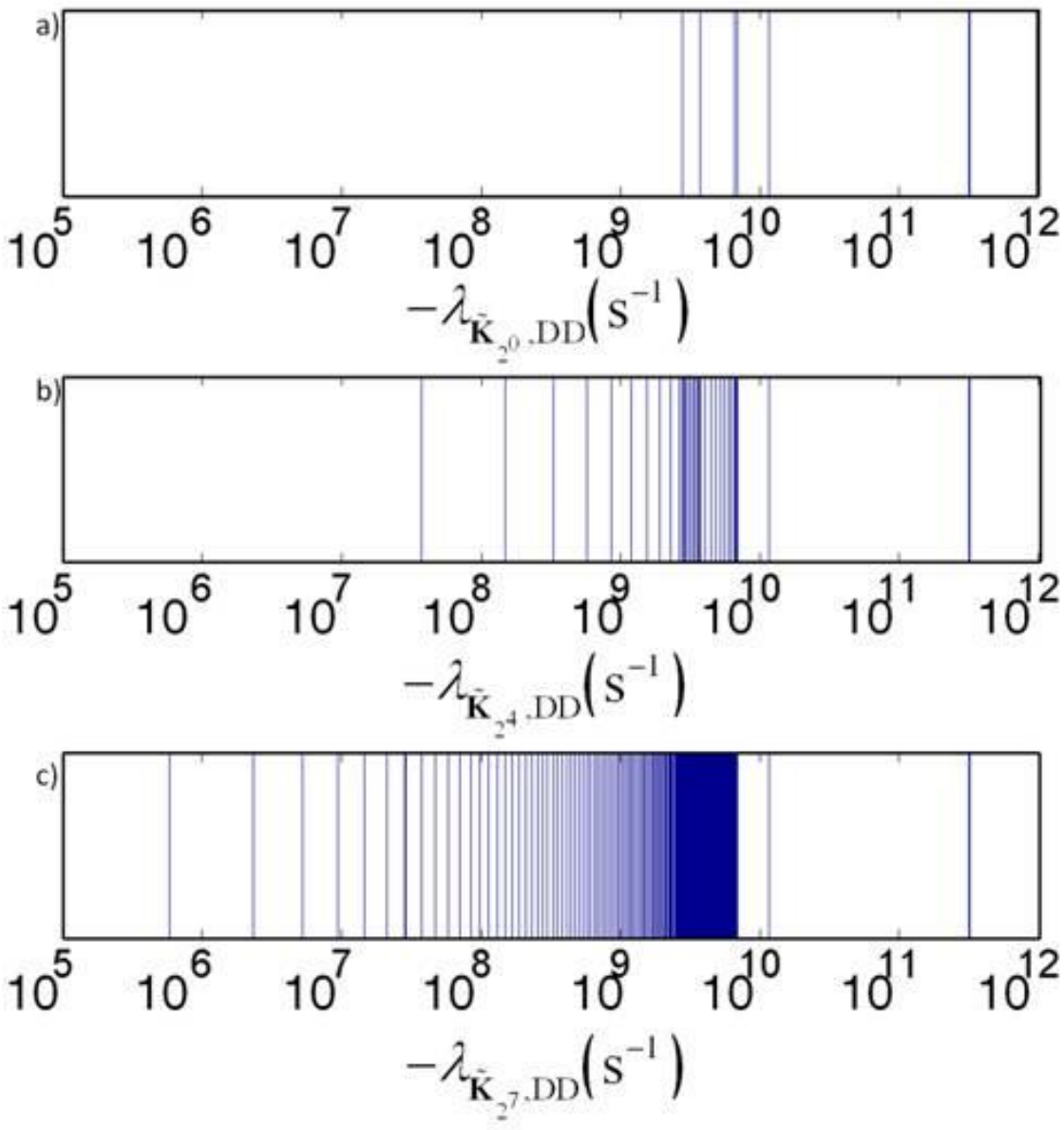

Figure 3.13 Spectrum of eigenvalues λ for diffusion in the x direction using direct diagonalization and IMSL routines for a) 1 unit cell system, b) 16 unit cell system, c) 128 unit cell system . The value λ=0 is not included.

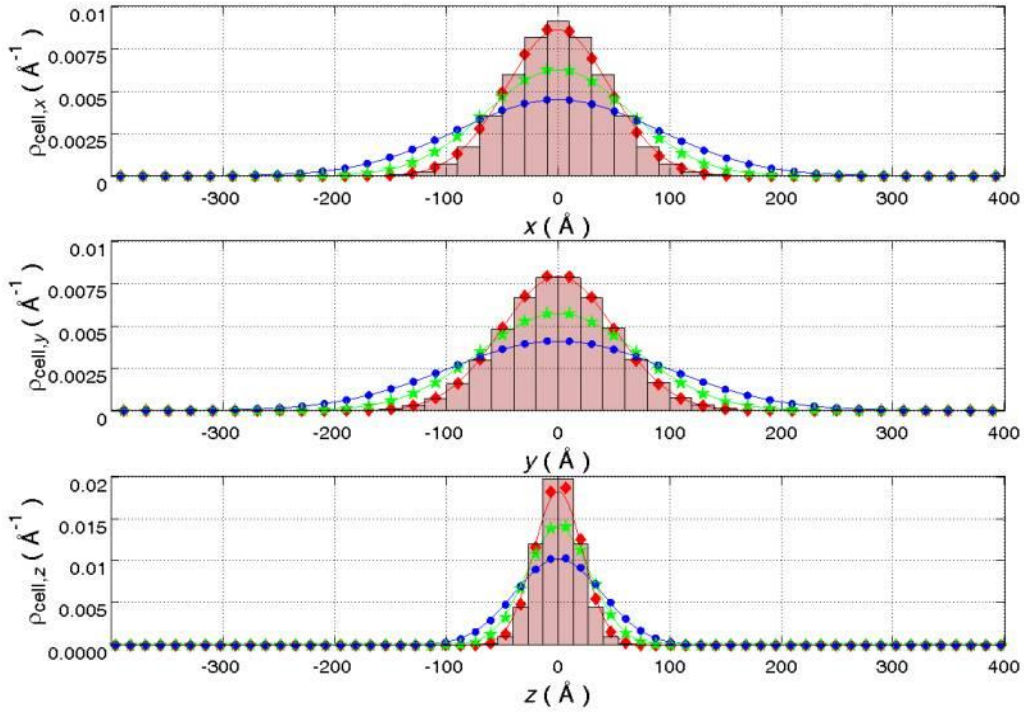

Figure 3.14 Probability density profiles for xenon in silicalite-1. Lines represent the fitting to the continuum diffusion equation. Red diamonds, green stars and blue circles display the profile from analytical solution of the master equation for 1×10^{-8}s, 2×10^{-8}s and 4×10^{-8}s, respectively through the MESoRReD scheme. The pink bars represent the probability density as obtained from numerical solution of the master equation by the Euler method for the same times.

The spectrum of eigenvalues of $\tilde{\mathbf{K}}_{2^0}, \tilde{\mathbf{K}}_{2^4}, \tilde{\mathbf{K}}_{2^7}$, as obtained from DD, is displayed in Figure 3.13, which is intended to show how eigenvalues change with the size of the system. We note that less than n=12 eigenvalues (11 if we do not count the zero eigenvalue) are displayed for $\tilde{\mathbf{K}}_{2^0}$. This is because some eigenvalues are double. As we can see from Eq. (3.7), (negative) eigenvalues with large absolute value contribute less to the probability density profile. In the system we study here, we associate the eigenvalue of largest absolute value with the fastest transition, which is the I→S. This eigenvalue of largest absolute value is observed for every direction *x*, *y*, *z*, as it is an eigenvalue of matrix $\tilde{\mathbf{K}}_{2^0}$.We remind the reader that the eigenvalues of $\tilde{\mathbf{K}}_{2^0}$ are eigenvalues of $\tilde{\mathbf{K}}_{2^\nu}$ for every direction *x*, *y* or *z*. In Figure 3.13 we can see that, as the system size increases, (negative) eigenvalues of smaller and smaller absolute value emerge. These correspond to slower, longer-range motions, which need a larger system to be expressed. Because a larger system needs longer time to equilibrate than a smaller one, we expect from Eq. (3.7) that the larger a system would have

a broader spectrum of eigenvalues, extending to eigenvalues of very small absolute value. Figure 3.13 verifies this expectation. The nonzero eigenvalue of smallest absolute magnitude, λ_1, becomes smaller and smaller as L_p increases.

Comparing the solution to the discrete master equation, Eq. (3.7), to the solution of the continuum diffusion problem, Eq. (3.36), we see similarities. Both solutions have the form of a sum of exponentially decaying functions of time. The preexponential factors appearing in each sum are dependent on the initial conditions, while the diffusion coefficient is, of course, independent of those. In order for the solution of the master equation to go over to the solution of the continuous Fickian diffusion problem at long times, the exponents of the exponentials in corresponding terms of Eqs. (3.7) and (3.36) must be the same for low-index (small absolute magnitude) eigenvalues. That is to say,

$$\lambda_f = -D\left(\frac{f\pi}{L_p}\right)^2, \quad f = 1,2,... \qquad \text{Eq. (3.44)}$$

where f=1 for the nonzero eigenvalue of smallest absolute value, f=2 for the nonzero eigenvalue of second smallest absolute value, etc. Index f here counts only distinct eigenvalues, in contrast to the index m appearing in Eq. (3.7). In other words, when f is used, multiple eigenvalues are counted as one. The nonzero eigenvalue of smallest absolute value will contribute most to Eq. (3.7) at very long times. As a result, the diffusion coefficient can be calculated from Eq. (3.45) for a large system, where the discrete description is expected to go over to the continuous one at long times.

$$D = \lim_{L_p \to +\infty} \left(-\lambda_1\right)\left(\frac{L_p}{\pi}\right)^2 \qquad \text{Eq. (3.45)}$$

A graph of the functional dependence of the eigenvalues $-\lambda_f$ on $(f\pi/L_p)^{1/2}$ suggested by Eq. (3.44) is shown in Figure 3.15 for periodic Xe/silicalite systems of different sizes along the x direction . From this Figure it is clear that for large systems ($L_p \to +\infty$), and for small values of f, there is a linear region in the graph, from the slope of which one can immediately obtain the diffusivity D. Figure 3.15 makes it clear that the set of eigenvalues for a $2^{\nu}n$ state system is a subset of the set of eigenvalues for a $2^{\nu'}n$ state system with $\nu' > \nu$, as predicted by the mathematical development of Part 3.2. From Figure 3.15 and Eqs. (3.44), (3.45) we see that a reliable calculation of the diffusivity requires that eigenvalues of small absolute magnitude be computed with very good accuracy. A method for increasing the accuracy in the calculation of small eigenvalues has been presented by Alfa et al[91].

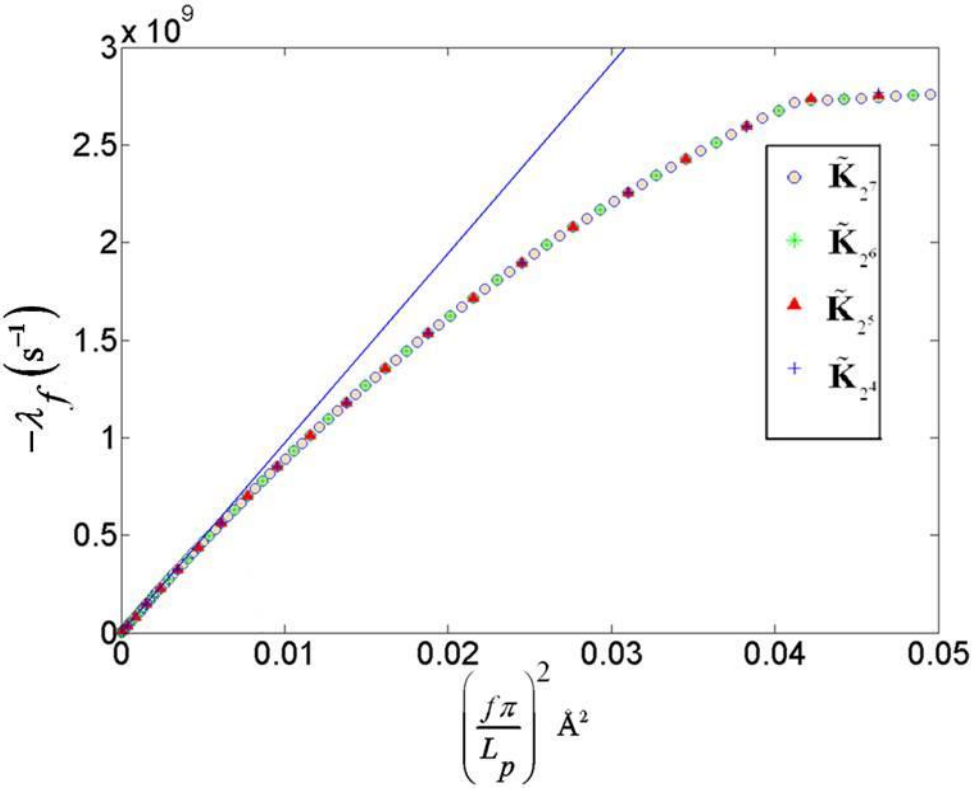

Figure 3.15 Dependence of eigenvalues on $\left(\frac{f\pi}{L_p}\right)^2$ for 128, 64, 32 and 16 cell-systems along the *x* direction. *f* is the index of the eigenvalue, after sorting their absolute values in ascending order. Multiple eigenvalues are taken as one. Blue line indicates where the dependence diverges from linearity.

In addition to finding the slope in Figure 3.15, we can calculate the diffusivity using Eq.(3.46)

$$D = \lim_{\nu\to+\infty}\left\{\left[\min\left(\left|\lambda_{\mathbf{A}_\nu}\right|\right)\right]\left(\frac{2^{\nu-1}L_d}{\pi}\right)^2\right\} \qquad \text{Eq. (3.46)}$$

where $\mathbf{A}_\nu = \tilde{\mathbf{K}}_1 - \left[1-\cos\left(\frac{\pi}{2^{\nu-1}}\right)\right]\tilde{\mathbf{K}}_{\mathrm{RL1}} \pm i\sin\left(\frac{\pi}{2^{\nu-1}}\right)\left(\tilde{\mathbf{K}}_{\mathrm{R1}} - \tilde{\mathbf{K}}_{\mathrm{L1}}\right)$ are the $n\times n$ matrices, within the MESoRReD scheme, which contribute the nonzero eigenvalue of $\tilde{\mathbf{K}}_{2^\nu}$ with smallest absolute magnitude. A proof can be found in Appendices G and H. Eq. (3.46) is strategically very important, for it reduces the problem of calculating the diffusivity in a spatially periodic system via MESoRReD to finding the absolutely smallest eigenvalue of a single $n\times n$ matrix!

For calculating the eigenvalues of $\mathbf{A}_v = \tilde{\mathbf{K}}_1 - \left[1-\cos\left(\frac{\pi}{2^{v-1}}\right)\right]\tilde{\mathbf{K}}_{\mathrm{RL1}} \pm i\sin\left(\frac{\pi}{2^{v-1}}\right)\left(\tilde{\mathbf{K}}_{\mathrm{R1}} - \tilde{\mathbf{K}}_{\mathrm{L1}}\right)$, or equivalently $\mathbf{A}_v = \mathbf{K}_1 - \left[1-\cos\left(\frac{\pi}{2^{v-1}}\right)\right]\mathbf{K}_{\mathrm{RL1}} \pm i\sin\left(\frac{\pi}{2^{v-1}}\right)\left(\mathbf{K}_{\mathrm{R1}} - \mathbf{K}_{\mathrm{L1}}\right)$ (the proof of MESoRReD with matrices $\tilde{\mathbf{K}}_1, \tilde{\mathbf{K}}_{\mathrm{RL1}}, \tilde{\mathbf{K}}_{\mathrm{R1}}, \tilde{\mathbf{K}}_{\mathrm{L1}}$ instead of $\mathbf{K}_1, \mathbf{K}_{\mathrm{RL1}}, \mathbf{K}_{\mathrm{R1}}, \mathbf{K}_{\mathrm{L1}}$ was used to prove the existence of double eigenvalues) we have found it convenient to use the eigs function of MATLAB R2009b.[92] This function calculates absolutely small eigenvalues very accurately, while it provides the user the ability to change the settings of eigenvalue convergence criteria. For example, with its default settings, the eigs function calculates the zero eigenvalue of $\tilde{\mathbf{K}}_1$ as -5.156×10^{-6} s^{-1} in 0.0242 CPU s on the machine we have used, which is far superior to the accuracy offered by the IMSL and LAPACK routines discussed above. Results from application of Eq.(3.46) to our system are shown in Figure 3.16. $D_v = \left[\min\left(\left|\lambda_{\mathbf{A}_v}\right|\right)\right]\left(\frac{2^{v-1}L_d}{\pi}\right)^2$ converges very quickly with increasing v to a specific value D for each direction. However, because eigenvalues λ_1 are extremely small for $v>21$ (for example, $\lambda_{1,v=21,x} = -2.1569 \times 10^{-3}$ s^{-1}), it is impossible to calculate the diffusivity with satisfactory accuracy for very large values of v. We remind the reader that $v=21$ means that we are dealing with a system of 2^{21}cells, which is huge. As we see from Figure 3.16, Eq.(3.46) gives us the ability to calculate diffusion for a wide range of system sizes.

3.4.3. Comparison with other methods for calculation of the diffusivity

As pointed out in the 3.1.1 section, there are several methods for solving the master equation for the evolution of state occupancy probabilities. We have applied some of these methods to our problem of low-temperature and low-occupancy diffusion of Xe in silicalite-1, using the states, state probabilities, interstate transitions and rate constants summarized in Figures 3.10 and 3.11 and Tables 3.1 and 3.2. This allows us to check whether diffusivity values extracted from these alternative methods are consistent with those obtained through our new MESoRReD scheme and to compare the computational requirements of these methods against those of our new method.

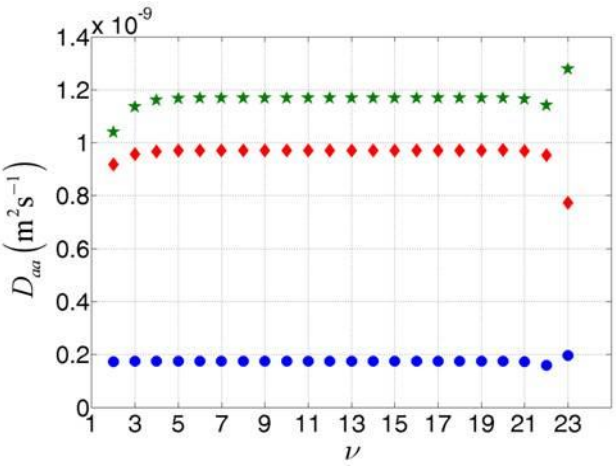

Figure 3.16 Diffusivity of Xe along each of the principal directions of a silicalite-1 crystal at 150 K, as calculated from Eq.(3.46) using the eigs function of MATLAB R2009b in periodic systems of 2^v cells as a function of v. Red diamonds, green stars and blue circles display the diffusion coefficient D_{xx}, D_{yy}, D_{zz} respectively.

The methods we have tried on our problem are the following:

A) Kinetic Monte Carlo (KMC) simulations. This is the most commonly used method for calculating diffusivities from a network of states with known state probabilities and interstate transition rate constants. It has been applied to the Xe/silicalite-1 problem by June et al.[62] We have performed our own KMC calculations to confirm consistency with the results of June et al.[62] In our work we used a three-dimensional network of $10 \times 10 \times 10$ unit cells (1000 unit cells total) with periodic boundary conditions in all three directions, on which we deployed $\mathcal{N}$=4000 walkers. We distributed the walkers according to the equilibrium probabilities of Table 3.1, which are consistent with the rate constants of Table 3.2. With these choices our KMC runs were efficient, with a low level of noise in the results, allowing for a fair comparison with other methods for calculating diffusivities. For KMC we used the algorithm described in Chapter 2.2.6.

The diffusivity along the x direction is computed as the slope of the mean square displacement with respect to time at long times, via the Einstein relation:

$$D_{xx} = \lim_{t\to\infty} \frac{\left\langle x(t) - x(0)^{\,2} \right\rangle}{2t} \qquad \text{Eq.(3.47)}$$

where the angular brackets symbolize averaging over all walkers using multiple time origins. Similar expressions are used along the y and z directions.

For applying KMC, we constructed a FORTRAN program and ran it on the machine described in the previous section. The maximum time we simulated was 1087800 steps, or 2.3×10^{-2} μs . Requirements to determine the diffusivity with an uncertainly comparable to that afforded by MESoRReD were:

a) 6 MB RAM memory

b) 6183.46 seconds (1 hour, 43 minutes, 3.46 seconds) of CPU time.

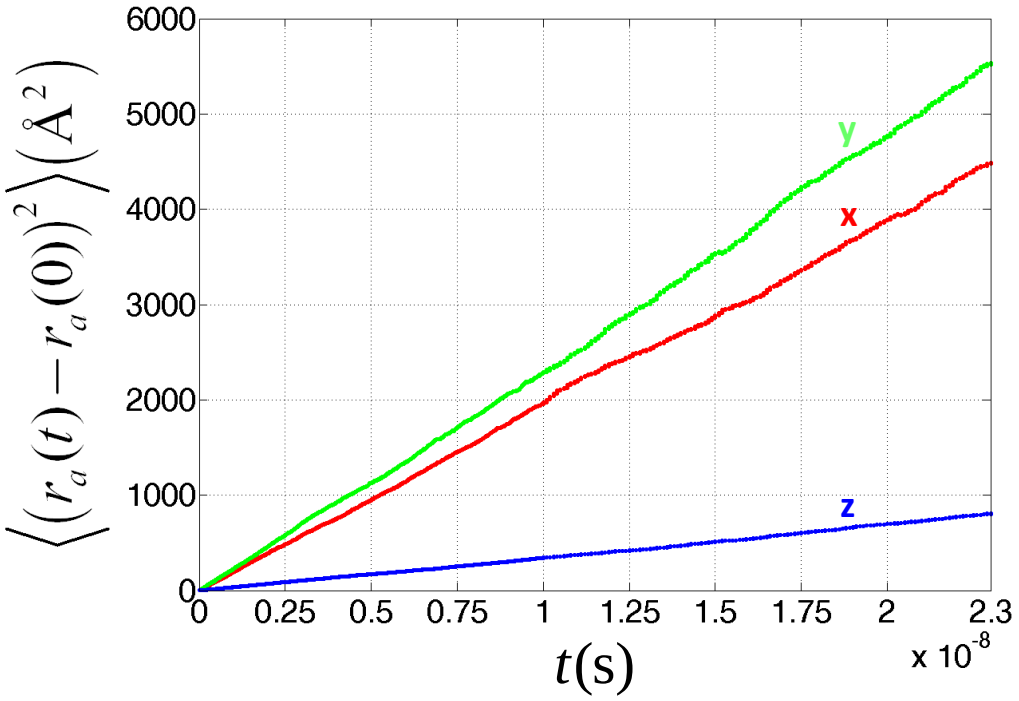

Figure 3.17 Mean Square Displacement as a function of time from our Kinetic Monte Carlo simulations. Red, green, and blue show results along the *x* (r_α=*x*), *y* (r_α=*y*) , *z* (r_α=*z*) direction, respectively.

Figure 3.17 displays the mean square displacement as a function of time along the *x*, *y*, and *z* directions as obtained from one of our KMC runs. Diffusivities extracted from the KMC method as functions of the number of executed KMC steps are shown in Figure 3.17. After an initial equilibration period, these diffusivity estimates are seen to fluctuate around well-defined mean values (red parts of the curves). The latter values, listed in the fifth row of Table 3.4 (row labeled "Our KMC-TST") are in excellent agreement with the KMC results of June et al[63] based on the dynamically uncorrected transition rate constants employed here (third row of the same table, labeled "June et al. KMC-TST"). Both sets of KMC results are

in excellent agreement with results from MESoRReD (sixth row of the same table). This is also seen from the comparison of the cyan horizontal lines (diffusivities from MESoRReD method) against the fluctuating KMC estimates of the diffusivities in Figure 3.18.

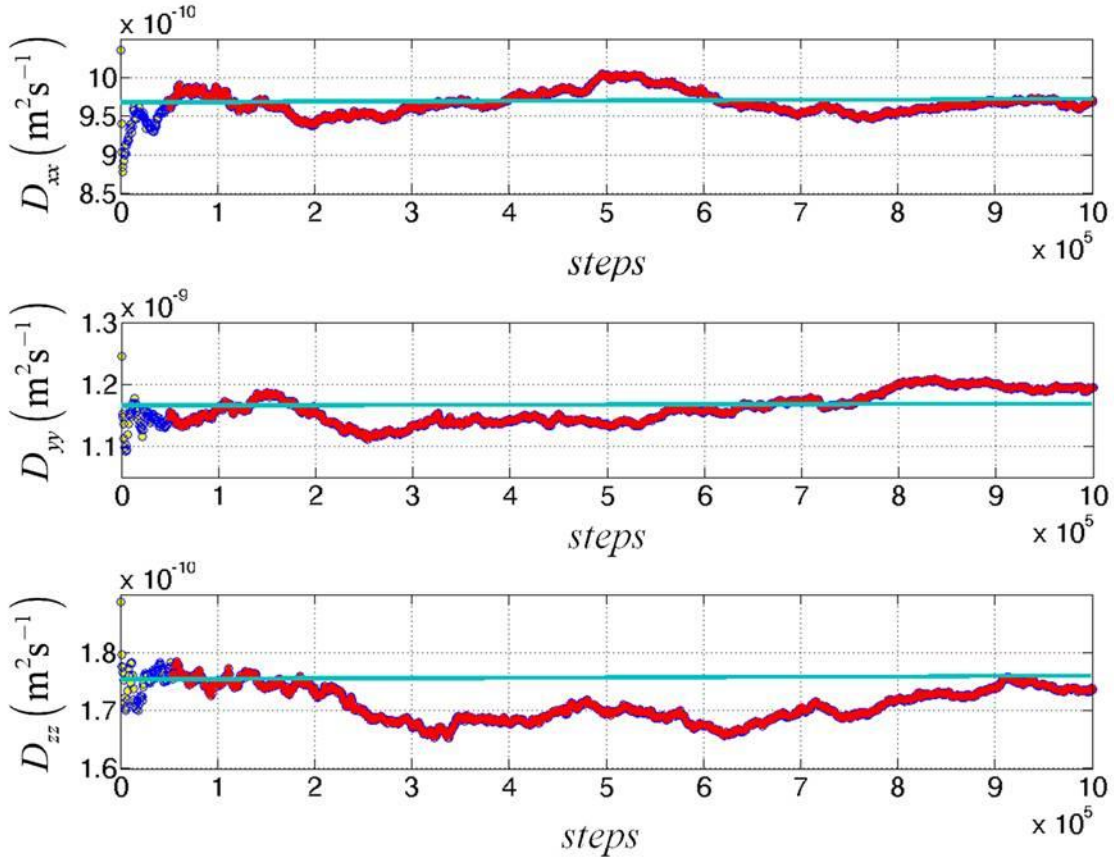

Figure 3.18 Diffusion coefficients along the *x,y,z* directions calculated via Eq. (3.45) from KMC, as functions of the number of KMC steps. The cyan lines indicate the values of diffusivity from MESoRReD based on analytical solution of the master equation by diagonalization of $n \times n$ matrices and the algorithm of Figure 3.9 .

Computational requirements for extracting the diffusivities from different methods in the xenon/silicalite-1 system are compared in Table 3.3. Clearly, KMC is slower by more than 3 orders of magnitude relative to our MESoRReD method with fitting to the solution of the continuum diffusion equation. KMC is slower by 5 orders of magnitude relative to MESoRReD with *D* calculated from the nonzero eigenvalue of smallest absolute magnitude [Eq. (3.45)]. It is also important to realize that KMC requires considerable effort in order to generate the lattice of states on which to conduct the KMC simulations. Different systems are characterized by different lattices, so the researcher must modify a KMC code considerably in order to port it to another system. The MESoRReD method is more robust in

this respect, as setting up the the $\tilde{\mathbf{K}}_1$ and $\tilde{\mathbf{K}}_{L1}$ matrices for a different system is quite straightforward.

Table 3.3 CPU time and Memory (RAM) requirements for each method

Method	CPU Time(s)	Memory(MB)
June et al MD[84]	309173*	-
Our Euler Method	23760.00	401
Our KMC	6183.46	6
Direct Diagonalization and Diffusion coefficient calculation from Figure 3.9 algorithm	3×37.81**	38
a)Find eigenvalues and eigenvectors	3×35.12	
b) Find Diffusion coefficient by fitting profile of cell probabilities	$3 \times$ 2.69	
MESoRReD and Diffusion coefficient calculation from Figure 3.9 algorithm:	$3 \times$ 2.83	44
a)Find eigenvalues and eigenvectors	$3 \times$ 0.14	
b) Find Diffusion coefficient by fitting profile of cell probabilities	$3 \times$ 2.69	
Direct Diagonalization (eigenvalues only) and Diffusion coefficient calculation from Eq.(3.45)	$3 \times$ 4.51	19
MESoRReD (eigenvalues of all MESoRReD matrices only) and Diffusion coefficient calculation from Eq.(3.45)	$3 \times$ 0.0059	2

*using CPU time of our KMC and a ratio 0.02 taken from June et al[63] for the CPU requirements of their MD and their KMC.

**we multiply by 3 to get CPU time needed for obtaining the diffusivity in all three directions.

B) Euler Method. The master equation, Eq. (3.4), is an initial value problem (system of first-order differential equations in time) and can therefore be solved by numerical methods developed for such problems. One such method is that of Euler,[88,93] which relies on a discretization of the differential equations using a constant time step δt. We have applied the

Euler method to solve the master equation for xenon in a system of 50×50×50 unit cells of silicalite-1 without periodic boundary conditions. In this calculation we have used a time step of $\delta t=10^{-12}$s, which proved satisfactory. Note that the Euler method is very unstable,[93] longer time steps leading to divergence. Initially all mass was placed at the center of the system, i.e., the probability for xenon to be in a central S state was set equal to 1, all other probabilities being zero. We integrated the master equation forward in time to obtain the three-dimensional state probability profile $\{ P_i(t) \}$. From the state probabilities we calculated the time-dependent cell probabilities via Eq. (3.32) and from those we obtained the three-dimensional probability density $\rho_{\text{cell}}(x,y,z,t)$ by dividing by the cell volume. Subsequently, we calculated marginal probability densities in each direction by projecting the three-dimensional distribution:

$$\rho_{\text{cell},x}(x,t) = \int \rho_{\text{cell}}(x,y,z,t)dydz \cong \sum_y \sum_z \rho_{\text{cell}}(x,y,z)\delta y \delta z \qquad \text{Eq. (3.48)}$$

and similarly for *y* and *z*. For sufficiently long, but not too long times, these marginal probability densities are immediately comparable to the one-dimensional probability density profiles obtained via our MESoRReD method applied to linear arrays of 2^7 unit cells with periodic boundary conditions. Marginal probability profiles obtained via the Euler method are given as histograms in Figure 3.14. Clearly, agreement with results from MESoRReD is excellent.

The probability density profile $\rho_{\text{cell}}(x,y,z,t)$ from our numerical solution to the master equation via the Euler method corresponds to a solution of the diffusion equation in three dimensions with a delta function initial condition. The marginal probability densities $\rho_{\text{cell},x}(x,t)$, $\rho_{\text{cell,y}}(y,t)$, $\rho_{\text{cell,z}}(z,t)$ correspond to solutions of the unidimensional diffusion equation, Eq. (3.33), with a delta function initial condition.[81] They should then be described by the Gaussian form, Eq. (3.40). By fitting this form to our results from the Euler method after 10000 time steps (time equal to 10^{-8}s) we have obtained the diffusivities shown in the fourth row of Table 3.4 (row labeled "Our Euler method- TST"). Clearly, these estimates are in excellent agreement with ones obtained from MESoRReD.

For applying the Euler method for solution of the master equation we have developed a FORTRAN program. The computational requirements of this program on the machine we have described above are:

a) 401 MB RAM memory

b) 2.4 CPU seconds per integration time step.

This means that we needed 6 hours and 36 minutes of CPU time for carrying out 10000 integration time steps, a time satisfactorily long for extracting the diffusivity through fitting with the analytical solution to the diffusion equation, Eq.(3.40). These computational requirements are summarized and compared to those of all other methods we have implemented in Table 3.3. Clearly, the Euler method is much more time-consuming than both KMC and MESoRReD. Also, from the point of view of ease of use, one should bear in mind that it is necessary for the researcher to modify the code every time he/she wishes to study a new system.

Table 3.4: Diffusion coefficient from different methods for Xenon in Silicalite at 150K

Method	D_{xx} (10^{-10} m^2 s^{-1})	D_{yy} (10^{-10} m^2 s^{-1})	D_{zz} (10^{-10} m^2 s^{-1})	D (10^{-10} m^2 s^{-1})
June et al MD[62]	4.3	10	0.99	5.1
June et al KMC-DC TST[62]	5.1	7.3	0.83	4.41
June et al KMC-TST[62]	10	12	1.7	7.9
Our Euler Method-TST	9.70	12.5	1.83	8.01
Our KMC-TST	9.67 ± 0.14	11.62 ± 0.25	1.71 ± 0.02	7.66 ± 0.14
Direct Diagonalization-TST	9.7088 ± 0.0029	11.676 ± 0.002	1.7627 ± 0.0093	7.7157 ± 0.0044
MESoRReD-TST (using Figure 3.9 algorithm)	9.7088 ± 0.0029	11.676 ± 0.002	1.7627 ± 0.0093	7.7157 ± 0.0044
MESoRReD-TST (using Eq.(3.45))	9.7132	11.684	1.7531	7.7171
PFG NMR[90]	-	-	-	1.633

C) Molecular Dynamics (MD). This is the most straightforward method for studying diffusion in zeolite/sorbate systems based on atomic-level structure and interactions. How useful MD will be for this purpose depends on how rarely the sorbate moves from one state to the other. For example, MD can be used in the xenon/silicalite-1 system to estimate the diffusion coefficient, as transitions of Xe between I, S, and Z states are not so rare, but it cannot be used for the benzene/silicalite-1 system. In the latter system, benzene prefers to reside within specific sites (primarily corresponding to I states) in silicalite and moves extremely rarely out of these sites, across very high free energy barriers. Interstate transition rate constants[39] $k_{i\rightarrow j}$ for benzene/silicalite-1 are on the order of 10^6 s^{-1}. In the case of benzene, a MD run would exhaust itself in tracking the fast motions of the sorbate within a sorption site and would hardly sample state-to-state jumps contributing to translational diffusion.

MD simulations for xenon in silicalite-1 have been performed by June et al.[62,84] They have not been repeated here. Instead, we have used the ratio of CPU times reported by June et al.[63] between their KMC and MD in order to estimate how long it would take in order to estimate the diffusivities along *x*, *y*, and *z* at 150 K via MD simulation on the machine we have used in our calculations. As seen in Table 3.3, brute-force MD would require 309173 s to calculate a diffusivity at 150 K. This time is extremely long compared to those of the rate constant-based methods, underlinng the utility of the latter at low temperatures.

Direct MD simulations provide an "exact solution" for the diffusivity for the force field used, free of any approximations associated with infrequent event analysis. The values of D_{xx}, D_{yy}, D_{zz} obtained by June et al.[62,84] at 150K are reproduced in the first row of Table 3.4 (row labeled "June et al. MD"). In the second row of the same table (row labeled "June et al. KMC-DMC TST") are provided the corresponding values obtained by June et al[62] via KMC using rate rate constants computed via *dynamically corrected* transition state theory in place of the dynamically uncorrected values listed in Table 3.2. Dynamically corrected TST is seen to provide a very good approximation of the exact MD results. If dynamical corrections are not applied (rows 3-8 of Table IV) the diffusivities are overestimated, as expected. In the last row of Table 3.4 (row labeled "PFG NMR") is the best experimental estimate of the orientationally averaged self-diffusivity at 150 K and an occupancy of 3-4 Xe atoms per 24 (Si + Al) atoms, or else 12-16 Xe molecules per unit cell, obtained via pulsed field gradient nuclear magnetic resonance measurements using ^{129}Xe.[90] Compared to experiment, the MD value of *D* is seen to be in the correct order of magnitude, but too high. This disparity is

partly due to the fact that experiments were conducted at finite occupancy, the self-diffusivity being a decreasing function of occupancy.[94] Defects present in the crystals used in the measurement may be another source for the difference between diffusivity estimates from PFG NMR and MD simulation. Most of the disparity, however, is probably due to the simple molecular model (orthorhombic, high-temperature form of silicalite-1) and force field invoked in the simulations.

Chapter 4

Application of the new modified umbrella sampling methodology to the system of benzene in silicalite-1 at infinite dilution

4.1 Silicalite-1 and benzene interactions

A forcefield for silicalite-1 has to be chosen. There is a wide range of charges on the silicon in forcefields for silicates from +4.0e[95], to +2.4e[96] , to 1.3e[97] to +1.1e[98], while the majority tends to the value of +1.6e.[99] More complicated models[100,101] which take into account polarizabilities for silica also exist. A nice discussion of charges found in the literature is given in the work of Bordat et al.[102] They choose to modify the BKS[96] model by assigning charges of +1.6e to silicon. Charges are an important parameter especially for silicalite-1, as its hydrophobicity is dependent on these.

A variety of models for silica or, more specifically, for zeolites and silicalite-1, are available in the literature. However, few of these models are in the Ortho phase over the temperature range where this phase is stable and, as a result, few of them can be used for simulations. The criterion by which we chose the model employed here was to have reasonably realistic results at a small computational cost. Because of its low compressibility (bulk modulus 18.2 GPa),[103] silicalite-1 is not distorted very much upon sorption; its atoms are displaced little from their equilibrium positions and, as a result, a harmonic approximation should be satisfactory for describing Si-O and O-O interactions. Another criterion was the ability to let the user choose his/her own electrostatics for the crystal, because of the wide range of charges suggested in the literature.

Firstly, we have adopted the Vlugt and Schenk and the Smirnov and Bougeart models to describe silicalite-1, as described in detail in section 4.2. The Vlugt and Schenk[104] model is a modified version of the model of Demontis et al.[105] The difference is that in the Vlugt and Schenk model each bond is considered to have its own equilibrium distance, equal to that extracted from the crystallographic measurements of Olson et al.[106] This yields average atom positions that are in good agreement with the crystallographic structure, which is very

important for predicting diffusion, as pointed out by Krishna and Van Baten[107] and by Zimmermann et al.[108] This model is simple (it does not invoke nonbonded interactions among the atoms of silicalite) and it is consistent with the RUM theory. When coupled with reasonable fluid-phase models for alkanes, it yields satisfactory predictions for their sorption equilibria.[104] It does not reproduce well the actual volumetric properties of pure silicalite-1, however, as we have established through MD simulations. We choose to apply the Vlugt and Schenk model here because of its simplicity, bearing in mind that it may not lead to fully satisfactory predictions.

We also chose to work with the charges of Snurr et al.[36] Their charges were +2.0e and -1.0e for Si and O atoms and +0.150 and –0.150 for H and C atoms of the benzene. Similar charges for benzene are recommended by Sun.[109]

From the COMPASS[109] model for benzene and the models of Demontis et al[105] and Smirnov et al[110] for silicalite-1, we can conclude that the bond stretching and bond angle bending forces in benzene are 2-5 times stronger than the corresponding forces in silicalite-1. As a result, it is a more reasonable choice to work with a flexible silicalite-1 and a rigid benzene, instead of a flexible benzene and a rigid silicalite-1. Here we have chosen to work with a rigid benzene with C-C and C-H bond lengths equal to 1.40 Å and 1.08 Å, respectively, for consistency with the previous work of Snurr et al.[36] and Forester and Smith.[39]

We chose to do most of our calculations with an electrostatic field that is fixed in space, emanating from the silicalite atoms in their equilibrium positions according to the charges of Snurr et al.[36] This trick saves us a lot of computational cost, as the computation of electrostatic interactions is the slowest stage of the energy calculation. We have chosen to work with a static electrostatic map in order to have the same electrostatic field as Snurr et al.[36] and therefore be justified in using the same Lennard-Jones parameters for zeolite-sorbate interactions as Snurr et al.[36] The latter parameters have been shown to reproduce Henry's law constants for low-occupancy sorption of aromatics in silicalite-1 very successfully. Another reason why we have chosen to work with a static electrostatic field is the great uncertainty in the partial charges attributed to silicalite-1 atoms mentioned in the beginning of this section; errors resulting from this uncertainty are likely to be more significant than errors due to neglect of thermal fluctuations in the electrostatic field. Thus, in our calculations we have two main types of interactions: 1) silicalite-1 atoms with silicalite-1 atoms, and 2) benzene with silicalite-1 interactions. The silicalite-1 atoms interact with each through 1-2 and 1-3

harmonic potentials based on the Vlugt and Schenk[104] model mentioned above. The benzene-silicalite interactions are divided into two categories:

a) Lennard-Jones interactions between the oxygen atoms of silicalite-1 with the carbon and hydrogen atoms of benzene. These interactions are presented in detail in Tables 4.1, 4.2, 4.3 and 4.4. Oxygens are considered as the only silicalite atoms with Lennard Jones interactions, as they are the outer atoms of the tetrahedra and "protect" the silicon atoms; this approximation, originally due to Kiselev, was taken from Makrodimitris et al.[111] and was also invoked by Snurr et al.[36] The Lennard-Jones parameters are the same as those of Snurr et al.[36] They are chosen in such a way as to yield results in good agreement with experiment for the sorption of rigid benzene in rigid silicalite.[38,50]

b) Electrostatic interactions. Here, forces are exerted only on the atoms of benzene and not on the atoms of silicalite-1. The partial charges of silicalite-1 are considered affixed to the equilibrium positions of Si and O atoms in the Ortho crystal, generating an electrostatic field which does not fluctuate with time. This electrostatic field is pretabulated at the nodes of a fine cubic grid with voxel edge length 0.2 Å and computed by three-dimensional Hermite interpolation based on the pretabulated values.[112,84] Clark and Snurr[45] have shown the great sensitivity of electrostatics on crystallographic positions. The combination of electrostatic map and Lennard-Jones interactions used here describe well the Henry's law constant of benzene in a rigid silicalite-1 model with atoms placed at the equilibrium positions of the flexible model we invoke in this work.[50] Vlugt and Schenk[104] have shown that Henry's law constants are not significantly influenced by the rigidity of the framework for small hydrocarbons.

To check the consequences of using a fixed electrostatic field on our results, we have performed some calculations with a fluctuating electrostatic field, wherein we assigned the partial charges of Table 4.3 to the instantaneous positions of Si and O atoms and let them move in space along with these atoms. How electrostatic interactions were computed by explicit summation in this model of fluctuating charges is explained in Section 4.3.

Furthermore, to check the consequences of keeping the benzene rigid, we performed some calculations using a flexible benzene model, described by the COMPASS force field. As the partial charges assigned to C and H atoms of the benzene in the COMPASS force field are somewhat different from those of Table 4.3, in these flexible benzene calculations we adjusted the charges on the Si and O atoms of the zeolite to ensure that framework-benzene electrostatic interactions would be described by the same potentials as when our rigid

benzene model was invoked. These adjusted charges on silicalite atoms, along with the COMPASS partial charges on flexible benzene, are given in Table 4.5 below.
By construction, the Vlugt and Schenk[104] model has an energy minimum at the crystallographically correct structure of Ortho silicalite-1.[106]

4.2 Choice of force-field for the description of intra-silicalite-1 interactions

The force-field of Vlugt and Schenk[104] is a modified edition of the force-field of Demontis et al.[107]. Actually, the Vlugt and Schenk[104] force-field uses the crystallographic equilibrium distances for all the bonds, while the Demontis et al.[105] force-field uses specific mean equilibrium values. As mentioned before, Clark and Snurr[45] found it necessary to keep the zeolite atoms in their crystallographically correct positions[106] in order to predict the Henry's law constant and the isosteric heat in close agreement with experimental values. The Demontis et al.[105] force-field describes the IR spectra of zeolites well; the same is expected of the Vlugt and Schenk[104] force-field, as they use the same spring constants. However, the Vlugt and Schenk[104] force-field fails to keep the volume of silicalite-1 (the lattice actually collapses) when used in MD simulations under constant pressure (Parrinnello-Rahman isothermal-isostress algorithm with characteristic time τ_P=1000fs)[113,114] and constant temperature (Nosé-Hoover algorithm with characteristic thermostat relaxation time τ_T=100fs)[114,115] simulation, and so it can be used only in constant volume simulations. The above characteristic times are defined by Melchionna et al[114] in the isothermal-isostress algorithm they present. From now on, we use the term DHFF-O (Demontis Harmonic Force Field-Original) for the Demontis et al. force-field and the term DHFF for the Vlugt and Schenk one. Calculations reported below will be based on DHFF, unless indicated otherwise.

A different force-field for zeolites has been proposed by Smirnov and Bougeard.[110] We use the term SGVFF-O (Simplified Generalized Force Field-Original) for this one. They introduced harmonic angle potentials in addition to a harmonic bond potential for the Si-O bond. They also used specific mean equilibrium values for all the bond lengths and angles. We need to modify this force field by using the equilibrium crystallographic bonds and angles[106], for the reasons mentioned before, if we want to study the diffusion of aromatics in silicalite-1. We call this modified force-field SGVFF. From our calculations, by conducting

constant pressure and temperature simulations with the parameters we mentioned, we obtained a bulk modulus 20.63GPa for the SGVFF-O and 40.46GPa for the SGVFF. We remind the reader that the experimental value is 18.2 GPa[103]. It is important to add that, for pressures around 1atm, a negative thermal expansion coefficient is observed. Experiments also show this behavior[116]. The volumetric properties of these force-fields are illustrated in Figure 4.1. In the literature one can find other force-fields for silicates.[95-102,116] However, these force fields incorporate explicit electrostatic and Lennard-Jones interactions among crystal atoms instead of the harmonic potentials invoked in DHFF and SGVFF. We have decided to use only the DHFF and the SGVFF force-fields in our simulations of benzene and p-xylene in silicalite-1 because of their simplicity and relative success in reproducing pure silicalite-1 properties.

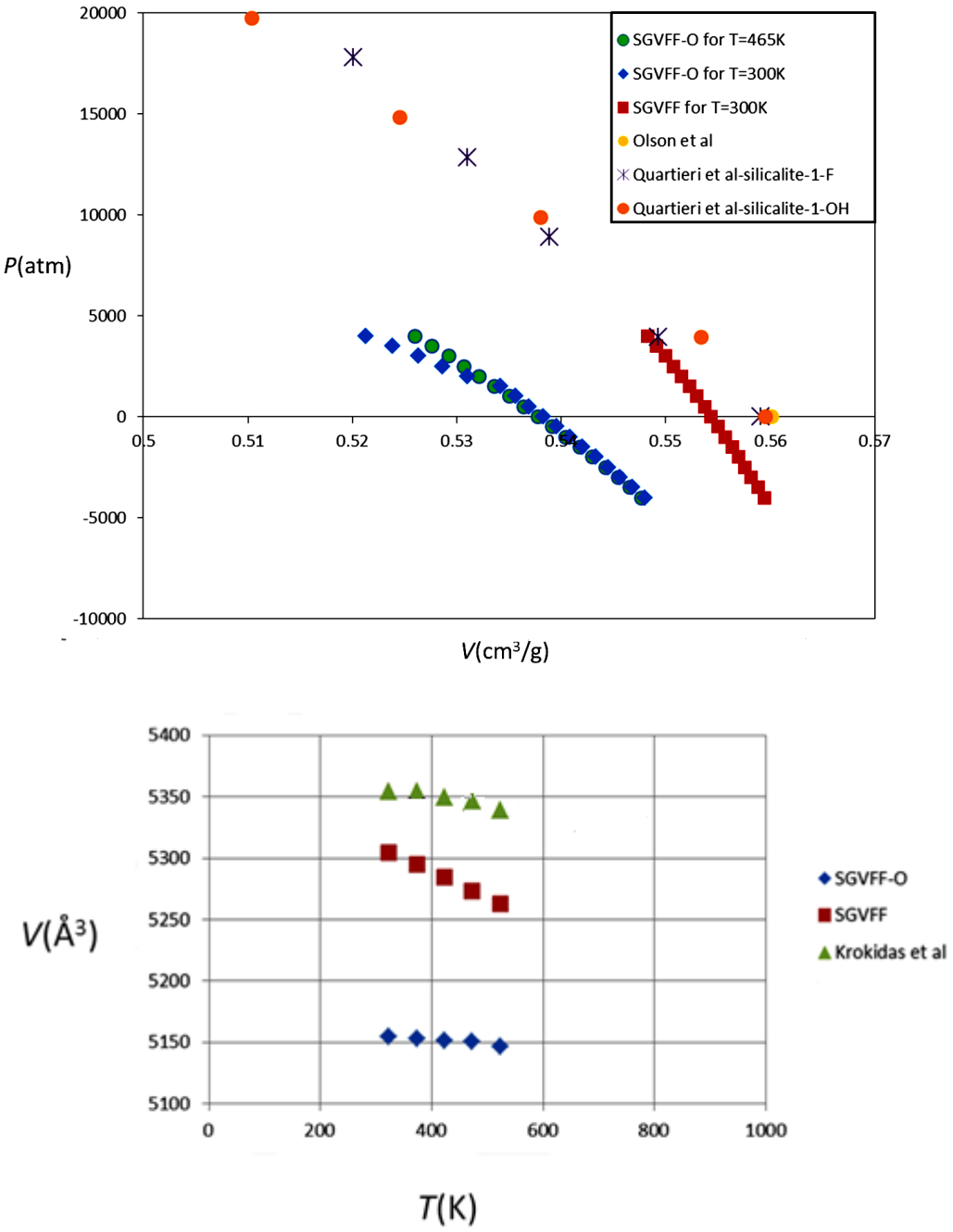

Figure 4.1 I) Pressure as a function of volume of silicalite-1, after 1ns of NPT MD simulation a) for SGVFF-O force field and temperature 300K (blue) b) for SGVFF-O force field and temperarure 465K (green) c) for SGVFF force field and temperature 300K (red) d) light orange point shows the experimental volume of Olson et al.[106] e) purple star points show the volumetric behavior of silicalite-1 as synthesized using a bulk material dissolution technique[103] (fluoride route) f) dark orange points show the properties of silicalite-1 which has been synthesized using NaOH, tetrapropylammonium bromide and tetraethyl orthosilicate as described in ref 103 (alkaline route) II) Volume of silicalite-1 unit cell as a function of temperature, a) after 10ns of NPT MD simulation using SGVFF-O force field b) after 10ns of NPT MD simulation using SGVFF force field c) experimental values by Krokidas et al.[116]

The comparative study of DHFF and SGVFF helps us examine how much the silicalite-1 force-field choice influences our final results (free energy profiles, rate constants, diffusion coefficients). All the force-fields parameters used in this work are provided in Tables 4.1-4.5.

a) Silicalite-1 – Silicalite-1 interactions

i) DHFF[104]

Table 4.1: Interactions between silicalite-1 atoms

Form of potential	Spring constant k/k_B (K/Å^2)	r_0(Å)
$\mathcal{V}_{Si\text{-}O}(r)=k_{Si\text{-}O}(r-r_0)^2$	1.3×10^5	Equilibrium bond distance Si-O from crystallography[106]
$\mathcal{V}_{O\text{-}O}(r)=k_{O\text{-}O}(r-r_0)^2$	2.6×10^4	Equilibrium bond distance O-O from crystallography[106]

ii) SGVFF [110]

Table 4.2: Interactions between silicalite-1 atoms

Form of potential	Spring constant k (kcal/mol/Å^2 or kcal/mol/rad^2)	r_0(Å) or θ_0(rad)
$\mathcal{V}_{Si\text{-}O}(r)=k_{Si\text{-}O}(r-r_0)^2$	298.65	Equilibrium bond distance Si-O from crystallography[106]
$\mathcal{V}_{O\text{-}Si\text{-}O}(\theta)=k_{O\text{-}Si\text{-}O}(\theta-\theta_0)^2$	69.055	Equilibrium angles O-Si-O from crystallography[106]
$\mathcal{V}_{Si\text{-}O\text{-}Si}(\theta)=k_{Si\text{-}O\text{-}Si}(\theta-\theta_0)^2$	9.067	Equilibrium angles Si-O-Si from crystallography[106]

b) Silicalite-1 – benzene interactions[36,50]

i) rigid benzene

α) electrostatic interactions

Table 4.3: Electrostatic interactions between silicalite-1 atoms with benzene atoms.

Form of potential	q_{Si}**(e)**	q_{O}**(e)**	q_{C}**(e)**	q_{H}**(e)**
$\mathcal{V}_{el} = \frac{1}{4\pi\varepsilon_0}\frac{q_i q_j}{r}$	+2.0	–1.0	–0.15	+0.15

β) Lennard-Jones interactions

Table 4.4: Van der Waals interactions between benzene atoms and silicalite-1 oxygens

Potential	A (kcal/mol Å^{12})	B (kcal/mol Å^{6})
$\mathcal{V}_{C\text{-}O}(r) = \frac{A_{C\text{-}O}}{r^{12}} - \frac{B_{C\text{-}O}}{r^{6}}$	319072.6577	431.8833
$\mathcal{V}_{H\text{-}O}(r) = \frac{A_{H\text{-}O}}{r^{12}} - \frac{B_{H\text{-}O}}{r^{6}}$	38217.017	122.0841

ii) flexible benzene

α) electrostatic interactions

Table 4.5: Electrostatic interactions between silicalite-1 atoms and benzene atoms.

Form of potential	q_{Si}**(e)**	q_{O}**(e)**	q_{C}**(e)**	q_{H}**(e)**
$\mathcal{V}_{el} = \frac{1}{4\pi\varepsilon_0}\frac{q_i q_j}{r}$	+2.3658	–1.1829	–0.1268	+0.1268

β) Lennard-Jones interactions

Same as for rigid benzene

4.3 Details of explicit calculation of electrostatics

For the explicit calculation of electrostatic interactions with fluctuating charges on the silicalite-1 framework, we chose to use the particle-particle-particle mesh Ewald[117-119] summation method (P^3M) in every timestep. Because we deal with a large number of atoms (more than 1000), the P^3M method was preferred to the classical Ewald technique. In the former method the computational time scales as $N\log N$, while in the latter it scales as $N^{3/2}$.[118] More specifically, in the P^3M method we split the partial charges into a Gaussian and its complementary distribution, so that their total sum is a delta function at the position of each partial charge. We used a value for the split parameter α=0.21732Å^{-1}, or equivalently, a standard deviation of $\sigma = 1/\left(\sqrt{2}\alpha\right) = 3.2538$ Å for the Gaussian charge distribution. In the P^3M method a mesh is also needed. The contribution of the Gaussian charge distribution to the total force and energy can be calculated directly. In this case, we used a cutoff of 13 Å. A special technique is needed to find the contribution of the complementary reciprocal charge distribution. More specifically, we used a mesh of 20×20×20 grid points for a system of 2×2×3 silicalite-1 unit cells to solve the Poisson equation and finally to get the electric field. To solve the Poisson equation in a specific mesh, a fast Fourier transform was performed in the reciprocal charge density and then a reverse fast Fourier transform was also used to get the electric field. The parameters of the Gaussian and the mesh size were chosen so that the relative error in forces is less than 8.76×10^{-5}, as is expected from theory.[120] The reason we chose to work with 2×2×3 unit cells instead of the 3×3×3 we have used in the past, is the high computational cost when we increase the number of atoms (see above). On the other hand, we want to have large model systems to avoid possible size effects. To limit overall translational motion of the crystal in our finite simulation box caused by its collisions with the sorbate molecules, or to avoid a possible flying ice cube effect[121], we have used a spring constant of 5000 kcal/mol/Å to tether the center of mass of the crystal in the simulation box to a fixed point in space. This spring force was applied only to the crystal, not to the sorbate molecules.

More adjustments were needed to compare the influence on free energy profiles of the rigid electrostatic map versus explicit calculation of the electrostatic interactions with fluctuating charges. As we mentioned, the model of Vlugt and Schenk[104] and a modified model of Smirnov and Bougeard[110] was used to describe the flexibility of silicalite-1 and to keep its

atoms near their crystallographic positions. In these models, electrostatic interactions among the atoms of silicalite-1 were effectively incorporated in the spring constants, i.e., no intra-zeolite electrostatic interactions were considered. To apply P^3M in this type of model, a special trick was needed because of the presence of the sorbate benzene molecule. In particular, in every timestep of the simulation, we first calculated the electrostatic forces for the system silicalite-benzene and secondly we calculated the electrostatic forces for the silicalite alone. Then, we subtracted the bare electrostatic silicalite-1 forces from the forces of the system silicalite-benzene. As a result, the electrostatic forces exerted on the benzene were calculated using the P^3M, while only the electrostatic forces because of the benzene were exerted on the crystal. Lennard-Jones interactions between benzene and silicalite-1, parameterized as in Tables 4.1-4.2, were added to the electrostatic forces. A neighbor list was constructed for a radius of 15 Å and was updated every time an atom was moved by more than 1 Å.

4.4 Details of the simulation of flexible benzene in flexible silcalite-1

As already mentioned, the COMPASS[109] model assigns different charges to benzene than those used in the works of Snurr et al.[36] that describe well the Henry's constant and the isosteric heat of benzene in the crystal. To deal with this, we decided to scale up by 1.1829 the charges of silicalite-1 so as to make the electrostatic interactions between benzene and silicalite the same as in the previous models, while simultaneously keeping the intra-benzene electrostatic interactions consistent with those of the COMPASS model. This does not influence the silicalite-silicalite interactions, as the electrostatic contributions to those have been effectively incorporated in the spring constants. For all these simulations we used the wall potential and its parameters described in Section 4.2. However, for the explicit P^3M calculation we used a timestep of 1fs rather than the 0.5fs that was used for the static electrostatic map calculations. In this way, fewer MD steps were needed for the same real time in the explicit P^3M calculations. In addition, a RESPA (Reference System Propagation Algorithm)[122] technique was used in integrating the equations of motion for the flexible benzene model, using an inner timestep of 0.5fs for the spring and the wall potential forces and an outer timestep of 1fs for the remaining forces. The total wall potential force, dependent on the center of mass position, was assigned to each atom of benzene

proportionally to its mass. In this way, the wall causes the same acceleration on all benzene atoms and no rotational motion is induced on the benzene molecule by the walls.

4.5 Molecular Dynamics Simulation details

We have used the Verlet[123,124] algorithm for moving the zeolite atoms and the Fincham[125] leap-frog scheme to move the rigid benzene. We thermostat the zeolite atoms only by rescaling of their velocities. With a timestep of 0.5fs, benzene manages to stabilize its translational and rotational temperature as it exchanges energy with the flexible crystal. To ensure this, we always calculate the distribution of speeds of the benzene center of mass. In all cases (see Figure 4.2) this was Maxwell-Boltzmann, as it should be in the NVT ensemble. Thus, the flexible crystal operates as a heat bath for the sorbate. Because the rigid benzene has only 6 degrees of freedom (3 translational of its center of mass and 3 rotational) instead of the 36 degrees of freedom that a flexible benzene would possess, the thermostating is difficult to establish in every area of the silicalite-1 channels. However as we can see in Figure 4.2, it is established in our simulations for the Vlugt and Schenk[104] model we have used.

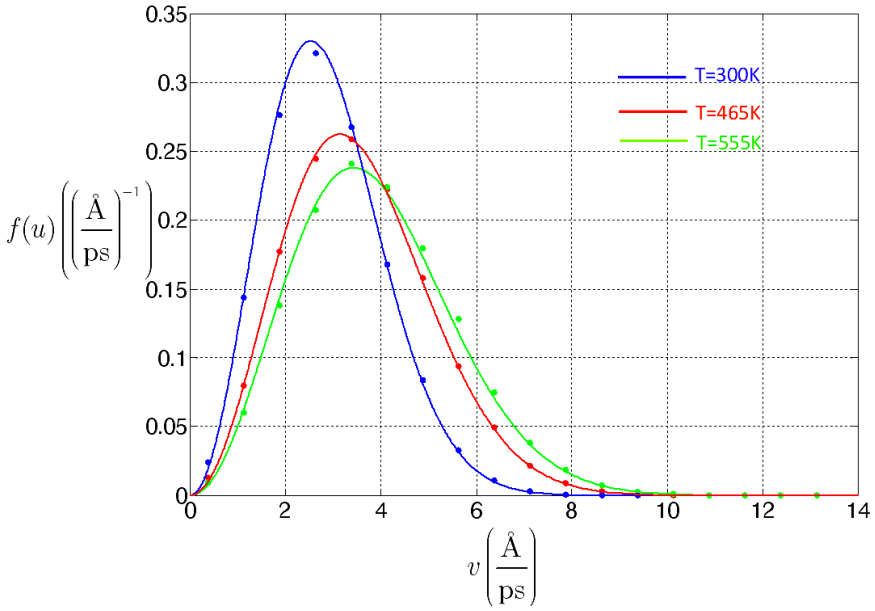

Figure 4.2 Points: Speed distributions of the benzene center of mass in areas with large slope of local free energy during our simulations for 300K, 465K, 555K. The lines are Maxwell-Boltzmann distributions at the corresponding temperatures.

To perform our simulations, we first had to introduce the geometry and topology of silicalite-1 in our program. From crystallography data and the symmetry rules of the Ortho Pnma structure we constructed the contents of 3×3×3 cells with periodic boundary conditions. The unit cell parameters were a = 20.07 Å, b = 19.92 Å, c = 13.42 Å, so the dimensions of our periodic simulation box were L_x= 3a, L_y=3b, L_z=3c along the x, y, z directions, respectively.

We chose to work with 27 unit cells in our box with periodic boundary conditions in order to minimize model system size effects. During our initial simulations we actually noticed a drift of the zeolite, which is attributed to the collisions of the benzene with the silicalite-1 tetrahedra. Clearly, this would not happen in the real material for benzene at infinite dilution, and is undesirable. To deal with this problem, we moved the zeolite and the sorbate every 10 MD simulation time steps so that the center of mass of the zeolite remained the same as in the beginning of the simulation. In addition, we subtracted from the velocities of silicalite-1 and benzene the silicalite-1 center of mass velocity. Use of a large model system ensures that this correction for the drift does not influence the local behavior of the system. In addition, the bigger the system, the smaller the drift. A system of 27 unit cells was found to be large enough for the measures described above to eliminate drift. If no correction for the drift were applied, the diffusivity of the benzene would be overestimated, as we shall see later.

4.6 Results and Discussion

From our first simulations with both flexible and rigid silicalite, we observed that benzene prefers to reside in the channel intersection regions of silicalite-1, contrary to smaller molecules such as Xenon[62] and the lower alkanes, which prefer to reside in the interiors of channel segments. This is also in agreement with the computational works of Snurr et al.[36] and Forester and Smith[39].

We focus on rigid benzene in flexible silicalite-1, which are more reliable, because our flexible crystals can thermostat benzene.

Following **Step 2** of the calculation, as described in Chapter 2, we have prepared video 2S. This video shows how we began from the 3-D free energy profile of the intersection and, while moving the walls, we discovered new 3-D free energy maps that we stitched together to obtain the total 3-D free energy map $A(\mathbf{r}_{CM})$. The free energy profiles we have obtained through the procedure described in Chapter 2 are presented in Figures 4.3 and 4.4. In these

Figures, one can see the sorption states in red color, while in blue color one sees areas that are rarely visited by the benzene.

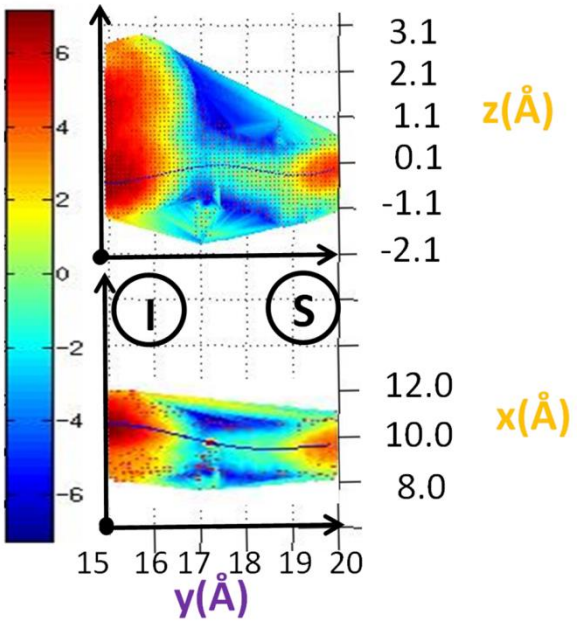

Figure 4.3 Cross-section of 3-D free energy profiles to planes for the straight channel at T=300K. The color bar is in units of $-k_BT$.

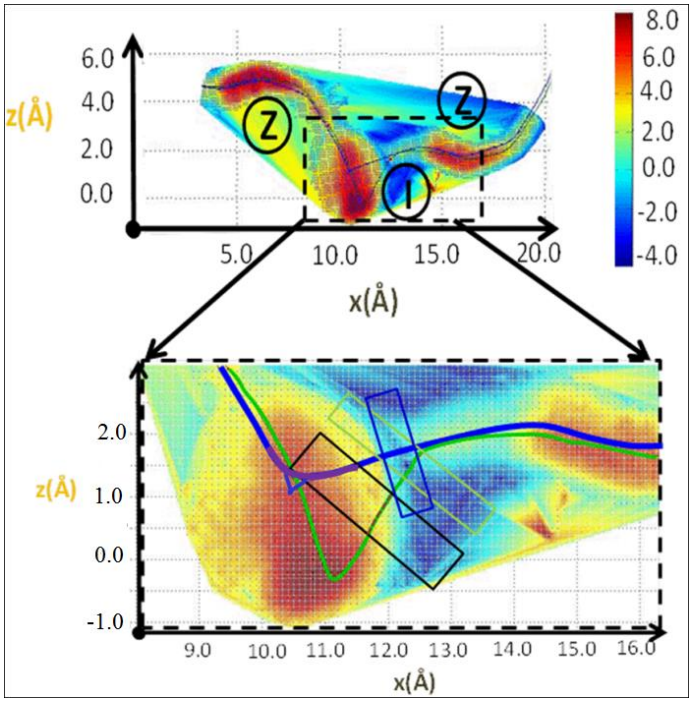

Figure 4.4 Cross-section of 3-D free energy profiles in the x-z plane going through a set of sinusoidal channels at y=14.94 Å. The color bar is in units of $-k_BT$. The blue line is our initial path. The purple is a smooth line added to this initial path. The green line is just another path that could be used. The boxes show the area where the benzene center of mass is allowed to go if walls are used in the indicated parts of the paths.

Because of the symmetry of silicalite, we have calculated the profile in the straight channel over a quite restricted area. However, we have calculated the 3-D free energy profile for the sinusoidal channel over a larger region than was necessary given the existing symmetries, to show that periodicity is not satisfied fully. In Figure 4.4 we can see the sorption states of benzene, which are indicated with red color. We discern two sorption states in the sinusoidal channel. One state inside the sinusoidal (or else zig-zag) channel segment, which we will symbolize with Z, and one more in the intersection, symbolized by I. From the colors, we see that the most preferable position is the intersection. We can see that state Z has different color on the left than the same state on the right. This is consequence of not fully accurate stitching of the free energy profiles in three dimensions. Despite these limitations, we can clearly see that it is easier, upon leaving an intersection region, to enter the sinusoidal channel segment to the left of the intersection (we will call this route a) than the sinusoidal channel segment to the right of the intersection (we will call this route b). In Figure 4.3 we see a cross-section of the 3-D free energy profile going through a straight channel. Here we discern two sorption states. The state of the intersection (I) we encountered in the case of the cross-section going through the sinusoidal channel, and one state inside a straight channel segment, symbolized as (S).

An example of an undesirable projection can be seen in the lower part of Figure 4.4. With green color we have sketched an arbitrary path. We see that, for this path, points are projected in the saddle point region that should not be (see points inside the green box). The green path of Figure 4.4 is a bad path. Benzene will visit the red area of the 3-D free energy profile within the black box much more frequently than the area near to the green path. The area in the black box of Figure 4.4 is not affected by the walls; however, because of the distance criterion, not all the points in the black box are projected on the path interval lying inside it. As a result, the free energy in this area of the 1-D free energy profile for the green path cannot be accurately computed. Probability values will need a very long time to be statistically equilibrated and the walls do not help in this, as they let benzene visit areas of higher probability. Our choice for this path was to modify the initial path (blue line in Figure 4.4) by smoothing a 1^{st} order discontinuity in the intersection region using a spline (purple color in Figure 4.4). First order discontinuities along paths are undesirable, as the normal vector of the path, **i**, cannot be defined at such points and, consequently, the projection and the free energy profile are not defined. The initial path can describe well the area near the saddle point. The points of the path are chosen to have a distance of 0.05 Å from each other.

For lower distances (higher resolution), we obtained more noisy results in the 1-D free energy profile extracted from the $A(\mathbf{r}_{CM})$ map via projection onto the path.

Following **Step 3** of Chapter 2, we studied the orientations adopted by benzene in each region of the intracrystalline space. We study orientation through a unit vector normal to the benzene plane, depicted schematically as a red vector in the explanatory graphic of Figure 4.5. From Figures 4.5, 4.6a, we can compute the rotational free energy profile of benzene in specific areas along the path. We see that it is possible for the benzene to rotate by 180 degrees and acquire the same position, as expected from its symmetry. It is also obvious that there are specific orientations in the straight and in the sinusoidal channels which benzene does not prefer (the sphere indicating the orientational distribution of the tip of the normal vector is blue in these areas). We compare our predictions for the benzene orientation against the orientations reported by Goyal et al.[126] on the basis of powder neutron and X-ray diffraction measurements. Predicted orientations within the S and the Z channel states are practically coincident with the measured ones. In the intersection (I), we have one orientation very similar to the one reported by Goyal et al.,[126] but also a second one that is slightly different, as we can see in Figures 4.4 and 4.5. The rotational free energy profiles show that benzene has one orientational state when located in most areas within the sinusoidal and straight channels. In case there are two orientations, as happens near the saddle points of $A(\mathbf{r}_{CM})$, the free energy barrier between them is small relative to $k_B T$ and can be overcome readily at the considered temperatures. In the intersection we also have two different orientations with low barrier between them, which means that they can be assigned as one state.

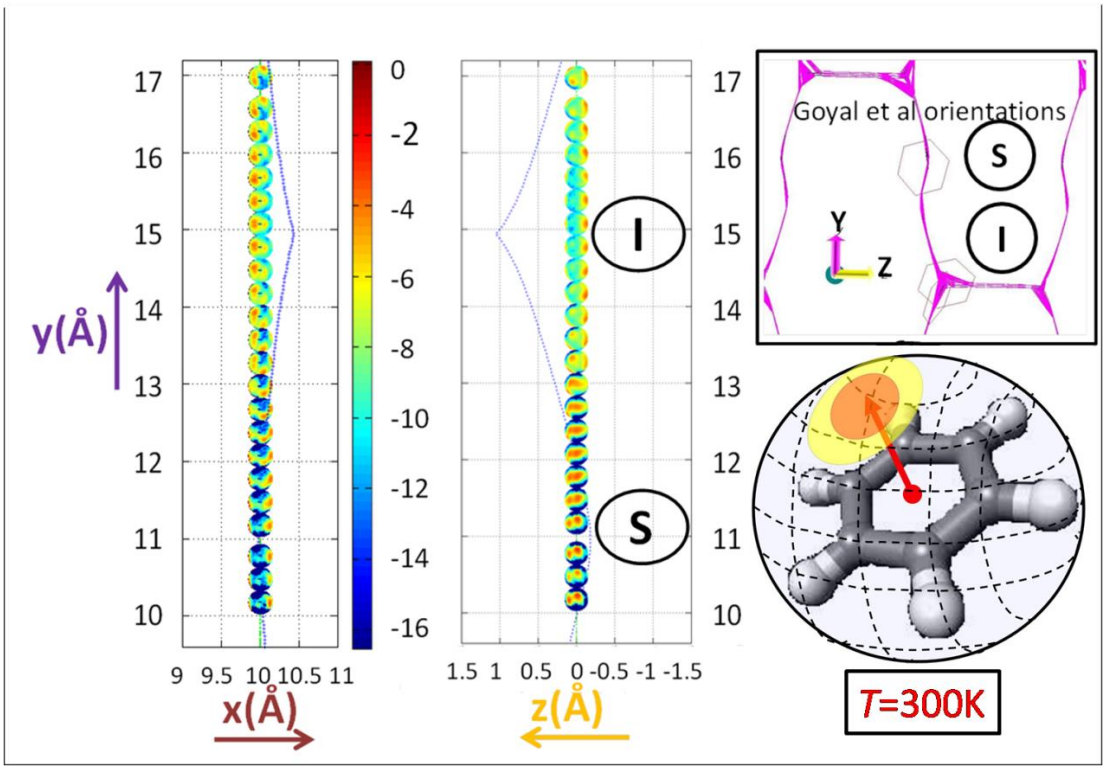

Figure 4.5 Local free energy associated with the orientational distribution of benzene at various center of mass positions along the straight channel at 300 K and experimentally determined orientations of Goyal et al.[126] Color bar is in units of ($-k_BT$).

Based on these graphs we can decipher the way in which a transition takes place from the intersections to the channel states. Benzene changes its orientation as it goes near the saddle points. Based on the graphs discussed above, we can proceed with reducing the free energy profile to 1-D. Also, we expect that the initial orientation of the benzene will not influence its final distribution of orientations in each run. Figure 4.6b helps us associate the x coordinate with the curvilinear position coordinate ξ_{zig} measured along the contour of the transition path going through a sinusoidal path and so to associate the 1-D free energy profiles (Figures 4.7- 4.10) with the orientation and the exact position along the path. No corresponding figure is presented for the straight channel, as it is not needed. The transition path considered is a straight line consisting of points with coordinates (x=10.00 Å, y=y, z=0.0), where y is the only variable that can change values, as we mentioned before. This path is the same as the initial one for the straight channel.

In Figures 4.7b and 4.8b one can see the fragments of the one-dimensional free energy profile $A(\xi)$ which are stitched together by vertical translation to give the 1-D free energy profile. Video 3S provides an animated description of the stitching process.

In Figures 4.7 and 4.8, we can see that the points from different overlapping fragments are very close to each other. We remind the reader that we used path intervals consisting of points that were 0.05 Å apart. With a smaller distance we would have more points to stitch but with more noise, while with a larger distance than 0.05 Å we would have less points to stitch, which gives rise to difficulties in areas with large slope of free energy profile, such as in the areas with ξ_{zig} =13-14 Å of the sinusoidal channel.

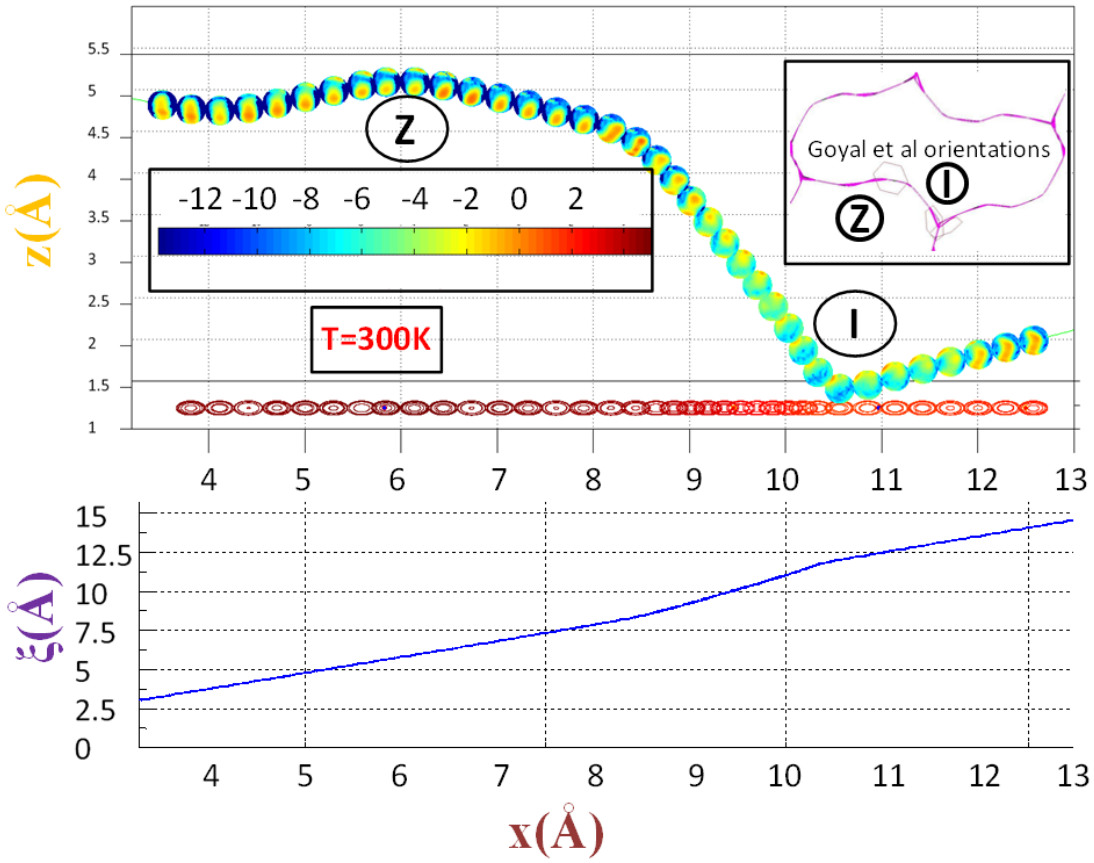

Figure 4.6 Top, a: Local free energy associated with the orientational distribution of benzene at 300 K at various positions along the sinusoidal channel in a unit cell. Bottom, b: Graph describing the relationship between the reaction coordinate ξ and the x coordinate along the sinusoidal path we used.

It is interesting to undertake a comparison of Figures 4.7 and 4.9 with Figures 4.3 and 4.4 for the 3-D free energy profiles as well as with Figures 4.5 and 4.6 for the orientational distributions. This comparison confirms the existence of 3 states (I,S,Z). Comparing our result with Forester and Smith's[39] free energy profiles and with the corresponding profiles obtained from the rigid zeolite model, we can see that, in our flexible silicalite, some small barriers inside the channels predicted by Forester and Smith[39] have disappeared. These barriers also exist in rigid free energy profiles. We attribute this change to the flexibility of

the Si-O-Si bond angle. The Vlugt and Schenk[104] model has no bending potential for this angle. In addition, artifactual barriers can arise in 1-D free energy profiles as a side effect of a path that does not curve well and because of the distance dependence of the definition of a projection. The rate constant depends on the shape of the free energy profile and not only on the difference between saddle point and minimum, as Eq. (2.9) shows. In the graphs obtained through stitching we see that the periodicity of the profile across an entire unit cell is satisfied. This provides additional confirmation that the stitching was successful.

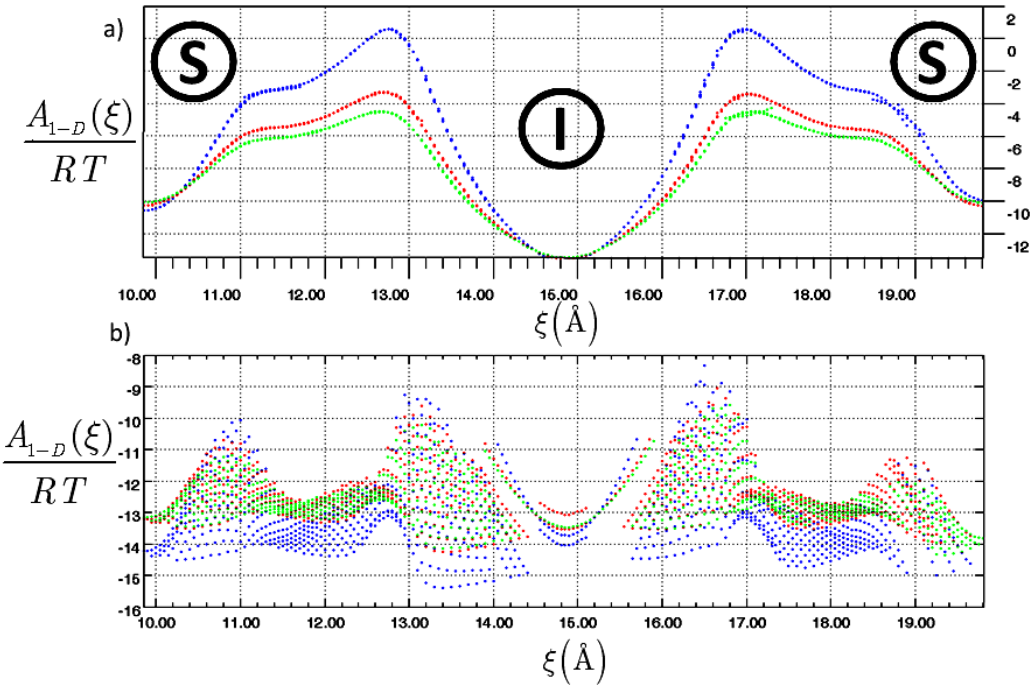

Figure 4.7 a) Free energy profiles for benzene, in *RT* units, as functions of the reaction coordinate at temperatures of i) 300K (blue) ii) 465K (red) iii) 555K (green) along the straight silicalite-1 channel for a crystal described by the DHFF force field and b) free energy fragments of the area between the walls (where there is no influence of the bias potential of the wall), from which the 1-dimensional local free energy profile has been derived by the stitching process. S and I mark sorption sites (free energy minimum regions) in the straight channels and intersections.

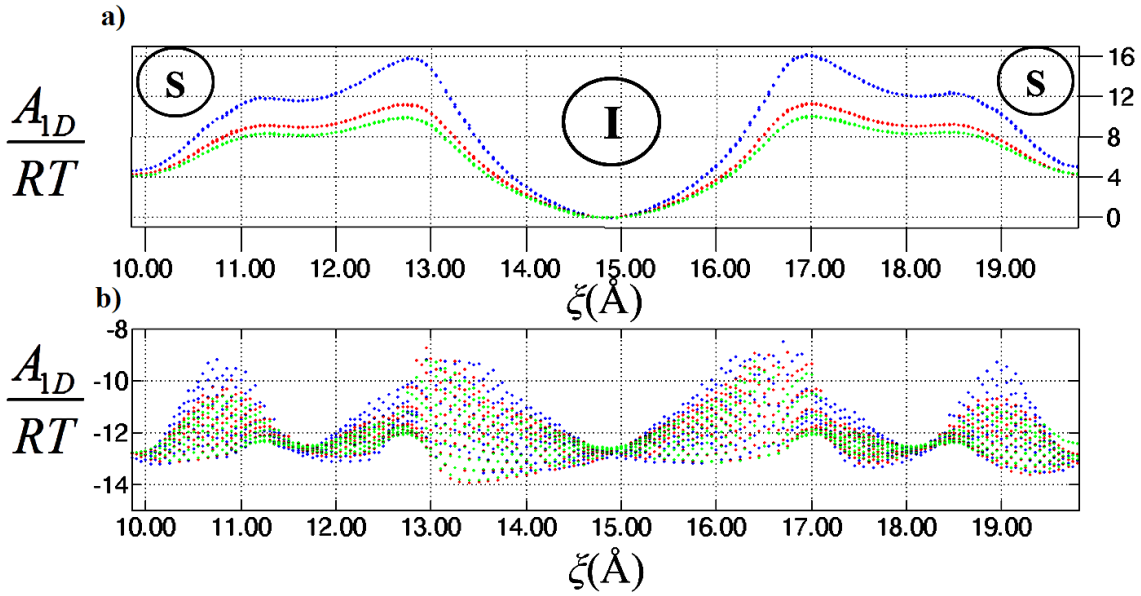

Figure 4.8 a) Free energy profiles for benzene, in *RT* units, as functions of the reaction coordinate at temperatures of i) 300K (blue) ii) 465K (red) iii) 555K (green) along the straight silicalite-1 channel for a crystal described by the SGVFF force field and b) free energy fragments of the area between the walls (where there is no influence of the bias potential of the wall), from which the 1-dimensional local free energy profile has been derived by the stitching process. S and I mark sorption sites (free energy minimum regions) in the straight channels and intersections.

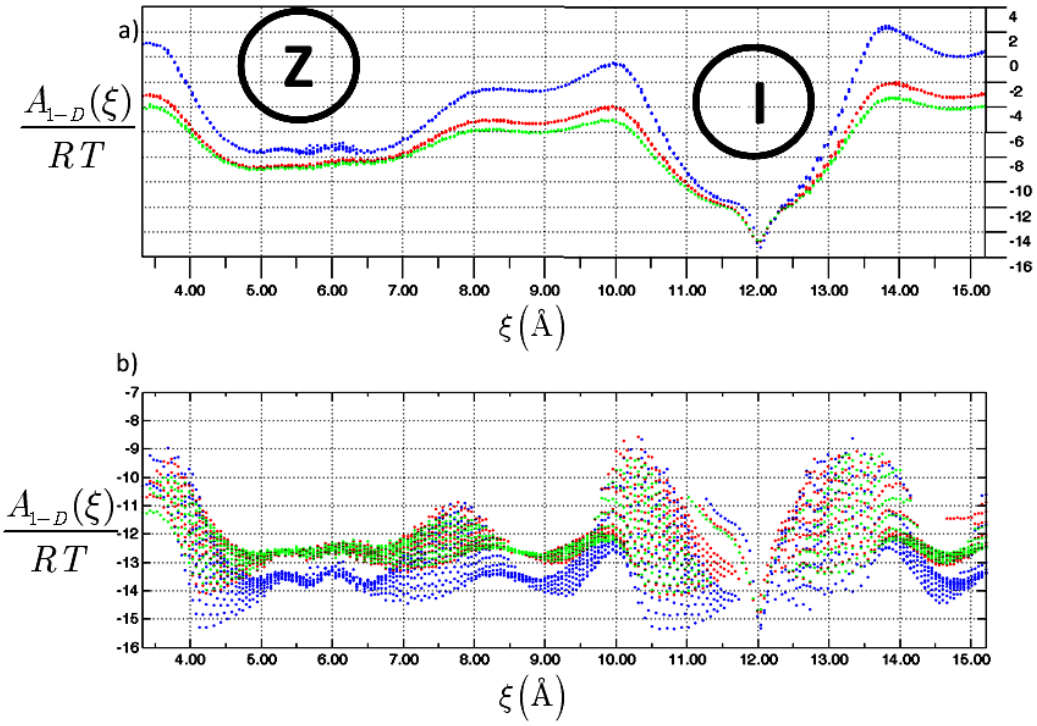

Figure 4.9 a) Free energy profiles for benzene, in *RT* units, as a function of the reaction coordinate at temperatures of i) 300K (blue) ii) 465K (red) iii) 555K (green) along the sinusoidal silicalite-1 channel for a crystal described by DHFF force field and b) free energy fragments of the area between the walls (where there is no influence of the bias potential of the wall), from which the 1-dimensional local free energy profile has been derived by the stitching process. Z and I mark sorption sites (free energy minimum regions) in the sinusoidal channels and intersections.

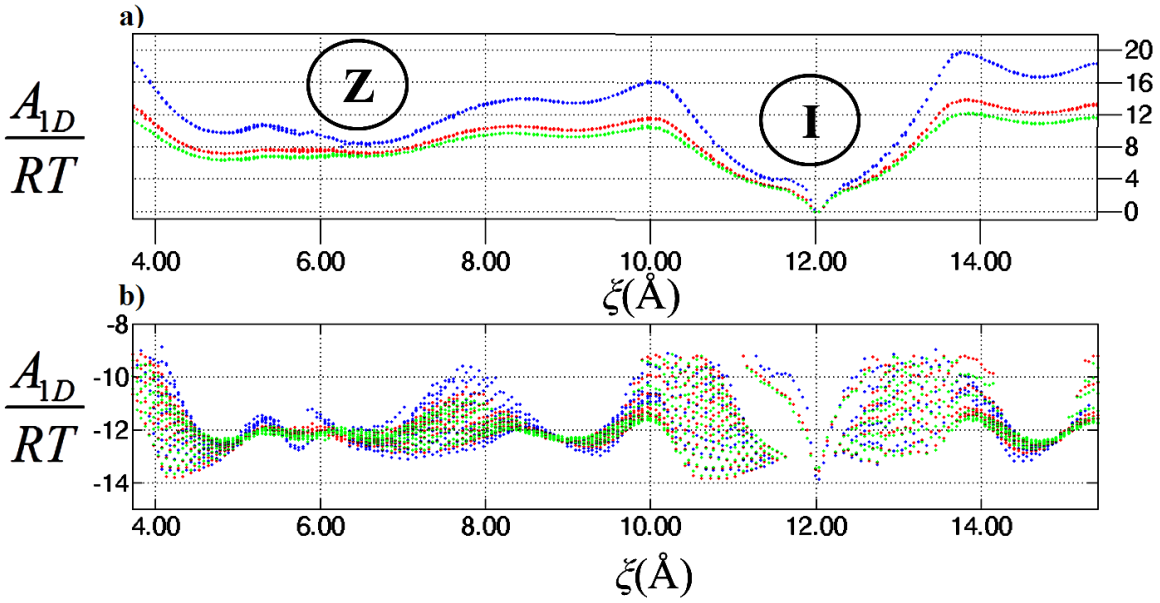

Figure 4.10 a) Free energy profiles for benzene, in *RT* units, as a function of the reaction coordinate at temperatures of i) 300K (blue) ii) 465K (red) iii) 555K (green) along the sinusoidal silicalite-1 channel for a crystal described by SGVFF force field and b) free energy fragments of the area between the walls (where there is no influence of the bias potential of the wall), from which the 1-dimensional local free energy profile has been derived by the stitching process. Z and I mark sorption sites (free energy minimum regions) in the sinusoidal channels and intersections.

From the three sets of free energy profiles we have calculated the rates for elementary transitions between states according to Eq. (2.14) at each of the three temperatures mentioned in Table 4.7, 4.8. This would cause the majority of trajectories which begin from the saddle point to be successful and limit barrier recrossing events.[68]

Table 4.6: Definitions of states used in rate constant calculation for the system benzene-silicalite-1 (SGVFF)

State	ξ(Å)
I (Figure 4.8)	(12.80,17.08)
I (Figure 4.10)	(9.96,13.80)
S (Figure 4.8)	(9.96,11.10)∪(18.60,19.92]
Z (Figure 4.10)	(3.50,8.56)

Table 4.7: Rate constants of transitions of benzene in silicalite-1 (DHFF)

Transition		**Temperature**		
From	**To**	300K	465K	555K
I	S	5.24×10^{5}	3.314×10^{7}	1.13×10^{8}
	$Z_{(route\ a)}$	1.76×10^{6}	6.18×10^{7}	2.01×10^{8}
	$Z_{(route\ b)}$	9.382×10^{4}	9.51×10^{6}	3.295×10^{7}
S	I	1.887×10^{7}	1.09×10^{9}	3.72×10^{9}
Z	I	3.04×10^{8}	3.22×10^{9}	8.66×10^{9}
	I	1.617×10^{7}	4.97×10^{8}	1.41×10^{9}

Table 4.8: Rate constants of transitions of benzene in silicalite-1 (SGVFF)

Transition		**Temperature**		
From	**To**	300K	465K	555K
I	S	1.284×10^{5}	1.1755×10^{7}	4.6391×10^{7}
	$Z_{(route\ a)}$	3.776×10^{5}	2.324×10^{7}	5.916×10^{7}
	$Z_{(route\ b)}$	8.77×10^{3}	2.08×10^{6}	1.064×10^{7}
S	I	2.21×10^{7}	1.0818×10^{9}	3.7563×10^{9}
Z	I	2.53×10^{8}	3.615×10^{9}	5.09×10^{9}
	I	5.881×10^{6}	3.239×10^{8}	9.16×10^{8}

Table 4.9: Residence Probabilities of benzene in silicalite-1 (DHFF)

Probabilities	**Temperature**		
	300K	465K	555K
I	0.9675	0.9528	0.949
S	0.0269	0.029	0.0288
Z	0.0056	0.0182	0.0222

Table 4.10: Residence Probabilities of benzene in silicalite-1 (SGVFF)

Probabilities	**Temperature**		
	300K	465K	555K
I	0.9928	0.9830	0.9766
S	0.0058	0.0107	0.0121
Z	0.0015	0.0063	0.0114

Table 4.11: Mean Potential Energies and isosteric heat of sorption for benzene in silicalite-1 (DHFF)

Potential Energies	**Temperature**		
kJ/mol	300K	465K	555K
I	–54.7794	–50.1793	–48.007
S	–58.8209	–54.3226	–52.0768
Z	–53.0205	–49.3032	–47.6678
Q_{st}	57.37242	54.14952	52.73095

Table 4.12: Mean Potential Energies and isosteric heat of sorption for benzene in silicalite-1(SGVFF)

Potential Energies	**Temperature**		
kJ/mol	300K	465K	555K
I	–54.5815	–50.4817	–48.5095
S	–53.949	–50.9064	–49.04
Z	–50.269	–47.3384	–45.97755
Q_{st}	57.071	54.33245	53.1061

*Q_{st}=56kJ/mol for benzene in rigid silicalite-1 at 250K [50]

**experimental values for benzene $Q_{st} \in [51.3,58.0]$ kJ/mol [50]

Results for the low-occupancy self-diffusivity obtained with the KMC algorithm are presented in Figure 4.11.

The results obtained at each temperature from KMC and MESoRReD are in excellent agreement. Those from MESoRReD are presented in Figure 4.12. From these two methods we calculated the diffusion coefficients shown in Table 4.13, which satisfy the Kärger relationship[42]

$$\frac{c^2}{D_{zz}} = \frac{a^2}{D_{xx}} + \frac{b^2}{D_{yy}} \qquad \text{Eq. (4.1)}$$

Knowing the diffusivity for each of these three temperatures, allows us to calculate the diffusion prefactor D_0, and the activation energy E_a in the Arrhenius expression, Eq. (4.2).

$$D=D_0\exp(-E_a/RT) \qquad \text{Eq. (4.2)}$$

We have found $D_0^{TST}= 1.8977\times10^{-8}$ m^2s^{-1} and $E_a^{TST}= 29.93$ kJ/mol. Experimental results[23] give $D_0= 2.30\times10^{-9}$ m^2s^{-1} and $E_a= 30$ kJ/mol.

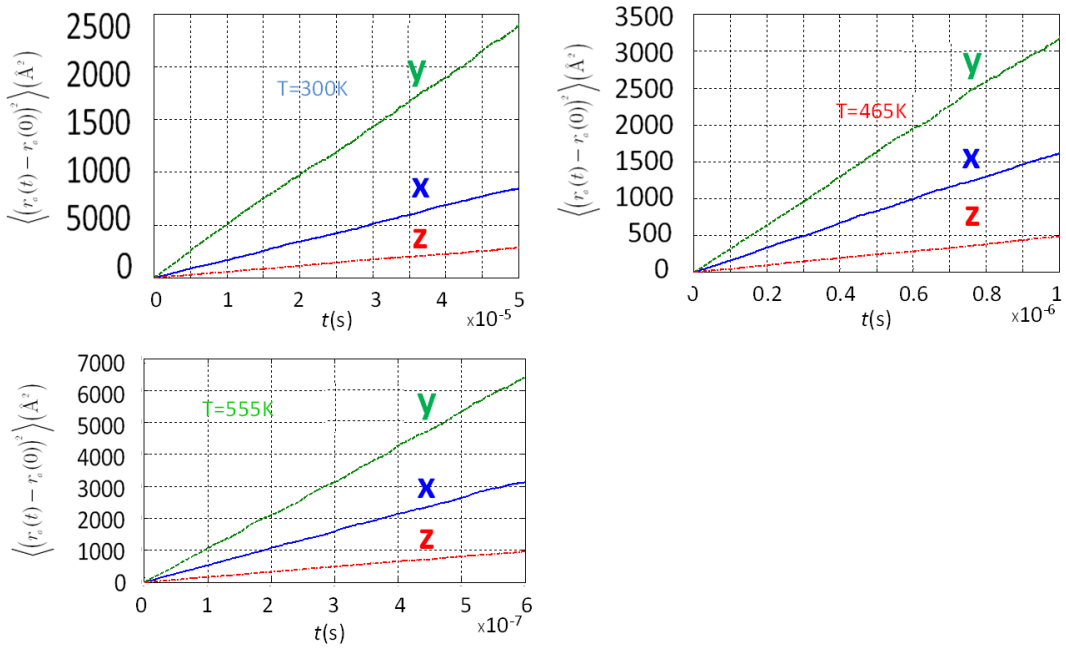

Figure 4.11 Mean square displacement graphs for 300K, 465K and 555K as a function of time

Other experimental results for diffusivity values available in the literature are presented in Figure 4.13, along with our predictions. The neutron spin-echo (NSE) results were obtained at the Institut Laue-Langevin using two different spectrometers. The first measurements were performed on IN11 with an incident neutron wavelength of 7.2 Å.[23] More recent experiments were carried out on IN15 with a higher resolution (incident wavelength of 14.5 Å).[129] The concentrations in benzene were the same in both studies, 3 molecules per unit cell, but silicalite was used in the recent experiments instead of ZSM-5.

In addition to diffusion coefficients by TST, dynamically corrected diffusion coefficients were also calculated after computing transmission coefficients for 300K, 465K and 555K. To obtain a transmission coefficient, we first analyzed the trajectories we had accumulated from simulations around the area of the saddle point. From these trajectories, whenever benzene was projected on the saddle point (ξ=16.95Å in the straight channel), we saved the velocities and the position vectors of all silicalite-1 atoms, the position vector, as well as the quaternions and the angular momentum of the benzene molecule only if 50 steps (1 step=0.5fs) at least had elapsed since the previous save and only if the *y* component of the benzene center of mass velocity was smaller than 0. Next, we used the first 270, 460, 530 saved configurations for 300K, 465K and 555K, respectively, as initial configurations for

new molecular dynamics runs in the absence of confining walls. These runs had a duration of 10 ps each, with a time step of 0.5fs; they quickly thermalized in one of the two states coming together at the saddle point. As we can see in Figure 4.2, the dynamical correction factor, obtained as discussed by Chandler and Voter,[67,68] quickly converged to $f_{I\leftrightarrow S,300K} = 0.81$, $f_{I\leftrightarrow S,465K} = 0.88$ and $f_{I\leftrightarrow S,555K} = 0.91$ for 300 K, 465 K and 555 K, respectively. So, transmission coefficients for rate constants are close 1, as was anticipated because of high and sharp barriers near the saddle points and the choice of a path that describes the dividing surface well.[59]

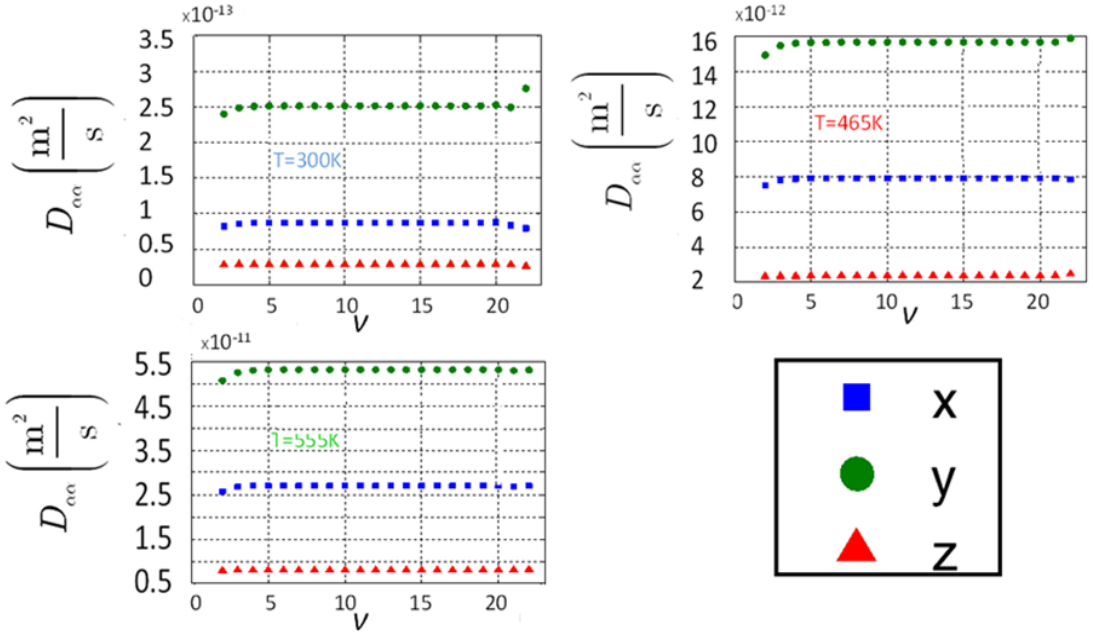

Figure 4.12 Plots for 300K, 465K and 555K of diffusion coefficient per direction as a function of *v*, as obtained from MESoRReD Eq. (3.46).

If we assume that the transmission coefficient at each temperature is the same for the remaining 2 transitions involving the sinusoidal channel, then from Eq. (3.46) we have an estimate of the self-diffusion coefficient

$$D = fD^{TST} \qquad \text{Eq. (4.3)}$$

Eq. (4.3) is a consequence of Eq. (3.46), if we consider that the eigenvalues of a scalar multiple of a matrix is the corresponding multiple of the eigenvalue. Using Eq. (4.3) we calculated the dynamically corrected diffusivities D_{300K}=0.987 $\times 10^{-13}$ m^2s^{-1}, D_{465K}=7.58 $\times$ 10^{-}

^{12} m^2s^{-1}, D_{555K}=2.672 × 10^{-11} m^2s^{-1}. Note that Figure 4.12 displays only the TST diffusivities we calculated from our simulations, which are slightly different from the dynamical corrected ones.

Table 4.13: Self-Diffusion coefficients of benzene in silicalite-1 (DHFF)

Self-Diffusivity (m^2s^{-1})	**Temperature**		
	300K	465K	555K
D_{xx}	8.67×10^{-14}	7.90×10^{-12}	2.707×10^{-11}
D_{yy}	2.50×10^{-13}	1.56×10^{-11}	5.3×10^{-11}
D_{zz}	2.895×10^{-14}	2.36×10^{-12}	8.6×10^{-12}
D	1.218×10^{-13}	8.62×10^{-12}	2.937×10^{-11}

Table 4.14: Self-Diffusion coefficients of benzene in silicalite-1 (SGVFF)

Self-Diffusivity(m^2s^{-1})	**Temperature**		
	300K	465K	555K
D_{xx}	8.568×10^{-15}	1.89×10^{-12}	8.869×10^{-12}
D_{yy}	6.323×10^{-14}	5.731×10^{-12}	2.247×10^{-11}
D_{zz}	3.38×10^{-15}	6.378×10^{-13}	2.855×10^{-12}
D	2.50×10^{-14}	2.75×10^{-12}	1.14×10^{-11}

From Figure 4.13 we can see that we overestimate the diffusion coefficient in comparison to all experiments for the DHFF model, while SGVFF shows excellent behavior for 300K, without being able to predict an activation energy near to experiment.[23,25-27] This is mainly due to the model we have invoked to describe the flexibility of the silicalite-1. It seems advisable to try other models, which describe better the volumetric properties of silicalite-1, in the future.

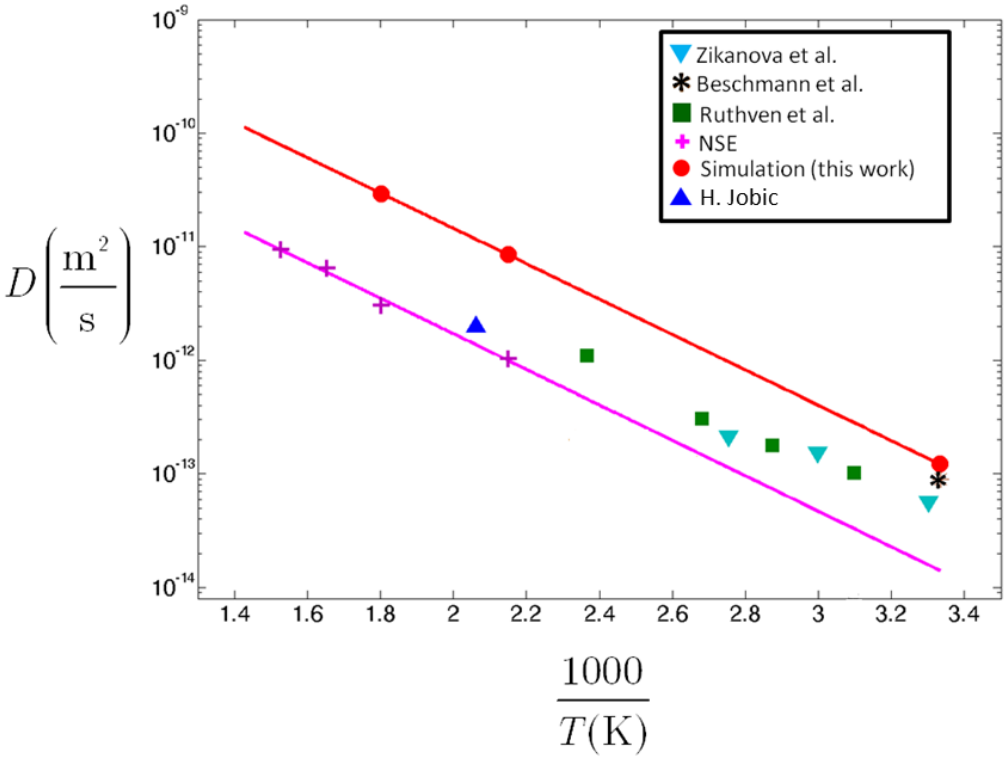

Figure 4.13 Diffusion coefficients calculated in this work for DHFF force-field and measured experimentally. Brown color shows our calculations and measurement.

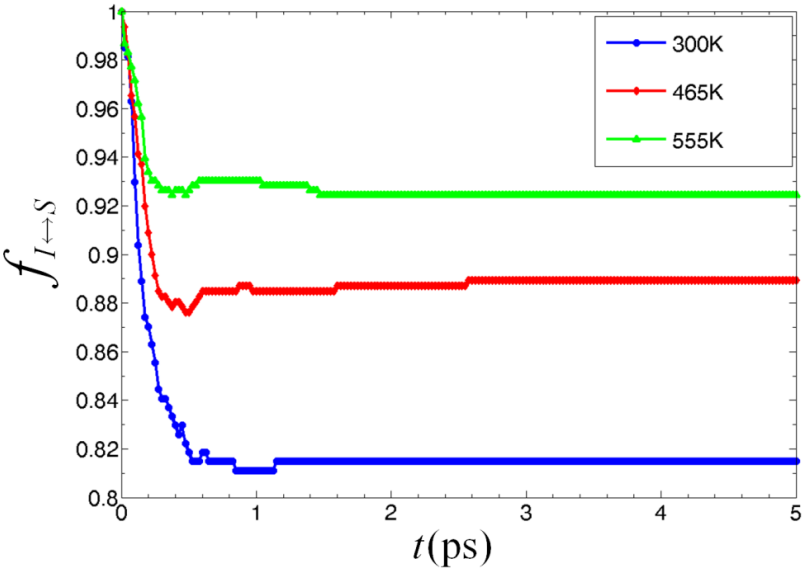

Figure 4.14 Transmission coefficient *f* as a function of time and temperature for the transition between Intersection (I) and Straight channel (S), as determined through MD runs initiated at the saddle point.

Chapter 5

Sensitivity of free energy profiles to i) electrostatics calculation and ii) flexibility of the sorbate

In chapter 4, we saw the results coming from the use of a static electrostatic map to describe the electrostatic interactions between silicalite-1 and benzene in order to enhance the speed of the calculations. This means that partial charges were considered fixed at the crystallographic positions corresponding to mechanical equilibrium of the pure crystal,[106] while the atoms of the crystal were able to move around these positions as dictated by a flexible model force field. The work of Clark and Snurr[45] showed that it is necessary for the atoms of the crystal to oscillate around their crystallographic positions, otherwise the predicted Henry's law constant will deviate significantly from experimental values. Having this in mind, the model of Vlugt and Schenk[104] was used to describe the flexibility of silicalite-1 and to keep its atoms near their crystallographic positions. In the present chapter we have decided to check the deviation in free energy profiles when we use a static electrostatic map versus explicit calculation of all electrostatics from moving partial charges on the zeolite. The latter explicit calculation is not trivial if we want to keep the atoms around their crystallographic positions, and special computational provisions are needed. The details of this explicit calculation are outlined in the chapter 4.

From Figure 5.1 one can see that molecular simulation using a static electrostatic map is 8 times faster in 1 CPU than a simulation which uses explicit P^3M[117-119] calculation, even though the former was conducted on a larger number of atoms (3×3×3 silicalite unit cells instead of 2×2×3 of the P^3M calculation). The static electrostatic map calculation is still faster, even though we use 8 CPUs in the P^3M calculation. At the same time the free energy profiles are practically the same, as one can see from Figure 5.2. A large number of MD simulations are needed to obtain fragments of the free energy profile. It is preferable to conduct many serial (1 CPU) simultaneous simulations than parallel ones on 8 CPUs, as Figure 5.1 shows that, in this way, we can achieve significant savings in computer time.

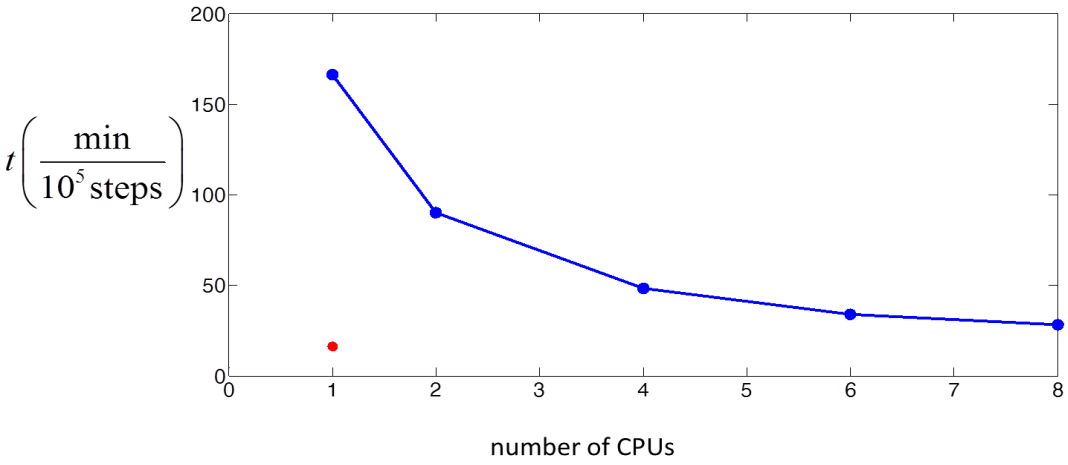

Figure 5.1 Computation time required a) for the system benzene-27 silicalite unit cells using a static map for the electrostatics and a time-step of δt=0.5fs (red color); b) for the system benzene-12 cells (blue color) with explicit summation of electrostatic interactions from moving partial charges on the zeolite and a time-step of δt=1fs. All calculations conducted on Dell PowerEdge 1950 QUAD Core Servers with Intel XEON E5430 processors at 2.66 GHz and 16GB Memory. It must be noted that the subroutine which projects the center of mass of the sorbate molecule has been written for one only processor. However, the calculation of electrostatic interactions is by far the limiting step in all calculations.

In addition to the simulations of the rigid benzene in flexible silicalite-1 with a) static electrostatic map and b) explicit calculation of electrostatic interactions with moving charges on the atoms, we decided to study the influence of the benzene flexibility on the free energy profiles. To do this, we used the Consensed-phase Optimized Potentials for Atomistic Simulation Studies (COMPASS) model to describe intra-benzene interactions.[109] Because of the high computational requirements of the P^3M calculation (see Figure 5.1), 1-dimensional free energy fragments were calculated for the range of 11.6 to 15.1 Å of the ξ coordinate of the straight channel. This range was chosen because of the large slope of free energy profiles observed inside it, which make it the most sensitive to flexibility issues.

The free energy profiles calculated from the previous simulations are illustrated in Figure 5.2. From these results one can see that neither the use of a static electrostatic map nor the flexibility of benzene influence at all the 1-dimensional free energy profile. In addition, combining Figure 5.2 with Figure 5.1, one can see that the use of a static electrostatic map

and a rigid benzene is the most profitable method for simulating the sorption and diffusion of benzene inside silicalite. Similar behavior is expected for simulation of sorbates in crystals at such loadings of sorbate that a phase transition of the crystal does not occur. The method of using a static electrostatic map along with Lennard-Jones interactions which follow the oscillations of the atoms of the crystal can be very useful in the simulation of systems with very large unit cells, such as MIL100[128], especially when one examines the diffusion of molecules with similar kinetic diameter as the MIL100 window. In these systems the diffusants of interest can be drug molecules, as MIL100 crystals have been developed having drug delivery systems in mind.

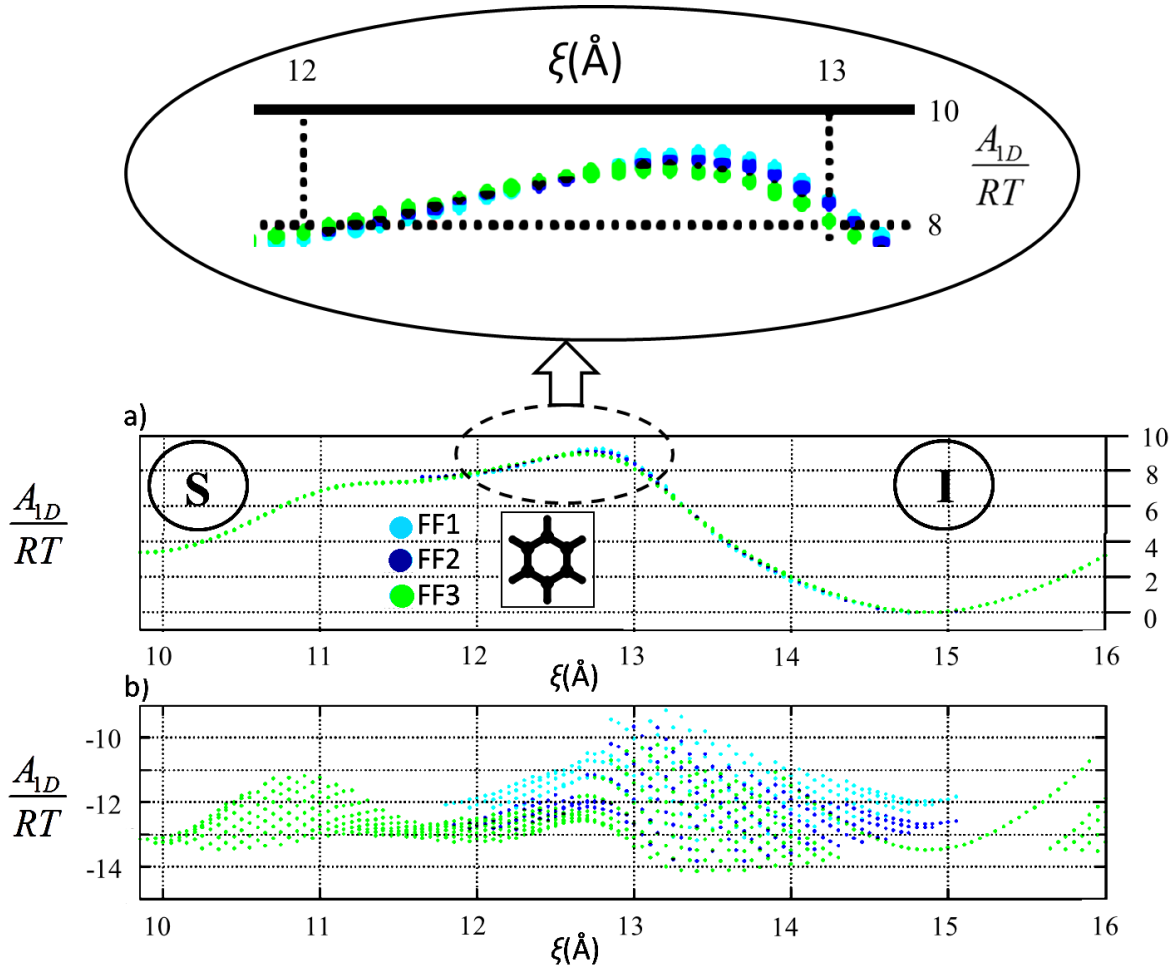

Figure 5.2 a) Local 1-dimensional free energy profile of benzene in silicalite-1 in the straight channel for a temperature of 555K using FF1(analytical calculation of electrostatic interactions with a flexible zeolite framework and a rigid benzene), FF2(analytical calculation of electrostatic interactions with a flexible zeolite framework and a flexible benzene), FF3(static electrostatic map and rigid benzene). b) free energy fragments of the area between the walls (where there is no influence of the bias potential of the wall), from which the 1-dimensional local free energy profile has been derived by the stitching process. ξ is the reaction coordinate along the straight channel. The labels S and I indicate the sorption sites (free energy minimum regions) corresponding to the benzene center of mass residing in the straight channel and in the channel intersection region, respectively

Chapter 6

Application of the new modified umbrella sampling methodology to the system of para-xylene – silicalite-1 at infinite dilution

6.1 Molecular dynamics details

To simulate p-xylene in silicalite-1 we have used the same algorithms (Verlet - rescale thermostat, Fincham),[123-125] timesteps, wall parameters, and reaction coordinate paths as in Chapter 4 for benzene. The parameters of the rigid p-xylene (charges, bond lengths, Lennard-Jones parameters) are described analytically in the Tables 6.1, 6.2 ; they have been used successfully in the past to describe Henry's constants, isosteric heats, and sorption isotherms of p-xylene in rigid silicalite-1[38,50]. The methyl group of p-xylene is represented in a united atom approximation.

c) Silicalite-1 – p-xylene interactions[38,50]

α) electrostatic interactions

Table 6.1: Electric charges of silicalite-1 atoms

Form of potential	q_{Si}**(e)**	q_O**(e)**
$\mathcal{V}_{el} = \frac{1}{4\pi\varepsilon_0}\frac{q_i q_j}{r}$	+2.0	–1.0

β) Lennard-Jones interactions

Table 6.2: Van der Waals interactions between silicalite-1 oxygens and p-xylene atoms.

Potential	A (kcal/mol Å^{12})	B (kcal/mol Å^{6})
$\mathcal{V}_{\text{C-O}}(r) = \frac{A_{\text{C-O}}}{r^{12}} - \frac{B_{\text{C-O}}}{r^{6}}$	319072.6577	431.8833
$\mathcal{V}_{\text{H-O}}(r) = \frac{A_{\text{H-O}}}{r^{12}} - \frac{B_{\text{H-O}}}{r^{6}}$	38217.017	122.0841
$\mathcal{V}_{\text{CH}_3\text{-O}}(r) = \frac{A_{\text{CH}_3\text{-O}}}{r^{12}} - \frac{B_{\text{CH}_3\text{-O}}}{r^{6}}$	1343213.291	926.023

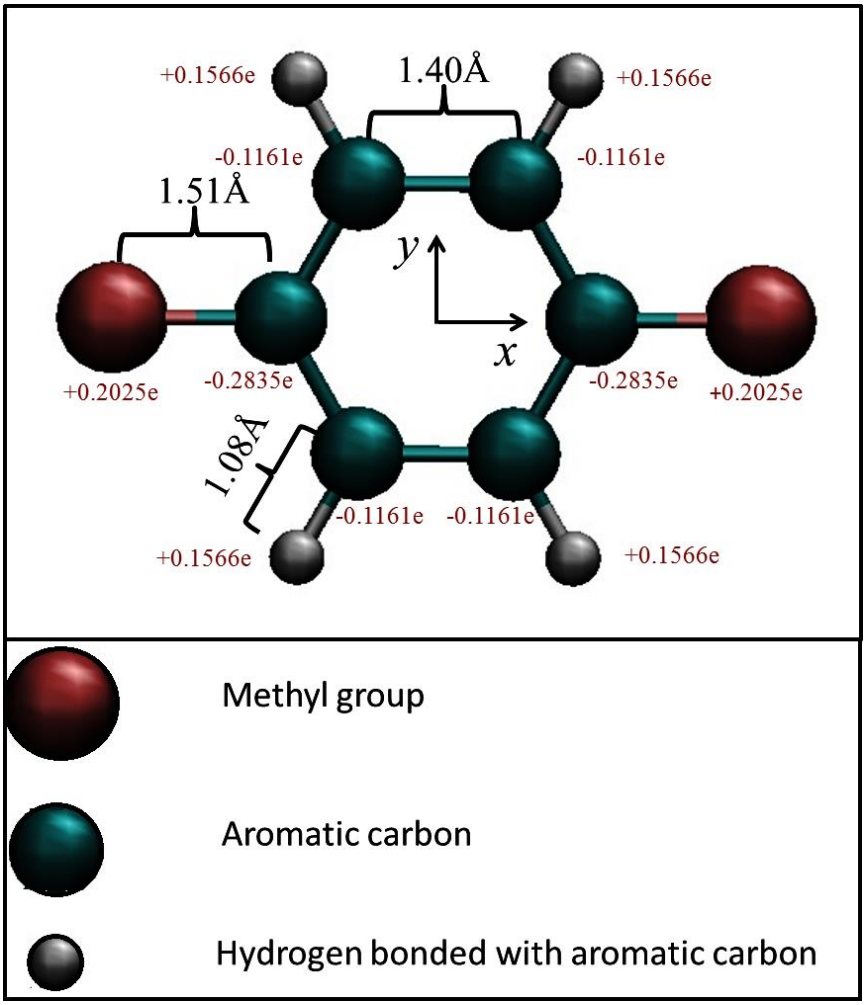

Figure 6.1 Para-xylene bond lengths and partial charges which were used in our simulations. The principal axes *x,y* are also illustrated and their start is the center of mass of p-xylene.

The principal axes of Figure 6.1 give I_{xx}=89.0112 amu Å^2 , I_{yy}=330.7534 amu Å^2, I_{zz}=419.7646 amu Å^2 . In the principal axis system the off-diagonal elements of the moment of inertia tensor are zero. The principal axes must be considered if we wish to apply the Fincham integration algorithm[125].

6.2 Results

In contrast to the benzene case, the 3-dimensional (3-D) free energy profiles of p-xylene in silicalite-1 have not been studied in the past. We have chosen to use the paths proven to be satisfactory for the study of benzene in silicalite-1 and, by moving the repulsive walls along them, to acquire the 3-D free energy fragments for p-xylene as well. As pointed out in Chapter 4, these fragments are not accurate enough for computing transition rate constants reliably because of their high resolution and corresponding limited sample size; their main purpose is to show us the locations of the minima (states) and the dividing surfaces.

The 3-D free energy profiles of p-xylene compared with those calculated in chapter 4 for benzene are illustrated in Figure 6.2a. Clearly, p-xylene is more restricted in the intersection than benzene. From these profiles we can see that the straight line used in chapter 4 is also satisfactory as a reaction coordinate (i.e., describes the dividing surface well) for projecting the center of mass of p-xylene and ultimately determining its 1-D free energy profile. Because we have used the same path (x=10 Å, y=y, z=0.0), we can compare the 1-D free energy profiles of benzene and p-xylene directly, as we can see in Figure 6.2b. There is a large difference between the 1-D free energy profiles in the region of the intersection.

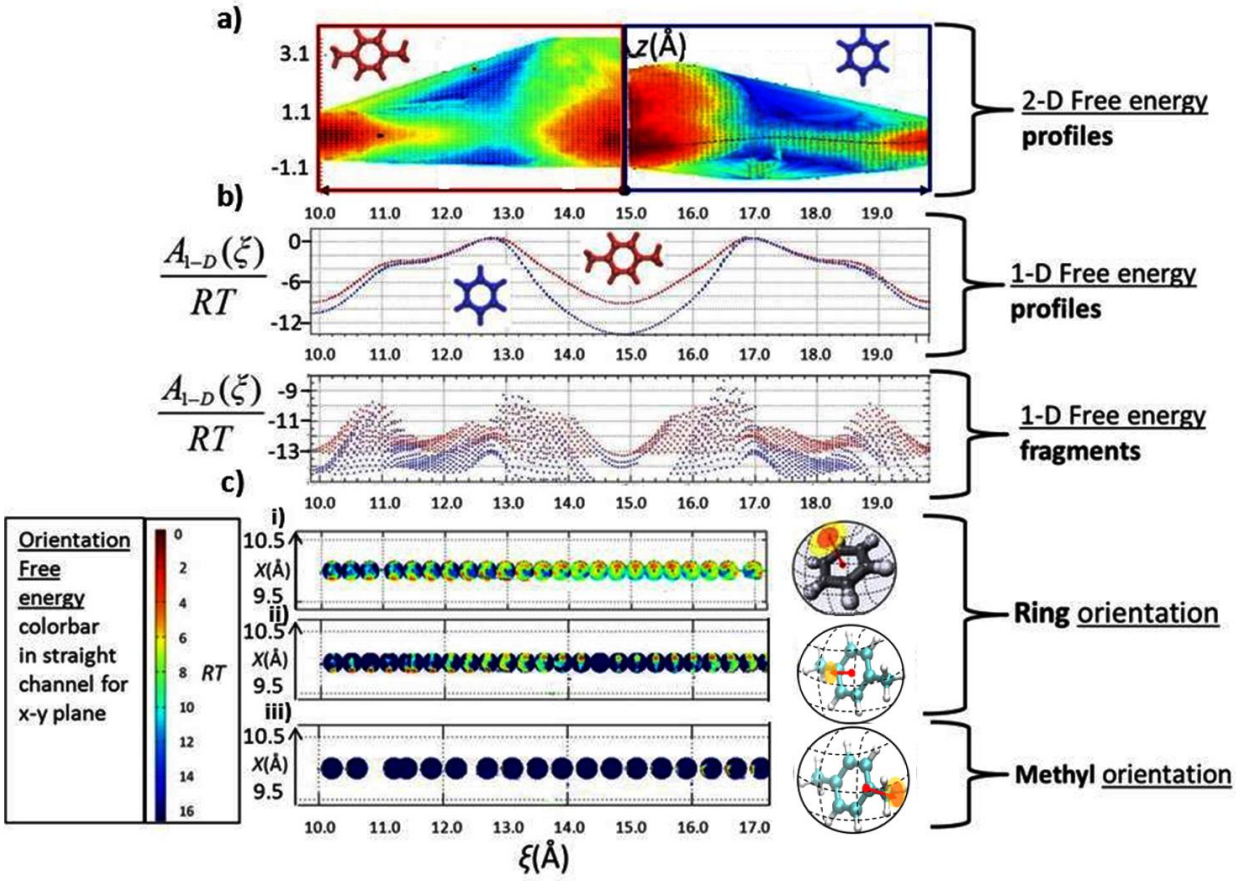

Figure 6.2 a) 2-dimensional cross-section through the 3-D free energy profile of p-xylene (left) and benzene (right) for the plane x=10Å b) 1-dimensional free energy profiles of p-xylene (red) and benzene (blue) and the 1-dimensional free energy fragments from which they have been constructed c) Orientational free energy profiles of i) normal vector to benzene ring ii) normal vector to p-xylene ring and iii) carbon-methyl bond (methyl stem) of p-xylene. The orientational free energy profiles have been determined from the natural logarithm of the probability density distribution of the vector shown in red in the small molecular diagrams and are depicted as contour plots on the surface of a sphere for various values ξ of the reaction coordinate along the straight channel. In these contour plots, red color signifies high probability for the orientation considered. All these calculations have been conducted with the DHFF force-field for a temperature of 300K.

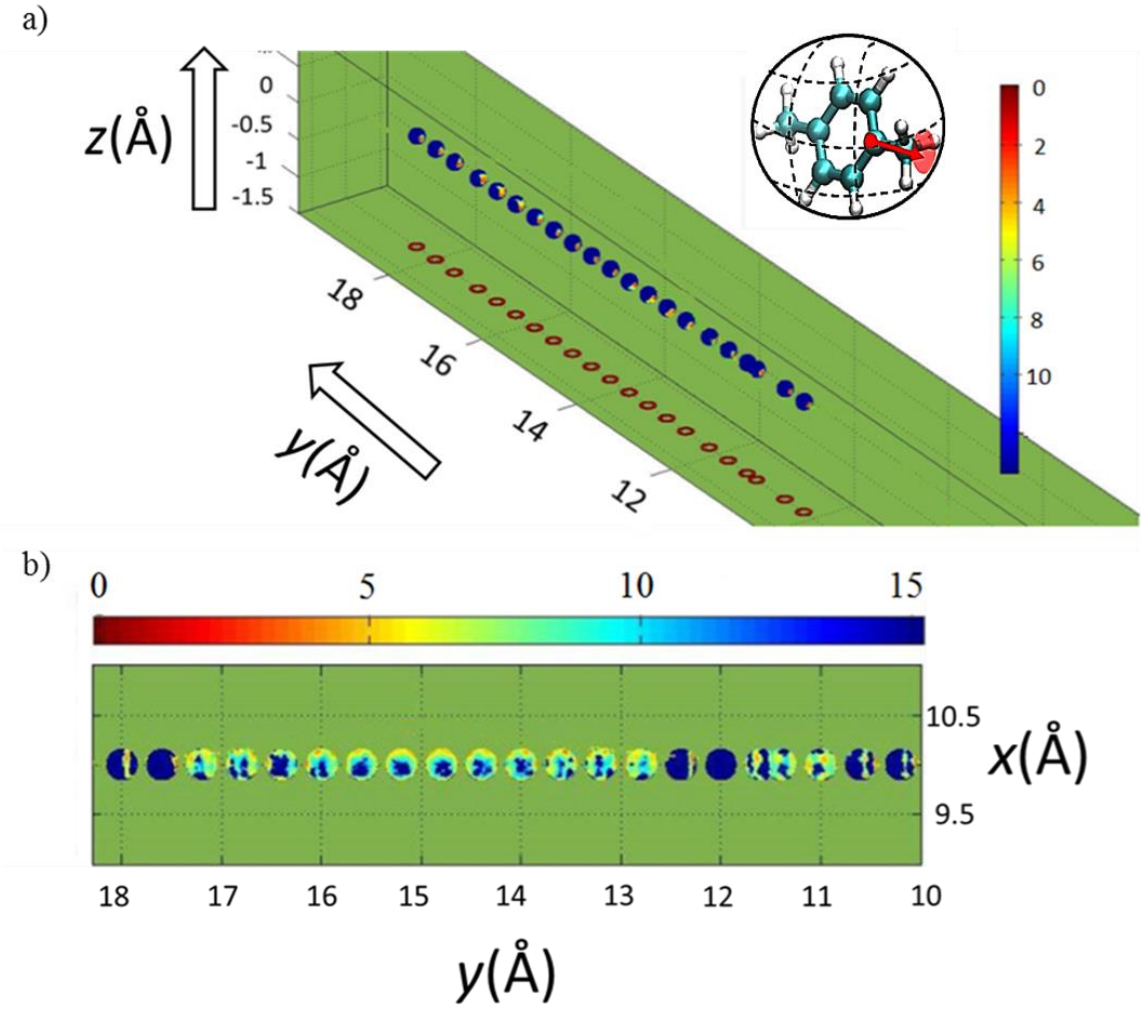

Figure 6.3 a) Orientation of one methyl of p-xylene along the straight channel of silicalite b) Orientation of one hydrogen of benzene along the same channel for a temperature of 300K. Colorbar is in *RT* units. All calculations have been performed with the DHFF forcefield.

To explain this, we use Figure 6.2c. In this Figure, the orientational free energy profiles of the phenyl rings of benzene and p-xylene are compared. We can see that in the intersection the benzene ring can orient easily in a variety of directions (cyan color on the surfaces of the little spheres), while it actually prefers one orientation (red color) for each position of its center of mass. P-xylene, on the other hand, behaves differently. The normal vector to its phenyl ring exhibits a far less diffuse orientational distribution and a strong preference for a specific orientation (sharp red points on the surfaces of the little spheres) at each position of its center of mass. It seems to be very difficult for p-xylene to turn to other directions and its

long axis seems restricted to be roughly parallel to the axis of the straight channel of the zeolite. This means that benzene in the intersection adopts a lot more microstates than does p-xylene and, as a result, its entropy in the intersection region is higher and its free energy displays a deeper minimum in the intersection region. Thus, the difference in the 1-D free energy profiles between benzene (blue) and p-xylene (red) in Figure 6.2b is attributable to entropic effects associated with the ability of the molecules to adopt different orientations in the intersection region. We will elaborate on this topic later. Similar conclusions can be reached if we compare the methyl orientational free energy profile of Figure 6.2c (and, for a better view, Figure 6.3a), with the benzene hydrogen orientational free energy profile, Figure 6.3b. The benzene hydrogen orientations have been measured by Quasi Elastic Neutron Scaterring and Nuclear Magnetic Resonance in the past[64,129] and are in perfect agreement with the orientational free energy profiles of Figure 6.3b. It is also important to add that the ring orientational free energy profiles of benzene and p-xylene in the interior of the straight channel (far from the intersection) are very similar and this is the reason for the small difference between their 1-D free energy profiles within the channel. Thus, we suspect the presence of a significantly higher barrier to translational motion along the straight channel in the case of benzene relative to p-xylene. This barrier is of entropic origin and arises in the intersection region.

We have performed simulations for the temperatures of 405K and 485K in addition to 300K, because as we will present later, Quasi Elastic Neutron Scattering measurements have also been conducted at those temperatures. The 1-D free energy profiles for these higher temperatures are illustrated in Figure 6.4.

Until now we have examined the free energy profiles in the straight channels. Next, we focus on the behavior of p-xylene in the sinusoidal channel. Similarly to the straight channel, we chose the sinusoidal channel path that has proved to be satisfactory for the study of benzene in silicalite-1. By moving the repulsive walls we have acquired the 3-D free energy fragments. We have stitched these 3-D free energy fragments together and the final 3-D free energy profile is illustrated in Figure 6.5.

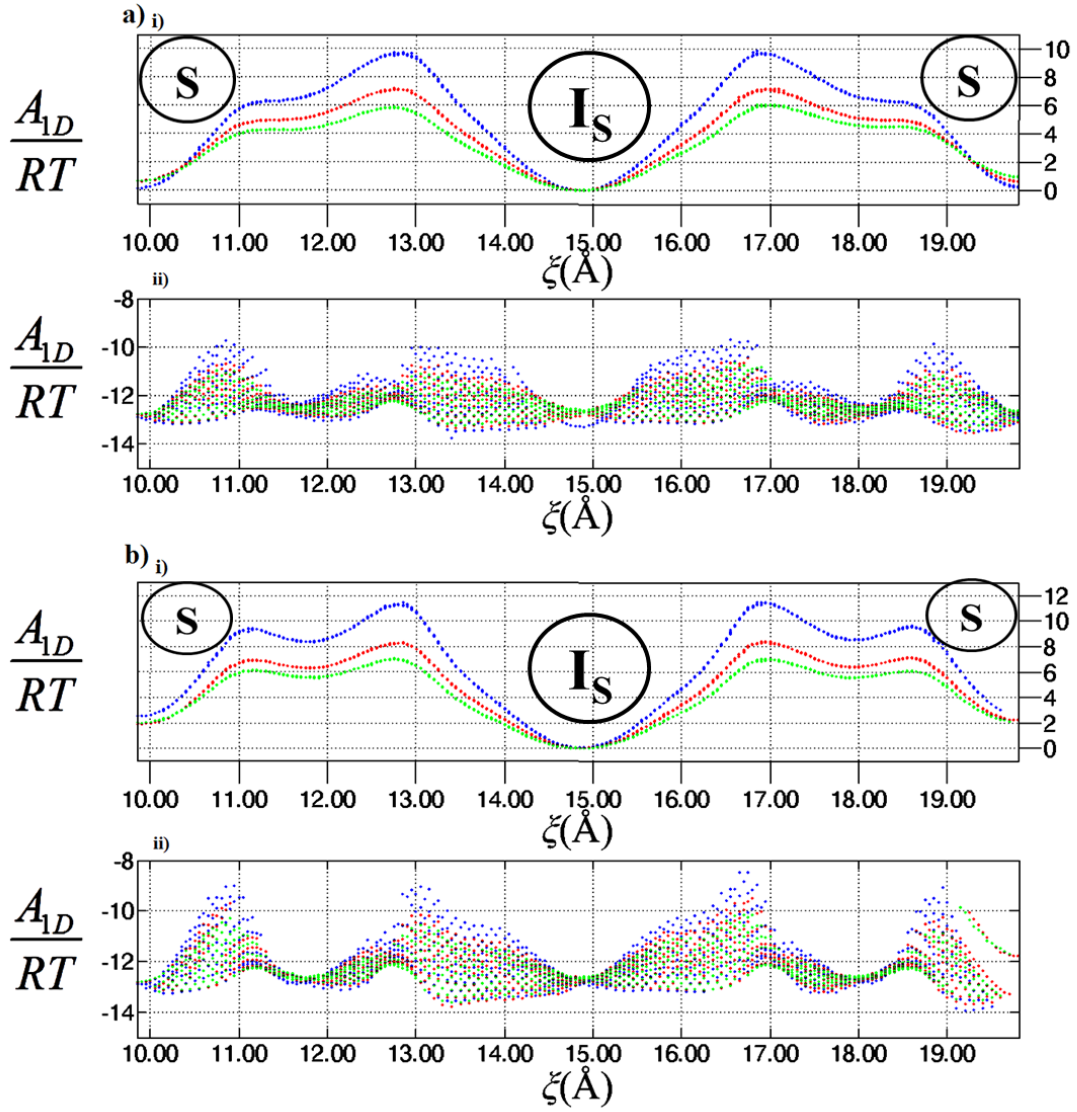

Figure 6.4 i) Free energy profiles of p-xylene, in *RT* units, as a function of the reaction coordinate for 300K (blue), 405K (red), and 485K(green) along the straight silicalite-1 channel for a crystal described by the DHFF force field (a) and the SGVFF force field (b) and ii) free energy fragments of the area between the walls (where there is no influence of the bias potential of the walls), from which the 1-dimensional local free energy profile has been derived by the stitching process

The path we used for the sinusoidal channel in chapter 4 and in Figure 6.6 was not able to describe well the areas of the intersection. The main reason for this is that p-xylene prefers the straight orientation (long axis of p-xylene parallel to the *y* direction, i.e., to the axis of the straight channels, marked as orientation C in Figure 6.5) when it finds itself in the intersection. As a result, it very rarely visits areas of the sinusoidal channel that are far from the red region within the intersection in Figure 5.6 and our sampling of these areas is not

reliable. Repulsive walls constructed vertical to the sinusoidal channel path are not able to keep p-xylene in specific areas of the intersection, as we can see in Figure 6.6. When placed in these areas, p-xylene prefers to leave and visit areas of the sinusoidal channel which are not constrained by the repulsive walls. In addition, from the 3-D free energy profile we can see that constraining walls must be constructed with a large distance between them, so that they do not influence sampling in the intersection. In case they influence the sampling, the 1-D free energy fragments will not stitch perfectly together. After making these observations, we have tried to use other paths, which are illustrated with bold purple and bold red color in Figure 6.7. The 1-D free energy fragments we obtained upon moving the repulsive walls along these paths were not able to be stitched together because they did not fit in some areas (see Figure 6.7). If we examine Figure 6.8, we can attribute this stitching problem to the existence of different orientational states. This means that we were not able to sample configuration space with precision, because p-xylene could be trapped in a free energy basin with low probability of escape.

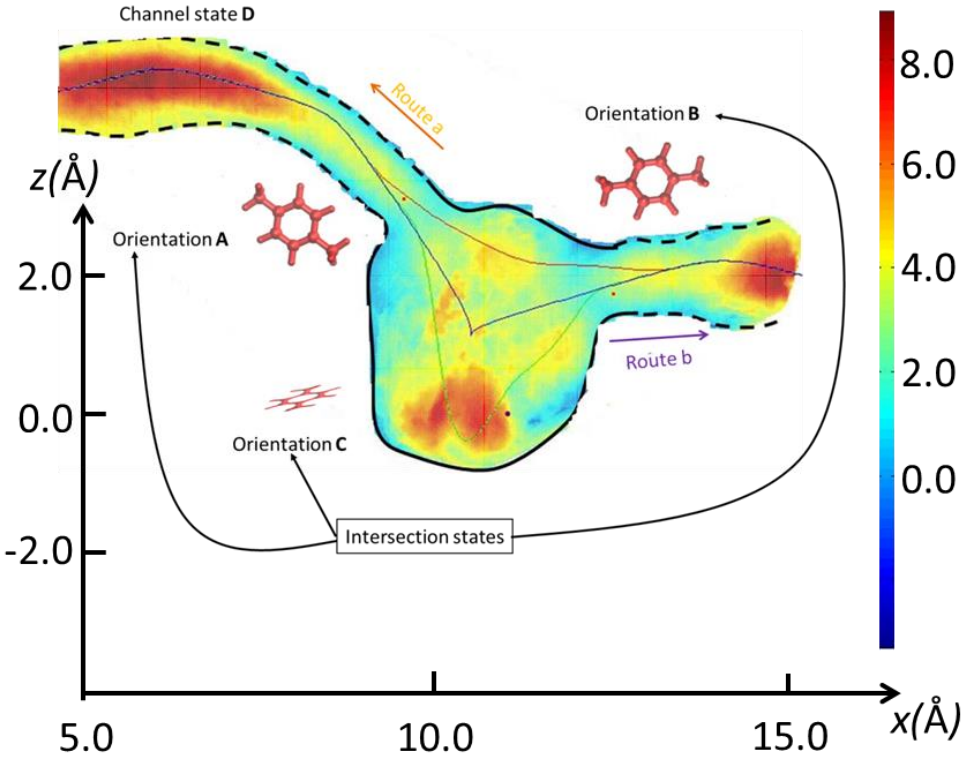

Figure 6.5 2-dimensional cross-section (at plane y=14.94Å) of the 3-dimensional free energy profile of p-xylene inside the sinusoidal channel for the DHFF force-field and temperature T=300K. Red color shows the areas where the p-xylene center of mass spends most of its time. The colorbar is in RT units.

In view of these problems, we chose to use a new path shown in red in Figure 6.5, instead of the old path shown in blue (actually including a spline to deal with the discontinuity in the intersection – see Chapter 5) in the same figure, and to deal with the issue of orientation within the intersection as discussed below. The difference between the old and the new paths is localized just in the intersection area. This means that the 1-D p-xylene free energy profile can be compared directly with that of benzene for values of the ξ reaction coordinate along the sinusoidal axis from 3.2 to 10 Å. The new red path is shorter than the old blue one. This new red path is the reaction coordinate of the 1-D free energy profiles of p-xylene shown in Figure 6.11. We will elaborate on this Figure later.

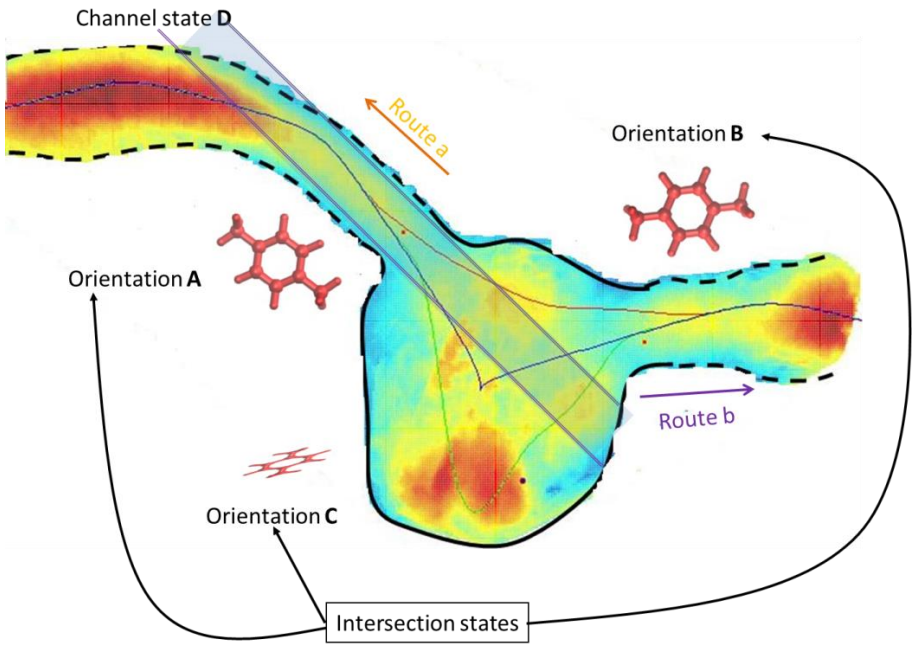

Figure 6.6 2-dimensional cross-section (at plane y=14.94Å) of the 3-D free energy profile of p-xylene in silicalite-1. The shaded area shows the space where no force from the walls is exerted if we use the green path. Blue and green lines were examined as alternative paths in the past

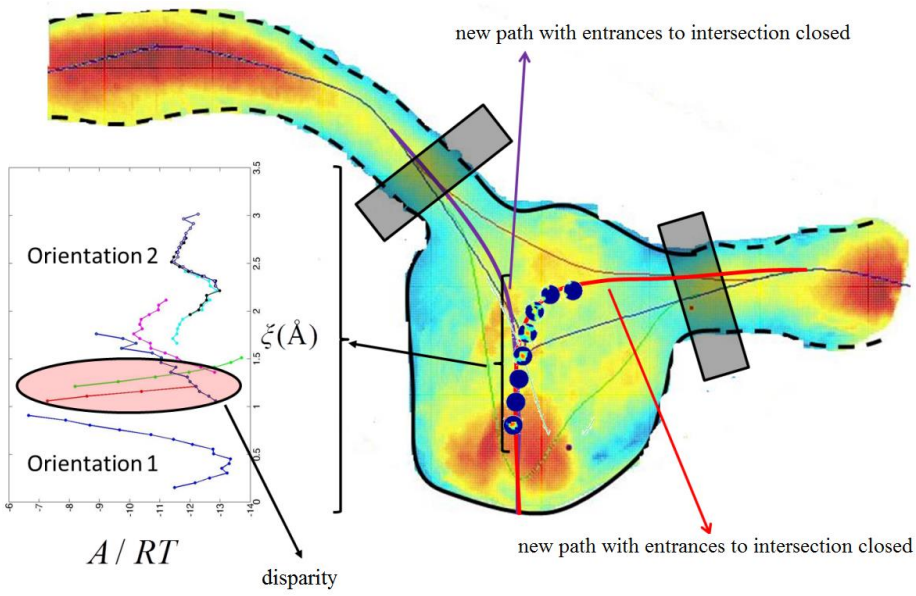

Figure 6.7 2-dimensional cross-section (at plane *y*=14.94Å) of the 3-D free energy profile of p-xylene in silicalite-1. The bold red and purple lines are the new paths we tried to use. The spheres show the orientation p-xylene wants to assume, when it is projected in the specific position of the bold red path. Thin blue and green lines were examined as alternative paths in chapter 4. The thin red path is another path we wish to examine. The 1-D free energy profiles we obtain along the bold red path are illustrated on the left. The grey colored boxes show the walls we used in the entrances of the intersection.

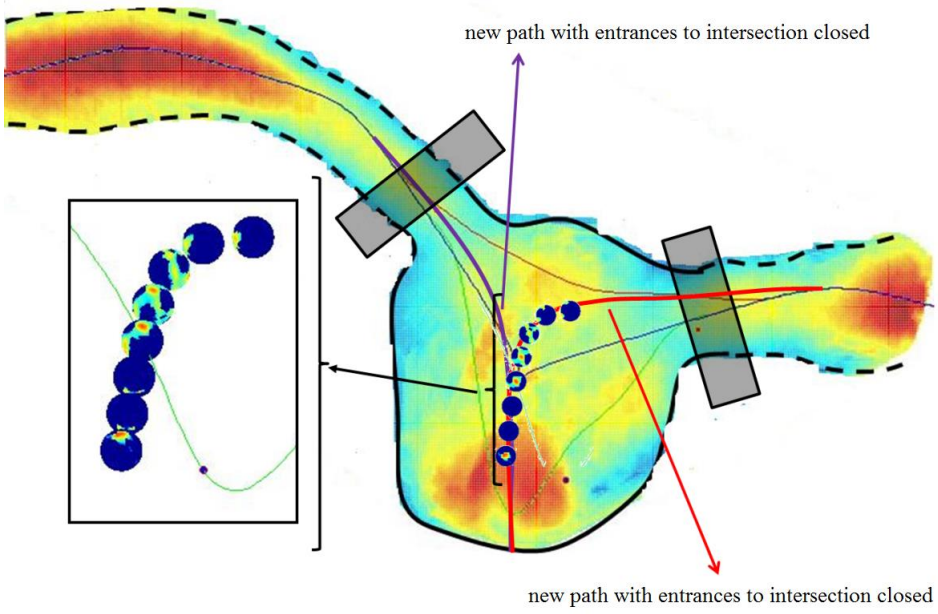

Figure 6.8 Same as Figure 6.7, the only difference being that we have zoomed on the orientation spheres on the left.

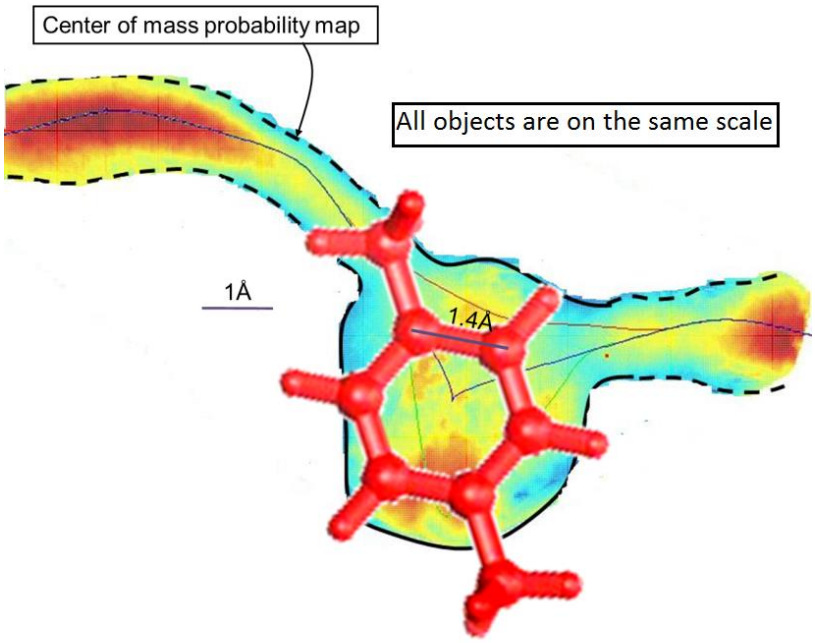

Figure 6.9 Center of mass of p-xylene contour plot with a p-xylene molecule illustrated on the same scale with this contour plot.

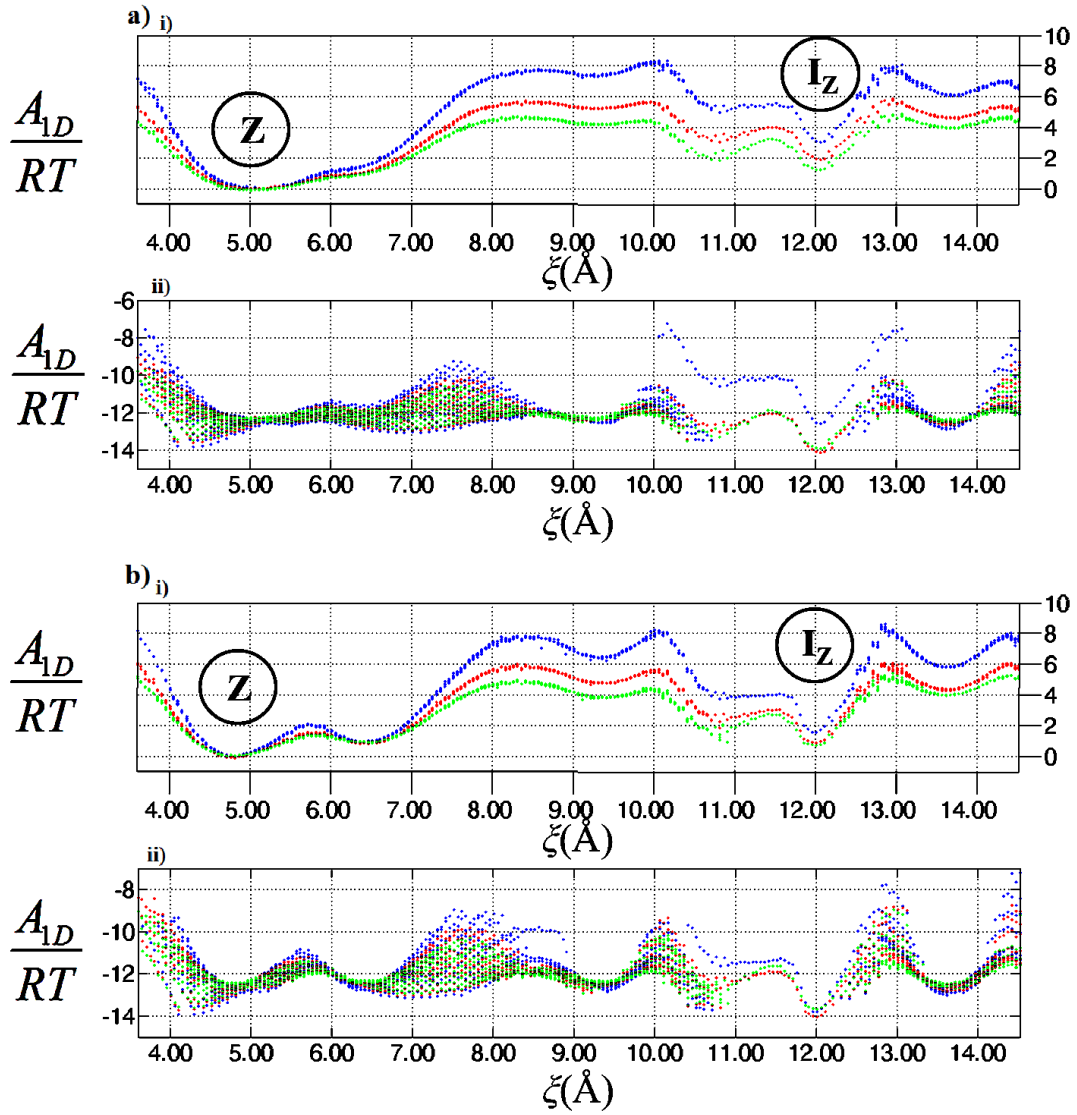

Figure 6.10 i) Free energy profiles of p-xylene, in *RT* units, as a function of the reaction coordinate for 300K (blue), 405K (red), and 485K (green) along the sinusoidal channel of silicalite-1 for a crystal described by DHFF force field (a) and the SGVFF force field (b) and ii) free energy fragments of the area between the walls (where there is no influence of the bias potential of the wall), from which the 1-dimensional local free energy profile has been derived by the stitching process

As we mentioned, the probability of p-xylene to visit areas in the intersection with orientations different from the orientation it adopts inside the straight channels is small. Consequently, a new technique must be used to constrain p-xylene to these orientations, so that we can sample them sufficiently. To do this, we have invented orientationally constraining walls. First, these walls must keep p-xylene in specific orientations without influencing the dynamics, as was done in the case of the center of mass constraining walls

we have already discussed. Secondly, these orientational walls must exert zero total force on p-xylene.

If we use a biased potential $\mathcal{V}(y_{17})$, where $y_{17}=y_7-y_1$, then a force will be exerted on the 1st and 7th atom only (see Figure 6.11) and only in the y direction (which seems to describe well the dividing surface of the orientational free energy-for the importance of the dividing surface, see Figure 2.2). This force is described in detail by Eqs (6.1) and (6.2).

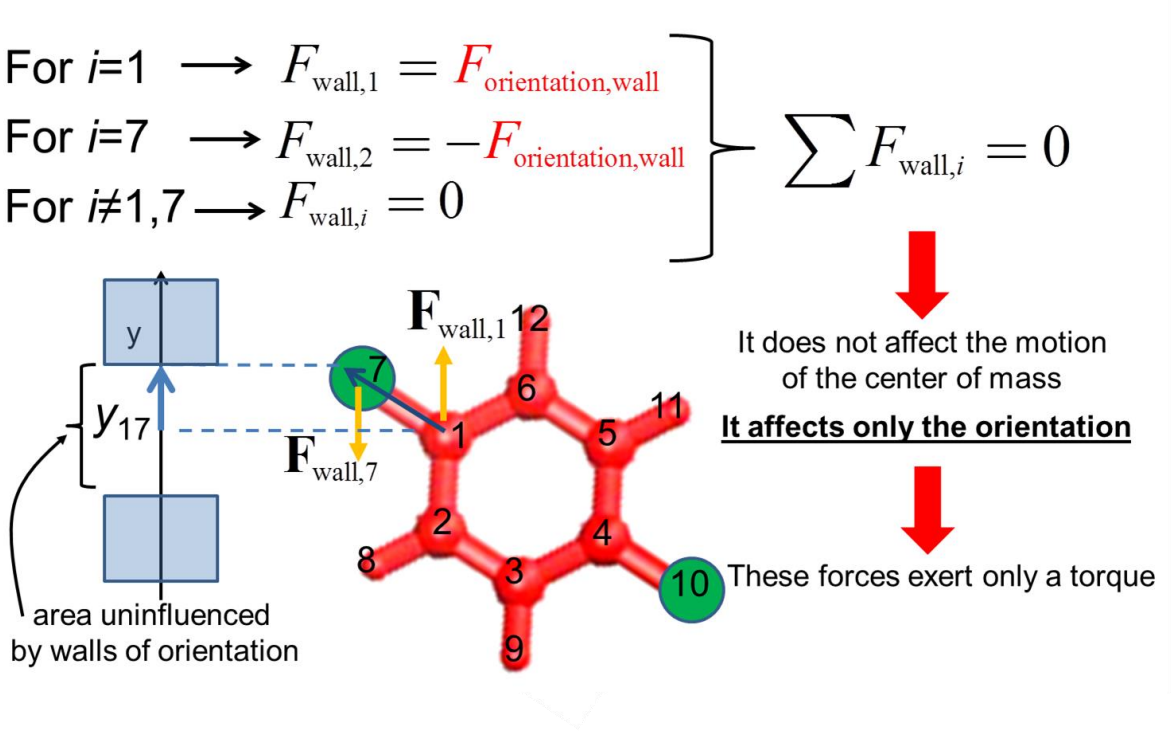

Figure 6.11 Description of the orientation wall and the way we can obtain the 1-D orientation free energy profiles. Green color is used for the methyl united atoms.

If we use a bias potential $V(y_{17})$, where $y_{17}=y_7-y_1$, then a force described by eq S2 will be exerted on atoms 1 and 7.

$$F_{i,y} = -\frac{\partial V(y_{17})}{\partial y_i} = -\frac{\partial V(y_{17})}{\partial y_{17}}\frac{\partial y_{17}}{\partial y_i} = -F_{\text{orientation,wall}}\frac{\partial y_{17}}{\partial y_i} =$$

$$= -F_{\text{orientation,wall}}\frac{\partial y_{17}}{\partial y_i} = -F_{\text{orientation,wall}}\frac{\partial (y_7 - y_1)}{\partial y_i} = -F_{\text{orientation,wall}}\left[\frac{\partial y_7}{\partial y_i} - \frac{\partial y_1}{\partial y_i}\right] \qquad \text{Eq.(6.1)}$$

The same force can be described more succinctly by Eq (6.2)

$$\left.\begin{array}{l}\text{For } i=1,\ F_{\text{wall}_1} = F_{\text{orientation,wall}} \\ \text{For } i=7,\ F_{\text{wall}_7} = -F_{\text{orientation,wall}} \\ \text{For } i \neq 1,7\ ,F_{\text{wall}_i} = 0\end{array}\right\} \rightarrow \sum F_{\text{wall}_i} = 0 \qquad \text{Eq.(6.2)}$$

The repulsive potential $\mathcal{V}(y_{17})$ has the same form as the repulsive walls on the center of mass described in Chapter 4. The *y* direction we chose for the orientation walls seems to describe well the orientational free energy dividing surface (see Figure 6.8). Moving these orientational walls along the y_{17} coordinate, we obtain 1-D orientational free energy profiles. To sample y_{17}, we bin it in steps of 0.01 Å. In the projection of the center of mass of p-xylene and benzene, we have used steps of 0.05Å instead of 0.01Å. Because y_{17} can have values from –1.51Å to 1.51Å (very short compared with center of mass paths), we do not face noise issues using 0.01Å. As a result, this choice helps us improve our stitching accuracy.

We remind the reader that the wall potential is given by Eqs. (2.3), (2.4). The parameter values for the center of mass walls used in all calculations here are:

σ_w =2.5 Å, ε_w =0.5975 kcal/mol = 2.5×10^2 amu Å^2/ps^2, R_1 / σ_w = 0.60. R_2 / σ_w =0.80

The parameter values for the orientational walls used in all calculations are:

σ_w =2.5 Å, ε_w =5.975 kcal/mol = 25×10^2 amu Å^2/ps^2, R_1 / σ_w = 0.60. R_2 / σ_w =0.80

The 1-D orientational free energy profiles we get applying this procedure are shown in Figure 6.12. Figure 6.12 shows the existence of two orientational states in the intersection. The first state is the domain $\xi \in$[–1.51 Å,–0.90 Å)$\cup$(0.90 Å, 1.51 Å] and we symbolize it as I_S, while the second state is the domain $\xi \in$[–0.90Å, 0.90 Å] and is symbolized as I_Z. In the first state p-xylene adopts the orientation it likes when it is in the straight channel, depicted in Figure 6.2c, in Figure 6.3 and in Figure 6.5 (orientation C). This orientational state is much more favorable than the second state. In the second state, p-xylene prefers to have its ring in the *x*-*z* plane. Because this state is unfavorable and p-xylene rarely visits it, we decided to use orientation walls located in the saddle points of Figure 6.12. Simultaneously, we conducted molecular dynamics simulations with the use of center of mass repulsive walls for ξ belonging to [10.00Å, 13.00 Å]. Using this method we managed to obtain the 1-D free energy profile of Figure 6.10.

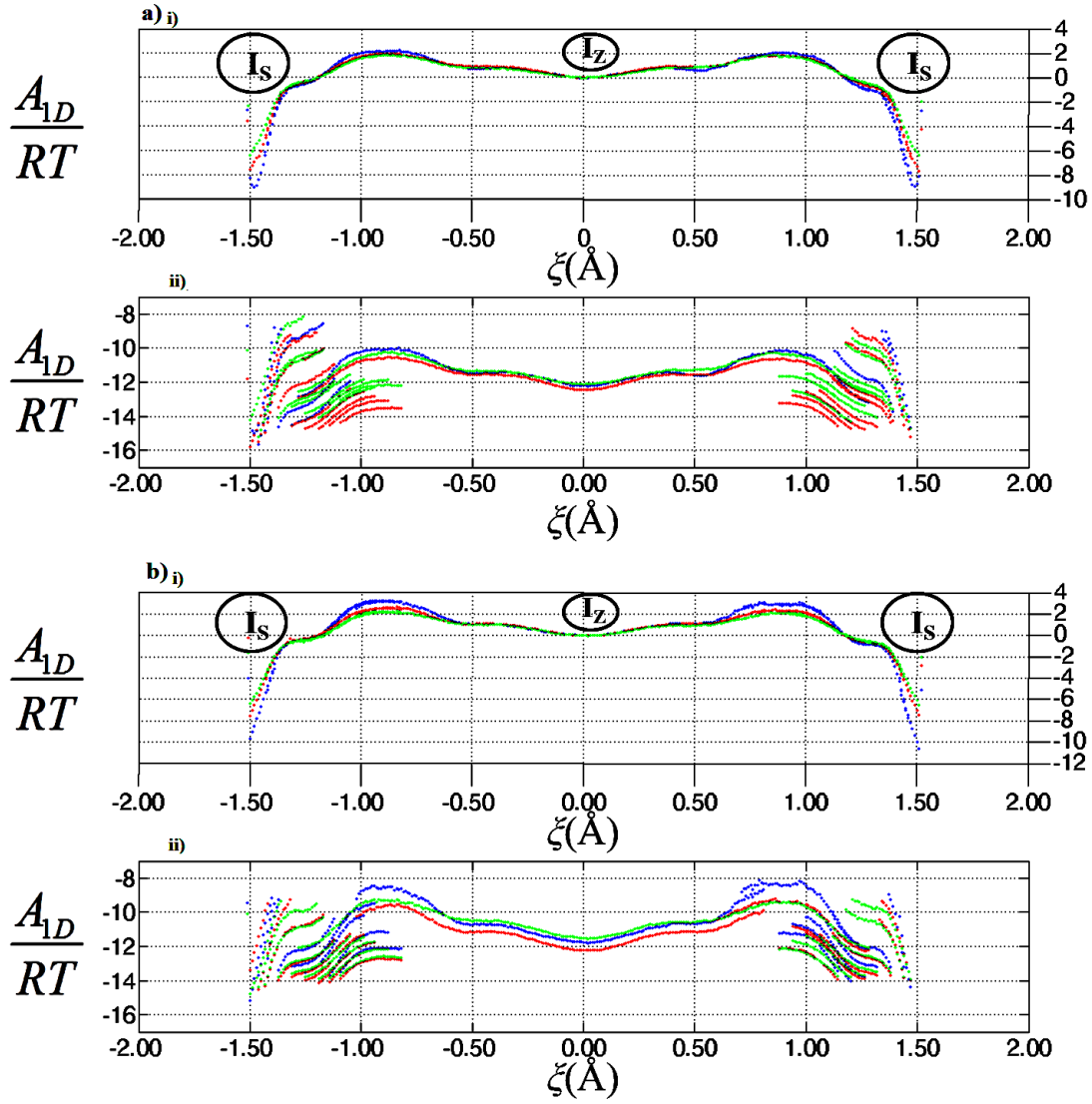

Figure 6.12 i) Profiles of the free energy of p-xylene, in *RT* units, as a function of the reaction coordinate at 300K (blue), 405K (red), and 485K (green) for a crystal described by the DHFF force field (a) and the SGVFF force field (b) and ii) free energy fragments of the area between the walls (where there is no influence of the bias potential of the wall), from which the 1-dimensional local free energy profile has been derived by the stitching process. The reaction coordinate is the projection of a C-CH_3 bond onto the *y* axis.

From Figure 6.12 of the main text, we can see that we have $I_{S,R}$ and $I_{S,L}$ states, where R stands for right and L is for left . From these states, we define I_S as $I_S = I_{S,R} \cup I_{S,L}$.

If we write the master equation of these states for the transitions between them, we have that

$$\frac{dP_{I_{S_L}}}{dt} = -k_{I_{S_L}\to Z}P_{I_{S_L}} + k_{Z\to I_{S_L}}P_{I_Z} \qquad \text{Eq.(6.3)}$$

$$\frac{dP_{I_{S_R}}}{dt} = -k_{I_{S_R}\to Z}P_{I_{S_R}} + k_{Z\to I_{S_R}}P_{I_Z} \qquad \text{Eq.(6.4)}$$

– –

$$\text{Eq.(6.3)} + \text{Eq.(6.4)} \xrightarrow{k_{I_{S_L}\to Z} = k_{I_{S_R}\to Z} = k_{I_S\to Z}} \frac{d\left(P_{I_{S_L}} + P_{I_{S_R}}\right)}{dt} = -k_{I_S\to Z}(P_{I_{S_L}} + P_{I_{S_R}}) + (k_{Z\to I_{S_L}} + k_{Z\to I_{S_R}})P_{I_Z}$$

$$\xrightarrow[P_{I_{S_L}} + P_{I_{S_R}} = P_{I_S}]{k_{Z\to I_{S_L}} + k_{Z\to I_{S_R}} = k_{Z\to I_S}} \boxed{\frac{dP_{I_S}}{dt} = -k_{I_S\to Z}P_{I_S} + k_{Z\to I_S}P_{I_Z}} \qquad \text{Eq.(6.5)}$$

– –

$$\frac{dP_{I_Z}}{dt} = -(k_{Z\to I_{S_L}} + k_{Z\to I_{S_R}})P_{I_Z} + k_{I_{S_L}\to Z}P_{I_{S_L}} + k_{I_{S_R}\to Z}P_{I_{S_R}}$$

$$\xrightarrow{k_{Z\to I_{S_L}} + k_{Z\to I_{S_R}} = k_{Z\to I_S}} \frac{dP_{I_Z}}{dt} = -k_{Z\to I_S}P_{I_Z} + k_{I_{S_L}\to Z}P_{I_{S_L}} + k_{I_{S_R}\to Z}P_{I_{S_R}}$$

$$\xrightarrow[P_{I_{S_L}} + P_{I_{S_R}} = P_{I_S}]{k_{I_{S_L}\to Z} = k_{I_{S_R}\to Z} = k_{I_S\to Z}} \frac{dP_{I_Z}}{dt} = -k_{Z\to I_S}P_{I_Z} + k_{I_S\to Z}(P_{I_{S_L}} + P_{I_{S_R}})$$

$$\rightarrow \boxed{\frac{dP_{I_Z}}{dt} = -k_{Z\to I_S}P_{I_Z} + k_{I_S\to Z}P_{I_S}} \qquad \text{Eq.(6.6)}$$

From Eqs (6.5) and (6.6), we can see that we can reduce the $I_{S,R}$, $I_{S,L}$ and I_Z states to I_S and I_Z states, without losing any information. The new rates for these new states are described by Eq. (6.7) and Eq. (6.8).

$$k_{Z\to I_S} = k_{Z\to I_{S_L}} + k_{Z\to I_{S_R}} \qquad \text{Eq.(6.7)}$$

$$k_{I_S\to Z} = k_{I_{S_L}\to Z} = k_{I_{S_R}\to Z} \qquad \text{Eq.(6.8)}$$

We collect all the results for rate constants, probabilities, isosteric heats and diffusion coefficients in Tables 6.3-6.12 for p-xylene-silicalite-1 (DHFF), and p-xylene-silicalite-1 (SGVFF).

Table 6.3 Definitions of states used in rate constant calculation for the system p-xylene-silicalite-1 (DHFF)

State	ξ(Å)
I_S (Figure 7 main text)	(12.80,17.08)
I_Z (Figure 9 main text)	(9.96,12.96)
S (Figure 7 main text)	(9.96,12.80)∪(17.08,19.92)
Z (Figure 9 main text)	(3.50,8.56)

Table 6.4 Definitions of states used in rate constant calculation for the system p-xylene-silicalite-1 (SGVFF)

State	ξ(Å)
I_S (Figure 12 main text)	(12.80,17.08)
I_Z (Figure 13 main text)	(9.96,12.96)
S (Figure 12 main text)	(9.96,11.10)∪(18.60,19.92]
Z (Figure 13 main text)	(3.50,8.56)

Table 6.5 Rate constants, in s^{-1}, of transitions of p-xylene in silicalite-1 (DHFF model)

Transition		**Temperature**		
From	**To**	300K	405K	485K
I_S	I_Z	2.34×10^{8}	1.74×10^{9}	5.61×10^{9}
	S	4.47×10^{7}	5.60×10^{8}	1.65×10^{9}
S	I_S	6.59×10^{7}	1.25×10^{9}	4.08×10^{9}
Z	I_Z (route a)	7.82×10^{7}	7.86×10^{8}	2.25×10^{9}
	I_Z (route b)	9.20×10^{7}	7.11×10^{8}	1.88×10^{9}
I_Z	Z(route a)	4.20×10^{9}	1.19×10^{10}	1.56×10^{10}
	Z(route b)	4.94×10^{9}	1.08×10^{10}	1.31×10^{10}
	I_S	1.87×10^{11}	2.90×10^{11}	2.81×10^{11}

*Routes a and b are defined in Figure 6.5

Table 6.6 Rate constants, in s^{-1}, of transitions of p-xylene in silicalite-1 (SGVFF model)

Transition		**Temperature**		
From	**To**	300K	405K	485K
I_S	I_Z	4.74×10^{7}	1.46×10^{9}	4.79×10^{9}
	S	7.25×10^{6}	1.50×10^{8}	4.35×10^{8}
S	I_S	9.86×10^{7}	1.31×10^{9}	3.71×10^{9}
Z	$I_{Z(route\ a)}$	9.77×10^{7}	8.05×10^{8}	2.45×10^{9}
	$I_{Z(route\ b)}$	6.19×10^{7}	5.43×10^{8}	1.40×10^{9}
I_Z	$Z_{(route\ a)}$	1.14×10^{9}	4.29×10^{9}	8.91×10^{9}
	$Z_{(route\ b)}$	7.25×10^{8}	2.89×10^{9}	5.09×10^{9}
	I_S	7.42×10^{10}	1.83×10^{11}	2.32×10^{11}

*Routes a and b are defined in Figure 6.5

Table 6.7 Residence probabilities of p-xylene in silicalite-1 (DHFF model)

Probabilities	**Temperature**		
	300K	405K	485K
I_S	0.5724	0.6485	0.6395
I_Z	7.16×10^{-4}	0.0039	0.0128
S	0.3884	0.2885	0.2589
Z	0.0385	0.0592	0.0889

Table 6.8 Residence Probabilities of p-xylene in silicalite-1 (SGVFF model)

Probabilities	**Temperature**		
	300K	405K	485K
I_S	0.9245	0.8586	0.8246
I_Z	5.9×10^{-4}	0.0069	0.0170
S	0.0680	0.0980	0.0965
Z	0.0069	0.0365	0.0619

Table 6.9 Mean Potential Energies and isosteric heat of sorption of p-xylene in silicalite-1(DHFF model)

Potential Energies	**Temperature**		
kJ/mol	300K	405K	485K
I_S	–69.02	–65.48	–62.66
I_Z	–53.21	–49.89	–47.65
S	–76.11	–72.33	–69.98
Z	–70.55	–67.97	–65.88
Q_{st}	74.31	70.92	68.69

Table 6.10 Mean Potential Energies and isosteric heat of sorption of p-xylene in silicalite-1 (SGVFF model)

Potential Energies	**Temperature**		
kJ/mol	300K	405K	485K
I_S	–68.95	–65.70	–63.06
I_Z	–53.86	–49.00	–47.56
S	–70.38	–68.07	–65.92
Z	–66.96	–64.73	–63.10
Q_{st}	71.51	69.15	67.10

*Q_{st}=70kJ/mol for p-xylene in rigid silicalite-1 at 250K [50]

**experimental values $Q_{st} \in [64.4,80.0]$ kJ/mol [50]

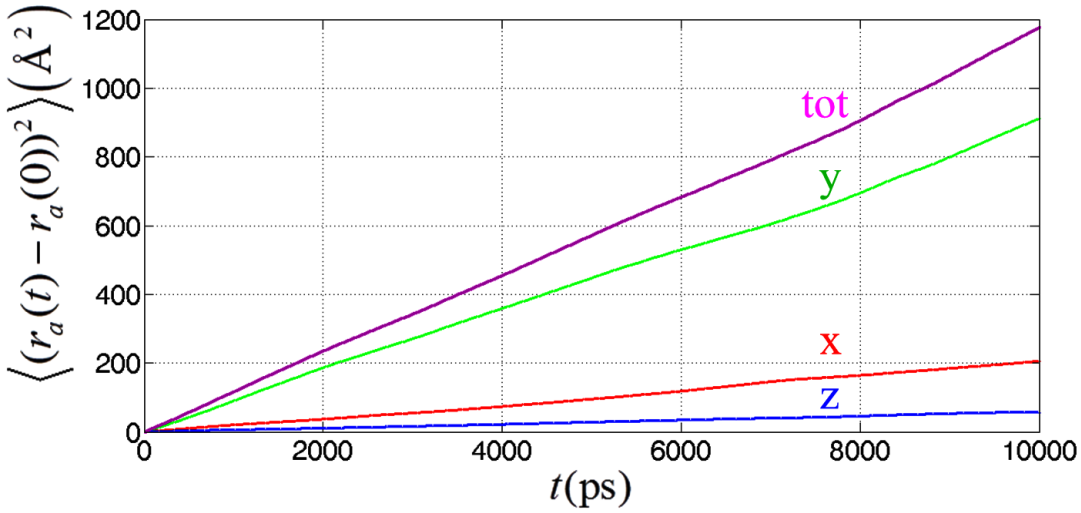

Figure 6.13 Mean Square Displacement as a function of time from direct Molecular Dynamics simulations for rigid p-xylene using the DHFF force-field at a temperature of 485K. Red, green and blue show results along the *x* (r_a=*x*), *y* (r_a=*y*), *z* (r_a=*z*) direction, respectively.

In addition to the application of the curvilinear umbrella sampling we introduced in Chapter 2, we conducted 48 Molecular Dynamics (MD) simulations of time of duration 14ns for 1 p-xylene in 27 unit cells of silicalite-1, starting from 48 different initial positions. In all these simulations we have used multiple time origins to improve statistics and we have obtained the mean square displacement versus time curves of Figure 6.13. From the slopes in this Figure, extracted via a linear least squares fit to the individual curves over the range of times, we have calculated the self-diffusion coefficients shown in Table 6.11 of the main text (right column).

$$D_{aa} = \lim_{t \to +\infty} \frac{\left\langle (r_a(t) - r_a(0))^2 \right\rangle}{2t} \qquad \text{Eq. (6.9)}$$

Table 6.11. Self-Diffusion coefficients of p-xylene in silicalite-1 (DHFF model)

Self-Diffusion(m^2s^{-1})	**Temperature (TST)**			**Temperature (MD- see Figure 6.13)**
	300K	405K	485K	485K
D_{xx}	1.641×10^{-12}	2.225×10^{-11}	9.179×10^{-11}	1.189×10^{-10}
D_{yy}	1.271×10^{-11}	1.800×10^{-10}	5.242×10^{-10}	4.451×10^{-10}
D_{zz}	6.239×10^{-13}	8.285×10^{-12}	3.221×10^{-11}	3.242×10^{-11}
D	4.991×10^{-12}	7.020×10^{-11}	2.160×10^{-10}	1.988×10^{-10}

Table 6.12 Self-Diffusion coefficients of p-xylene in silicalite-1 (SGVFF model)

Self-Diffusion(m^2s^{-1})	**Temperature**		
	300K	405K	485K
D_{xx}	2.643×10^{-13}	1.194×10^{-11}	5.558×10^{-11}
D_{yy}	3.327×10^{-12}	6.395×10^{-11}	1.780×10^{-10}
D_{zz}	1.072×10^{-13}	4.369×10^{-12}	1.823×10^{-11}
D	1.232×10^{-12}	2.680×10^{-11}	8.390×10^{-11}

The values of Table 6.13 have been derived by linear least squares fitting of Eq. (6.10) on the data of Tables 6.11 and 6.12.

$$D = D_0 \exp\left(-\frac{E_a}{RT}\right) \rightarrow \ln D = \ln D_0 - \frac{E_a}{RT} \qquad \text{Eq. (6.10)}$$

Table 6.13 Diffusion prefactors (D_0) and Activation Energies (E_a)

System		$\boldsymbol{D_0}$(m^2s^{-1})	$\boldsymbol{E_a}$(kJ/mol)
benzene	Silicalite-1(DHFF)	1.89777×10^{-8}	29.82232
	Silicalite-1(SGVFF)	1.49284×10^{-8}	33.1895
	QENS	1.42371×10^{-9}	27.4362
p-xylene	Silicalite-1(DHFF)	1.03883×10^{-7}	24.75909
	Silicalite-1(SGVFF)	9.3062×10^{-8}	27.9101
	QENS	1.62136×10^{-9}	10.3676

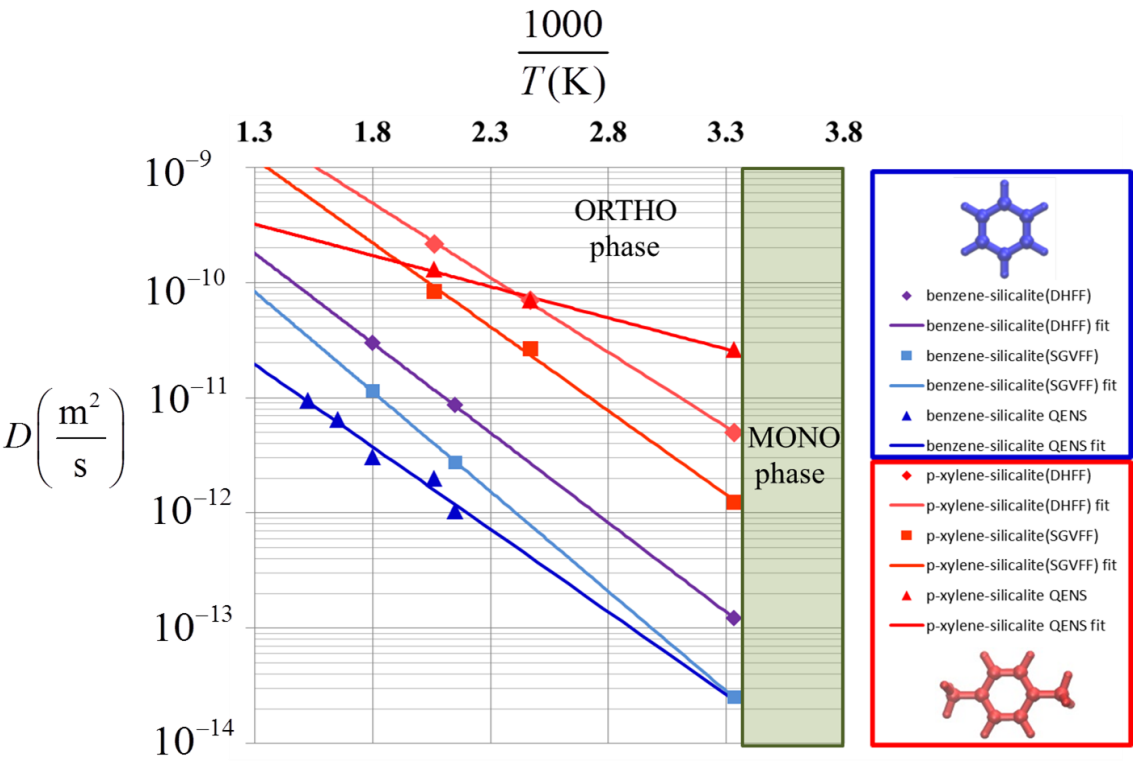

Figure 6.14 Diffusion coefficients calculated via simulations and Quasi Elastic Neutron Scattering (QENS).

Chapter 7

Investigation of entropic effects

From the tables of the mean potential energies for each state (Tables 4.11, 4.12, 6.9 and 6.10) we can see that p-xylene has lower potential energy than benzene. We also have in mind that $A = U - TS = \langle K + \mathcal{V} \rangle_{NVT} - TS$ where U is the internal energy, K is the kinetic energy, $\mathcal{V}$ is the potential energy, T is the temperature and S is the entropy. In addition, we already know the Helmholtz free energy barrier ΔA from Figures 4.7, 4.8, 6.2, 6.5. From now on, we define $\Delta A = A_{\max,I_S} - A_{\min,I_S}$. Similarly, we define the barriers for the internal, the kinetic, the potential energies and the entropy. It is important to mention that ΔK=0 because the simulations are in the canonical ensemble and, consequently, $(\Delta U)_{NVT} = (\Delta \langle \mathcal{V} \rangle)_{NVT}$. From the previous analysis we see that we just need to calculate the average potential energy around the maximum (we remind the reader that we have already calculated the potential energy around the minimum in the intersection in Tables 4.11, 4.12, 6.9 and 6.10) if we want to calculate the entropic barriers for the transition from the intersection to the straight channel. To do this we use the repulsive walls to keep the center of mass of benzene and p-xylene in the interval $\xi \in$[12.60 Å,–12.90 Å) of the straight channel. As a result, benzene and p-xylene move around the maximum of the 1-D free energy profile. At the same time, we write down every 1ps the potential energy between the sorbate and the crystal. The total time of the simulations is 5ns. From this sampling, we calculate the mean potential energy around the saddle point and finally we calculate the internal energy barrier. We performed the calculations for 300K only, because this is the common temperature between benzene and p-xylene in the simulations we mentioned before. We see these results in Figure 7.1 and Tables 7.1, 7.2. From Figure 7.1 it is clear that the entropy barriers for benzene are much higher than those for p-xylene, while the internal energy barrier contributes the most to the free energy barrier. We would expect $S_{\max,Is} < S_{\min,Is}$ because of the larger number of microstates in the minimum than in the saddle point. as we can see in 3-D orientational free energy profiles of Figures 6.2 and 6.3. From these Figures we can also see that benzene has much more entropy than p-xylene generally. This, of course, does not ensure that the same will happen with the entropy barriers. However, in Figure 7.1 we see that the entropy barriers lead to a much

faster diffusion of p-xylene than benzene. As a result, benzene is more entropic than p-xylene and it also experiences larger entropy barriers. This conclusion does not depend on the intra-silicalite-1 force-field chosen (DHFF or SGVFF).

Table 7.1: Potential energy, free energy and entropy barriers according to DHFF force field for the temperature of 300K.

DHFF	**Benzene**		**p-xylene**	
	A(kJ/mol)	$\mathcal{V}_{S\text{-}Z}$ (kJ/mol)	A(kJ/mol)	$\mathcal{V}_{S\text{-}Z}$ (kJ/mol)
Minimum	–34.2204	–54.779	0	–69.0200
Maximum	1.3967	–34.217	24.0391	–51.5931
ΔA or ΔU	35.6171	20.562	24.0391	17.4269
$T\Delta S$	–15.0551		–6.6122	
ΔS(kJ/mol/K)	–0.0501		–0.0220	

Table 7.2: Potential energy, free energy and entropy barriers according to SGVFF force field for the temperature of 300K

SGVFF	**benzene**		**p-xylene**	
	A(kJ/mol)	$\mathcal{V}_{S\text{-}Z}$ (kJ/mol)	A(kJ/mol)	$\mathcal{V}_{S\text{-}Z}$ (kJ/mol)
Minimum	0	–54.5815	0	–68.9500
Maximum	39.2575	–30.4226	28.4464	–49.3074
ΔA or ΔU	39.2575	24.1589	28.4464	19.6426
$T\Delta S$	–15.0986		–8.8038	
ΔS(kJ/mol/K)	–0.0503		–0.0293	

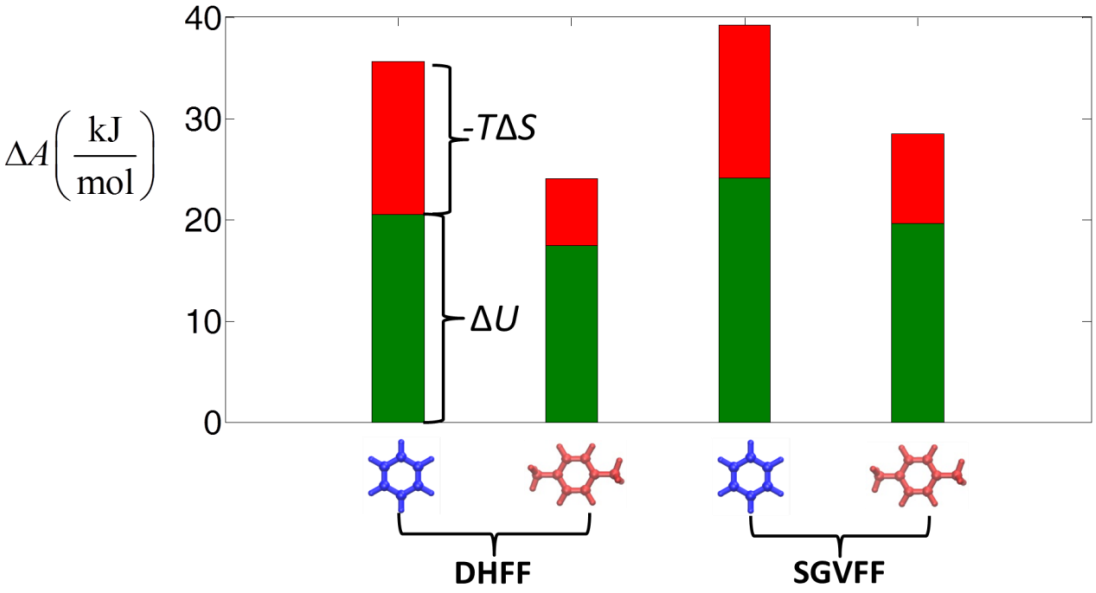

Figure 7.1. Free energy barriers at 300K between the saddle point of the straight channel and the minimum of the intersection for benzene and p-xylene using the DHFF and the SGVFF force-fields, and their energy and entropy components. Green color shows the internal energy barrier, while the red color shows the contribution of the entropic barrier.

From Figures 6.2, and comparing the rates of Table 6.5, 6.6 of p-xylene with those of Table 4.7, 4.8, we see the existence of small differences in rates for the transition S to I for benzene from the transition S to I_s for p-xylene. In contrast, there is a large difference between the transition I to S of benzene and I_s to S for p-xylene. Here we have to add that, from Eq. (2.17), if the free energy profiles were the same, one would expect the heavier molecule (p-xylene) to diffuse more slowly than the lighter benzene. The same conclusion would be arrived at by naively comparing the kinetic diameters of benzene and p-xylene. In this interesting system, the heavier and larger molecule diffuses faster than the lighter and smaller one. This apparent paradox is explained by the entropic barriers we discussed in Figure 7.1.

From the 1-D free energy profile Figures, we see that the 1-D free energy fragments in all cases stitch perfectly together. This is evidence that we have sampled sufficiently the same micro-state or micro-states with low barriers between them. It also provides evidence that the parts of free energy fragments we stitch together are not influenced by the repulsive walls (center of mass walls or orientational walls). Comparing the 1-D free energy profiles along the straight channels derived by DHFF and SGVFF force-fields, no significant differences for the potential energies in the intersections were found. However, differences were found in the S state, where, whether we look at benzene or p-xylene, the mean potential energy is always smaller in DHFF than SGVFF. Differences with the same trend for benzene and p-xylene appear for the 1-D free energy barrier in the intersection, where this barrier is always smaller according to the DHFF force-field than according to the SVGFF one. In the 1-D free energy profiles in the straight channels computed according to DHFF, the small barrier at ξ=11.2 Å has disappeared. The same is true of the barriers at ξ=8.5 Å and ξ=14.5 Å noted along the sinusoidal channel. This could be an evidence that DHFF is more flexible than the SGVFF. We can also see from Tables 6.7, 6.8 that p-xylene has a very large probability to be in the intersection in SGVFF. The intersection is still the most favorable state, but with much lower probability in DHFF. As regards the 1-D orientational free energy, the stitch continues to be very good. This constitutes proof that the Orientations A and B of Figure 6.5 have small barriers between them and can be lumped into one state, which we have called I_Z . This was not obvious from Figure 6.8. Figure 6.8 shows the orientation preferred in spheres in a very constrained area of the intersection each time. For the 1-D orientational free energy profile we used all the intersection area.

In the beginning we mentioned that the Henry's law constant and isosteric heat for p-xylene sorbed in silicalite-1 have been predicted in excellent agreement with experimental results for a rigid silicalite-1 model described by the Olson coordinates[106]. In this work, we also calculate the isosteric heat using Eq. (2.18) combined with transition state theory. Another way to calculate the isosteric heat is the biased insertion method introduced by Snurr et al. for the rigid crystal[38]. However, because our crystal is flexible, a large number of frames would be needed to apply the same methodology with sufficient accuracy. We found it preferable to apply transition state theory-derived probabilities along with eq (2.18). In our flexible crystal model, the isosteric heat continues to be in excellent agreement with experimental measurements. This is evidence that p-xylene-silicalite-1 interactions remain satisfactory for the study of sorption in flexible silicalite-1 besides the rigid one. Probabilities calculated in this work show that the intersection is more preferable for p-xylene and that the S state follows. X-ray measurements confirm this behavior [130,131].

From Figure 6.10 in the interval ξ=(5,7) Å the free energy profile at 300K has a different shape than the profiles at the other two temperatures. We attribute this difference to the existence of two different orientations inside the sinusoidal channel. Because of the low temperature, benzene cannot pass from one to the other and it prefers to stay in the orientation it likes to have in the previous interval. We do not encounter this behavior at the other temperatures, because the higher temperatures help benzene to undergo the transition easily and, as a result, all the phase space is sampled. These two orientations in the sinusoidal channels can be also seen in Figure 4.6.

It is important to add that a jump model is used in the interpretation of QENS measurements, considering diffusion only along the *y*-axis for p-xylene. From our results, we see that p-xylene diffuses much faster in the *y* direction than in the other two and, as a result, this justifies the jump model used here to derive the diffusion coefficients from QENS.

From Figure 6.14 we see that simulations and QENS agree qualitatively that p-xylene diffuses much faster than benzene in silicalite-1 for the range of the temperatures we studied. Comparing the force-fields DHFF and SGVFF for the same range of temperatures, we see that SGVFF results for the benzene are in better agreement with experiment than those of DHFF. We cannot make the same statement for the p-xylene. QENS results display a much lower activation energy (E_a) for p-xylene than for benzene in silicalite-1. The same behavior, but less strong, is noted from the simulations if we compare SGVFF-benzene with SGVFF-p-

xylene activation energies and DHFF-benzene with DHFF-p-xylene activation energies respectively (compare Table 6.13). We have to add that the QENS activation energy for benzene has been calculated for all the 5 experimental points, one of which has been measured in a bare silicalite (Si/Al=∞) and the others in ZSM-5 crystal with Si/Al=35.[23] In Chapter 4, we had calculated separately the activation energy only for the ZSM-5 experimental points. Here we remind the reader that the QENS measurements have been performed at an occupancy of 3 benzene molecules per unit cell and 2.5 p-xylene molecules per unit cell. If we bear in mind that a unit cell contains 4 intersection states, and that benzene and p-xylene prefer to reside in intersections, then we have less than one benzene or p-xylene per intersection in these states. As a result, these loadings are not expected to behave very differently from infinite dilution. Furthermore, it is important to add that the activation energy for benzene using the DHFF force-field is in perfect agreement with the QENS results (see Table 6.13). From the SGVFF force-field for benzene, we obtain a larger activation energy than from the QENS measurements (by approximately 3.5kJ/mol). The activation energy agreement is very important, because it defines the behavior for a broad range of temperatures. Small activation energy would result if the lines of 1-D Free Energy profiles (measured in *RT* units) exhibited only a slight dependence on temperature. The transmission coefficient for individual transitions was not calculated in this work, as it is expected to be close to unity, as shown in Figure 4.14. Actually, for the temperature of 485K and using the DHFF model we see from Table 6.11 that there is excellent agreement between the transition state theory-based diffusion coefficients and diffusion coefficients derived from direct molecular dynamics simulations. Here it is important to add that, for lower temperature, diffusion coefficients are extremely difficult to compute directly by MD, because of the large computer time we need. In addition, conducting transition state theory-based analysis helps us understand exactly the mechanism of diffusion via the free energy profiles. The rate constants can be also used for mesoscopic simulations in the future. In Figure 6.14, other experiments are not mentioned. The large differences in diffusivity between benzene and p-xylene, which are found on the microscopic scale, cannot be observed by other experimental techniques, probably because of defects in the silicalite structure.[132]

Chapter 8

Conclusions

We have presented a new method for solving the master equation of a system evolving on a network of states that is formed by periodic replication of a "unit cell" of n states. The mathematical development focused on networks consisting of 2^ν unit cells arranged along one coordinate direction with periodic boundary conditions at the ends, although different numbers of unit cells and replication in more than one coordinate directions could be handled by similar strategies. Our new method rests upon expressing the time-dependent probabilities of occupancy of all states analytically as sums of exponentially decaying contributions from $2^\nu n$ relaxation modes. The time constants and amplitudes of these modes are calculated from the eigenvalues and eigenvectors of the matrix of interstate transition rate constants, transformed into a symmetric matrix by virtue of the conditions of microscopic reversibility.[74-76]

We have analyzed how the symmetrized $(2^\nu n)\times(2^\nu n)$ rate constant matrix $\tilde{\mathbf{K}}_{2^\nu}$ for the periodic system can be written in terms of the corresponding $n\times n$ matrix $\tilde{\mathbf{K}}_1$ of the unit cell and the $n\times n$ matrices $\tilde{\mathbf{K}}_{\mathrm{L1}}$ and $\tilde{\mathbf{K}}_{\mathrm{R1}} = \tilde{\mathbf{K}}_{\mathrm{L1}}^{\mathrm{T}}$ which collect the rate constants "to the left" and "to the right" out of a unit cell across its periodic boundaries in the direction of replication. We have then shown that the eigenvalues and eigenvectors of $\tilde{\mathbf{K}}_{2^\nu}$ can be obtained through a recursive reduction scheme involving the diagonalization exclusively of $n\times n$ matrices. A detailed algorithm for this new recursive reduction (MESoRReD) has been presented in Figures 3.4-3.7.

We have applied MESoRReD to the problem of low-temperature, low-occupancy diffusion of xenon in silicalite-1, studied previously with MD[84] and infrequent event analysis[62] methods by June et al. In our application we have employed the sorption states and interstate transitions identified by June et al.[62] (Figures 3.10, 3.11 and Table 3.1). We have also employed the transition rate constants computed by June et al.[62] based on transition-state theory without dynamical corrections (Table 3.2), to ensure direct comparability with previously reported results. Diffusivities were calculated by matching our MESoRReD solution to the corresponding solution of the continuum diffusion equation

under the same initial and boundary conditions (Figures 3.9, 3.12). Furthermore, by comparing the analytical solution to the master equation as a sum of exponentially decaying functions [Eq. (3.7)] to the analytical solution to the continuum diffusion problem [Eq. (3.36)] we have shown that the diffusivity can be obtained straightforwardly from the nonzero eigenvalue of smallest absolute magnitude obtained by MESoRReD [Eq. (3.45) and Figure 3.15]. Our new method yields estimates for the diffusivities D_{xx}, D_{yy}, D_{zz} along the three coordinate directions and for the orientationally averaged diffusivity D that are within 3.5% and 2.5%, respectively, of the values reported by June et al.[86] based on KMC simulations (Table 3.4). Our own KMC runs in a three-dimensional array of unit cells yielded values which are within simulation error from those from MESoRReD. As an additional check of consistency of results obtained by the MESoRReD method, we have solved the master equation numerically as an initial value problem using the Euler method. Diffusivities from the Euler method display the same high level of consistency with those from our new method (Table 3.4).

Thanks to its reduction of a $(2^{\nu}n)\times(2^{\nu}n)$ matrix diagonalization problem to 2^{ν} $n\times n$ matrix diagonalization problems, the new method affords great savings in computer time and in computer memory (RAM), especially as regards the calculation of the eigenvectors. We have compared the computational requirements of MESoRReD against those of Kinetic Monte Carlo, numerical solution of the master equation by the Euler method, and direct MD simulation for the problem of calculating diffusion coefficients for Xe in silicalite-1 at 150 K and low occupancy to the same level of accuracy (Table 3.3). Calculation of the diffusivity after determination of all eigenvalues of the rate constant matrix of the periodic system through MESoRReD is faster than KMC by a factor of 3.493×10^{5}, faster than the Euler method by a factor of 1.342×10^{6}, and faster than direct MD by a factor of roughly 1.747×10^{7}. These acceleration factors are expected to be more favorable in more complex problems characterized by more rugged energy landscapes.

Furthermore, for diffusion problems, we have tracked down which $n\times n$ matrices within the MESoRReD reduction scheme contributes the nonzero eigenvalue of smallest absolute magnitude to the $(2^{\nu}n)\times(2^{\nu}n)$ rate constant matrix of the full periodic system. This allows us to obtain the diffusivity through determination of the absolutely smallest eigenvalue of a *single* $n\times n$ matrix [Eq. (3.46) and Figure 3.16], which is trivial computationally.

We conclude that the new method proposed here for solving the master equation by spectral decomposition based on recursive reduction of the dimensionality of the rate constant

matrix (MESoRReD) offers great computational advantages, relative to alternative deterministic or stochastic methods, for tracking the long-time evolution of material systems characterized by spatial periodicity. Furthermore, setting up the $\tilde{\mathbf{K}}_1$ and $\tilde{\mathbf{K}}_{R1}$ matrices for implementing the method is quite straightforward. FORTRAN codes implementing the method are available from the authors upon request.

In addition to MESoRReD, a new infrequent event-based study of diffusion of benzene in silicalite-1 has been presented to complement the two main simulation studies that have been conducted on the subject in the past.[36,39] We have used a flexible model for silicalite-1 described by Vlugt and Schenk,[104] and a second flexible model based on the work of Smirnov and Bougeard.[110] We have also introduced a new algorithm to reduce the possibility of overestimating the rate constants, hence the diffusion coefficients, in Transition State Theory calculations. We have discussed the risks associated with reducing the Transition State Theory calculation to 1-D from the full multidimensional problem.

The orientational distribution of benzene in a variety of positions has been tested and compared against available experimental results. Good agreement has been found with the 3 of the 4 orientations extracted from experiments. We show that, in the case of benzene, orientational states are separated by low free energy barriers, permitting an analysis of the local free energy as a function of the center of mass position only.

We have introduced a technique for computing the local free energy using isothermal MD simulations in the presence of confining soft repulsive walls. Using these tools, we have calculated the 3 dimensional free energy profile $A(\mathbf{r}_{CM})$ which helped us find one-dimensional paths on which the benzene center of mass motion should be projected. We defined projections from 3-D to 1-D curvilinear transition paths, identified states and computed interstate rate constants from the 1-D local free energy profiles, $A(\xi)$. Three sorption states were located for benzene, a dominant one in the channel intersection region and two additional ones in the interiors of straight and sinusoidal channel segments.

From the transition rate constants we have calculated the elements of the self-diffusivity tensor by two different methods, Kinetic Monte Carlo and MESoRReD. Results from the two methods were in excellent agreement. Consistent with previous investigators, we have found that the diffusion is fastest along the *y* crystallographic axis and slowest along the *z*. The orientationally averaged diffusion coefficient based on the DHFF force field was overestimated by one order of magnitude relative to experimental results, while the activation

energy from the simulation came out in almost perfect agreement with quasi-elastic neutron scattering measurements. The SGVFF force field, on the other hand, yielded diffusivity values that are within a factor of 3 of those measured by QENS, but an activation energy that is by 20% higher than the QENS-based value.

Previous works have pointed out the importance of framework flexibility for transport modeling in zeolite-type materials.[133,134]

In this work we have first conducted a sensitivity analysis to determine how umbrella sampling-based free energy profiles of aromatic molecules in the zeolite silicalite-1 depend on the force field used to represent these systems. We have shown that the use of a static electrostatic map in conjunction with a flexible zeolite model cast in terms of harmonic potentials among the atoms is the fastest method by far for conducting our molecular simulations, without significant departure of the final results from those obtained by more elaborate model representations. The flexibility of the benzene model also does not seem to influence the results. One can conclude that representing the equilibriun structure and the vibrations of the zeolite lattice reasonably realistically is the key factor for the diffusion of aromatics in silicalite-1. Of the two flexible force fields we have studied, the SGVFF yields volumetric properties for pure silicalite which are close to the experimental ones, including a negative thermal expansion coefficient. A method for applying the P^3M technique for a zeolite crystal where intra-zeolite interactions are described by spring constants only, without simultaneously eliminating the electrostatic interactions with the sorbate, was explained. Furthermore, our repulsive wall curvilinear umbrella sampling strategy has been applied for the first time for a flexible sorbate. Finally, diffusion coefficients were calculated by finding the absolutely minimal nonzero eigenvalue of an appropriately designed rate constant matrix. The equation underpinning this calculation was proposed in the context of the MESoRReD method and allows going directly from interstate transition rate constants to diffusivities with negligible computer time, circumventing the need for costly kinetic Monte Carlo computations. Results from these infrequent event analysis-based techniques were found to be in excellent agreement with the corresponding results obtained from direct molecular dynamics simulation of p-xylene in silicalite-1 at a temperature of 485K. The reader is reminded that only for p-xylene at this elevated temperature is intracrystalline dynamics fast enough to be captured reliably by direct MD, so our consistency check was necessarily confined to this state point.

Our simulation showed the existence of entropic barriers to translational motion with both flexible force-fields we have used for silicalite. These entropic barriers are much larger for benzene than for p-xylene in the channel intersection region. A new technique of orientational confining walls was used to calculate the rate constant for transitions between different orientations of p-xylene in the intersection region. This technique is an extension of our umbrella sampling using repulsive walls, invoked in computing the free energy of the sorbate molecule as a function of its center of mass position. From the orientational free energy profiles accumulated, it became clear that p-xylene strongly prefers to orient itself parallel to the straight channel axis when residing in the channel intersection region; transitions from this orientation to an orientation parallel to the sinusoidal channels are rare. Thus, diffusion along the straight channels and diffusion along the sinusoidal channels take place largely independently for p-xylene in silicalite-1. A new path was proposed for translational motion along the sinusoidal channel for p-xylene, which differs from the corresponding path that has been used in the past for benzene. A new technique for lumping sorption states and simplifying the network of transitions was also proposed. The atomistic dynamics can be described at a coarse-grained level through introduction of two orientational states for p-xylene residing in the intersection region, I_S and I_Z. Rate constants for all transitions involving these states have been computed by transition state theory. The situation for p-xylene in the intersection is markedly different from that of benzene, which can rapidly sample a variety of orientations and, as a consequence, can be described satisfactorily through a single intersection state, I, of low free energy (high entropy). This difference is the physical reason for the much higher entropic barriers to translational motion experienced by benzene in comparison to p-xylene and for the lower diffusivity of benzene.

Our simulations show that, for both aromatic sorbate molecules, channel intersections are the most favorable positions for sorption, with sites inside the straight channels coming second. Isosteric heats of sorption were calculated based on the transition rate constant analysis for both benzene and p-xylene with both flexible zeolite models (DHFF anf SGVFF) and found to be in excellent agreement with experiment.

QENS measurements were conducted and the obtained diffusivities were compared with those computed from the simulations. Despite differences among simulation predictions obtained from different model representations, both QENS measurements and computer simulations lead to the conclusion that microscopic diffusion in silicalite-1 is by roughly two orders of magnitude faster for p-xylene than for benzene, because of the entropic barriers to

translational motion encountered by the latter due to its ability to reorient within channel intersections. The elongated shape of p-xylene largely deprives it of this reorientational ability and enables it to move faster through channel intersections.

In future work, other aromatics, such as toluene, ortho- and meta-xylene, can be also studied applying the methodology proposed here. In addition, the rate constants calculated here can be used in mesoscale calculations to address diffusion and reaction phenomena over larger length and time scales, e.g. within beds of silicalite-1 or ZSM-5.

Chapter 9

Future Work

As we mentioned in Chapter 4, there is a wide range of partial charges for silicalite-1 and for silicates general. Consequently, it would be good if a case study of the influence of the silicalite-1 charges on the self-diffusion coefficient was conducted in the future. It is very probable that a new, more sophisticated force-field for the sorbate-zeolite interactions may predict better the small entropy barriers that Quasi Elastic Neutron Scattering measurements show, which were impossible to predict with the existent force-field. In this thesis, we also saw that explicit electrostatics and flexible benzene give the same free energy profiles as a static electrostatic map and a rigid benzene. It is most probable that the same would happen with p-xylene. However, in order to be sure about this, it can be tested in the future. Furthermore, in this study we focused on the comparison of the self-diffusion of benzene and p-xylene inside silicalite-1 at infinite dilution. This comparison can include other aromatics that we did not study in this thesis (toluene, o-xylene, m-xylene) so that we can have a more general idea about the diffusion of aromatics in silicalite-1 at infinite dilution and its mechanism.

Another study that would be useful to undertake is the calculation of self-diffusion coefficients for the mixture benzene/p-xylene. At infinite dilution, this could be accomplished using the transition rate constants we have calculated in this thesis and zero rate constants in case a position in silicalite lattice is already occupied by another sorbate. Of course, these rate constants can be used in combination with Kinetic Monte Carlo. This cannot be extended to larger loadings of benzene and p-xylene. To calculate self-diffusion coefficients in such high-occupancy systems, we have to apply again the CUS method just on one only sorbate molecule in the presence of other sorbate molecules, leaving the other sorbates uninfluenced by the walls. In this way, we can calculate transition rate constants appropriate for higher loadings. Applying this CUS methodology for different loadings, we can get the transition rate constants for every combination of loadings. Then we can use these rate constants (which will depend on the loading around the state the rate constant of which we want to calculate) by applying Kinetic Monte Carlo. In this way, Kinetic Monte Carlo will be much more realistic. Another aspect that can also be studied in the future is the surface barriers and the

rate constants for the transition from the crystal surface to the bulk phase and vice versa. Finally, application of the CUS methodology for the study of sorbates which are tight-fitting to new kinds of materials, such as Metal Organic Frameworks, would be valuable.

Appendices-Mathematical Proofs

Appendix A: General solution of the Master Equation

The symmetrized Master Equation, Eq. (3.6) of the main text, is actually a system of differential equations of first order. The general solution such a system is of the form

$$\tilde{\mathbf{P}}(t) = \sum_{m=0}^{n-1} c_m \mathbf{x}_m e^{\lambda_m t} \tag{A1}$$

with λ_m, $\mathbf{x}_m$ being the eigenvalues and eigenvectors of the matrix $\tilde{\mathbf{K}}$ of constant coefficients on the right-hand side.

For t=0, Eq. (A1) gives:

$$\tilde{\mathbf{P}}(0) = \sum_{m=0}^{n-1} c_m \mathbf{x}_m \text{ , hence } \mathbf{x}^*_{m'} \cdot \tilde{\mathbf{P}}(0) = \sum_{m=0}^{n-1} c_m \mathbf{x}^*_{m'} \cdot \mathbf{x}_m \quad (0 \le m' \le n-1) \tag{A2}$$

where $\mathbf{x}^*_{m'}$ symbolizes a vector whose elements are complex conjugate to those of eigenvector $\mathbf{x}_{m'}$. If $\tilde{\mathbf{K}}$ is Hermitian, its eigenvalues λ_m are real. Furthermore, eigenvectors corresponding to different eigenvalues are orthogonal to each other. This allows us to calculate the coefficients c_m from Eq.(A2) as follows:

$$\mathbf{x}^*_m \cdot \tilde{\mathbf{P}}(0) = c_m \left\| \mathbf{x}_m \right\|_2^2, \text{ hence } c_m = \frac{\mathbf{x}^*_m \cdot \tilde{\mathbf{P}}(0)}{\left\| \mathbf{x}_m \right\|_2^2}. \tag{A3}$$

and consequently

$$\tilde{\mathbf{P}}(t) = \sum_{m=0}^{n-1} \frac{\mathbf{x}^*_m \cdot \tilde{\mathbf{P}}(0)}{\left\| \mathbf{x}_m \right\|_2^2} \mathbf{x}_m e^{\lambda_m t} \tag{A4}$$

In our application, $\tilde{\mathbf{K}}$ is a real symmetric matrix (a special case of a Hermitian matrix). Furthermore, one can choose the eigenvectors as $\tilde{\mathbf{u}}_m = \mathbf{x}_m / \left\| \mathbf{x}_m \right\|_2$ and therefore $\left\| \tilde{\mathbf{u}}_m \right\|_2 = 1$, i.e., such that they form an orthonormal set. Under these conditions, Eq. (A4) reduces to Eq. (3.7) of the main text.

For $t \to \infty$, using Eqs. (A1), (A4):

$$\tilde{\mathbf{P}}^{\text{eq}} = \tilde{\mathbf{P}}(\infty) = \lim_{t\to\infty} \sum_{m=0}^{n-1} c_m \mathbf{x}_m e^{\lambda_m t} = c_0 \mathbf{x}_0 = \left[\tilde{\mathbf{u}}_0 \cdot \tilde{\mathbf{P}}(0) \right] \tilde{\mathbf{u}}_0 = \left[\sum_{i=1}^{n} \sqrt{P_i^{\text{eq}}} \tilde{P}_i(0) \right] \tilde{\mathbf{u}}_0 = \left(\sum_{i=1}^{n} P_i(0) \right) \tilde{\mathbf{u}}_0 = \tilde{\mathbf{u}}_0 \tag{A5}$$

Appendix B: Proof of Theorem 1

By Eqs. (3.13-3.15) of the main text, $\tilde{\mathbf{K}}_{2^{\nu-1}} - 2\tilde{\mathbf{K}}_{\mathrm{RL}2^{\nu-1}}$ can be rewritten as:

$$\tilde{\mathbf{K}}_{2^{\nu-1}} - 2\tilde{\mathbf{K}}_{\mathrm{RL}2^{\nu-1}} = \begin{bmatrix} \tilde{\mathbf{K}}_{2^{\nu-2}} - \tilde{\mathbf{K}}_{\mathrm{RL}2^{\nu-2}} & \tilde{\mathbf{K}}_{\mathrm{RL}2^{\nu-2}} \\ \tilde{\mathbf{K}}_{\mathrm{RL}2^{\nu-2}} & \tilde{\mathbf{K}}_{2^{\nu-2}} - \tilde{\mathbf{K}}_{\mathrm{RL}2^{\nu-2}} \end{bmatrix} - 2\begin{bmatrix} \mathbf{0} & \tilde{\mathbf{K}}_{\mathrm{R}2^{\nu-2}} \\ \tilde{\mathbf{K}}_{\mathrm{L}2^{\nu-2}} & \mathbf{0} \end{bmatrix}, \text{ or}$$

$$\tilde{\mathbf{K}}_{2^{\nu-1}} - 2\tilde{\mathbf{K}}_{\mathrm{RL}2^{\nu-1}} = \begin{bmatrix} \tilde{\mathbf{K}}_{2^{\nu-2}} - \tilde{\mathbf{K}}_{\mathrm{RL}2^{\nu-2}} & \tilde{\mathbf{K}}_{\mathrm{R}2^{\nu-2}} + \tilde{\mathbf{K}}_{\mathrm{L}2^{\nu-2}} - 2\tilde{\mathbf{K}}_{\mathrm{R}2^{\nu-2}} \\ \tilde{\mathbf{K}}_{\mathrm{R}2^{\nu-2}} + \tilde{\mathbf{K}}_{\mathrm{L}2^{\nu-2}} - 2\tilde{\mathbf{K}}_{\mathrm{L}2^{\nu-2}} & \tilde{\mathbf{K}}_{2^{\nu-2}} - \tilde{\mathbf{K}}_{\mathrm{RL}2^{\nu-2}} \end{bmatrix}, \text{ or}$$

$$\tilde{\mathbf{K}}_{2^{\nu-1}} - 2\tilde{\mathbf{K}}_{\mathrm{RL}2^{\nu-1}} = \begin{bmatrix} \tilde{\mathbf{K}}_{2^{\nu-2}} - \tilde{\mathbf{K}}_{\mathrm{RL}2^{\nu-2}} & \tilde{\mathbf{K}}_{\mathrm{L}2^{\nu-2}} - \tilde{\mathbf{K}}_{\mathrm{R}2^{\nu-2}} \\ \tilde{\mathbf{K}}_{\mathrm{R}2^{\nu-2}} - \tilde{\mathbf{K}}_{\mathrm{L}2^{\nu-2}} & \tilde{\mathbf{K}}_{2^{\nu-2}} - \tilde{\mathbf{K}}_{\mathrm{RL}2^{\nu-2}} \end{bmatrix} \tag{B1}$$

Let $\lambda_{\tilde{\mathbf{K}}_{2^{\nu-1}} - 2\tilde{\mathbf{K}}_{\mathrm{RL}2^{\nu-1}}}$ be an eigenvalue of $\tilde{\mathbf{K}}_{2^{\nu-1}} - 2\tilde{\mathbf{K}}_{\mathrm{RL}2^{\nu-1}}$, with corresponding eigenvector

$$\mathbf{x}_{\tilde{\mathbf{K}}_{2^{\nu-1}} - 2\tilde{\mathbf{K}}_{\mathrm{RL}2^{\nu-1}}} = \begin{bmatrix} \mathbf{x}_{2^{\nu-2},\mathrm{C}} \\ \mathbf{x}_{2^{\nu-2},\mathrm{D}} \end{bmatrix} \tag{B2}$$

Using Eqs. (B1) and (B2), we write the eigenvalue equation as

$$\begin{bmatrix} \tilde{\mathbf{K}}_{2^{\nu-2}} - \tilde{\mathbf{K}}_{\mathrm{RL}2^{\nu-2}} & \tilde{\mathbf{K}}_{\mathrm{L}2^{\nu-2}} - \tilde{\mathbf{K}}_{\mathrm{R}2^{\nu-2}} \\ \tilde{\mathbf{K}}_{\mathrm{R}2^{\nu-2}} - \tilde{\mathbf{K}}_{\mathrm{L}2^{\nu-2}} & \tilde{\mathbf{K}}_{2^{\nu-2}} - \tilde{\mathbf{K}}_{\mathrm{RL}2^{\nu-2}} \end{bmatrix} \begin{bmatrix} \mathbf{x}_{2^{\nu-2},\mathrm{C}} \\ \mathbf{x}_{2^{\nu-2},\mathrm{D}} \end{bmatrix} = \lambda_{\tilde{\mathbf{K}}_{2^{\nu-1}} - 2\tilde{\mathbf{K}}_{\mathrm{RL}2^{\nu-1}}} \begin{bmatrix} \mathbf{x}_{2^{\nu-2},\mathrm{C}} \\ \mathbf{x}_{2^{\nu-2},\mathrm{D}} \end{bmatrix} \tag{B3}$$

or

$$\begin{aligned} \left(\tilde{\mathbf{K}}_{2^{\nu-2}} - \tilde{\mathbf{K}}_{\mathrm{RL}2^{\nu-2}}\right)\mathbf{x}_{2^{\nu-2},\mathrm{C}} + \left(\tilde{\mathbf{K}}_{\mathrm{L}2^{\nu-2}} - \tilde{\mathbf{K}}_{\mathrm{R}2^{\nu-2}}\right)\mathbf{x}_{2^{\nu-2},\mathrm{D}} &= \lambda_{\tilde{\mathbf{K}}_{2^{\nu-1}} - 2\tilde{\mathbf{K}}_{\mathrm{RL}2^{\nu-1}}} \mathbf{x}_{2^{\nu-2},\mathrm{C}} \\ \left(\tilde{\mathbf{K}}_{\mathrm{R}2^{\nu-2}} - \tilde{\mathbf{K}}_{\mathrm{L}2^{\nu-2}}\right)\mathbf{x}_{2^{\nu-2},\mathrm{C}} + \left(\tilde{\mathbf{K}}_{2^{\nu-2}} - \tilde{\mathbf{K}}_{\mathrm{RL}2^{\nu-2}}\right)\mathbf{x}_{2^{\nu-2},\mathrm{D}} &= \lambda_{\tilde{\mathbf{K}}_{2^{\nu-1}} - 2\tilde{\mathbf{K}}_{\mathrm{RL}2^{\nu-1}}} \mathbf{x}_{2^{\nu-2},\mathrm{D}} \end{aligned} \tag{B4}$$

Multiplying the second of Eqs. (B4) with a coefficient *a* and adding the two equations together, we obtain:

$$\left[\left(\tilde{\mathbf{K}}_{2^{\nu-2}} - \tilde{\mathbf{K}}_{\mathrm{RL}2^{\nu-2}}\right) + a\left(\tilde{\mathbf{K}}_{\mathrm{R}2^{\nu-2}} - \tilde{\mathbf{K}}_{\mathrm{L}2^{\nu-2}}\right)\right]\mathbf{x}_{2^{\nu-2},\mathrm{C}} + \left[a\left(\tilde{\mathbf{K}}_{2^{\nu-2}} - \tilde{\mathbf{K}}_{\mathrm{RL}2^{\nu-2}}\right) + \left(\tilde{\mathbf{K}}_{\mathrm{L}2^{\nu-2}} - \tilde{\mathbf{K}}_{\mathrm{R}2^{\nu-2}}\right)\right]\mathbf{x}_{2^{\nu-2},\mathrm{D}} =$$

$$\lambda_{\tilde{\mathbf{K}}_{2^{\nu-1}} - 2\tilde{\mathbf{K}}_{\mathrm{RL}2^{\nu-1}}} \left(\mathbf{x}_{2^{\nu-2},\mathrm{C}} + a\mathbf{x}_{2^{\nu-2},\mathrm{D}}\right) \tag{B5}$$

or

$$\left[\left(\tilde{\mathbf{K}}_{2^{\nu-2}} - \tilde{\mathbf{K}}_{\mathrm{RL}2^{\nu-2}}\right) + a\left(\tilde{\mathbf{K}}_{\mathrm{R}2^{\nu-2}} - \tilde{\mathbf{K}}_{\mathrm{L}2^{\nu-2}}\right)\right]\mathbf{x}_{2^{\nu-2},\mathrm{C}} + \left[\left(\tilde{\mathbf{K}}_{2^{\nu-2}} - \tilde{\mathbf{K}}_{\mathrm{RL}2^{\nu-2}}\right) - \frac{1}{a}\left(\tilde{\mathbf{K}}_{\mathrm{R}2^{\nu-2}} - \tilde{\mathbf{K}}_{\mathrm{L}2^{\nu-2}}\right)\right]a\mathbf{x}_{2^{\nu-2},\mathrm{D}} =$$

$$\lambda_{\tilde{\mathbf{K}}_{2^{\nu-1}} - 2\tilde{\mathbf{K}}_{\mathrm{RL}2^{\nu-1}}} \left(\mathbf{x}_{2^{\nu-2},\mathrm{C}} + a\mathbf{x}_{2^{\nu-2},\mathrm{D}}\right) \tag{B6}$$

If coefficient *a* is chosen such that $a = -\frac{1}{a}$, or $a^2 = -1$, or $a = \pm i$ (B7)

where *i* is the imaginary unit, then Eq. (B7) reduces to a single eigenvalue equation,

$$\left[\left(\tilde{\mathbf{K}}_{2^{\nu-2}}-\tilde{\mathbf{K}}_{\mathrm{RL}2^{\nu-2}}\right)+a\left(\tilde{\mathbf{K}}_{\mathrm{R}2^{\nu-2}}-\tilde{\mathbf{K}}_{\mathrm{L}2^{\nu-2}}\right)\right]\left(\mathbf{x}_{2^{\nu-2},\mathrm{C}}+a\mathbf{x}_{2^{\nu-2},\mathrm{D}}\right)=\lambda_{\tilde{\mathbf{K}}_{2^{\nu-1}}-2\tilde{\mathbf{K}}_{\mathrm{RL}2^{\nu-1}}}\left(\mathbf{x}_{2^{\nu-2},\mathrm{C}}+a\mathbf{x}_{2^{\nu-2},\mathrm{D}}\right) \quad \text{(B8)}$$

Eq. (B8) is valid for both $a=i$ and $a=-i$; thus, the following equations are satisfied simultaneously:

$$\begin{aligned}\left[\left(\tilde{\mathbf{K}}_{2^{\nu-2}}-\tilde{\mathbf{K}}_{\mathrm{RL}2^{\nu-2}}\right)+i\left(\tilde{\mathbf{K}}_{\mathrm{R}2^{\nu-2}}-\tilde{\mathbf{K}}_{\mathrm{L}2^{\nu-2}}\right)\right]\left(\mathbf{x}_{2^{\nu-2},\mathrm{C}}+i\mathbf{x}_{2^{\nu-2},\mathrm{D}}\right)&=\lambda_{\tilde{\mathbf{K}}_{2^{\nu-1}}-2\tilde{\mathbf{K}}_{\mathrm{RL}2^{\nu-1}}}\left(\mathbf{x}_{2^{\nu-2},\mathrm{C}}+i\mathbf{x}_{2^{\nu-2},\mathrm{D}}\right)\\ \left[\left(\tilde{\mathbf{K}}_{2^{\nu-2}}-\tilde{\mathbf{K}}_{\mathrm{RL}2^{\nu-2}}\right)-i\left(\tilde{\mathbf{K}}_{\mathrm{R}2^{\nu-2}}-\tilde{\mathbf{K}}_{\mathrm{L}2^{\nu-2}}\right)\right]\left(\mathbf{x}_{2^{\nu-2},\mathrm{C}}-i\mathbf{x}_{2^{\nu-2},\mathrm{D}}\right)&=\lambda_{\tilde{\mathbf{K}}_{2^{\nu-1}}-2\tilde{\mathbf{K}}_{\mathrm{RL}2^{\nu-1}}}\left(\mathbf{x}_{2^{\nu-2},\mathrm{C}}-i\mathbf{x}_{2^{\nu-2},\mathrm{D}}\right)\end{aligned} \quad \text{(B9)}$$

As we shall see below (Theorem 2) the matrices $\left(\tilde{\mathbf{K}}_{2^{\nu-2}}-\tilde{\mathbf{K}}_{\mathrm{RL}2^{\nu-2}}\right)-i\left(\tilde{\mathbf{K}}_{\mathrm{R}2^{\nu-2}}-\tilde{\mathbf{K}}_{\mathrm{L}2^{\nu-2}}\right)$ and $\left(\tilde{\mathbf{K}}_{2^{\nu-2}}-\tilde{\mathbf{K}}_{\mathrm{RL}2^{\nu-2}}\right)+i\left(\tilde{\mathbf{K}}_{\mathrm{R}2^{\nu-2}}-\tilde{\mathbf{K}}_{\mathrm{L}2^{\nu-2}}\right)$ have the same eigenvalues, which are real. On the other hand, $\tilde{\mathbf{K}}_{2^{\nu-2}}-\tilde{\mathbf{K}}_{\mathrm{RL}2^{\nu-2}}$, $\tilde{\mathbf{K}}_{\mathrm{R}2^{\nu-2}}-\tilde{\mathbf{K}}_{\mathrm{L}2^{\nu-2}}$, $\mathbf{x}_{2^{\nu-2},\mathrm{C}}$, and $\mathbf{x}_{2^{\nu-2},\mathrm{D}}$ are also real. Thus, the second of Eqs. (B9) follows from the first by taking the complex conjugate of both sides. The vectors $\mathbf{x}_{2^{\nu-2},\mathrm{C}}\pm i\mathbf{x}_{2^{\nu-2},\mathrm{D}}$ cannot be zero, as this would lead to a $\mathbf{x}_{\tilde{\mathbf{K}}_{2^{\nu-1}}-2\tilde{\mathbf{K}}_{\mathrm{RL}2^{\nu-1}}}$ that is identically zero. We conclude that $\lambda_{\tilde{\mathbf{K}}_{2^{\nu-1}}-2\tilde{\mathbf{K}}_{\mathrm{RL}2^{\nu-1}}}$ must necessarily be an eigenvalue of both matrices $\left(\tilde{\mathbf{K}}_{2^{\nu-2}}-\tilde{\mathbf{K}}_{\mathrm{RL}2^{\nu-2}}\right)\pm i\left(\tilde{\mathbf{K}}_{\mathrm{R}2^{\nu-2}}-\tilde{\mathbf{K}}_{\mathrm{L}2^{\nu-2}}\right)$. Let $\mathbf{x}_{2^{\nu-2}+}$ be the (complex) eigenvector of $\left(\tilde{\mathbf{K}}_{2^{\nu-2}}-\tilde{\mathbf{K}}_{\mathrm{RL}2^{\nu-2}}\right)+i\left(\tilde{\mathbf{K}}_{\mathrm{R}2^{\nu-2}}-\tilde{\mathbf{K}}_{\mathrm{L}2^{\nu-2}}\right)$ corresponding to eigenvalue $\lambda_{\tilde{\mathbf{K}}_{2^{\nu-1}}-2\tilde{\mathbf{K}}_{\mathrm{RL}2^{\nu-1}}}$ and $\mathbf{x}_{2^{\nu-2}-}$ be the eigenvector of $\left(\tilde{\mathbf{K}}_{2^{\nu-2}}-\tilde{\mathbf{K}}_{\mathrm{RL}2^{\nu-2}}\right)-i\left(\tilde{\mathbf{K}}_{\mathrm{R}2^{\nu-2}}-\tilde{\mathbf{K}}_{\mathrm{L}2^{\nu-2}}\right)$ corresponding to eigenvalue $\lambda_{\tilde{\mathbf{K}}_{2^{\nu-1}}-2\tilde{\mathbf{K}}_{\mathrm{RL}2^{\nu-1}}}$. Then, by Eq. (B9) we have:

$$\mathbf{x}_{2^{\nu-2},\mathrm{C}}+i\mathbf{x}_{2^{\nu-2},\mathrm{D}}=\mathbf{x}_{2^{\nu-2}+}$$

$$\mathbf{x}_{2^{\nu-2},\mathrm{C}}-i\mathbf{x}_{2^{\nu-2},\mathrm{D}}=\mathbf{x}_{2^{\nu-2}-}$$

Hence,

$$\begin{aligned}\mathbf{x}_{2^{\nu-2},\mathrm{C}}&=\left(\mathbf{x}_{2^{\nu-2}+}+\mathbf{x}_{2^{\nu-2}-}\right)/2\\ \mathbf{x}_{2^{\nu-2},\mathrm{D}}&=\left(\mathbf{x}_{2^{\nu-2}+}-\mathbf{x}_{2^{\nu-2}-}\right)/(2i)\end{aligned} \quad \text{(B10)}$$

or, allowing for multiplicative constants in the eigenvalues,

$$\mathbf{x}_{2^{\nu-2},\mathrm{C}}=\zeta\mathbf{x}_{2^{\nu-2}+}+\xi\mathbf{x}_{2^{\nu-2}-}$$

$$\mathbf{x}_{2^{\nu-2},\mathrm{D}}=\left(\zeta\mathbf{x}_{2^{\nu-2}+}-\xi\mathbf{x}_{2^{\nu-2}-}\right)/i$$

$$\mathbf{x}_{\tilde{\mathbf{K}}_{2^{\nu-1}}-2\tilde{\mathbf{K}}_{\mathrm{RL}2^{\nu-1}}}=\begin{bmatrix}\mathbf{x}_{2^{\nu-2},\mathrm{C}}\\ \mathbf{x}_{2^{\nu-2},\mathrm{D}}\end{bmatrix}=\zeta\begin{bmatrix}\mathbf{x}_{2^{\nu-2}+}\\ \mathbf{x}_{2^{\nu-2}+}/i\end{bmatrix}+\xi\begin{bmatrix}\mathbf{x}_{2^{\nu-2}-}\\ -\mathbf{x}_{2^{\nu-2}-}/i\end{bmatrix}$$

Thus, the procedure of diagonalizing $\tilde{\mathbf{K}}_{2^{\nu-1}}-2\tilde{\mathbf{K}}_{\mathrm{RL}2^{\nu-1}}$ is reduced to diagonalizing the two matrices $\left(\tilde{\mathbf{K}}_{2^{\nu-2}}-\tilde{\mathbf{K}}_{\mathrm{RL}2^{\nu-2}}\right)\pm i\left(\tilde{\mathbf{K}}_{\mathrm{R}2^{\nu-2}}-\tilde{\mathbf{K}}_{\mathrm{L}2^{\nu-2}}\right)$, Q.E.D.

Appendix C: Proof of Theorem 2

As pointed out following the definition, Eq. (3.15) of the main text, applied here for ν-1 in place of ν, matrices $\tilde{\mathbf{K}}_{\mathrm{R}2^{\nu-2}}$ and $\tilde{\mathbf{K}}_{\mathrm{L}2^{\nu-2}}$ are transpose of each other, while their sum, matrix $\tilde{\mathbf{K}}_{\mathrm{RL}2^{\nu-2}}$, is a symmetric matrix. On the other hand, by the definition, Eq. (3.12) of the main text, matrix $\tilde{\mathbf{K}}_{2^{\nu-2}}$ is symmetric. Therefore,

$$\begin{aligned}\left[\left(\tilde{\mathbf{K}}_{2^{\nu-2}}-\tilde{\mathbf{K}}_{\mathrm{RL}2^{\nu-2}}\right)+i\left(\tilde{\mathbf{K}}_{\mathrm{R}2^{\nu-2}}-\tilde{\mathbf{K}}_{\mathrm{L}2^{\nu-2}}\right)\right]^{\mathrm{T}}&=\left(\tilde{\mathbf{K}}_{2^{\nu-2}}-\tilde{\mathbf{K}}_{\mathrm{RL}2^{\nu-2}}\right)^{\mathrm{T}}+i\left(\tilde{\mathbf{K}}_{\mathrm{R}2^{\nu-2}}-\tilde{\mathbf{K}}_{\mathrm{L}2^{\nu-2}}\right)^{\mathrm{T}}\\&=\left(\tilde{\mathbf{K}}_{2^{\nu-2}}-\tilde{\mathbf{K}}_{\mathrm{RL}2^{\nu-2}}\right)^{\mathrm{T}}+i\left(\tilde{\mathbf{K}}^{\mathrm{T}}_{\mathrm{R}2^{\nu-2}}-\tilde{\mathbf{K}}^{\mathrm{T}}_{\mathrm{L}2^{\nu-2}}\right)\\&=\left(\tilde{\mathbf{K}}^{\mathrm{T}}_{2^{\nu-2}}-\tilde{\mathbf{K}}^{\mathrm{T}}_{\mathrm{RL}2^{\nu-2}}\right)+i\left(\tilde{\mathbf{K}}_{\mathrm{L}2^{\nu-2}}-\tilde{\mathbf{K}}_{\mathrm{R}2^{\nu-2}}\right)\\&=\left(\tilde{\mathbf{K}}_{2^{\nu-2}}-\tilde{\mathbf{K}}_{\mathrm{RL}2^{\nu-2}}\right)-i\left(\tilde{\mathbf{K}}_{\mathrm{R}2^{\nu-2}}-\tilde{\mathbf{K}}_{\mathrm{L}2^{\nu-2}}\right)\end{aligned}$$

QED (C1)

Appendix D: Proof of Theorem 3

It suffices to show that the matrices corresponding to two successive values of the index, b–1 and b, are characterized by the same eigenvalues.

Let $\lambda_{2^{\mu-b}}$ be an eigenvalue of one of the $(2^{\mu-b}n)\times(2^{\mu-b}n)$ –dimensional matrices $\left(\tilde{\mathbf{K}}_{2^{\mu-b}}-\tilde{\mathbf{K}}_{\mathrm{RL}2^{\mu-b}}\right)+\left[a_b\tilde{\mathbf{K}}_{\mathrm{R}2^{\mu-b}}+(a_1\ldots a_b)\tilde{\mathbf{K}}_{\mathrm{L}2^{\mu-b}}\right]$, for a specific choice of the coefficients a_1, a_2, …, a_b, defined by the prescription given in the theorem. We wish to relate $\lambda_{2^{\mu-b}}$ to the eigenvalues of either one of the $(2^{\mu-b-1}n)\times(2^{\mu-b-1}n)$-dimensional matrices $\left(\tilde{\mathbf{K}}_{2^{\mu-1-b}}-\tilde{\mathbf{K}}_{\mathrm{RL}2^{\mu-1-b}}\right)+\left[a_{b+1}\tilde{\mathbf{K}}_{\mathrm{R}2^{\mu-1-b}}+(a_1\ldots a_{b+1})\tilde{\mathbf{K}}_{\mathrm{L}2^{\mu-1-b}}\right]$, with a_{b+1} being one of the two values defined from a_b according to the prescription.

Let $\mathbf{x}_{2^{\mu-b}} = \begin{bmatrix} \mathbf{x}_{2^{\mu-b-1},\mathrm{E}} \\ \mathbf{x}_{2^{\mu-b-1},\mathrm{F}} \end{bmatrix}$ be the eigenvector corresponding to eigenvalue $\lambda_{2^{\mu-b}}$ of matrix $\left(\tilde{\mathbf{K}}_{2^{\mu-b}} - \tilde{\mathbf{K}}_{\mathrm{RL}2^{\mu-b}}\right) + \left[a_b \tilde{\mathbf{K}}_{\mathrm{R}2^{\mu-b}} + (a_1 \ldots a_b)\tilde{\mathbf{K}}_{\mathrm{L}2^{\mu-b}}\right]$, where $\mathbf{x}_{2^{\mu-b-1},\mathrm{E}}$ and $\mathbf{x}_{2^{\mu-b-1},\mathrm{F}}$ are ($2^{\mu\text{-}1\text{-}b}n$)-dimensional vectors. From the definition of $\tilde{\mathbf{K}}_{2^{\mu-b}}$, $\tilde{\mathbf{K}}_{\mathrm{R}2^{\mu-b}}$, $\tilde{\mathbf{K}}_{\mathrm{L}2^{\mu-b}}$, and $\tilde{\mathbf{K}}_{\mathrm{RL}2^{\mu-b}}$ [Eqs. (3.12), (3.14), (3.15) of the main text] we can write [compare also Eq. (3.13) of the main text]:

$$\tilde{\mathbf{K}}_{2^{\mu-b}} = \begin{bmatrix} \tilde{\mathbf{K}}_{2^{\mu-b-1}} - \tilde{\mathbf{K}}_{\mathrm{RL}2^{\mu-b-1}} & \tilde{\mathbf{K}}_{\mathrm{RL}2^{\mu-b-1}} \\ \tilde{\mathbf{K}}_{\mathrm{RL}2^{\mu-b-1}} & \tilde{\mathbf{K}}_{2^{\mu-b-1}} - \tilde{\mathbf{K}}_{\mathrm{RL}2^{\mu-b-1}} \end{bmatrix}, \quad \tilde{\mathbf{K}}_{\mathrm{RL}2^{\mu-b}} = \begin{bmatrix} \mathbf{0} & \tilde{\mathbf{K}}_{\mathrm{R}2^{\mu-b-1}} \\ \tilde{\mathbf{K}}_{\mathrm{L}2^{\mu-b-1}} & \mathbf{0} \end{bmatrix},$$

$$\tilde{\mathbf{K}}_{\mathrm{R}2^{\mu-b}} = \begin{bmatrix} \mathbf{0} & \tilde{\mathbf{K}}_{\mathrm{R}2^{\mu-b-1}} \\ \mathbf{0} & \mathbf{0} \end{bmatrix}, \quad \tilde{\mathbf{K}}_{\mathrm{L}2^{\mu-b}} = \begin{bmatrix} \mathbf{0} & \mathbf{0} \\ \tilde{\mathbf{K}}_{\mathrm{L}2^{\mu-b-1}} & \mathbf{0} \end{bmatrix} \text{ hence}$$

$$\left(\tilde{\mathbf{K}}_{2^{\mu-b}} - \tilde{\mathbf{K}}_{\mathrm{RL}2^{\mu-b}}\right) + \left[a_b \tilde{\mathbf{K}}_{\mathrm{R}2^{\mu-b}} + (a_1 \ldots a_b)\tilde{\mathbf{K}}_{\mathrm{L}2^{\mu-b}}\right] =$$

$$\begin{bmatrix} \tilde{\mathbf{K}}_{2^{\mu-b-1}} - \tilde{\mathbf{K}}_{\mathrm{RL}2^{\mu-b-1}} & \tilde{\mathbf{K}}_{\mathrm{RL}2^{\mu-b-1}} \\ \tilde{\mathbf{K}}_{\mathrm{RL}2^{\mu-b-1}} & \tilde{\mathbf{K}}_{2^{\mu-b-1}} - \tilde{\mathbf{K}}_{\mathrm{RL}2^{\mu-b-1}} \end{bmatrix} - \begin{bmatrix} \mathbf{0} & \tilde{\mathbf{K}}_{\mathrm{R}2^{\mu-b-1}} \\ \tilde{\mathbf{K}}_{\mathrm{L}2^{\mu-b-1}} & \mathbf{0} \end{bmatrix} + a_b \begin{bmatrix} \mathbf{0} & \tilde{\mathbf{K}}_{\mathrm{R}2^{\mu-b-1}} \\ \mathbf{0} & \mathbf{0} \end{bmatrix} +$$

$$(a_1 \ldots a_b) \begin{bmatrix} \mathbf{0} & \mathbf{0} \\ \tilde{\mathbf{K}}_{\mathrm{L}2^{\mu-b-1}} & \mathbf{0} \end{bmatrix} = \begin{bmatrix} \tilde{\mathbf{K}}_{2^{\mu-b-1}} - \tilde{\mathbf{K}}_{\mathrm{RL}2^{\mu-b-1}} & \tilde{\mathbf{K}}_{\mathrm{L}2^{\mu-b-1}} + a_b \tilde{\mathbf{K}}_{\mathrm{R}2^{\mu-b-1}} \\ \tilde{\mathbf{K}}_{\mathrm{R}2^{\mu-b-1}} + (a_1 \ldots a_b)\tilde{\mathbf{K}}_{\mathrm{L}2^{\mu-b-1}} & \tilde{\mathbf{K}}_{2^{\mu-b-1}} - \tilde{\mathbf{K}}_{\mathrm{RL}2^{\mu-b-1}} \end{bmatrix} \tag{D1}$$

The eigenvalue equation for $\left(\tilde{\mathbf{K}}_{2^{\mu-b}} - \tilde{\mathbf{K}}_{\mathrm{RL}2^{\mu-b}}\right) + \left[a_b \tilde{\mathbf{K}}_{\mathrm{R}2^{\mu-b}} + (a_1 \ldots a_b)\tilde{\mathbf{K}}_{\mathrm{L}2^{\mu-b}}\right]$ is thus written:

$$\begin{bmatrix} \tilde{\mathbf{K}}_{2^{\mu-b-1}} - \tilde{\mathbf{K}}_{\mathrm{RL}2^{\mu-b-1}} & \tilde{\mathbf{K}}_{\mathrm{L}2^{\mu-b-1}} + a_b \tilde{\mathbf{K}}_{\mathrm{R}2^{\mu-b-1}} \\ \tilde{\mathbf{K}}_{\mathrm{R}2^{\mu-b-1}} + (a_1 \ldots a_b)\tilde{\mathbf{K}}_{\mathrm{L}2^{\mu-b-1}} & \tilde{\mathbf{K}}_{2^{\mu-b-1}} - \tilde{\mathbf{K}}_{\mathrm{RL}2^{\mu-b-1}} \end{bmatrix} \begin{bmatrix} \mathbf{x}_{2^{\mu-b-1},\mathrm{E}} \\ \mathbf{x}_{2^{\mu-b-1},\mathrm{F}} \end{bmatrix} = \lambda_{2^{\mu-b}} \begin{bmatrix} \mathbf{x}_{2^{\mu-b-1},\mathrm{E}} \\ \mathbf{x}_{2^{\mu-b-1},\mathrm{F}} \end{bmatrix} \tag{D2}$$

or

$$\begin{aligned} \left(\tilde{\mathbf{K}}_{2^{\mu-b-1}} - \tilde{\mathbf{K}}_{\mathrm{RL}2^{\mu-b-1}}\right)\mathbf{x}_{2^{\mu-b-1},\mathrm{E}} + \left(\tilde{\mathbf{K}}_{\mathrm{L}2^{\mu-b-1}} + a_b \tilde{\mathbf{K}}_{\mathrm{R}2^{\mu-b-1}}\right)\mathbf{x}_{2^{\mu-b-1},\mathrm{F}} &= \lambda_{2^{\mu-b}} \mathbf{x}_{2^{\mu-b-1},\mathrm{E}} \\ \left[\tilde{\mathbf{K}}_{\mathrm{R}2^{\mu-b-1}} + (a_1 \ldots a_b)\tilde{\mathbf{K}}_{\mathrm{L}2^{\mu-b-1}}\right]\mathbf{x}_{2^{\mu-b-1},\mathrm{E}} + \left(\tilde{\mathbf{K}}_{2^{\mu-b-1}} - \tilde{\mathbf{K}}_{\mathrm{RL}2^{\mu-b-1}}\right)\mathbf{x}_{2^{\mu-b-1},\mathrm{F}} &= \lambda_{2^{\mu-b}} \mathbf{x}_{2^{\mu-b-1},\mathrm{F}} \end{aligned} \tag{D3}$$

Multiplying the second of Eqs. (D3) by a_{b+1} and adding the two equations together, we obtain:

$$\begin{aligned} &\left[\left(\tilde{\mathbf{K}}_{2^{\mu-b-1}} - \tilde{\mathbf{K}}_{\mathrm{RL}2^{\mu-b-1}}\right) + a_{b+1}\tilde{\mathbf{K}}_{\mathrm{R}2^{\mu-b-1}} + (a_1 \ldots a_b a_{b+1})\tilde{\mathbf{K}}_{\mathrm{L}2^{\mu-b-1}}\right]\mathbf{x}_{2^{\mu-b-1},\mathrm{E}} + \\ &\left[\tilde{\mathbf{K}}_{\mathrm{L}2^{\mu-b-1}} + a_b \tilde{\mathbf{K}}_{\mathrm{R}2^{\mu-b-1}} + a_{b+1}\left(\tilde{\mathbf{K}}_{2^{\mu-b-1}} - \tilde{\mathbf{K}}_{\mathrm{RL}2^{\mu-b-1}}\right)\right]\mathbf{x}_{2^{\mu-b-1},\mathrm{F}} = \lambda_{2^{\mu-b}}\left(\mathbf{x}_{2^{\mu-b-1},\mathrm{E}} + a_{b+1}\mathbf{x}_{2^{\mu-b-1},\mathrm{F}}\right) \end{aligned} \tag{D4}$$

or

$$\left(\tilde{\mathbf{K}}_{2^{\mu-b-1}}-\tilde{\mathbf{K}}_{\mathrm{RL}2^{\mu-b-1}}\right)\left(\mathbf{x}_{2^{\mu-b-1},\mathrm{E}}+a_{b+1}\mathbf{x}_{2^{\mu-b-1},\mathrm{F}}\right)+\left[a_{b+1}\tilde{\mathbf{K}}_{\mathrm{R}2^{\mu-b-1}}+\left(a_1...a_b a_{b+1}\right)\tilde{\mathbf{K}}_{\mathrm{L}2^{\mu-b-1}}\right]\mathbf{x}_{2^{\mu-b-1},\mathrm{E}}+$$
$$+\left(\tilde{\mathbf{K}}_{\mathrm{L}2^{\mu-b-1}}+a_b\tilde{\mathbf{K}}_{\mathrm{R}2^{\mu-b-1}}\right)\mathbf{x}_{2^{\mu-b-1},\mathrm{F}}=\lambda_{2^{\mu-b}}\left(\mathbf{x}_{2^{\mu-b-1},\mathrm{E}}+a_{b+1}\mathbf{x}_{2^{\mu-b-1},\mathrm{F}}\right) \tag{D5}$$

We note that

$$\begin{aligned}&\left[a_{b+1}\tilde{\mathbf{K}}_{\mathrm{R}2^{\mu-b-1}}+\left(a_1...a_b a_{b+1}\right)\tilde{\mathbf{K}}_{\mathrm{L}2^{\mu-b-1}}\right]a_{b+1}=a_{b+1}^2\tilde{\mathbf{K}}_{\mathrm{R}2^{\mu-b-1}}+\left(a_1...a_b a_{b+1}^2\right)\tilde{\mathbf{K}}_{\mathrm{L}2^{\mu-b-1}}=\\&=a_b\tilde{\mathbf{K}}_{\mathrm{R}2^{\mu-b-1}}+\left(a_1...a_b a_b\right)\tilde{\mathbf{K}}_{\mathrm{L}2^{\mu-b-1}}=a_b\tilde{\mathbf{K}}_{\mathrm{R}2^{\mu-b-1}}+\left(a_1...a_b^2\right)\tilde{\mathbf{K}}_{\mathrm{L}2^{\mu-b-1}}=\\&=a_b\tilde{\mathbf{K}}_{\mathrm{R}2^{\mu-b-1}}+\left(a_1...a_{b-1}a_{b-1}\right)\tilde{\mathbf{K}}_{\mathrm{L}2^{\mu-b-1}}=...\\&=a_b\tilde{\mathbf{K}}_{\mathrm{R}2^{\mu-b-1}}+a_1^2\tilde{\mathbf{K}}_{\mathrm{L}2^{\mu-b-1}}=a_b\tilde{\mathbf{K}}_{\mathrm{R}2^{\mu-b-1}}+\tilde{\mathbf{K}}_{\mathrm{L}2^{\mu-b-1}}\end{aligned} \tag{D6}$$

Hence, Eq. (D5) can be rewritten as

$$\left(\tilde{\mathbf{K}}_{2^{\mu-b-1}}-\tilde{\mathbf{K}}_{\mathrm{RL}2^{\mu-b-1}}\right)\left(\mathbf{x}_{2^{\mu-b-1},\mathrm{E}}+a_{b+1}\mathbf{x}_{2^{\mu-b-1},\mathrm{F}}\right)+\left[a_{b+1}\tilde{\mathbf{K}}_{\mathrm{R}2^{\mu-b-1}}+\left(a_1...a_b a_{b+1}\right)\tilde{\mathbf{K}}_{\mathrm{L}2^{\mu-b-1}}\right]\mathbf{x}_{2^{\mu-b-1},\mathrm{E}}+$$
$$+\left[a_{b+1}\tilde{\mathbf{K}}_{\mathrm{R}2^{\mu-b-1}}+\left(a_1...a_b a_{b+1}\right)\tilde{\mathbf{K}}_{\mathrm{L}2^{\mu-b-1}}\right]a_{b+1}\mathbf{x}_{2^{\mu-b-1},\mathrm{F}}=\lambda_{2^{\mu-b}}\left(\mathbf{x}_{2^{\mu-b-1},\mathrm{E}}+a_{b+1}\mathbf{x}_{2^{\mu-b-1},\mathrm{F}}\right)$$

or

$$\left\{\left(\tilde{\mathbf{K}}_{2^{\mu-b-1}}-\tilde{\mathbf{K}}_{\mathrm{RL}2^{\mu-b-1}}\right)+\left[a_{b+1}\tilde{\mathbf{K}}_{\mathrm{R}2^{\mu-b-1}}+\left(a_1...a_b a_{b+1}\right)\tilde{\mathbf{K}}_{\mathrm{L}2^{\mu-b-1}}\right]\right\}\left(\mathbf{x}_{2^{\mu-b-1},\mathrm{E}}+a_{b+1}\mathbf{x}_{2^{\mu-b-1},\mathrm{F}}\right)=\lambda_{2^{\mu-b}}\left(\mathbf{x}_{2^{\mu-b-1},\mathrm{E}}+a_{b+1}\mathbf{x}_{2^{\mu-b-1},\mathrm{F}}\right) \tag{D7}$$

From Eq. (D7) we conclude that at least one of the following two statements is true: (a) $\lambda_{2^{\mu-b}}$ is an eigenvalue of the $(2^{\mu\text{-}1\text{-}b}n)\times(2^{\mu\text{-}1\text{-}b}n)$-dimensional matrix $\left(\tilde{\mathbf{K}}_{2^{\mu-1-b}}-\tilde{\mathbf{K}}_{\mathrm{RL}2^{\mu-1-b}}\right)+\left[a_{b+1}\tilde{\mathbf{K}}_{\mathrm{R}2^{\mu-1-b}}+\left(a_1...a_{b+1}\right)\tilde{\mathbf{K}}_{\mathrm{L}2^{\mu-1-b}}\right]$, with corresponding eigenvector $\mathbf{x}_{2^{\mu-b-1},\mathrm{E}}+a_{b+1}\mathbf{x}_{2^{\mu-b-1},\mathrm{F}}$; (b) $\mathbf{x}_{2^{\mu-b-1},\mathrm{E}}+a_{b+1}\mathbf{x}_{2^{\mu-b-1},\mathrm{F}}=0$, Q.E.D.

Appendix E: Proof that the matrices in the recursive scheme with the same signs after the 2nd coefficient, have the same eigenvalues.

We calculate the conjugate of $\left(\tilde{\mathbf{K}}_{2^{\mu-b-1}}-\tilde{\mathbf{K}}_{\mathrm{RL}2^{\mu-b-1}}\right)+\left[a_{b+1}\tilde{\mathbf{K}}_{\mathrm{R}2^{\mu-b-1}}+\left(a_1...a_b a_{b+1}\right)\tilde{\mathbf{K}}_{\mathrm{L}2^{\mu-b-1}}\right]$ in Eq. (E1), symbolizing the conjugate of a complex number or matrix with an asterisk (*) as superscript.

$$\begin{aligned}
&\left[\left(\tilde{\mathbf{K}}_{2^{\mu-b-1}}-\tilde{\mathbf{K}}_{\mathrm{RL}2^{\mu-b-1}}\right)+\left[a_{b+1}\tilde{\mathbf{K}}_{\mathrm{R}2^{\mu-b-1}}+\left(a_1\ldots a_b a_{b+1}\right)\tilde{\mathbf{K}}_{\mathrm{L}2^{\mu-b-1}}\right]\right]^*= \\
&=\left(\tilde{\mathbf{K}}^*_{2^{\mu-b-1}}-\tilde{\mathbf{K}}^*_{\mathrm{RL}2^{\mu-b-1}}\right)+\left[\left(a_{b+1}\tilde{\mathbf{K}}_{\mathrm{R}2^{\mu-b-1}}\right)^*+\left(\left(a_1\ldots a_b a_{b+1}\right)\tilde{\mathbf{K}}_{\mathrm{L}2^{\mu-b-1}}\right)^*\right] \\
&=\left(\tilde{\mathbf{K}}^*_{2^{\mu-b-1}}-\tilde{\mathbf{K}}^*_{\mathrm{RL}2^{\mu-b-1}}\right)+\left[a^*_{b+1}\tilde{\mathbf{K}}^*_{\mathrm{R}2^{\mu-b-1}}+\left(a_1\ldots a_b a_{b+1}\right)^*\tilde{\mathbf{K}}^*_{\mathrm{L}2^{\mu-b-1}}\right] \\
&=\left(\tilde{\mathbf{K}}^*_{2^{\mu-b-1}}-\tilde{\mathbf{K}}^*_{\mathrm{RL}2^{\mu-b-1}}\right)+\left[a^*_{b+1}\tilde{\mathbf{K}}^*_{\mathrm{R}2^{\mu-b-1}}+a^*_1\ldots a^*_b a^*_{b+1}\tilde{\mathbf{K}}^*_{\mathrm{L}2^{\mu-b-1}}\right]
\end{aligned} \tag{E1}$$

Because $\tilde{\mathbf{K}}_{2^{\mu-b-1}},\tilde{\mathbf{K}}_{\mathrm{RL}2^{\mu-b-1}},\tilde{\mathbf{K}}_{\mathrm{R}2^{\mu-b-1}},\tilde{\mathbf{K}}_{\mathrm{L}2^{\mu-b-1}}$ are real matrices, they equal their complex conjugates. As result, from Eq. (E1) we get Eq. (E2)

$$\begin{aligned}
&\left[\left(\tilde{\mathbf{K}}_{2^{\mu-b-1}}-\tilde{\mathbf{K}}_{\mathrm{RL}2^{\mu-b-1}}\right)+\left[a_{b+1}\tilde{\mathbf{K}}_{\mathrm{R}2^{\mu-b-1}}+\left(a_1\ldots a_b a_{b+1}\right)\tilde{\mathbf{K}}_{\mathrm{L}2^{\mu-b-1}}\right]\right]^*= \\
&\left(\tilde{\mathbf{K}}_{2^{\mu-b-1}}-\tilde{\mathbf{K}}_{\mathrm{RL}2^{\mu-b-1}}\right)+\left[a^*_{b+1}\tilde{\mathbf{K}}_{\mathrm{R}2^{\mu-b-1}}+a^*_1\ldots a^*_b a^*_{b+1}\tilde{\mathbf{K}}_{\mathrm{L}2^{\mu-b-1}}\right]
\end{aligned} \tag{E2}$$

In addition, it is valid that if we have a complex number $\psi=re^{i\theta}=r\ \cos\theta+i\sin\theta$ where θ is the angle and take values $-\pi<\theta\le\pi$ with direction from Real number axis to Image number axis, then its principal square root is

$$\psi^{1/2}=r^{1/2}\left(\cos\left(\frac{\theta}{2}\right)+i\sin\left(\frac{\theta}{2}\right)\right) \tag{E3}$$

It is also known that the conjucate of ψ is $\psi^*=re^{i(-\theta)}=r\ \cos\ -\theta\ +i\sin\ -\theta$ and its principle square root is

$$\psi^{*\ 1/2}=r^{1/2}\left(\cos\left(\frac{-\theta}{2}\right)+i\sin\left(\frac{-\theta}{2}\right)\right)=r^{1/2}\left(\cos\left(\frac{\theta}{2}\right)-i\sin\left(\frac{\theta}{2}\right)\right)=\psi^{1/2} \tag{E4}$$

Because we proved in Eq.(E3-E4) that the principle square root of a complex number is the conjugate of the principle square root of its conjugate number, if $a_j=\mathrm{sign}_j\sqrt{a_{j-1}}$ and $a'_j=\mathrm{sign}'_j\sqrt{a'_{j-1}}$, where $a_2=i$ and $a'_2=-i$ and $\mathrm{sign}_j=\mathrm{sign}'_j$ for $j=3,\ldots,b+1$, then $a^*_j=a_j$, for $j=2,\ldots b+1$, and consequently, the matrices with these *a* coefficients are conjugate matrices. Because a) the eigenvalues of conjugate matrices are conjugate too and b) we have already proved that these matrices have real eigenvalues, we conclude that they have the same eigenvalues, as the conjugate of real number is the same real number.

Appendix F: Solution of the continuum diffusion problem of Eqs. (3.33)-(3.35) of the main text

Applying the method of separation of variables on the partial differential Eq. (3.33) and imposing the periodic boundary conditions of Eq. (3.34) of the main text leads to the following expression for the probability density as a function of position and time:

$$\rho_{\text{cell}}(l,t)=\sum_{f=0}^{\infty}A_f\cos\left(\frac{f\pi l}{L_p}\right)e^{-D\left(\frac{f\pi}{L_p}\right)^2 t}+\sum_{f=1}^{\infty}B_f\sin\left(\frac{f\pi l}{L_p}\right)e^{-D\left(\frac{f\pi}{L_p}\right)^2 t} \tag{F1}$$

The constants can be calculated based on the initial condition:

$$A_0=\frac{1}{2L_p}\int_{-L_p}^{L_p}\rho_{\text{cell}}(l,t=0)dl$$

$$A_f=\frac{1}{2L_p}\int_{-L_p}^{L_p}\rho_{\text{cell}}(l,t=0)\cos\left(\frac{f\pi l}{L_p}\right)dl\ ,\ f=1,2,3,...,+\infty \tag{F2}$$

$$B_f=\frac{1}{2L_p}\int_{-L_p}^{L_p}\rho_{\text{cell}}(l,t=0)\sin\left(\frac{f\pi l}{L_p}\right)dl\ ,\ f=1,2,3,...,+\infty$$

Substituting the initial condition of Eq.(3.35) of the main text in Eqs.(E2), we obtain

$$A_0=\frac{1}{2L_p}$$

$$A_f=\frac{\sin\left(\frac{f\pi L_d}{L_p}\right)}{f\pi L_d}\ ,\quad f=1,2,3,...,+\infty \tag{F3}$$

$$B_f=0\ ,\quad f=1,2,3,...,+\infty$$

As a result, Eq. (F1) takes the form of Eq. (3.36) of the main text.

Appendix G: Alternative form of the matrices $\left(\tilde{\mathbf{K}}_1-\tilde{\mathbf{K}}_{\text{RL1}}\right)+\left[a_\mu\tilde{\mathbf{K}}_{\text{R1}}+\left(a_1a_2...a_\mu\right)\tilde{\mathbf{K}}_{\text{L1}}\right]$ obtained using positive signs after the second coefficient in the recursive scheme and convergence of these matrices to $\tilde{\mathbf{K}}_1$ for very large μ

Following the definition of Theorem 3 with the restriction that only positive signs be used after the second coefficient in the recursive scheme, the coefficients a_j appearing in the matrices $\left(\tilde{\mathbf{K}}_1-\tilde{\mathbf{K}}_{\text{RL1}}\right)+\left[a_\mu\tilde{\mathbf{K}}_{\text{R1}}+\left(a_1a_2...a_\mu\right)\tilde{\mathbf{K}}_{\text{L1}}\right]$ satisfy $a_1=-1,\ a_2=\pm i,\ \ a_j=\sqrt{a_{j-1}}$, $3\le j\le\mu$.

a) Let $a_2=i$ whose polar coordinates are $r=1$ and $\theta=\pi/2$. Then,

$$a_\mu=i^{\left(\frac{1}{2}\right)^{\mu-2}}=i^{\frac{1}{2^{\mu-2}}}\ ,\quad \mu\ge 2 \tag{G1}$$

and

$$a_1a_2...a_\mu=-i^{1+\frac{1}{2}+\frac{1}{4}+...+\frac{1}{2^{\mu-2}}}=-i^{\frac{1-\frac{1}{2^{\mu-1}}}{1-\frac{1}{2}}}=-i^{2\left(1-\frac{1}{2^{\mu-1}}\right)}=-i^2i^{-\frac{1}{2^{\mu-2}}}=i^{-\frac{1}{2^{\mu-2}}} \tag{G2}$$

It is also known that $\psi^{1/\gamma} = r^{1/\gamma}\left(\cos\left(\frac{\theta}{\gamma}\right)+i\sin\left(\frac{\theta}{\gamma}\right)\right)$ (G3)

where ψ is a complex number. As a result,

$$a_\mu = i^{1/2^{\mu-2}} = \left(\cos\left(\frac{\pi/2}{2^{\mu-2}}\right)+i\sin\left(\frac{\pi/2}{2^{\mu-2}}\right)\right) = \left(\cos\left(\frac{\pi}{2^{\mu-1}}\right)+i\sin\left(\frac{\pi}{2^{\mu-1}}\right)\right) \quad \text{(G4)}$$

Similarly,

$$\begin{aligned} a_1 a_2 ... a_\mu &= i^{-\frac{1}{2^{\mu-2}}} = \frac{1}{i^{\frac{1}{2^{\mu-2}}}} = \frac{1}{\left(\cos\left(\frac{\pi}{2^{\mu-1}}\right)+i\sin\left(\frac{\pi}{2^{\mu-1}}\right)\right)} \\ &= \frac{\left(\cos\left(\frac{\pi}{2^{\mu-1}}\right)-i\sin\left(\frac{\pi}{2^{\mu-1}}\right)\right)}{\left(\cos\left(\frac{\pi}{2^{\mu-1}}\right)\right)^2+\left(\sin\left(\frac{\pi}{2^{\mu-1}}\right)\right)^2} = \left(\cos\left(\frac{\pi}{2^{\mu-1}}\right)-i\sin\left(\frac{\pi}{2^{\mu-1}}\right)\right) \end{aligned} \quad \text{(G5)}$$

Therefore

$$\begin{aligned} \left(\tilde{\mathbf{K}}_1-\tilde{\mathbf{K}}_{\mathrm{RL1}}\right)+\left[a_\mu\tilde{\mathbf{K}}_{\mathrm{R1}}+\left(a_1a_2...a_\mu\right)\tilde{\mathbf{K}}_{\mathrm{L1}}\right] &= \left(\tilde{\mathbf{K}}_1-\tilde{\mathbf{K}}_{\mathrm{RL1}}\right)+\left[i^{\frac{1}{2^{\mu-2}}}\tilde{\mathbf{K}}_{\mathrm{R1}}+i^{-\frac{1}{2^{\mu-2}}}\tilde{\mathbf{K}}_{\mathrm{L1}}\right] = \\ \tilde{\mathbf{K}}_1-\left[1-\cos\left(\frac{\pi}{2^{\mu-1}}\right)\right]\tilde{\mathbf{K}}_{\mathrm{RL1}}+i\sin\left(\frac{\pi}{2^{\mu-1}}\right)&\left(\tilde{\mathbf{K}}_{\mathrm{R1}}-\tilde{\mathbf{K}}_{\mathrm{L1}}\right) \end{aligned} \quad \text{(G6)}$$

Note that, for μ=1, Eq. (G6) gives the matrix $\left(\tilde{\mathbf{K}}_1-2\tilde{\mathbf{K}}_{\mathrm{RL1}}\right)$ (compare Eq. (3.20) of the main text), while for μ=2 , Eq. (G6) gives the matrix $\left(\tilde{\mathbf{K}}_1-\tilde{\mathbf{K}}_{\mathrm{RL1}}\right)+i\left(\tilde{\mathbf{K}}_{\mathrm{R1}}-\tilde{\mathbf{K}}_{\mathrm{L1}}\right)$ (compare the matrices appearing in Theorem 1 in the main text).

b) Let $a_2 = -i$ whose polar coordinates are r=1 and θ=-π/2. Similarly,

$$a_\mu = \left(-i\right)^{\left(\frac{1}{2}\right)^{\mu-2}} = \left(-i\right)^{\frac{1}{2^{\mu-2}}} \quad , \quad \mu \geq 2$$

$$\begin{aligned} a_\mu &= (-i)^{\frac{1}{2^{\mu-2}}} = \left(\cos\left(-\frac{\pi}{2}\right)+i\sin\left(-\frac{\pi}{2}\right)\right)^{\frac{1}{2^{\mu-2}}} = \left(\cos\left(-\frac{\pi}{2^{\mu-1}}\right)+i\sin\left(-\frac{\pi}{2^{\mu-1}}\right)\right) \\ &= \left(\cos\left(\frac{\pi}{2^{\mu-1}}\right)-i\sin\left(\frac{\pi}{2^{\mu-1}}\right)\right) \end{aligned} \quad \text{(G7)}$$

and

$$a_1 a_2 ... a_\mu = -\left(-i\right)^{1+\frac{1}{2}+\frac{1}{4}+...+\frac{1}{2^{\mu-2}}} = -\left(-i\right)^{\frac{1-\frac{1}{2^{\mu-1}}}{1-\frac{1}{2}}} = -i^{2\left(1-\frac{1}{2^{\mu-1}}\right)} = -i^2\left(-i\right)^{-\frac{1}{2^{\mu-2}}} = \left(-i\right)^{-\frac{1}{2^{\mu-2}}}$$
$$= \frac{1}{i^{-\frac{1}{2^{\mu-2}}}} = i^{\frac{1}{2^{\mu-2}}} = \left(\cos\left(\frac{\pi}{2^{\mu-1}}\right) + i\sin\left(\frac{\pi}{2^{\mu-1}}\right)\right) \quad \text{(G8)}$$

Therefore

$$\left(\tilde{\mathbf{K}}_1 - \tilde{\mathbf{K}}_{\mathrm{RL1}}\right) + \left[a_\mu \tilde{\mathbf{K}}_{\mathrm{R1}} + \left(a_1 a_2 ... a_\mu\right)\tilde{\mathbf{K}}_{\mathrm{L1}}\right] = \left(\tilde{\mathbf{K}}_1 - \tilde{\mathbf{K}}_{\mathrm{RL1}}\right) + \left[\left(-i\right)^{\frac{1}{2^{\mu-2}}}\tilde{\mathbf{K}}_{\mathrm{R1}} + \left(-i\right)^{-\frac{1}{2^{\mu-2}}}\tilde{\mathbf{K}}_{\mathrm{L1}}\right] =$$
$$\tilde{\mathbf{K}}_1 - \left[1-\cos\left(\frac{\pi}{2^{\mu-1}}\right)\right]\tilde{\mathbf{K}}_{\mathrm{RL1}} - i\sin\left(\frac{\pi}{2^{\mu-1}}\right)\left(\tilde{\mathbf{K}}_{\mathrm{R1}} - \tilde{\mathbf{K}}_{\mathrm{L1}}\right) \quad \text{(G9)}$$

For μ=1, Eq. (G9) gives again the matrix $\left(\tilde{\mathbf{K}}_1 - 2\tilde{\mathbf{K}}_{\mathrm{RL1}}\right)$, while for μ=2 , Eq. (G9) gives the matrix $\left(\tilde{\mathbf{K}}_1 - \tilde{\mathbf{K}}_{\mathrm{RL1}}\right) - i\left(\tilde{\mathbf{K}}_{\mathrm{R1}} - \tilde{\mathbf{K}}_{\mathrm{L1}}\right)$ (compare the matrices appearing in Theorem 1 in the main text). As shown in Appendix E above, the matrices produced by Eq. (G6) are complex conjugate of those produced by Eq. (G6).

Taking the limit $\mu \to +\infty$ we see that the argument of the trigonometric functions in Eqs. (G6) and (G9) goes to zero. In this limit, the matrix $\left(\tilde{\mathbf{K}}_1 - \tilde{\mathbf{K}}_{\mathrm{RL1}}\right) + \left[a_\mu \tilde{\mathbf{K}}_{\mathrm{R1}} + \left(a_1 a_2 ... a_\mu\right)\tilde{\mathbf{K}}_{\mathrm{L1}}\right]$ obtained using positive signs after the second coefficient in the MESoRReD recursive scheme converges to $\tilde{\mathbf{K}}_1$ and its eigenvalue of smallest absolute magnitude converges to the corresponding eigenvalue of $\tilde{\mathbf{K}}_1$, which is zero.

Appendix H: Proof that matrices $\left(\tilde{\mathbf{K}}_1 - \tilde{\mathbf{K}}_{\mathrm{RL1}}\right) + \left[a_\mu \tilde{\mathbf{K}}_{\mathrm{R1}} + \left(a_1 a_2 ... a_\mu\right)\tilde{\mathbf{K}}_{\mathrm{L1}}\right]$ with at least one negative sign after the second coefficient, do not converge or converge more slowly to $\tilde{\mathbf{K}}_1$ than matrices with positive signs after the second coefficient

$$\lim_{\mu\to+\infty} a_\mu = \lim_{\mu\to+\infty} \mathrm{sign}_\mu \sqrt{\mathrm{sign}_{\mu-1}\sqrt{\mathrm{sign}_{\mu-2}\sqrt{\mathrm{sign}_{\mu-3}.....\sqrt{\mathrm{sign}_2 i}}}}$$
$$= \mathrm{sign}_\mu \sqrt{\mathrm{sign}_{\mu-1}}\sqrt[4]{\mathrm{sign}_{\mu-2}}\sqrt[8]{\mathrm{sign}_{\mu-3}}....\sqrt[+\infty]{\mathrm{sign}_2 i} \quad \text{(H1)}$$
$$= \mathrm{sign}_\mu \mathrm{sign}_{\mu-1}^{1/2}\mathrm{sign}_{\mu-2}^{1/4}\mathrm{sign}_{\mu-3}^{1/8}....\mathrm{sign}_2^{1/+\infty} i^{1/+\infty}$$

where sign_μ we symbolize the sign of a_μ , and so it can be either +1 or -1.

As a result, we can write (H1) as

$$\lim_{\mu\to+\infty} a_\mu = (+1 \text{ or } -1)(1 \text{ or } i)(1 \text{ or } i^{1/2})(1 \text{ or } i^{1/4})(1 \text{ or } i^{1/8})....1$$
$$= \pm i^{b_{\mu-1}} i^{b_{\mu-2}(1/2)} i^{b_{\mu-3}(1/4)} .....i^{b_0(1/+\infty)} \qquad \text{(H2)}$$
$$= \pm i^{(b_{\mu-1}+b_{\mu-2}(1/2)+b_{\mu-3}(1/4)+.....+1/(+\infty))}$$

Where b coefficients are one if the sign is + or zero if the sign is -1.

If $\lim_{\mu\to+\infty} a_\mu = 1$ then it must happen that

$$b_\mu + b_{\mu-1}(1/4) + b_{\mu-2}(1/8) + b_{\mu-3}(1/16) + ... + 0 \to 0 \qquad \text{(H3)}$$

Because b coefficients take values 1 or zero, we can see from Eq.(H3) that the a_μ of matrix with only positive signs(=all *b* coefficients to be zero) converges quickest to 1 than the rest matrices. From Eq.(H3) we can also see that a_μ of matrices with negative signs at the first *a* coefficients converge quickier to 1 than the a_μ of matrices with negative signs at the last *a* coefficients.

Next, we examine how $\left(a_1 a_2 a_3 ... a_\mu\right)$ converges for $\mu \to +\infty$

$$\left(a_1 a_2 a_3 ... a_\mu\right) = \left(-a_2 a_3 ... a_\mu\right) = -a_2 \underbrace{\text{sign}_3\sqrt{a_2}}_{a_3} \underbrace{\text{sign}_4\sqrt{\text{sign}_3\sqrt{a_2}}}_{a_4} .... \underbrace{\text{sign}_\mu\sqrt{\text{sign}_{\mu-1}\sqrt{\text{sign}_{\mu-2}\sqrt{\text{sign}_{\mu-3}.....\sqrt{\alpha_2}}}}}_{a_\mu}$$

$$= \text{sign}_3\text{sign}_4....\text{sign}_\mu\left((-a_2)\left(\sqrt{a_2}\right)\left(\sqrt{\text{sign}_3\sqrt{a_2}}\right)\left(\sqrt{\text{sign}_4\sqrt{\text{sign}_3\sqrt{a_2}}}\right)....\sqrt{\text{sign}_{\mu-1}\sqrt{\text{sign}_{\mu-2}\sqrt{\text{sign}_{\mu-3}.....\sqrt{\alpha_2}}}}\right)$$

$$= \left(\prod_{\iota=3}^{\mu}\text{sign}_\iota\right)\left((-a_2)\left(a_2^{1/2}\right)\left(\text{sign}_3^{1/2}a_2^{1/4}\right)\left(\text{sign}_4^{1/2}\text{sign}_3^{1/4}a_2^{1/8}\right)....\left(\text{sign}_{\mu-1}^{1/2}\text{sign}_{\mu-2}^{1/4}\text{sign}_{\mu-3}^{1/8}.....a_2^{1/2^{\mu-1}}\right)\right)$$

$$= \left(\prod_{\iota=3}^{\mu}\text{sign}_\iota\right)\left[-\left(\text{sign}_3^{1/2+1/4+...1/2^{\mu-1}}\text{sign}_4^{1/2+1/4+...1/2^{\mu-2}}...\text{sign}_{\mu-1}^{1/2}\right)\right]a_2^{1+1/2+1/4+1/8+...1/2^{\mu-1}}$$

(H4)

$$\lim_{\mu\to+\infty}\left(a_1a_2a_3...a_\mu\right)=\lim_{\mu\to+\infty}\left(\prod_{\iota=3}^{\mu}\text{sign}_\iota\right)\left[-\left(\text{sign}_3{}^{1/2+1/4+...1/2^{\mu-1}}\text{sign}_4{}^{1/2+1/4+...1/2^{\mu-2}}...\text{sign}_{\mu-1}{}^{1/2}\right)\right]a_2{}^{1+1/2+1/4+1/8+...1/2^{\mu-1}}$$

$$=\lim_{\mu\to+\infty}\left(\prod_{\iota=3}^{\mu}\text{sign}_\iota\right)\left[-\left(\text{sign}_3{}^{1/2+1/4+...1/2^{\mu-1}}\text{sign}_4{}^{1/2+1/4+...1/2^{\mu-2}}...\text{sign}_{\mu-1}{}^{1/2}\right)\right]a_2{}^{2}$$

$$=\lim_{\mu\to+\infty}-\left(\prod_{\iota=3}^{\mu}\text{sign}_\iota\right)\left(\text{sign}_3{}^{1/2+1/4+...1/2^{\mu-1}}\text{sign}_4{}^{1/2+1/4+...1/2^{\mu-2}}...\text{sign}_{\mu-1}{}^{1/2}\right)\left(\pm\iota\right)^2$$

$$=\lim_{\mu\to+\infty}-\left(\prod_{\iota=3}^{\mu}\text{sign}_\iota\right)\left(\text{sign}_3{}^{1/2+1/4+...1/2^{\mu-1}}\text{sign}_4{}^{1/2+1/4+...1/2^{\mu-2}}...\text{sign}_{\mu-1}{}^{1/2}\right)\left(\pm1\right)^2\iota^2$$

$$=\lim_{\mu\to+\infty}-\left(\prod_{\iota=3}^{\mu}\text{sign}_\iota\right)\left(\text{sign}_3{}^{1/2+1/4+...1/2^{\mu-1}}\text{sign}_4{}^{1/2+1/4+...1/2^{\mu-2}}...\text{sign}_{\mu-1}{}^{1/2}\right)(-1)$$

$$=\lim_{\mu\to+\infty}\left(\prod_{\iota=3}^{\mu}\text{sign}_\iota\right)\left(\text{sign}_3{}^{1/2+1/4+...1/2^{\mu-1}}\text{sign}_4{}^{1/2+1/4+...1/2^{\mu-2}}...\text{sign}_{\mu-1}{}^{1/2}\right)$$

(H5)

So, only if all signs after the second coefficient are positive, $\lim_{\mu\to+\infty}\left(a_1a_2a_3...a_\mu\right)=1$. In the rest cases, we can see that the $\left(a_1a_2a_3...a_\mu\right)$ of some matrices can converge to 1 but slower than the matrices with only positive signs after the second coefficient. As a result, matrices from Eq. (G6), Eq.(G9) which are $\tilde{\mathbf{K}}_1-\left[1-\cos\left(\frac{\pi}{2^{\mu-1}}\right)\right]\tilde{\mathbf{K}}_{\text{RL1}}\pm i\sin\left(\frac{\pi}{2^{\mu-1}}\right)\left(\tilde{\mathbf{K}}_{\text{R1}}-\tilde{\mathbf{K}}_{\text{L1}}\right)$ converge quickest than any other matrix to $\tilde{\mathbf{K}}_1$.

In the limit $\mu\to+\infty$, the matrices $\mathbf{A}_\mu=\tilde{\mathbf{K}}_1-\left[1-\cos\left(\frac{\pi}{2^{\mu-1}}\right)\right]\tilde{\mathbf{K}}_{\text{RL1}}\pm i\sin\left(\frac{\pi}{2^{\mu-1}}\right)\left(\tilde{\mathbf{K}}_{\text{R1}}-\tilde{\mathbf{K}}_{\text{L1}}\right)$ converge quickier than any other matrix of MESoRReD to $\tilde{\mathbf{K}}_1$ and as a result their eigenvalue of smallest absolute magnitude(they have the same eigenvalues as the are conjugate matrices and they have real eigenvalues-see Appendix E) converges quickier than any other matrix of MESoRReD to the corresponding eigenvalue of $\tilde{\mathbf{K}}_1$, which is zero. As a result, the smallest in absolute value eigenvalue of these matrices is the nonzero eigenvalue λ_1 of matrix $\tilde{\mathbf{K}}_{2^\nu}$ with smallest absolute magnitude.

As seen from Eq. (3.45), λ_1 is of strategic importance in extracting the diffusivity in periodic systems. Thus, the diffusivity can be calculated from the eigenvalue of smallest absolute magnitude of a single $n\times n$ matrix, given by Eq. (G6) or Eq. (G9) . We can also see that $\mu=\nu$, where 2^ν is the number of cells in a periodic system.

References

[1]A. W. Chester, E. G. Derouane (**2009**) Zeolite Characterization and Catalysis, A tutorial, Springer, Berlin.

[2]E. M. Flanigen, J. M. Bennett, R. W. Grose, J. P. Cohen, R. L. Patton, R. M. Kirchner and J. V. Smith, Silicalite, a new hydrophobic crystalline silica molecular sieve, *Nature* 271 (**1978**), pp. 512 – 516.

[3]G. T. Kokotailo, S. L. Lawton, D. H. Olson and W. M. Meier, Structure of synthetic zeolite ZSM-5, *Nature* 272 (**1978**), pp. 437-438.

[4]C. Baerlocher, L.B. McCusker, and D.H. Olson D.H. (**2007**) Atlas of Zeolite Framework Types, Elsevier, Amsterdam.

[5]H. van Koningsveld, J. C. Jansen, H. van Bekkum, The monoclinic framework structure of zeolite H-ZSM-5. Comparison with the orthorhombic framework of as-synthesized ZSM-5, *Zeolites* 10 (**1990**), pp. 235-242.

[6]B. F. Mentzen and M. Sacerdote-Peronnet, Flexibility of the framework structure in highly crystalline silicalite during the reversible monoclinic/orthorhombic solid state polymorphic phase transition, *Mat. Res. Bull.* 28 (**1993**), pp.1017-1024.

[7]H. van Koningsveld, F. Tuinstra, H. van Bekkum and J. C. Jansen, The location of p-xylene in a single crystal of zeolite H-ZSM-5 with a new, sorbate-induced, orthorhombic framework symmetry, *Acta Crystallogr. Sect. B* 45 (**1989**), pp. 423-431.

[8]H. van Koningsveld, J.C. Jansen and H. van Bekkum, The location of p-dichlorobenzene in a single crystal of zeolite H-ZSM-5 at high sorbate loading, *Acta Crystallogr. Sect. B* 52 (**1996**), pp. 140-144.

[9]M. Pera-Titus, Thermodynamic Analysis of Type VI Adsorption Isotherms in MFI Zeolites *J. Phys. Chem. C* 115 (**2011**), pp 3346–3357.

[10]A. Sartbaeva, J. Haines, O. Cambon, M. Santoro, F. Gorelli, C. Levelut, G. Garbarino and S. A. Wells, Flexibility windows and compression of monoclinic and orthorhombic silicalites, *Phys. Rev. B* 85 (**2012**), 064109.

[11]D. G. Hay and H. Jaeger, Orthorhombic-monoclinic phase changes in ZSM-5 zeolite/silicalite, *J. Chem. Soc., Chem. Commun*. (**1984**), pp. 1433-1433.

[12]C. A. Fyfe, G. J. Kennedy, G. T. Kokotailo, J. R. Leyrla and W. W. Flemming, The effect of temperature on the ^{29}Si magic angle spinning n.m.r. spectrum of highly siliceous ZSM-5, *J. Chem. Soc., Chem. Commun.* (**1985**), pp. 740-742.

[13]R. Grau-Crespo, E. Acuay and A. R. Ruiz-Salvador, A free energy minimisation study of the monoclinic–orthorhombic transition in MFI zeolite, *Chem. Commun.* (**2002**), pp. 2544–2545.

[14]G. T. Kokotailo, L. Riekert and A. Tissler in *Zeolites as Catalysts, Sorbents and Detergent Builders*, ed. H. G. Karge and J. Weitkamp, Elsevier, Amsterdam, **1989**, p. 821.

[15]M. T. Dove, . K. A. Pryde and D. A. Keen, Phase transitions in tridymite studied using 'Rigid Unit Mode' theory, Reverse Monte Carlo methods and molecular dynamics simulations , *Mineralogical Magazine* 64 (**2000**), pp.267-283.

[16]E. G. Derouane, in *Intercalation Chemistry*, ed. M. Stanley Whittingham and A. J. Jacobson, Academic Press, New York, **1982**, p. 101.

[17]J. Kärger, D. M. Ruthven, D. N. Theodorou (**2012**) Diffusion in Nanoporous Materials, Wiley VCH, Weinheim.

[18]Chapter 4 of the DOE's Office of Energy Efficiency and Renewable Energy (EERE) report entitled "Energy and Environmental Profile of the U.S. Chemical Industry", May **2000**

[19]S. Brandani, M. Jama and D. Ruthven, Diffusion, self-diffusion and counter-diffusion of benzene and p-xylene in silicalite, *Micropor. Mesopor. Mater.* 35-36 (**2000**), pp. 283-300.

[20]V.S. Nayak, and L. Riekert, Factors influencing sorption and diffusion in pentasil zeolites, *Acta Phys. Chem.* ,31 (**1985**), pp. 157

[21]D. Prinz and L. Riekert (1986) Observation of rates of sorption and diffusion in zeolite crystals at constant temperature, Ber. Busenenges, *Phys. Chem.*,90 (**1986**), pp. 413

[22]K. Beschmann, G.T. Kokotailo, and L. Riekert, Kinetics of sorption of aromatics in zeolite ZSM-5 . *Chem. Eng. Process* 22, (**1987**), pp.,223-229.

[23]H. Jobic, M. Bée, S. Pouget, Diffusion of Benzene in ZSM-5 Measured by the Neutron Spin−Echo Technique, *J. Phys. Chem. B* 104 (**2000**) pp.7130-7133.

[24]D. B. Shah, D. T. Hayhurst, G. Evanina and C. J. Guo, Sorption and diffusion of benzene in HZSM-5 and silicalite crystals, *AIChE J.* 34 (**1988**), pp.1713-1717.

[25]A. Zikanova, M. Bülow and H. Schlodder, Intracrystalline diffusion of benzene in ZSM-5 and silicalite, *Zeolites* 7 (**1987**), pp.115-118.

[26]K. Beschmann, S. Fuchs and L. Riekert, Kinetics of sorption of benzene and n-paraffins in large crystals of MFI zeolites, *Zeolites* 10 (**1990**), pp.798-801.

[27]D. M. Ruthven, M. Eic and E. Richard, Diffusion of C8 aromatic hydrocarbons in silicalite, *Zeolites* 11 (**1991**), pp. 647-653.

[28]D. Shen and L. V. C. Rees, Diffusivities of benzene in HZSM-5, silicalite-I, and NaX determined by frequency-response techniques, *Zeolites* 11 (**1991**), pp. 666-671.

[29]L. Song and L.V.C. Rees, in *Adsorption and Diffusion*, eds H.G. Karge and J. Weitkamp, Springer, Berlin, **2008**, pp. 235

[30]L. J. Song, Z. L. Sun and L. V. C. and Rees, Experimental and molecular simulation studies of adsorption and diffusion of cyclic hydrocarbons in silicalite-1, *Micropor. Mesopor. Mater.* 55 (**2002**), pp. 31-49.

[31]L. Song and L. V. C. Rees, Adsorption and diffusion of cyclic hydrocarbon in MFI-type zeolites studied by gravimetric and frequency-response techniques, *Micropor. Mesopor. Mater.* 35-36 (**2000**), pp. 301-314.

[32]Lai Z., Bonilla G., Diaz I., Nery J. G.,Sujaofi K.,Amat M. A., Kokkoli, E. Terasaki, O., Thompson, R. W. and Tsapatsis, M. D. G. Vlachos, Microstructural Optimization of a Zeolite Membrane for Organic Vapor Separation, *Science* 300 (**2000**), pp. 456-460

[33]A. K. Nowak, A. K. Cheetham, S. D. Pickett and S. Ramdas, A Computer Simulation of the Adsorption and Diffusion of Benzene and Toluene in the Zeolites Theta-1 and Silicalite, *Mol. Simul.* 1 (**1987**), pp. 67-77.

[34]S. D. Pickett, A. K. Nowak, J. M. Thomas and A. K. Cheetham, Computer simulation of the adsorption and diffusion of benzene in silicalite, theta-1, and a new zeolite, EU-1, *Zeolites* 9 (**1989**), pp. 123-128.

[35]O. Talu, Behavior of Aromatic Molecules in Silicalite by the Direct Integration of the Configurational Integral, *Mol. Simul.* 8 (**1991**), pp. 119-132.

[36]R. Q. Snurr, A. T. Bell and D. N. Theodorou, Investigation of the dynamics of benzene in silicalite using Transition-State Theory, *J. Phys. Chem.* 98 (**1994**), pp. 11948-11961.

[37]J. Baker, An algorithm for the location of transition states, *J. Comput. Chem.*,7 (**1986**), pp. 385-395.

[38]R. Q. Snurr, A. T. Bell and D. N. Theodorou, Prediction of adsorption of aromatic hydrocarbons in silicalite from grand canonical Monte Carlo simulations with biased insertions, *J. Phys. Chem.* 97 (**1993**), pp. 13742-13752.

[39]T. R. Forester and W. Smith, Bluemoon simulations of benzene in silicalite-1 Prediction of free energies and diffusion coefficients, *J. Chem. Soc. Faraday Trans.* 93 (**1997**), pp. 3249-3257.

[40]E.A. Carter, G. Ciccotti, J. T. Hynes and R. Kapral, Constrained reaction coordinate dynamics for the simulation of rare events, *Chem. Phys. Lett.* 156 (**1989**), pp. 472-477.

[41]K. A. Fichthorn, W. H. Weinberg, Theoretical foundations of dynamical Monte Carlo simulations, *J. Chem. Phys.* 95 (**1991**), pp. 1090-1096.

[42]J. Kärger, Random walk through two-channel networks: a simple means to correlate the coefficients of anisotropic diffusion in ZSM-5 type zeolites, *J. Phys. Chem.* 95 (**1991**), pp. 5558-5560.

[43]T. J. H. Vlugt, C. Dellago and B. Smit, Diffusion of isobutane in silicalite studied by transition path sampling, *J. Chem. Phys.* 113 (**2000**), pp. 8791-8799.

[44]K. P. Schröder and J. Sauer, Computer Simulation of Benzene in Silicalite 1. Low-Coverage Sorbate Structures and Diffusion, *J. Phys. Chem. (Leipzig)* 271 (**1990**), pp. 489.

[45]L. A. Clark, R. Snurr, Adsorption isotherm sensitivity to small changes in zeolite structure, *Chem. Phys. Lett.* 308 (**1999**), pp. 155-159

[46] R. Rungsirisakun, T. Nanok, M. Probst and J. Limtrakul, Adsorption and diffusion of benzene in the nanoporous catalysts FAU, ZSM-5 and MCM-22: A molecular dynamics study, *Journal of Molecular Graphics and Modelling* 24 (**2006**), pp. 373-382.

[47]G. Sastre, N. Raj, C.R.A. Catlow, R. Roque-Malherbe, A., *J. Phys. Chem. B* 102 (**1998**) 3198–3209.

[48]S. Amirjalayer and R. Schmid, Mechanism of benzene diffusion in MOF-5: A molecular dynamics investigation, *Micropor. Mesopor. Mater.* 125 (**2009**), pp. 90-96.

[49]S. D. Pickett, A. K. Nowak, A. K. Cheetham, J. M Thomas, Computer Simulation of the Location of Para-Xylene in Silicalite, *Mol. Sim.* 2, (**1988)**, pp. 353-360

[50]R.Q. Snurr, A.T. Bell, D.N. Theodorou, Molecular Simulations of Low Occupancy Adsorption of Aromatics in Silicalite, in Proceedings of the 9th International Zeolite Conference, Montreal 1992, ed. R. von Ballmoos, J.G. Higgins, M.M.J. Treacy, M.M.J., Butterworth-Heinemann: Stoneham, **1993**, pp 71-78.

[51]G. Ciccotti, M. Ferrario, Bluemoon approach to rare events *Mol. Sim.*,30, (**2004**), 30, pp. 787-793.

[52]J. Hénin, C. Chipot,Overcoming free energy barriers using unconstrained molecular dynamics simulations, *J. Chem. Phys.*,121 (**2004)**,pp. 2904.

[53]G. M. Torrie and J. P. Valleau, Nonphysical sampling distributions in Monte Carlo free-energy estimation: Umbrella sampling, *J. Comp. Phys.* 23 (**1977**), pp. 187-199.

[54]I. V. Khavrutkii, J. Dzubiella, J. A. McCammon, Computing accurate potentials of mean force in electrolyte solutions with the generalized gradient-augmented harmonic Fourier beads-method, *J. Chem. Phys.*, 128 (**2008**), pp. 044106

[55]S. Kumar, D. Bouzida, R. H. Swendsen, P. Kollman, J. M. Rosenberg, The weighted histogram analysis method for free energy calculations on biomolecules. I. Method, *J. Comput. Chem.*, 13 (**1992**), pp. 1011-1021

[56]B. Roix, The calculation of the potential of mean force using computer simulations, *Comput. Phys. Commun.*, 91 (**1995**), pp. 275-282

[57]R. J. Verploegh, S. Nair, D. S. Sholl Temperature and Loading-Dependent Diffusion of Light Hydrocarbons in ZIF-8 as Predicted Through Fully Flexible Molecular Simulations, *J. Am. Chem. Soc.*, 137 **(2015)**, pp. 15760-15771.

[58]J. Camp, D. S. Sholl, Transition State Theory Methods to Measure Diffusion in Flexible Nanoporous Materials: Application to a Porous Organic Cage Crystal, *J. Phys. Chem. C*, 120, (**2016**), pp. 1110–1120.

[59]H.A. Kramers, Brownian motion in a field of force and the diffusion model of chemical reactions, *Physica*, 7 (**1940**), pp. 284-304.

[60]E. J. Maginn, A. T. Bell and D. N. Theodorou, Transport Diffusivity of Methane in Silicalite from Equilibrium and Nonequilibrium Simulations, *J. Phys. Chem.*, 97 (**1993**), pp. 4173-4181.

[61]K. Fukui, The path of chemical reactions - the IRC approach, *Acc. Chem. Res.* 14 (1981), pp. 363-368.

[62]R. L. June, A. T. Bell, D. N. Theodorou, Transition-state studies of xenon and SF6 diffusion in silicalite, *J. Phys. Chem.*, 95, (**1991**),pp.8866-8878

[63]D. N. Theodorou, U. W. Suter, Detailed Molecular Structure of a Vinyl Polymer Glass, *Macromolecules* 18 (**1985**), pp. 1467-1478.

[64]H. Jobic, M. Bée, A. J. Dianoux, Quasi-elastic neutron scattering study of benzene adsorbed in ZSM-5, *J. Chem. Soc., Faraday Trans. 1*, 85 (**1989**) , pp. 2525-2534

[65]C. Dellago, P. G. Bolhuis, P. L. Geissler, Transition Path Sampling, *Adv. Chem. Phys.*, 123, (**2001**), pp.1-84

[66] B. Smit, T. L. M. Maesen, Molecular Simulations of Zeolites: Adsorption, Diffusion and Shape Selectivity, *Chem. Rev.* 108 (**2008**), pp. 4125-4184

[67]D. Chandler, Statistical-mechanics of isomerization dynamics in liquids and transition-state approximation, *J. Chem. Phys.*, 68 (**1978**), pp. 2959-2970.

[68]A. F. Voter, J.D. Doll, Dynamical corrections to transition state theory for multistate systems: Surface self-diffusion in the rare-event regime, *J. Chem. Phys.*, 83, **(1985)**, pp. 80-93.

[69]A. B. Bortz, M. H Kalos, J. L Lebowitz, A new algorithm for Monte Carlo simulation of Ising spin systems, *J. Comp. Phys.*, 17 (**1975**), pp. 10-18.

[70]C.H. Bennett, Exact defect calculations in model substances, in *Diffusion in Solids: Recent Developments*, edited by A.S. Nowick and J.J. Burton (Academic Press, New York, 1975), pp. 73-113.

[71]W. Feller, *An Introduction to Probability Theory and Its Applications*, Vol.2 (John Wiley, New York, **1971**).

[72]A. F. Voter, Introduction to the Kinetic Monte Carlo Method, in *Radiation Effects in Solids*, edited by K. E. Sickafus and E. A. Kotomin (Springer NATO Publishing Unit: Dordrecht, The Netherlands, **2005**).

[73]D.N. Theodorou, Principles of molecular simulation of gas transport in polymers, in *Materials Science of Membranes for Gas and Vapor Separation*, edited by Yu. Yampolskii, I. Pinnau, and B.D. Freeman (John Wiley, Hoboken, NJ, **2006**), pp. 47-92.

[74]N.V. Buchete and G. Hummer, Coarse Master Equations for Peptide Folding Dynamics, *J. Phys. Chem. B*, 112, (**2008**), pp. 6057

[75]G.C. Boulougouris, D.N. Theodorou, "Probing subglass relaxation in polymers via a geometric representation of probabilities, observables, and relaxation modes in discrete stochastic systems" *J. Chem. Phys.*, 130 (**2009**), pp. 044905.

[76]C. Blanco, C. Saravanan, M. Allen, and S. M. Auerbach, Modeling benzene orientational randomization in Na–Y zeolite at finite loadings with kinetic Monte Carlo and master equation methods. *J. Chem. Phys.* 113, (**2000**), pp. 9778.

[77]N. G. van Kampen, *Stochastic Processes in Physics and Chemistry* (North Holland, New York, **1981**).

[78]K.E. Shuler, Relaxation processes in multistate systems, Phys. Fluids, **2**, 442 (**1959**).

[79]M. O. Gonzalez, *Classical Complex Analysis*, Marcel Dekker Inc., New York, pp.47

[80]M.S. Gockenbach, *Partial Differential Equations-Analytical and Numerical Methods*, (Society for Industrial and Applied Mathematics, Philadelphia, PA, **2002**), pp. 72-74 and 245-249.

[81]H.S. Carlslaw, J.C. Jaeger, Conduction of Heat in Solids, Clarendon, Oxford, **1959**

[82]E. Zauderer, *Partial Differential Equations of Applied Mathematics*, 2nd Edition, (Wiley, New York, **1989**), pp. 8.

[83]J. Kärger and D.M. Ruthven, *Diffusion in Zeolites and Other Microporous Solids*, John Wiley, New York (**1992**).

[84]R. L. June, A. T. Bell, and D. N. Theodorou, Molecular dynamics study of methane and xenon in silicalite, *J. Phys. Chem*,. 94 (**1990**), pp. 8232-8240.

[85]*User's Manual, Imsl Stat/library: Fortran Subroutines for Statistical Analysis*. (IMSL, Houston, TX, **1989**).

[86]*User's Manual: Imsl Math/library : Fortran Subroutines for Mathematical Applications* (IMSL, Houston, TX, **1989**).

[87]E. Anderson, Z. Bai, C. Bischof, S. Blackford,J. Demmel, J. Dongarra, J. Du Croz, A., Greenbaum, S. Hammarling, A.McKenney, D.Sorensen, *LAPACK user's guide*, 3rd Edition (Society for Industrial and Applied Mathematics, Philadelphia, PA, **1999**).

[88]W.H. Press, S.Teukolsky, W.Vetterling, and B. Flannery, *Numerical Recipes in Fortran 90. The Art of Parallel Scientific Computing*, 2nd Edition, Cambridge University Press, Cambridge **1996**.

[89]J. Ma, Z.Y. Dong, P. Zhang, Comparison of BR and QR eigenvalue algorithms for power system small signal stability, *IEEE trans. on power systems*, 21, (**2006**) pp.1856

[90]J. Kärger**,** H. Pfeifer**,** F. Stallmach, N.N. Feoktistova**,** and S.P. Zhdanov**,** *Zeolites*, 13, (**1993**), pp.50

[91]A. S. Alfa, J. Xue, Q. Ye, Accurate computation of the smallest eigenvalue of a diagonally dominant M-matrix, *Math. Comp.*, 71 (**2001**), pp. 217-236

[92]MATLAB Version R2009b, The MathWorks Inc., Natick, MA, (**2009**).

[93]E. Hairer, S.P. Norset, G. Wanner, *Solving Ordinary Differential equations I- Nonstiff Problems*, 2nd Revised Edition (Springer, Berlin, **1993**), pp. 80 and 132-187.

[94]L.V.C. Rees and D. Shen , Frequency-response measurements of diffusion of xenon in silicalite-1, *J. Chem. Soc., Faraday Trans.*, 86, (**1990**), pp. 3687.

[95]C. R. Catlow, C. M. Freeman, M. S. Islam, R. A. Jackson, M. Leslie and S M. Tomlinson, Interatomic potentials for oxides, *Philos. Mag. A*, 58 (**1988**), pp.123-141.

[96]B. W. H. van Beest, G. J. Kramer and R. A. van Santen, Force Fields for silicas and Aluminophosphates based on Ab Intitio Calculations, *Phys. Rev. Lett.*, 64 (**1990**), pp. 1955-1958.

[97]S. Leroch and M. Wendland, Simulation of Forces between Humid Amorphous Silica Surfaces: A Comparison of Empirical Atomistic Force Fields, *J. Phys. Chem. C*, 116 (**2012**), pp. 26247-26261.

[98]J. B. Nicholas, A. J. Hopfinger, F. R. Trouw and L. E. Iton, Molecular modeling of zeolite structure. 2. Structure and dynamics of silica sodalite and silicate force field, *J. Am. Chem. Soc.*, 113 (**1991**), pp. 4792-4800.

[99]D. Herzbach,K. Binder, M. H. Muser, Comparison of model potentials for molecular-dynamics simulations of silica, *J. Chem. Phys.*, 123 (**2005**), 124711.

[100]E. Demiralp, T. Çağin and W. A. Goddard III, Morse Stretch Potential Charge Equilibrium Force Field for Ceramics: Application to the Quartz-Stishovite Phase Transition and to Silica Glass, *Phys. Rev. Lett.*, 82, (**1999**), pp. 1708-1711.

[101]P. Tangney and S. Scandolo, An ab initio parametrized interatomic force field for silica, *J. Chem. Phys.*, 117 (**2002**), pp. 8898-8904.

[102]P. Bordat, P. Cazade, I. Baraille, R. Brown, Host and adsorbate dynamics in silicates with flexible frameworks: Empirical force field simulation of water in silicalite, *J. Chem. Phys*., 132 (**2010**), pp. 094501.

[103]S. Quartieri, R. Arletti, G. Vezzalini, F. Di Renzo, V. Dmitriev, Elastic behavior of MFI-type zeolites: 3-compressibility of silicalite and mutinate, J. *Solid State Chem*., 191, (**2012**) , pp.201-212.

[104]T. J. H. Vlugt and M. Schenk, Influence of Framework Flexibility on the Adsorption Properties of Hydrocarbons in the Zeolite Silicalite, *J. Phys. Chem. B*, 106 (**2002**), pp. 12757-12763.

[105]P. Demontis, G. B. Suffriti, S. Quartieri, E. S. Fois and A. Gamba, Molecular dynamics studies on zeolites. 3. Dehydrated zeolite A, *J. Phys. Chem*,. 92 (**1988**), pp. 867-871.

[106]D. H. Olson, G. T. Kokotailo, S. L. Lawton and W. M. Meier, Crystal structure and structure-related properties of ZSM-5, *J. Phys. Chem.*, 85 (**1981**), pp. 2238-2243.

[107]R. Krishna, J. M. van Baten, Comment on "Modelling Adsorption and Self-Diffusion of Methane in LTA Zeolites: The Influence of Framework Flexibility", *J. Phys. Chem. C*, 114 (**2010**), pp. 18017-18021

[108]N. E. R. Zimmermann, S. Jakobtorweihen, E. Beerdsen, B. Smit, F. J. Keil, In Depth Study of the Influence of Host-Framework Flexibility on the Diffusion of Small Gas Molecules in One-Dimensional Zeolitic Pore Systems, *J. Phys. Chem. C*, 111 (**2007**), pp.17370-17381

[109]H. Sun, COMPASS: An ab Initio Force-Field Optimized for Condensed-Phase Applications-Overview with Details on Alkane and Benzene Compounds, J. Phys. Chem. B, 102 (**1998**), pp. 7338-7364.

[110]K. S. Smirnov and D. Bougeard, Molecular dynamics study of the vibrational spectra of siliceous zeolites built from sodalite cages, *J. Phys. Chem.*, 97 (**1993**), pp. 9434-9440.

[111]K. Makrodimitris, G. K. Papadopoulos and D. N. Theodorou, Prediction of Permeation Properties of CO2 and N2 through Silicalite via Molecular Simulations, *J. Phys. Chem. B* 105 (**2001**), pp. 777-788.

[112]M.H. Shultz (1973), Spline Analysis, Prentice-Hall, Englewood Cliffs, p. 29. D. Kanaher, C. Moler, and S. Nash, (1988), Numerical Methods and Software, Prentice Hall, Englewood Cliffs, Ch 4 .

[113]M. Parrinello, A. Rahman, Polymorphic transitions in single crystals: A new molecular dynamics method, *J. Appl, Phys.*, 52 (**1981**), pp. 7182-7190.

[114]S. Melchionna, G. Ciccotti, B. Lee Holian, Hoover NPT dynamics for systems varying in shape and size. *Mol. Phys.*, 78 (**1993)**, pp.533-544.

[115]W. G. Hoover, Canonical Dynamics: Equilibrium Phase-space Distributions. *Phys. Rev. A*, (**1985**), pp. 1695-1697.

[116]P. G. Krokidas, V. Nikolakis, V. N. Burganos, Heating and sorption effects on silicalite-1 unit cell size and geometry, *Microporous Mesoporous Mater*, 155 (**2012**), pp. 65-70.

[117]R. W. Hockney, J. W. Eastwood, *Computer Simulation using Particles*, Adam Hilger, New York, U.S.A., **1989**

[118]E. L. Pollock, J. Glosli, Comments on P 3 M, FMM, and the Ewald method for large periodic Coulombic systems, *Comput. Phys. Commun.* 95 (**1996**), pp. 93-110.

[119]S. Plimpton, R. Pollock, M. Stevens "Particle-Mesh Ewald and rRESPA for Parallel Molecular Dynamics Simulations." *PPSC*. (**1997**), pp. 1-5.

[120]M. Deserno, C. Holm, How to mesh up Ewald sums. II. An accurate error estimate for the particle–particle–particle-mesh algorithm, *J. Chem. Phys.* ,108 (**1998**), pp. 7694

[121]S. C. Harvey, R. K. Z. Tan, T. E. Cheatham"The flying ice cube: Velocity rescaling in molecular dynamics leads to violation of energy equipartition".*J. Comput. Chem.*,19 (**1998**), pp.726–740.

[122]M. Tuckerman, B. J. Berne, G.J. Martyna, Reversible multiple time scale molecular dynamics, *J .Chem. Phys.*, 97 (**1992**), pp. 1990-2001

[123]M. P. Allen, D. J. Tildesley, *Molecular Simulation of Liquids*, Oxford University Press, Oxford, U.K., **1987** ; Ch. 7.4.3

[124]D. Brown, J. H. R. Clarke, A comparison of constant energy, constant temperature and constant pressure ensembles in molecular dynamics simulations of atomic liquids, *Mol. Phys*, 51 (**1984**), pp. 1243-1252.

[125] D. Fincham, Leapfrog Rotational Algorithms, *Mol. Sim.*, 8 (**1992**), pp. 165-178.

[126]R. Goyal, A. N. Fitch, H. Jobic, Powder Neutron and X-ray Diffraction Studies of Benzene Adsorbed in Zeolite ZSM-5, *J. Phys. Chem. B*, 104 (**2000**), pp.2878-2884.

[127]H. Jobic et al. (in preparation).

[128]P.D. Kolokathis, E. Pantatosaki, G.K . Papadopoulos, "Atomistic Modeling of Thermodynamics and Kinetics of Water within MIL-100(Fe)", *J. Phys. Chem. C*, 119 (**2015**), pp. 20074-20084

[129]B. Zibrowius, J. Carro, H. Pfeiper, Deuterium nuclear magnetic resonance studies of the molecular dynamics of benzene in zeolites, *J. Chem. Soc., Faraday Trans. 1*, 84 (**1988**), pp. 2347-2356

[130]B. F. Mentzen, Characterization of guest molecules adsorbed on zeolites of known structure by combined X-ray powder profile refinements and conventional difference-Fourier techniques. Part I — Localization of the benzene molecule in a pentasil type zeolite, *Mat. Res. Bull.*, 22 (**1987**), pp. 337-343.

[131]B. F. Mentzen, Characterization of guest molecules adsorbed on zeolites of known structure by combined x-ray powder profile refinements and conventional difference-fourier techniques. Part II - Localization of the n-hexane, TPA and p-xylene guests in a pentasil type zeolite, *Mat. Res. Bull*, 22 (**1987**), pp. 489-496.

[132]H. Jobic, W. Schmidt, C.B. Krause, J. Kärger, PFG NMR and QENS diffusion study of n-alkane homologues in MFI-type zeolites, *Microporous Mesoporous Mater.*, 90 (**2006**), pp. 299-306.

[133]E. Pantatosaki, G. Megariotis, A.-K. Pusch , Ch. Chmelik, F. Stallmach and G. K. Papadopoulos, On the Impact of Sorbent Mobility on the Sorbed Phase Equilibria and Dynamics: A Study of Methane and Carbon Dioxide within the Zeolite Imidazolate Framework-8, *J. Phys. Chem. C*, 116 (**2012**), pp. 201–207.

[134]E. Pantatosaki, H. Jobic, D. I. Kolokolov, Sh. Karmakar, R. Biniwale and G. K. Papadopoulos, Probing the hydrogen equilibrium and kinetics in zeolite imidazolate frameworks via molecular dynamics and quasi-elastic neutron scattering experiments, *J. Chem. Phys.*, 138 (**2013**), pp. 034706.